



HAL
open science

Nouveaux mécanismes du développement des tumeurs cérébrales

Joris Guyon

► **To cite this version:**

Joris Guyon. Nouveaux mécanismes du développement des tumeurs cérébrales. Biologie cellulaire. Université de Bordeaux, 2021. Français. NNT : 2021BORD0344 . tel-03576571

HAL Id: tel-03576571

<https://theses.hal.science/tel-03576571>

Submitted on 16 Feb 2022

HAL is a multi-disciplinary open access archive for the deposit and dissemination of scientific research documents, whether they are published or not. The documents may come from teaching and research institutions in France or abroad, or from public or private research centers.

L'archive ouverte pluridisciplinaire **HAL**, est destinée au dépôt et à la diffusion de documents scientifiques de niveau recherche, publiés ou non, émanant des établissements d'enseignement et de recherche français ou étrangers, des laboratoires publics ou privés.

Université de Bordeaux

École Doctorale des Sciences de la Vie et de la Santé

Année 2021

Thèse pour l'obtention du

Doctorat de l'Université de Bordeaux

Mention : Biologie cellulaire et Physiopathologie

Nouveaux mécanismes du développement des tumeurs cérébrales

Présentée et soutenue publiquement par

Joris GUYON

Le 17 Décembre 2021

Membres du jury

| | | |
|---------------------------|--|--------------------|
| Mme Sophie JAVERZAT | Professeure, Université de Bordeaux | Présidente |
| Mme Marie-Pierre JUNIER | Directeur de recherche, Université de Paris - Sorbonne | Rapporteur |
| Mr Eric CHEVET | Directeur de recherche, Université de Renne | Rapporteur |
| Mme Audrey CARRIERE-PAZAT | Chargée de recherche, Université de Toulouse | Examinatrice |
| Mr Andréas BIKFALVI | Professeur, Université de Bordeaux | Directeur de thèse |
| Mr Thomas DAUBON | Chargé de recherche, Université de Bordeaux | Invité |

Remerciements

J'exprime toute ma gratitude à Madame le Professeur Sophie Javerzat pour avoir accepté de présider le jury de thèse.

J'adresse tous mes remerciements à Madame Marie-Pierre Junier et Monsieur Éric Chevet, de l'honneur qu'ils m'ont fait en acceptant d'être rapporteurs de ce travail.

Je remercie Madame Audrey Carriere-Pazat pour avoir accepté d'examiner mon travail de thèse.

Je tiens à remercier Monsieur le Professeur Andréas Bikfalvi, qui m'a encadré tout au long de cette thèse et qui a su « Bikfalviser » mes écrits. Je lui suis reconnaissant pour son écoute bienveillante et ses encouragements.

Je souhaite également exprimer ma gratitude à Monsieur Thomas Daubon qui a aiguillé mes travaux tout au long de ma thèse. Je le remercie pour le temps qu'il m'a accordé, sa participation active à la relecture et à la correction de cette thèse, ainsi qu'aux collaborations auxquelles il m'a invité, me permettant ainsi d'enrichir ma culture scientifique.

Enfin, je tiens à remercier tous les membres du LAMC, pour leur soutien et leurs réponses aux questions quotidiennes dont je les accablais.

Je remercie également l'équipe Biodynamit pour leur accueil et leur grande contribution à ce projet de thèse.

Dédicaces

Aux membres du labo et univers étendu

A Jean, pour nos échanges sans queue ni tête et nos délires sur tout est n'importe quoi.

A Nico, pour nos conversations sur le monde, les genres et la permaculture.

A Capucine, pour sa générosité, son sourire et sa bonne humeur permanente.

A Nadège, la maman du labo, pour son accompagnement, son apprentissage et son écoute.

A Oui², la mascotte du labo, chevalier (jedi) dans l'âme prêt à secourir veuves et orphelins.

A Marie-Alix, pour ce nombre incalculable de sphéroïdes que je t'ai envoyé.

A Laëtitia, pour ses conseils techniques et son soutien réconfortant.

A Fafa, pour son énergie et son attention quotidienne.

A Isabelle et Patrick, pour leur bienveillance et leur gentillesse.

A Andrea et Tiffanie,

A Kristell et Laura, les petites bretonnes dernières arrivées.

A toute l'équipe de choc de Thomas : Claire, Cyrielle, Boutaina, Antonio et Mr Sylvain.
Également à Arnaud pour ses conseils et sa passion pour la Science.

A la famille et aux amis d'enfance

A mes parents, qui m'ont soutenu tout au long de ce parcours. Je les remercie pour leurs encouragements et leur amour inconditionnel.

A Loan et Isaure, vous m'avez accompagné tout au long de mon enfance et je vous remercie pour tous ces moments partagés.

A Mémée, je te remercie pour tes délicieux desserts, jamais encore égalés, qui m'ont régalié depuis toujours.

A Dominique et Louissette dont je te suis reconnaissant d'avoir su déceler mon potentiel et m'avoir encouragé à faire des études ambitieuses.

A Georges, je vous suis reconnaissant pour votre soutien et pour nos échanges scientifiques qui ont su nourrir et inspirer mes réflexions autour de mes travaux de recherche.

A Véronique, merci pour votre soutien et l'intérêt que vous avez porté à mon travail.

A Jean, pour ton soutien informatique et nos discussions qui m'ouvraient à d'autres horizons.

A Hélène, merci pour ton enthousiasme lors de ton stage dans le laboratoire, tu m'as donné la chance de t'encadrer et de partager ma passion pour la science avec toi.

A Louis, Clément et Raphaël, pour tous nos moments passés devant la console ou dehors lors nos escapades au skate parc avec les 180 qui finissaient toujours bien (pour moi en tout cas).

Aux autres copains

A Sophie T, pour son énergie infinie et sa bonne humeur.

A Sophie L, pour être l'une des rares à supporter mes musiques de soirée.

A Simon, éternel mystère de la vie aux talents immenses.

Je remercie chaleureusement tous les autres personnes dont leur chemin a croisé mon aventure.

Et puis à toi, Marie, le soleil qui illumine ma vie. Tu as toujours été là pour moi, je te remercie encore pour ton soutien, ton aide et ton réconfort permanent.

Ainsi qu'à Aloïs et Oscar, mes deux petits bonhommes qui me remplissent de joie et de bonheur. Je vous dédie ce travail.

Table des matières

| | |
|---|-----------|
| Liste des tableaux | 7 |
| Liste des figures | 7 |
| Abbréviations | 8 |
| 1 Introduction | 11 |
| 1.1 Généralités sur les cancers | 11 |
| 1.2 Les tumeurs du système nerveux central et glioblastomes | 12 |
| 1.2.1 Terminologie et épidémiologie | 12 |
| 1.2.2 Classification des gliomes | 12 |
| 1.2.3 Origine des GBMs | 16 |
| 1.2.4 Cellules souches cancéreuses..... | 17 |
| 1.2.5 Aspect clinique et diagnostic..... | 17 |
| 1.2.6 Prise en charge | 18 |
| 1.3 Exploration thérapeutique | 19 |
| 1.3.1 Thérapie ciblée | 19 |
| 1.3.2 Immunothérapies | 21 |
| 1.4 Métabolisme énergétique tumoral | 24 |
| 1.4.1 Notions de base..... | 24 |
| 1.4.2 Métabolisme cérébral..... | 30 |
| 1.4.3 Dérégulation énergétique et reprogrammation métabolique des tumeurs | 32 |
| 1.5 Lignées cellulaires | 35 |
| 1.5.1 Lignées cellulaires établies..... | 36 |
| 1.5.2 Xénogreffes dérivées de patient (PDX) | 36 |
| 1.5.3 Lignées non-adhérentes..... | 36 |
| 1.6 Infiltration tumorale | 37 |
| 1.7 Objectifs | 38 |
| 2 Modélisation expérimentale | 39 |
| 2.1 Liste des articles relatifs à ce chapitre | 39 |
| 2.2 Réglementation | 39 |
| 2.3 Extraction, établissement et entretien | 39 |
| 2.4 Expérimentations <i>in vitro</i> | 41 |

| | | |
|------------|---|------------|
| 2.4.1 | Introduction | 41 |
| 2.4.2 | Préparation de sphéroïdes de taille homogène | 42 |
| 2.4.3 | Expériences de croissance..... | 42 |
| 2.4.4 | Expériences d'invasion..... | 43 |
| 2.4.5 | Analyse des expériences | 44 |
| 2.4.6 | Coupe coronale d'un sphéroïde envahissant une matrice de collagène | 48 |
| 2.4.7 | Co-culture avec des neurones | 49 |
| 2.5 | Expérimentations <i>in vivo</i> | 53 |
| 3 | Articles | 55 |
| 3.1 | The invasive proteome of glioblastoma revealed by laser-capture microdissection..... | 55 |
| 3.2 | Specific expression of lactate dehydrogenases in glioblastoma controls intercellular lactate transfer to promote tumor growth and invasion..... | 69 |
| 4 | Conclusion - Discussion | 123 |
| 4.1 | Pertinence des modèles d'expérimentation | 123 |
| 4.2 | Étude de l'infiltration des GBMs..... | 126 |
| 4.3 | Blocage du métabolisme fermentatif des GBMs..... | 127 |
| 4.4 | Conclusion générale..... | 130 |
| | Bibliographie | 131 |
| | Annexe..... | 151 |

Liste des tableaux

| | |
|---|----|
| Tableau 1 : Classification OMS 2021 des gliomes, tumeurs glioneuronales et tumeurs neuronales | 15 |
| Tableau 2 : Valeurs des couleurs..... | 45 |

Liste des figures

| | |
|---|-----|
| Figure 1 : Classification de 2021 d'après l'OMS selon les altérations moléculaires des tumeurs gliales | 16 |
| Figure 2 : Aperçu des principales stratégies thérapeutiques du GBM..... | 23 |
| Figure 3 : Schéma des principales voies métaboliques énergétiques issues du glucose..... | 24 |
| Figure 4 : La glycolyse | 26 |
| Figure 5 : Le cycle de Krebs..... | 28 |
| Figure 6 : La fermentation lactique | 29 |
| Figure 7 : Formation des différents isomères des LDHs..... | 30 |
| Figure 8 : Schéma de la navette lactate entre astrocytes et neurones | 32 |
| Figure 9 : Modèles cellulaires issus d'une biopsie tumorale..... | 35 |
| Figure 10 : Établissement d'une lignée cellulaire issue de patient..... | 40 |
| Figure 11 : Marquage de cellules adhérentes provenant de sphéroïdes dissociés..... | 41 |
| Figure 12 : Le sphéroïde est un modèle intermédiaire pour mimer les tumeurs solides..... | 42 |
| Figure 13 : Aperçu des expérimentations réalisables avec des sphéroïdes..... | 44 |
| Figure 14 : Présentation de l'algorithme de segmentation..... | 47 |
| Figure 15 : Processus pour manipuler, paraffiner et marquer des sphéroïdes invasifs en matrice de collagène | 49 |
| Figure 16 : Coculture des cellules de GBM sur un tapis de neurones | 52 |
| Figure 17 : Immunohistologie sur une coupe coronale d'un cerveau de souris | 53 |
| Figure 18 : Voie du métabolisme du lactate..... | 128 |

Abbréviations

Général

BHE : Barrière-Hémato-Encéphalique
CD : Cellules Dendritiques
CSCs : Cellules Souches Cancéreuses
GBM : Glioblastome
IRM : Imagerie par Résonance Magnétique
iTK : inhibiteur de Tyrosine Kinase
KPS : Performance Statuts selon Karnofsky
LT : Lymphocyte T
OMS : Organisation Mondiale de la Santé
NOS : Not Other Specified
PDX : Xénogreffe Dérivée de Patient
RCP : Réunions de concertations pluridisciplinaires
SNC : Système Nerveux Central
SI : Système Immunitaire
TMZ : Témazolomide

Nucléotides

AMP : Adénosine MonoPhosphate
AMPc : Adénosine MonoPhosphate cyclique
ADP : Adénosine DiPhosphate
ATP : Adénosine TriPhosphate
CMP : Cytidine MonoPhosphate
CDP : Cytidine DiPhosphate
CTP : Cytidine TriPhosphate
GMP : Guanosine MonoPhosphate
GMPc : Guanosine MonoPhosphate cyclique
GDP : Guanosine DiPhosphate
GTP : Guanosine TriPhosphate

Voies de signalisation

EGFR : Récepteur au Facteur de Croissance Épidermique

PD-1 : Programmed Death-1

PD-L1 : Programmed Death-1 Ligand

VEGF : Facteur de Croissance Endothélial Vasculaire

Enzymes diverses

MGMT : O⁶-méthylguanine-DNA méthyltransférase

TERT : TElomerase Reverse Transcriptase

Métabolisme

α -KG : α -Cétoglutarate

DHAP : Dihydroxyacétone Phosphate

FAD : Flavine Adénine Dinucléotide

F6P : Fructose-6-Phosphate

FbP : Fructose-1,6-biphosphate

G6P : Glucose-6-Phosphate

GA3P : Glycéraldéhyde-3-Phosphate

GLUT : Transporteur au GLUCose

HK : Hexokinase

IDH : Isocitrate Déshydrogénase

LDH : Lactate Déshydrogénase

MCT : Transporteur aux MonoCarboxylates

NAD : Nicotinamide Adénine Dinucléotide

OAA : Oxaloacétate

OxPhos : Oxydation Phosphorylante

PEP : PhosphoEnolPyruvate

PFK1 : Phosphofructokinase

PKM : Pyruvate Kinase

PG : Phosphoglycérate

TCA : Cycle de Krebs (TriCarboxylic Acid cycle)

1

Introduction

1.1 Généralités sur les cancers

Le cancer est une maladie caractérisée par la transformation de cellules qui vont proliférer de manière exagérée et non contrôlée. Une masse anormale se développe, les cellules envahissent le tissu sain, se détachent de la tumeur et passent par la circulation sanguine pour former de nouvelles niches tumorales (métastases).

La présence de lésions similaires à celles des tumeurs malignes sur des os de dinosaures suggère que le cancer existe depuis des millions d'années (1,2). C'est un phénomène observé dans la plupart des organismes multicellulaires avec une susceptibilité plus prononcée pour le règne animal (3). Actuellement, l'Homme présente des taux et des types de cancer qui diffèrent grandement de ce qui est observé dans l'Ordre des primates (4). Bien que l'Homme puisse encore être soumis à une pression de sélection pour s'adapter à son environnement, le prolongement de son espérance de vie dépend grandement des outils et des moyens qu'il a su développer pour survivre (5). Ainsi les cancers humains qui apparaissent précocement pourraient être liés aux processus évolutifs (mutations, prédispositions génétiques) alors que ceux qui apparaissent plus tardivement pourraient être sous l'influence de l'environnement et du mode de vie (4).

En France, les décès par cancer représentent la 1^{ère} cause de mortalité chez l'homme et la 2^{ème} chez la femme. L'incidence normalisée selon l'âge de tous cancers confondus en 2020 est estimée à 341,9 cas par 100 000 habitants (6). Dans le monde, les cancers les plus fréquemment recensés sont les cancers du sein (\approx 2,3 millions), du poumon (\approx 2,2 millions), colorectal (\approx 1,9 millions) et de la prostate (\approx 1,4 millions) (6).

1.2 Les tumeurs du système nerveux central et glioblastomes

1.2.1 Terminologie et épidémiologie

Selon l'Organisation Mondiale de la Santé, les tumeurs du système nerveux central (SNC) représentent environ de 2% des cancers. Chez les enfants, elles sont la principale cause de décès par tumeur solide et la deuxième tumeur la plus fréquente, après les leucémies (7). L'incidence annuelle chez les adultes est de 21 cas pour 100 000 habitants.

Les tumeurs cérébrales constituent un groupe hétérogène de maladies divisées en trois grandes catégories selon le tissu ou le type cellulaire atteint. Les tumeurs des méninges prennent naissance dans les enveloppes englobant le cerveau, à savoir la dure-mère, l'arachnoïde et la pie-mère. Les neurinomes se développent à partir des nerfs crâniens et spinaux. Enfin, les tumeurs neuro-épithéliales sont issues de la transformation des constituants du SNC (neurones et cellules de soutien) et sont les plus fréquentes.

Issus de cette dernière catégorie, les gliomes représentent plus du tiers de l'ensemble des tumeurs cérébrales. Ils sont divisés en deux sous-groupes qui distinguent les gliomes de bas grade (grades 1 et 2), d'évolution lente et peu infiltratifs, des gliomes de haut grade ou « malins » (grades 3 et 4) à caractère anaplasique, prolifératif et diffus. Tumeur la plus fréquente des gliomes, le glioblastome (GBM) est également la plus agressive avec une médiane de survie des patients d'environ de 15 mois après traitement (8–10). La survie tend à diminuer avec l'avancement de l'âge des patients (11). Son incidence dans le monde varie entre 2 et 4 cas par 100 000 habitants (10). En France, les principales sources de données épidémiologiques pour les GBMs sont le Recensement national histologique des tumeurs cérébrales et le registre des tumeurs cérébrales de la Gironde, ce dernier informant d'une incidence locale de 5 cas par 100 000 habitants (12,13).

1.2.2 Classification des gliomes

La classification des tumeurs du SNC selon l'OMS évolue en parallèle de la progression des nouvelles technologies en biologie moléculaire. En 2016, elle réutilisait les critères anatomopathologiques proposés en 2007, tout en introduisant des approches basées sur la génétique moléculaire des gliomes (14,15). La classification de 2016 permettait

d'homogénéiser des entités tumorales en termes de pronostic et de réponse au traitement (15). Concrètement, le diagnostic histologique des gliomes diffus basé sur des critères morphologiques sépare astrocytomes, oligodendrogliomes et GBMs. Ensuite, le statut mutationnel de certains gènes était utilisé comme marqueur diagnostique et pronostic des gliomes :

- Les mutations des gènes de l'isocitrate déshydrogénase 1 et 2 (IDH1 et IDH2) apparaissent comme un facteur de meilleur pronostic (16). Ces gènes codent pour des enzymes qui catalysent la conversion réversible de l'isocitrate en α -cétoglutarate (ou 2-oxoglutarate) (17). Les mutations entraînent un changement de l'activité catalytique avec la production du 2-hydroxyglutarate (18) et l'altération du métabolisme tumoral (19). Elles sont généralement observées dans les gliomes de bas grades, évoquant l'apparition précoce de ces mutations lors du développement des gliomes (20).
- La perte du bras court du chromosome 1 et la perte du bras long du chromosome 19 (co-délétion 1p/19q) est une signature moléculaire des oligodendrogliomes (21). Elle est de meilleur pronostic et rend la tumeur plus sensible à la chimiothérapie (22).
- La protéine p53, nommée « gardienne du génome », est impliquée dans une grande partie des processus cellulaires, des interactions complexes entre les différentes voies de signalisation mais également sur les différents états de phase cellulaire (23). Elle est encodée par le gène TP53 et agit principalement comme un gène suppresseur de tumeur. Une mutation de TP53 est caractéristique des astrocytomes (24).
- Le promoteur TERT (*TElomerase Reverse Transcriptase*) intervient dans l'activité des télomérases et régule la sénescence répllicative. Une mutation du promoteur TERT est fréquemment retrouvée dans les GBMs et est associée à un très mauvais pronostic vital (25).
- Les mutations somatiques du gène codant pour la protéine chaperonne des histones ATRX (alpha thalassémie liée à l'X avec retard mental) joue un rôle épigénétique dans la régulation des télomères (26). Elle est souvent concomitante

avec des mutations de TP53 et du gène codant pour l'histone H3 dans les formes pédiatriques (27).

- L'hyperméthylation du promoteur du gène MGMT (O⁶-méthylguanine-DNA méthyltransférase) induit une perte d'expression de son enzyme qui répare les brins d'ADN. Sa présence est un facteur prédictif de réponse à la chimiothérapie alkylante, elle influence favorablement la survie des patients (28–30).
- Une amplification du gène du récepteur au facteur de croissance épidermique (EGFR) situé sur le chromosome 7 est détecté dans presque 60% des GBMs (31). Une surexpression de ce récepteur contribue à la tumorigenèse, à la résistance et à progression des GBMs (32). Il existe également des variants à ces récepteurs dont le III (EGFRvIII) qui est retrouvé dans 10% des GBMs et est activé sans liaison avec son ligand (33,34).

Lorsque les tests moléculaires s'avéraient non contributifs et que la tumeur ne pouvait être précisément catégorisée alors elle était classée dans la catégorie NOS (Not Other Specified). Enfin, le grade histo-pronostique des gliomes était établi en fonction des paramètres précédents. Les gliomes de grade I et II correspondent à des tumeurs bénignes ou à évolution très lente alors que ceux de grade III et IV regroupent des tumeurs à croissance rapide avec une forte infiltration du tissu sain.

Cependant, chaque classification présente ses limites (manque de reproductibilité, variabilité diagnostic) reflétant principalement l'état de l'art du domaine à un moment donné (35). La nouvelle classification des tumeurs cérébrales de 2021, prenant essence dans les précédentes, propose des changements substantiels pour faire progresser le rôle des diagnostics moléculaires (36). Les gliomes sont classés dans la catégorie « Gliomes, tumeurs glioneuronales et tumeurs neuronales » divisée en 6 familles (**Tableau 1**) : (1) les gliomes diffus de type adulte, (2) les gliomes diffus de bas grade de type pédiatrique et (3) les gliomes diffus de haut grade de type pédiatrique, (4) les gliomes astrocytaires circonscrits, (5) les tumeurs glioneuronales et neuronales, et enfin (6) les épendymomes. Ainsi, les gliomes pédiatriques sont séparés des gliomes des adultes car leurs différences moléculaires sont importantes (37). La classification de 2016 comptait 15 entités de gliomes chez les adultes, ce nombre est réduit à 3 types dans la nouvelle : (1) les astrocytomes IDH_{muté}, (2) les Oligodendrogliomes IDH_{muté} avec co-délétion 1p/19q et (3) les GBMs IDH_{wild-type}. Le statut

mutationnel d'IDH permet d'isoler les GBMs des astrocytomes et oligodendrogliomes (**Figure 1**). Les GBMs secondaires issus de l'évolution progressive de gliomes de plus bas grade (38) sont reclassés : ceux qui présentaient auparavant des mutations d'IDH deviennent des astrocytomes de haut grade (36).

Les GBMs appartiennent aux tumeurs de grade 4. Il s'agit de tumeurs malignes à croissance rapide et très infiltratives au niveau du parenchyme cérébral, elles n'envahissent généralement pas les organes distants. Les GBMs se caractérisent également par une angiogenèse locale et l'apparition de zones nécrotiques.

Tableau 1 : Classification OMS 2021 des gliomes, tumeurs glioneuronales et tumeurs neuronales (36)

| Gliomas, glioneuronal tumors, and neuronal tumors | | Grade |
|---|---|---------------------|
| Adult-type diffuse gliomas | <ul style="list-style-type: none"> • Astrocytoma, IDH-mutant • Oligodendroglioma, IDH-mutant, and 1p/19q-codeleted • Glioblastoma, IDH-wildtype | 2, 3, 4 2,3 4 |
| Pediatric-type diffuse low-grade gliomas | <ul style="list-style-type: none"> • Diffuse astrocytoma, <i>MYB</i>- or <i>MYBL1</i>-altered • Angiocentric glioma • Polymorphous low-grade neuroepithelial tumor of the young • Diffuse low-grade glioma, MAPK pathway-altered | 1 1 |
| Pediatric-type diffuse high-grade gliomas | <ul style="list-style-type: none"> • Diffuse midline glioma, H3 K27-altered • Diffuse hemispheric glioma, H3 G34-mutant • Diffuse pediatric-type high-grade glioma, H3-wildtype and IDH-wildtype • Infant-type hemispheric glioma | 4 |
| Circumscribed astrocytic gliomas | <ul style="list-style-type: none"> • Pilocytic astrocytoma • High-grade astrocytoma with piloid features • Pleomorphic xanthoastrocytoma • Subependymal giant cell astrocytoma • Chordoid glioma • Astroblastoma, <i>MN1</i>-altered | 2, 3 |
| Glioneuronal and neuronal tumors | <ul style="list-style-type: none"> • Ganglioglioma • Desmoplastic infantile ganglioglioma / desmoplastic infantile astrocytoma • Dysembryoplastic neuroepithelial tumor • <i>Diffuse glioneuronal tumor with oligodendroglioma-like features and nuclear clusters</i> • Papillary glioneuronal tumor • Rosette-forming glioneuronal tumor • Myxoid glioneuronal tumor • Diffuse leptomeningeal glioneuronal tumor • Gangliocytoma • Multinodular and vacuolating neuronal tumor • Dysplastic cerebellar gangliocytoma (Lhermitte-Duclos disease) • Dysplastic cerebellar gangliocytoma (Lhermitte-Duclos disease) • Extraventricular neurocytoma • Cerebellar liponeurocytoma | 1 |
| Ependymal tumors | <ul style="list-style-type: none"> • Supratentorial ependymoma • Supratentorial ependymoma, <i>ZFTA</i> fusion-positive • Supratentorial ependymoma, <i>YAP1</i> fusion-positive • Posterior fossa ependymoma • Posterior fossa ependymoma, group PFA • Posterior fossa ependymoma, group PFB • Spinal ependymoma • Spinal ependymoma, <i>MYCN</i>-amplified • Myxopapillary ependymoma • Subependymoma | 2, 3 2, 3 2 |

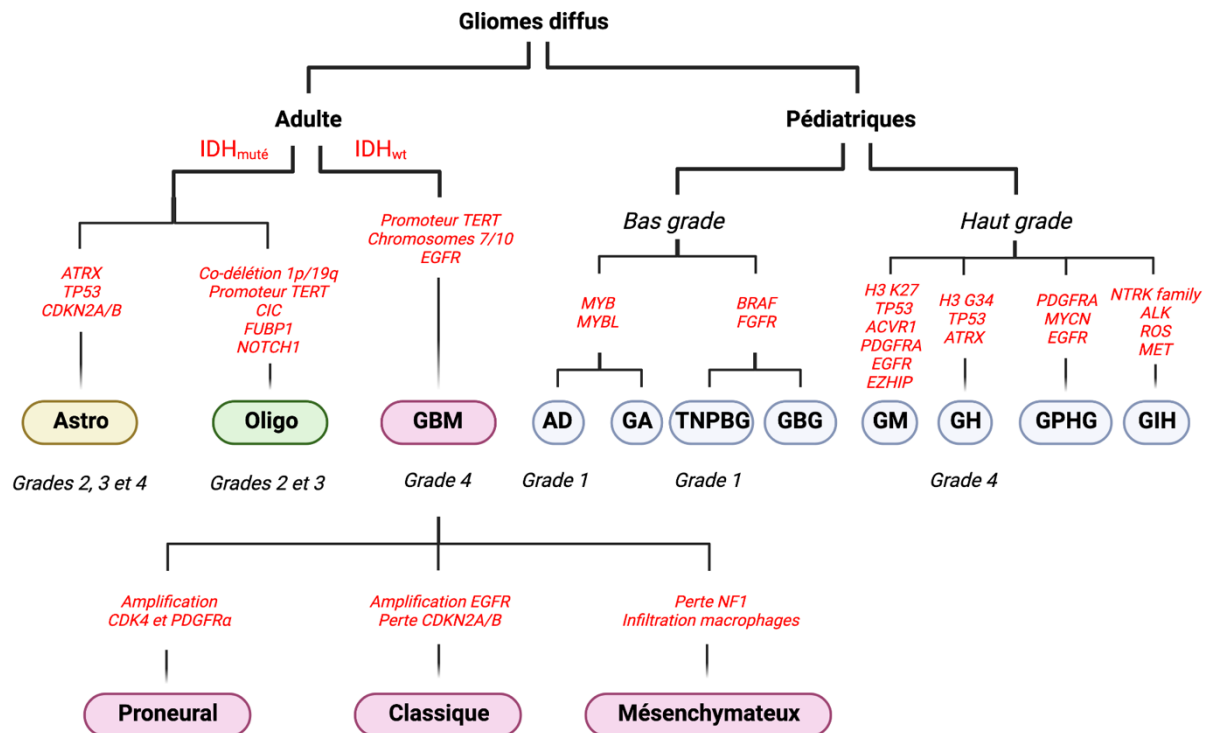


Figure 1 : Classification de 2021 d'après l'OMS selon les altérations moléculaires des tumeurs gliales

D'après (36,39) ; Astro = astrocytome ; Oligo = oligodendrogliome ; GBM = glioblastome ; AD = astrocytome diffus ; GA = gliomes angiocentrique ; TNPBG = tumeur neuroépithéliale polymorphe de bas grade ; GBG = gliome diffus de bas grade ; GM = gliome diffus médian ; GH = gliome diffus hémisphérique ; GPHG = gliome pédiatrique diffus de haut grade ; GIH = gliome infantile diffus hémisphérique.

1.2.3 Origine des GBMs

Les GBMs sont des tumeurs hétérogènes, les cellules existent sous différents états de différenciation et peuvent être assimilées à des progéniteurs neuronaux et oligodendrocytaires, à des astrocytes et à des cellules mésenchymateuses (40). Les cellules cancéreuses progénitrices exprimant des caractéristiques de cellules souches neurales sont capables de se différencier et de s'organiser comme la hiérarchie de la lignée neurale normale (41,42). La connaissance de l'origine cellulaire des GBMs, *via* des cellules progénitrices neurales (43) ou *via* des cellules différenciées devenant anaplasiques (44), présente un intérêt dans la prédiction de la réponse thérapeutique (45).

Les causes de survenue des GBMs sont mal connues et peuvent être multiples. Parmi les facteurs de risque, peuvent être cités l'exposition aux rayonnements ionisants (46,47) ainsi que l'existence de prédispositions génétiques (48,49). Certains facteurs environnementaux et professionnels (pesticides, métaux lourds) sont mis en doute dans la survenue de gliomes malgré l'observation de variabilités géographiques et de différences observées entre les

hommes et les femmes (50–52). D'autres cancers s'initient suite à des infections virales (papillomavirus et cancers du col de l'utérus) (53) ou bactériennes (*helicobacter pylori* et cancers gastriques) (54). L'étiologie virale représente 10 à 15% des cancers dans le monde (55). Certaines infections virales à *herpesviridae* (virus Epstein-Barr - EBV ou cytomégalovirus humain - HCMV) pourraient jouer un rôle dans le développement de certains sous-types GBMs (56–58). D'autant plus que l'infection à HCMV peut induire la dédifférenciation cellulaire et générer des cellules cancéreuses souches géantes à l'origine de cancers à mauvais pronostic (59).

1.2.4 Cellules souches cancéreuses

Les cellules souches cancéreuses (CSCs) correspondent à une population de cellules initiatrices de tumeur capables de s'auto renouveler et de se différencier en plusieurs sous-types cellulaires (60). Elles expriment des protéines retrouvées chez les cellules souches neuronales comme par exemple Sox2 ou la nestine. Sox2 est un facteur de transcription qui forme un complexe avec Nanog et Oct4, ils interviennent dans le maintien du phénotype souche (61) et la neurogenèse (62). La nestine est un filament intermédiaire exprimée par progéniteurs du SNC (63), elle apparait comme un marqueur d'invasion des CSCs (64). Il existe d'autres marqueurs potentiels de CSCs comme CD44, CD90, CD133, CXCR4, L1CAM ET SSEA1 ayant un rôle dans le maintien du phénotype souche ou de la migration/invasion.

Les CSCs ont la capacité d'être cultivées sous la forme de neurosphères et de reformer la tumeur originelle après xenogreffe cérébrale (60). Cette population s'adapte et développe des résistances aux traitements (65).

1.2.5 Aspect clinique et diagnostic

Le diagnostic et la prise en charge thérapeutique d'un GBM doivent être réalisés en urgence du fait de l'évolution rapide de la tumeur et des séquelles neurologiques rarement réversibles qu'elle engendre. L'imagerie par résonance magnétique (IRM) est l'examen de référence pour investiguer l'apparition récente de signes cliniques neurologiques (céphalées, épilepsies, déficits minimes) (66). L'examen clinique comporte également des indices de performance statuts selon Karnofsky (KPS) ou selon l'OMS (PS) pour évaluer l'état de santé général de la personne (66).

En raison de l'hétérogénéité cellulaire des GBMs, le diagnostic combine des approches de profiling moléculaires à l'analyse histologique issus de plusieurs prélèvements (36).

1.2.6 Prise en charge

La stratégie thérapeutique est envisagée après discussion d'au moins trois médecins de spécialités différentes en réunions de concertations pluridisciplinaires (RCP - généralement un neurochirurgien, un oncologue et un radiothérapeute). Elle va dépendre du type de la tumeur, de sa localisation, des antécédents médicaux et comorbidités, de l'âge et de l'état général du patient. Le traitement standard des GBMs nouvellement diagnostiqués consiste en une exérèse complète de la tumeur suivie de l'association radiothérapie et témozolomide concomitant puis adjuvant (protocole de Stupp). Cette prise en charge standard basée sur un essai clinique de phase III de 2005 (8), consolidé en 2009 (9), est toujours d'actualité à la suite d'un examen par consensus de deux sociétés de neuro-oncologie (SNO et EANO) (39).

Le traitement chirurgical doit être le plus agressif possible tout en limitant l'impact fonctionnelle de la résection. Comme les GBMs sont des tumeurs infiltrantes, la résection est toujours incomplète mais demeure un facteur pronostic important pour les patients (67,68). La radiothérapie associée à la chimiothérapie débute quelques semaines après la chirurgie, sous la dépendance de la cicatrisation du scalp. La dose totale délivrée en radiothérapie conventionnelle est de 60 Gy fractionnée en 30 doses de 2 Gy sur 6 semaines (5 jours par semaine). Le témozolomide (TMZ) est administré oralement en traitement concomitant (75 mg/m²/jour) sur les 6 semaines de radiothérapie puis en traitement adjuvant (150 à 200 mg/m²/jour) par cure de 5 jours, chaque cure étant répétée tous les 28 jours pour une durée de 6 cycles (8). Le TMZ est un agent alkylant qui, lorsqu'il est converti en monométhyl triazénoïmidazole carboxamide, soumet à la méthylation (ajout d'un groupement -CH₃) l'oxygène en position 6 ou l'azote en position 7 de la guanine. L'ajout de cet adduit génère une non-concordance base/base avec la thymine reconnue par le système de réparation des mésappariements (*mismatch repair*) et ceci entraîne des cassures de l'ADN, cytotoxiques pour la cellule. Le bénéfice du TMZ est principalement observé pour les GBMs présentant la méthylation du promoteur MGMT, d'où l'intérêt de dépister son statut chez les patients nouvellement diagnostiqués.

Cependant, les GBMs récidivent et progressent invariablement les mois qui suivent cette prise en charge (8,9). Devant cette impasse thérapeutique et l'absence de consensus de prise en charge pour les récurrences, il est recommandé de réaliser une RCP afin de discuter des différentes options thérapeutiques possibles (69). Selon certains facteurs pronostics comme l'âge ou l'indice de KPS, une reprise de la chirurgie et/ou de la radiothérapie peut être envisagée (70,71). La lomustine seule est actuellement l'agent alkylant de la famille des nitrosourées qui présente les meilleurs résultats dans les premières récurrences des GBMs (72). Il est également possible de déposer directement des agents antinéoplasiques dans la cavité formée après la résection pour augmenter leur biodisponibilité locale. L'implant à la carmustine (Gliadel®), agent lipophile capable de traverser la barrière-hémato-encéphalique (BHE), est indiqué dans les GBM nouvellement diagnostiqués et récidivants. Cependant les bénéfices thérapeutiques de cette formulation restent limités (73,74).

L'exploration de nouvelles pistes thérapeutiques est nécessaire et les patients doivent pouvoir être inclus en essais cliniques lorsque cela est possible (39).

1.3 Exploration thérapeutique

En raison du pronostic défavorable des GBMs malgré les traitements standards, diverses approches expérimentales ont été développées et sont évaluées en essais cliniques (75). Cependant, le plus grand défi pour cibler les GBMs est d'utiliser des composés capables de franchir la BHE, réduisant drastiquement le nombre de candidats envisageables (76). Les stratégies thérapeutiques exposées ci-dessous s'intègrent dans une médecine de précision en proposant des traitements adaptés aux anomalies de la tumeur qui complètent l'arsenal thérapeutique actuel.

1.3.1 Thérapie ciblée

L'ère de la biologie moléculaire des gliomes amorcée en 2016 a permis de déterminer des biomarqueurs spécifiques qui sont généralement impliqués dans le développement ou la dissémination des GBMs (15). Les thérapies ciblées agissent spécifiquement sur ces anomalies moléculaires pour altérer les processus indispensables à la croissance tumorale.

L'un des processus les plus étudiés dans les GBMs est le phénomène d'angiogenèse tumorale. Les mécanismes généraux sur l'angiogenèse, les différentes cibles thérapeutiques et le développement de médicaments à visée anti-angiogénique ont été introduits lors d'un travail parallèle qui a été réalisé au laboratoire en collaboration avec le service de pharmacologie clinique du CHU de Bordeaux (« *Sécurité cardiovasculaire des médicaments anticancéreux agissant sur l'angiogenèse* ») (77). – Brièvement, l'angiogenèse est un processus de création de nouveaux vaisseaux à partir d'un système vasculaire préexistant (78). Ce processus est hautement déséquilibré dans les cancers avec une sécrétion de facteurs pro-angiogéniques en faveur de la synthèse vasculaire pour subvenir aux besoins nutritifs de la tumeur (79). Le facteur de croissance de l'endothélium vasculaire (VEGF) en est le principal représentant, cibler sa voie de signalisation apparaît dès lors comme une stratégie potentielle pour traiter le GBM (80). – Le bevacizumab, anticorps monoclonal dirigé contre le VEGF, a été approuvé par la Food and Drug Administration (FDA) et le Japanese Ministry of Health, Labour and Welfare (MHLW) suite à trois essais cliniques de phase III en association avec le protocole standard pour les GBMs nouvellement diagnostiqués (81,82) ou en association avec la lomustine pour les récurrences (83). Cependant la survie globale dans ces essais n'étant pas modifiée avec une balance bénéfice/risque défavorable, l'Agence Européenne du Médicament (EMA) n'a pas approuvé son utilisation dans la prise en charge des GBMs. Cette initiative est également appuyée par les lignes directrices du National Institute for Health and Care Excellence (NICE) (84). La biodisponibilité du bevacizumab est limitée dans le cerveau sain car il ne peut traverser la BHE intacte. Néanmoins, sa diffusion est possible dans une certaine mesure car la BHE est partiellement interrompue dans le GBM (85). D'autres molécules de plus petite taille ont été développées pour cibler les voies de signalisation sous-jacentes du récepteur au VEGF. Il s'agit des inhibiteurs de tyrosine kinase (iTK) : cediranib, dovitinib, tivozanib, cabozantinib et regorafenib. Censés avoir une meilleure perméabilité cellulaire, seul le regorafenib a montré des résultats encourageants dans les GBMs récurrents (86). À ce jour, il n'y a pas de bénéfices cliniques établis pour l'utilisation des médicaments antiangiogéniques dans les GBMs nouvellement diagnostiqués (**Annexe**) (87).

La voie de signalisation de l'EGFR, fréquemment altérée dans les GBMs, apparaît également comme pertinente à cibler. Des iTK de première (erlotinib, lapatinib, vandetanib), deuxième (afatinib, dacomitinib, tesevatinib) et de troisième génération (osimertinib) ainsi que des anticorps monoclonaux (cetuximab) ont été développés et testés cliniquement dans

les GBMs. Cependant, les résultats de ces études montrent très peu de bénéfices pour les patients (88,89).

Actuellement, les études sur les thérapies ciblées n'ont pas démontré une efficacité supérieure à la chimiothérapie alkylante.

1.3.2 Immunothérapies

L'immunothérapie est une approche alternative qui vise à stimuler les cellules du système immunitaire (SI) contre les cellules cancéreuses et à les détruire. Il existe plusieurs stratégies pour activer la réponse immunitaire anti-tumorale.

La première approche consiste à utiliser des inhibiteurs de points de contrôle immunitaire (ou immunomodulateurs) qui lèvent le mécanisme d'inhibition du SI induit par la tumeur. Ces agents bloquent la reconnaissance de molécules spécifiques produites par les cellules tumorales impliquées dans l'inhibition des lymphocytes T (LT). L'ipilimumab est un anticorps monoclonal qui se fixe sur l'antigène 4 des LT cytotoxique (CTLA-4), régulateur majeur de leur activité. Le blocage de la voie du CTLA-4 augmente le nombre de cellules réactives au niveau de la tumeur. Son efficacité clinique dans les GBMs nouvellement diagnostiqués en plus du traitement standard est en cours d'évaluation (90). La liaison du récepteur PD-1 (programmed death-1) à son ligand PD-L1 régule négativement l'activation des LT cytotoxiques. PD-1 se situe sur les LT alors que PD-L1 est exprimée par les cellules présentatrices d'antigènes et les cellules tumorales. Le nivolumab est un anticorps monoclonal se fixant sur PD-1, bloquant ainsi l'interaction ligand/récepteur. Il a été évalué lors d'un essai clinique de phase III (CheckMate 143) en comparaison avec le bévacizumab chez des patients avec une récurrence de GBM, mais aucun avantage en termes de survie n'a été observé (91). De plus, l'association synergique nivolumab - ipilimumab permettant le blocage double de PD-1 et CTLA-4 a été étudié lors d'un essai clinique de phase I mais cette association présentait un profil de toxicité plus défavorable que le nivolumab seul pour des GBMs récidivants (92). Ayant le même mécanisme d'action, le pembrolizumab ne réussit pas à induire une réponse immunologique cytotoxique au sein de la tumeur (93). Autre anticorps monoclonal, l'atezolizumab est dirigé contre les ligands PD-L1. Cependant, il présente une faible activité clinique dans les GBMs nouvellement diagnostiqués (94). De plus, ces thérapies sont fréquemment associées avec des événements immunologiques qui sont principalement

d'ordre dermatologique (prurit, rash cutané), gastro-intestinal (diarrhée, colite), et dans une moindre mesure endocrinien et hépatique (91,95).

L'approche de la thérapie cellulaire adoptive consiste à prélever les LT des patients, les multiplier puis les modifier génétiquement pour qu'ils puissent exprimer un récepteur chimérique capable de reconnaître un antigène spécifique de la tumeur (lymphocytes CAR-T – *chimeric antigen receptor-T*) (96). Théoriquement, la reconnaissance de l'antigène tumoral active le processus de cytotoxicité cellulaire et détruit les cellules tumorales. Les essais cliniques évaluant les lymphocytes CAR-T visant, par exemple, EGFRvIII (variant 3 du récepteur à l'EGFR), ou HER2 dans les GBMs n'ont pas montré de résultats aussi encourageants que dans les leucémies ou lymphomes (97).

Contrairement à l'approche précédente utilisant des procédés de modifications synthétiques, la vaccination thérapeutique anticancéreuse permet d'armer « physiologiquement » les cellules du SI contre la tumeur. Le vaccin est généralement composé de fragments d'antigènes adaptés au profil moléculaire du GBM. Ils sont présentés aux cellules immunitaires qui pourront ensuite reconnaître les cellules tumorales et déclencher une réponse cytotoxique. Ces vaccins présenteraient une plus grande spécificité, moins d'effets indésirables mais surtout une activité anticancéreuse continue et de longue durée (98). Le rindopépimut est un vaccin constitué d'un peptide spécifique de EGFRvIII conjugué à une hémocyanine de patelle. Évalué lors d'un essai clinique de phase III, son utilisation en association n'a pas montré de supériorité quand comparé au traitement standard (99). Normalement inactive dans les cellules saines et différenciées, la télomérase est un oncogène majeur qui limite le phénomène de sénescence. La présence d'une mutation dans son promoteur résulte en une augmentation de son expression et de son activité (100). Elle est fréquemment retrouvée dans les cancers et dans plus de 80% des GBMs (25,101). Apparaissant comme une cible universelle, le vaccin thérapeutique anticancéreux (UCPVax[®]-Glio) est actuellement en cours d'évaluation pour le GBM (NCT04280848). En plus des cellules effectrices comme les LT cytotoxiques, la réponse immunitaire fait intervenir des cellules régulatrices comme les cellules dendritiques (CD). Les CD sont capables de reconnaître un antigène, de migrer et de le présenter aux LT pour induire une réponse cytotoxique. L'administration d'un vaccin autologue aux CD pulsées par lysat tumoral (DCVax[®]-L) a permis de prolonger la survie des patients nouvellement diagnostiqués de GBM de plus de 7 mois par rapport au contrôle historique (23 vs 16 mois). Lorsqu'ils présentaient une méthylation du

promoteur MGMT, l'augmentation de la survie dépassait les 13 mois (34 vs 21 mois) (9,102). Toutefois, le développement de tels vaccins s'avère long (quelques mois) et coûteux (103).

La dernière approche est celle de la virothérapie avec l'utilisation de virus oncolytique. Il s'agit de modifier un virus à tropisme spécifique pour directement attaquer la tumeur ou stimuler les réponses immunitaires. Le poliovirus de type 1 a une forte affinité pour CD155 qui se trouve surexprimé dans les gliomes (104,105). Une fois atténué, il n'induit plus d'effets neuronaux délétères (106). Il se multiplie dans les cellules tumorales et induit directement leur lyse ou indirectement par la présentation à la membrane des antigènes viraux, reconnus par le SI. Évalué en essai clinique, cette stratégie a montré des résultats intéressants : peu de différence pendant 18 mois par rapport au groupe historique puis une phase de plateau est observée (9,107).

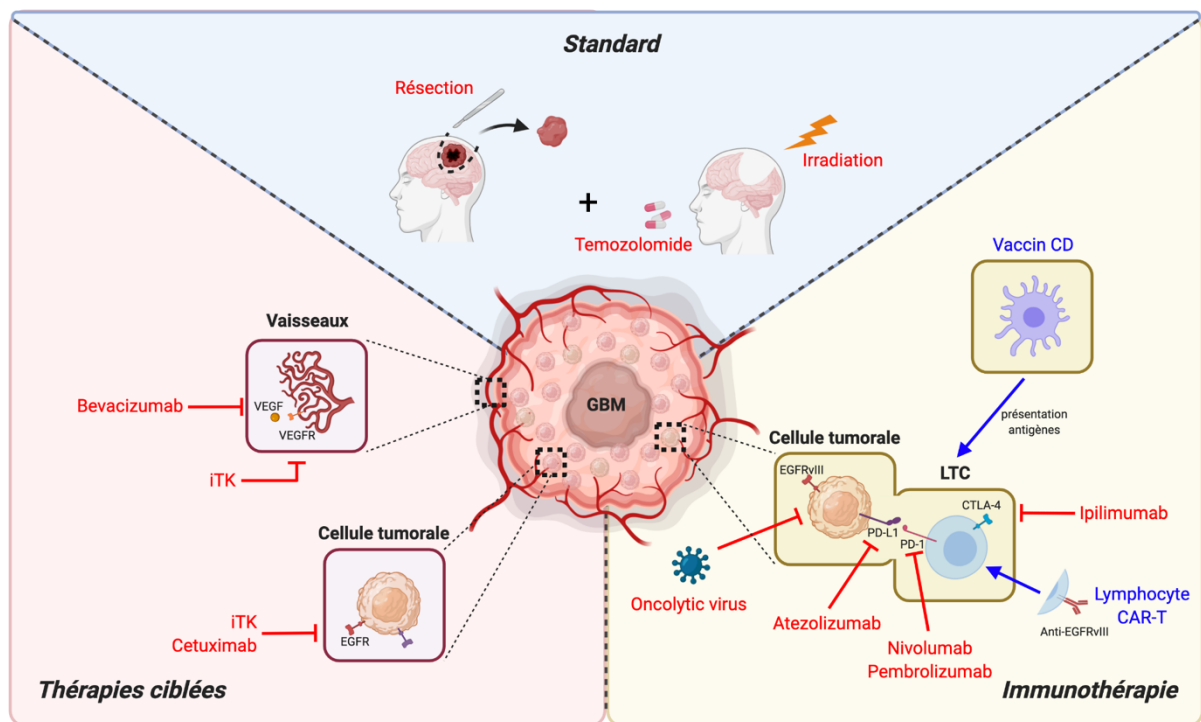


Figure 2 : Aperçu des principales stratégies thérapeutiques du GBM

La prise en charge standard consiste en une résection tumorale la plus large possible suivie d'une radio- et chimiothérapie au TMZ. Les autres stratégies thérapeutiques comprennent les thérapies ciblées qui visent principalement à inhiber les processus de signalisation vasculaire ou tumorale et l'immunothérapie qui stimule le système immunitaire pour permettre une réponse cytotoxique.

1.4 Métabolisme énergétique tumoral

1.4.1 Notions de base

Le métabolisme comprend, au sens large, l'ensemble des réactions chimiques au sein de la matière vivante. Il fait intervenir des enzymes qui catalysent la transformation de métabolites (acides aminés, glucides, lipides) et s'organise en voies métaboliques spécifiques interconnectées. Le terme de catabolisme est utilisé pour désigner les processus de dégradation thermodynamiquement favorable des métabolites libérant ainsi de l'énergie (réactions exergoniques). De façon opposée, l'anabolisme désignant les processus de synthèse puis d'assemblage de molécules et ces réactions non spontanés requiert de l'énergie (réactions endergoniques). Il s'agit d'un système conservé au cours de l'évolution, bien que les animaux, les plantes et les bactéries aient leurs variantes métaboliques, il existe de nombreux intermédiaires communs et réactions similaires (108).

Chez l'homme, le métabolisme énergétique est divisé en de nombreuses voies métaboliques dont s'en distinguent trois majeures : la glycolyse, la fermentation lactique et l'oxydation phosphorylante (OxPhos) (**Figure 3**). Outre la production d'énergie, ces voies permettent également la synthèse d'intermédiaires métaboliques nécessaires à la production de biomasse, indispensable pour la croissance et la multiplication des cellules.

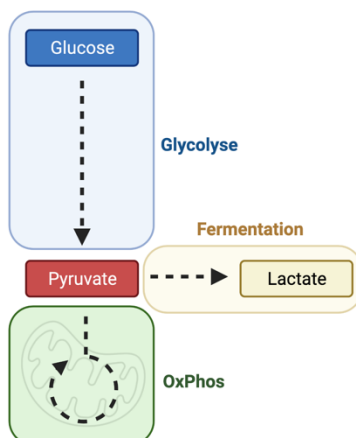


Figure 3 : Schéma des principales voies métaboliques énergétiques issues du glucose

La glycolyse correspond à la dégradation du glucose en pyruvate. En condition d'oxygénation normale, le pyruvate est oxydé dans la mitochondrie. Lorsque l'oxygène est limité ou dans le cadre tumoral, le pyruvate est fermenté en lactate.

a. La glycolyse

La glycolyse est la voie de dégradation du glucose, elle se déroule dans le cytoplasme de la cellule. Indépendamment du niveau d'oxygène, elle fait intervenir une série de 10 réactions enzymatiques qui aboutissent à la formation du pyruvate (**Figure 4**).

Les cellules incorporent le glucose *via* les transporteurs au glucose (GLUT) puis le phosphorylent en glucose-6-phosphate (G6P). Cette réaction irréversible est catalysée par les hexokinases (HK) 1, 2, 3 et 4 (ou glucokinase), elle consomme une molécule d'énergie : l'ATP (Adénosine TriPhosphate). Le G6P formé sert de voie d'entrée pour la glycolyse mais également pour la voie des pentoses phosphates. Il est ensuite isomérisé en fructose-6-phosphate (F6P) par la G6P isomérase. La phosphofructokinase-1 (PFK1) catalyse la deuxième réaction irréversible où le F6P est phosphorylé en fructose-1,6-biphosphate (FbP) avec la consommation d'une autre molécule d'ATP.

Le F6P est ensuite clivé en deux trioses : le glycéraldéhyde-3-phosphate (GA3P) et la dihydroxyacétone phosphate (DHAP). Cette dernière est isomérisée en GA3P par la triose-phosphate isomérase.

La GA3P déshydrogénase est l'enzyme catalysant l'unique réaction d'oxydoréduction de la glycolyse, l'oxydation du GA3P en 1,3-bisphosphoglycérate s'accompagne de la réduction du nicotinamide adénine dinucléotide (NAD). Cette réaction génère une liaison à haut potentiel énergétique qui sera ensuite déplacé par la phosphoglycérate kinase sur une molécule d'ADP pour former de l'ATP et du 3-phosphoglycérate (PG). La phosphoglycérate mutase catalyse l'isomérisation du 3PG en 2PG. Le phosphoenolpyruvate (PEP) formé à partir de la déshydratation du 2PG *via* l'énolase présente également une liaison énol à très fort potentiel énergétique. La formation du pyruvate et la synthèse d'une molécule d'ATP sont issues de l'hydrolyse de cette liaison médiée par la pyruvate kinase (PKM).

Au final, la glycolyse produit 2 molécules d'ATP et de NADH/H⁺ à partir d'une molécule de glucose et génère deux molécules de pyruvate, véritable carrefour des voies métaboliques.

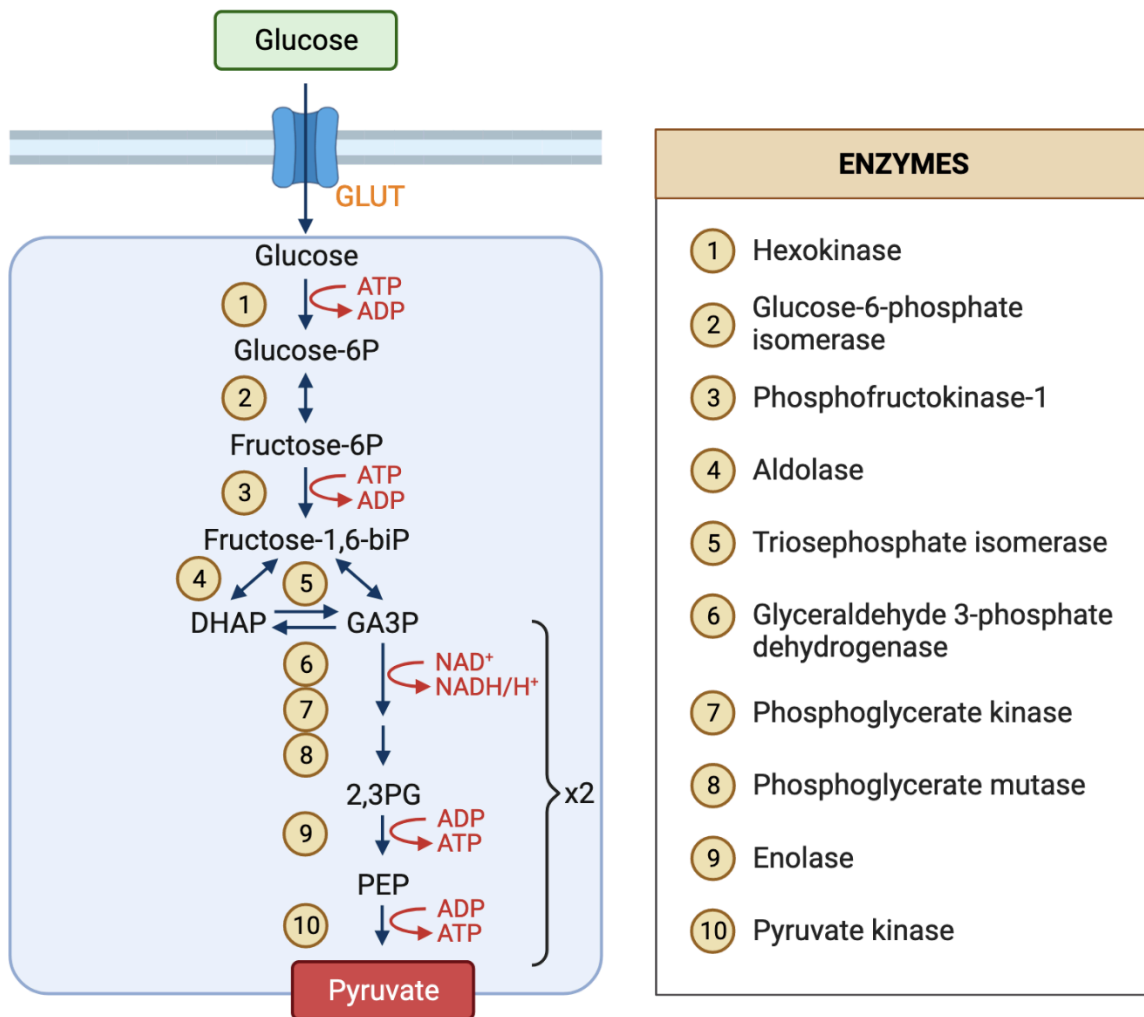


Figure 4 : La glycolyse

Voie d'assimilation du glucose également connue sous le nom de voie d'Emden-Meyerhof-Parnas qui permet de générer 2 molécules d'ATP, de NADH/H⁺ et de pyruvate.

b. L'oxydation phosphorylante mitochondriale

Le pyruvate est transporté à travers la membrane interne de la mitochondrie par un transporteur spécifique au pyruvate (MPC). Il alimente le cycle de Krebs qui produit principalement des électrons (NADH/H⁺) nécessaire à la synthèse d'ATP via la chaîne respiratoire (**Figure 5**).

Le pyruvate est décarboxylé en acétyl-Coenzyme-A (CoA) par le complexe pyruvate déshydrogénase et s'accompagne d'une réduction d'un NAD⁺. Ce thioester activé sera condensé à l'oxaloacétate (OAA) puis hydrolysé pour former le citrate, point d'entrée du cycle de Krebs (ou cycle du citrate – *tricarboxylic acid cycle* – TCA). – Lorsque la concentration en OAA diminue, le pyruvate peut également être carboxylé en OAA par la pyruvate carboxylase. Il s'agit d'un phénomène d'anaplerose pour maintenir le flux du cycle. – Le citrate est

déshydraté puis réhydraté en isocitrate sous la dépendance de l'aconitase. Cette réaction d'isomérisation permet le déplacement du groupement hydroxyle (-OH) de la position 3 (alcool tertiaire) en position 4 (alcool secondaire) et ainsi de rendre l'intermédiaire sensible aux réactions d'oxydo-réduction. L'oxydation de l'isocitrate catalysée par l'IDH réduit le NAD^+ et forme un intermédiaire β -cétoacide instable (oxalosuccinate). Ce dernier est rapidement décarboxylé en α -cétoglutarate (α -KG), métabolite pivot d'une autre voie d'anaplérotique, celle de la glutamine. L' α -KG déshydrogénase est un complexe multienzymatique composé de trois activités distinctes. Tout d'abord, une décarboxylase oxyde l' α -KG en succinaldéhyde, le fixe au thiamine pyrophosphate (TPP) puis le transfère au lipoamide. Au cours de cette réaction d'oxydoréduction, le carbonyle du succinaldéhyde se fixe à l'atome de soufre du lipoamide, il se forme un acide succinique et un dihydrolipoamide dont la liaison acyl-thiol possède un fort potentiel énergétique. Une transsuccinylase libère le dihydrolipoamide en transférant le groupement succinyl sur un CoA (succinyl-CoA). Le lipoamide est régénéré à partir de l'oxydation du dihydrolipoamide et la réduction du NAD^+ médiée par la lipoyl déshydrogénase. L'énergie de la liaison du succinyl-CoA est déplacée sur une molécule de GDP via la succinyl-CoA synthétase libérant le CoA du succinate et générant une molécule de GTP. Une nucléoside diphosphate kinase catalyse le déplacement d'un groupement phosphate de la molécule de GTP sur une molécule d'ADP pour former une molécule d'ATP. Au niveau du complexe 2 de la chaîne respiratoire, la succinate déshydrogénase transmet les protons du succinate à l'ubiquinone (coenzyme-Q) par le biais du flavine adénine dinucléotide (FAD). Le fumarate, produit de l'oxydation du succinate, est un acide dicarboxylé présentant une insaturation entre ses deux groupements carboxyles. La fumarase catalyse l'hydratation du fumarate, réaction d'addition d'une molécule d'eau sur la double liaison, pour former du malate. La dernière enzyme du cycle de Krebs est la malate déshydrogénase, réaction d'oxydoréduction faisant de nouveau intervenir le NAD^+ et produisant l'OAA.

Les NAD^+ qui sont utilisés lors de l'oxydation des intermédiaires du cycle de Krebs sont régénérés au niveau du complexe 1 de la chaîne respiratoire mitochondriale. La NADH déshydrogénase transmet les électrons au coenzyme-Q qui joue le rôle de transporteur d'électrons des complexes 1 et 2 vers le complexe 3. La coenzyme-Q cytochrome réductase catalysera le transfert de ces électrons sur le cytochrome C. Enfin, le cytochrome C donnera ses électrons aux molécules d' O_2 au niveau du complexe 4 de la chaîne respiratoire mitochondriale. Ces réactions permettent de générer un gradient électrochimique de protons

H⁺ à travers la membrane interne pour la synthèse de molécules d'ATP au niveau du complexe 5 (ATP synthase) (109).

La décarboxylation d'une molécule de pyruvate suivie d'un cycle d'oxydation phosphorylante génère 4 NADH/H⁺, 1 FADH₂ et 1 équivalent d'ATP. Au sein de la mitochondrie, les coenzymes NADH/H⁺ et FADH₂ permettent la synthèse de 3 et 2 molécules d'ATP, respectivement. Le bilan de l'OxPhos à partir d'une molécule de glucose s'élève donc à la production de 30 molécules d'ATP, soit quinze fois plus que la glycolyse.

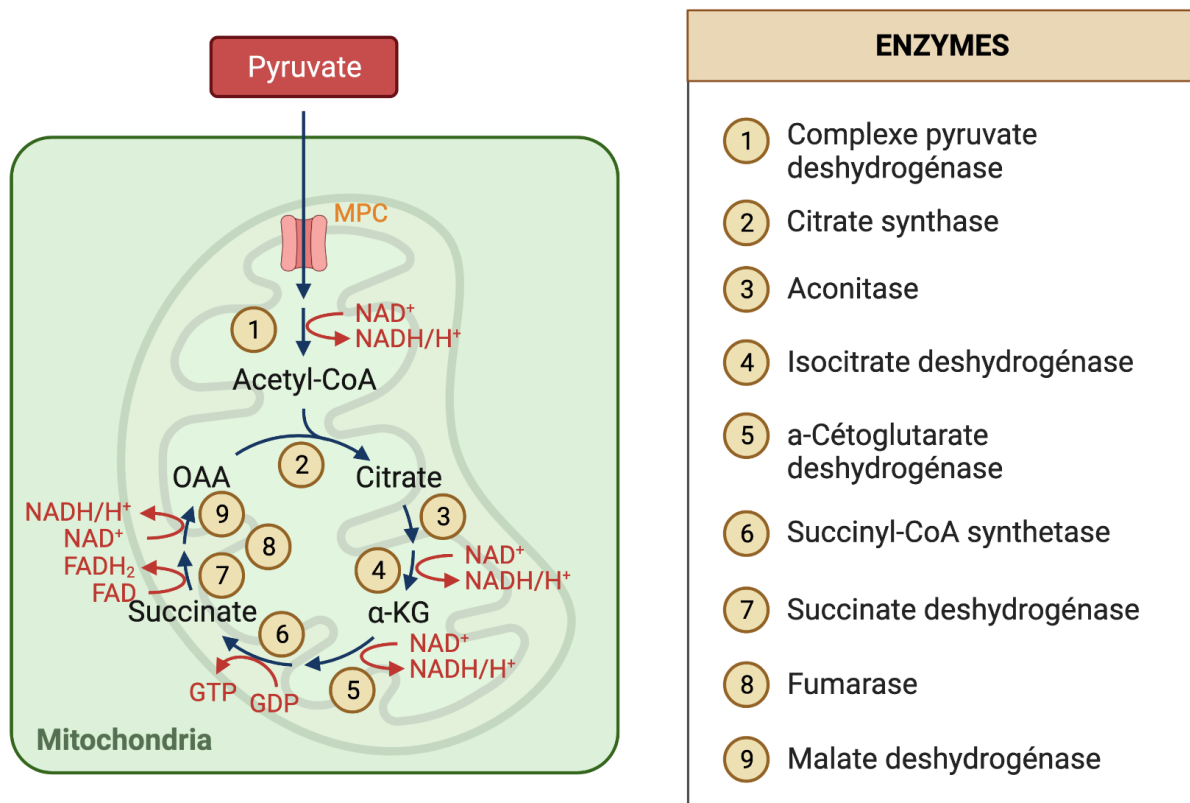


Figure 5 : Le cycle de Krebs

Voie d'oxydation du pyruvate et d'autres précurseurs de différentes voies métaboliques (acides aminés, acides gras) également connue sous le nom de cycle du citrate qui permet de générer 1 équivalent d'ATP (*via* le GTP), 4 molécules de NADH/H⁺ et 1 de FADH₂.

c. La fermentation lactique et lactates déshydrogénases

Physiologiquement, ce processus intervient principalement lorsque les niveaux d'oxygène diminuent. Il est de faible rendement énergétique puisque seulement deux molécules de lactate sont produites et deux NADH,H⁺ sont réoxydés à partir d'une molécule de glucose (**Figure 6**). Cependant la réaction est rapide, non limitée, permet de maintenir le flux de la glycolyse en réapprovisionnant la GA3P déshydrogénase en NAD⁺ et le lactate peut être

reconverti en pyruvate lorsque les conditions d'oxygénation redeviennent normales permettant d'alimenter le cycle de Krebs ou de reformer du glucose (*via* le cycle de Cori).

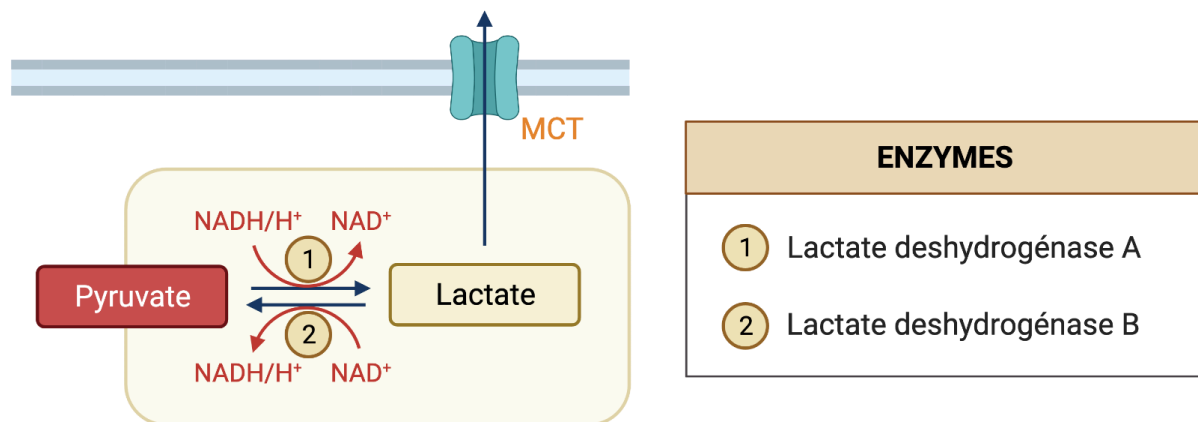


Figure 6 : La fermentation lactique

Voie de régénération du NAD^+ qui permet de réguler le potentiel redox de la cellule.

L'enzyme catalysant cette conversion est la lactate déshydrogénase (LDH). Elle présente deux sous-unités H (cœur) et M (muscle) qui s'assemblent en homo- ou hétérotétramère pour former 5 isotypes différents : LDH1 (4H), LDH2 (3H1M), LDH3 (2H2M), LDH4 (1H3M) et LDH5 (4M) (**Figure 7**). La sous-unité H est codée par le gène *LDHA* localisé sur le chromosome 11 (110) alors que la M par le gène *LDHB* localisé sur le chromosome 12 (111). Toutes les LDHs catalysent l'interconversion du pyruvate et du lactate mais présentent des paramètres cinétiques différents (112). Ces enzymes sont généralement simplifiées en LDHA et LDHB. LDHA est abondante dans les muscles et le foie, elle privilégie la conversion du pyruvate en lactate alors que LDHB, qui prédomine dans le cœur et les reins, privilégie la réaction du lactate en pyruvate (113). Toutefois, il existe d'autres isoformes particulières : les LDHC, D-LDH et LDHBx. LDHC (anciennement LDHX) est un homotétramère codé par le gène *LDHC* sur le chromosome 11. Elle est spécifique des cellules germinales mais peut être exprimée dans certains cancers (114–116). L'enzyme D-LDH catalyse la réaction de conversion de la forme dextrogyre du lactate (D-lactate) mais demeure moins abondante que la forme classique (117). Enfin, LDHBx est impliquée dans la régulation du potentiel redox du péroxysome. Codée par le même gène que l'enzyme LDHB, elle diffère de cette dernière par un déplacement de lecture du codon stop. Ce qui se traduit par un ajout de sept acides aminés sur la protéine (118).

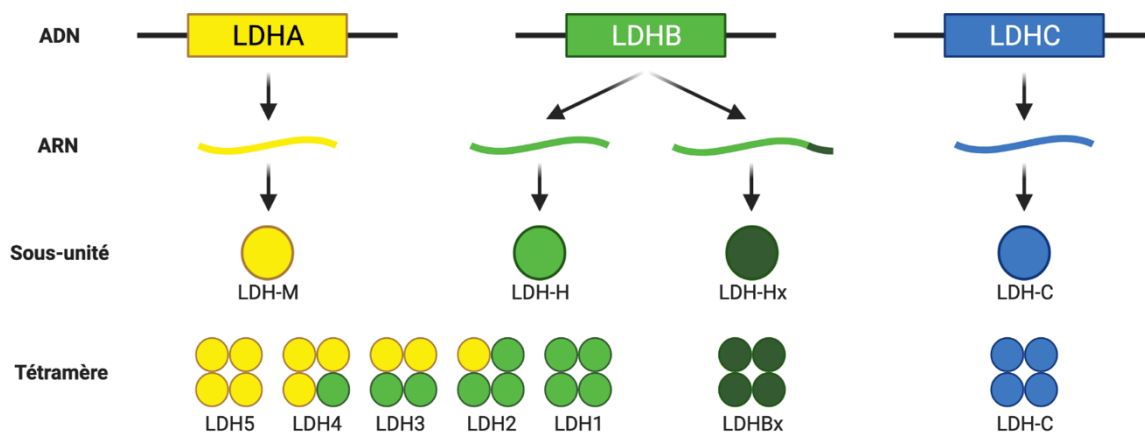


Figure 7 : Formation des différents isomères des LDHs

Les isotypes LDH1 à 5 sont issus de l'assemblage de sous-unité provenant de la transcription de *LDHA* et de *LDHB*. L'isoforme LDHBx provient d'un allongement du brin transcrit de *LDHB* et LDHC de l'assemblage homotétramérique de sous-unités LDH-C. Figure adaptée de (119).

1.4.2 Métabolisme cérébral

Le cerveau est un organe tout à fait singulier d'un point de vue fonctionnel. Il est le siège d'activités complexes comme le contrôle de la motricité, le traitement des informations sensorielles, la régulation hormonale, la pensée, la mémoire et les émotions qui nécessitent des besoins énergétiques considérables. Reffet des dépenses en énergie, il mobilise le cinquième de la consommation en oxygène alors qu'il ne pèse que de 2% de la masse totale du corps (120). L'activité métabolique de cerveau dépend essentiellement de l'oxydation complète du glucose dont en découle la production d'une grande quantité d'ATP (121). Cette énergie est principalement utilisée pour la communication synaptique glutamatergique (122,123). Le glucose entre dans les neurones par le transporteur GLUT3 ayant une forte affinité pour ce substrat puis est complètement oxydé dans la mitochondrie (124).

Les capillaires cérébraux amenant les nutriments sont recouverts par les extensions des astrocytes (125,126). Le glucose et autres nutriments sont en partie absorbés par les astrocytes avant d'atteindre les neurones. Les astrocytes sont des cellules de soutien des cellules nerveuses qui possèdent une activité glycolytique plus élevée que les neurones (127). Ils peuvent aussi stocker le glucose sous forme de glycogène *via* l'action de la glycogène synthase *a contrario* des neurones où cette enzyme est maintenue inactive par le glycogène synthase kinase 3 (128). La différence entre les isoformes des transporteurs et enzymes du métabolisme exprimés par les neurones (MCT2 et LDHB) par rapport aux astrocytes (MCT1/4 et LDHA) distingue l'activité métabolique des cellules neurales (129–131). De ces observations

est apparu le concept de la navette lactate entre astrocytes et neurones, basé sur des expériences de culture de tissus (132). La LDHA des astrocytes convertit le pyruvate en lactate puis ce lactate est exporté dans le milieu extracellulaire par MCT1/4. Assimilé par les neurones en passant à travers MCT2, il est reconverti en pyruvate par LDHB et alimente le cycle de Krebs (**Figure 8**) (132,133). Cette hypothèse est appuyée par une étude *in vivo* montrant un gradient de lactate des astrocytes vers les neurones (134). Physiologiquement, le lactate n'est peut-être pas la source majeure d'énergie des neurones, contrairement au glucose (135), mais il s'agit d'une source énergétique annexe pouvant devenir importante lors de certaines conditions particulières comme l'hyperlactatémie (136,137) ou l'hypoglycémie (138).

Le glucose est dilué dans un grand nombre de voies métaboliques fournissant énergie et des intermédiaires métaboliques nécessaire à la synthèse des nucléotides, des protéines ou des lipides (139). La majeure partie du lactate est principalement oxydée dans le cycle de Krebs pour produire de l'énergie (140,141). Il peut également servir pour la synthèse d'acides gras, qui sont ensuite transférés aux astrocytes sous forme de gouttelettes lipidiques (142).

Le lactate joue un rôle important dans le métabolisme cérébral que ce soit pour la régulation du potentiel redox cellulaire ou en tant que substrat énergétique. De plus, il agit comme un neuroprotecteur contre la toxicité excitatrice du glutamate (143) et promeut la résistance au stress oxydatif (144). Sa régulation dépend étroitement de celle des LDHs qui catalysent sa conversion en pyruvate ou la réaction inverse.

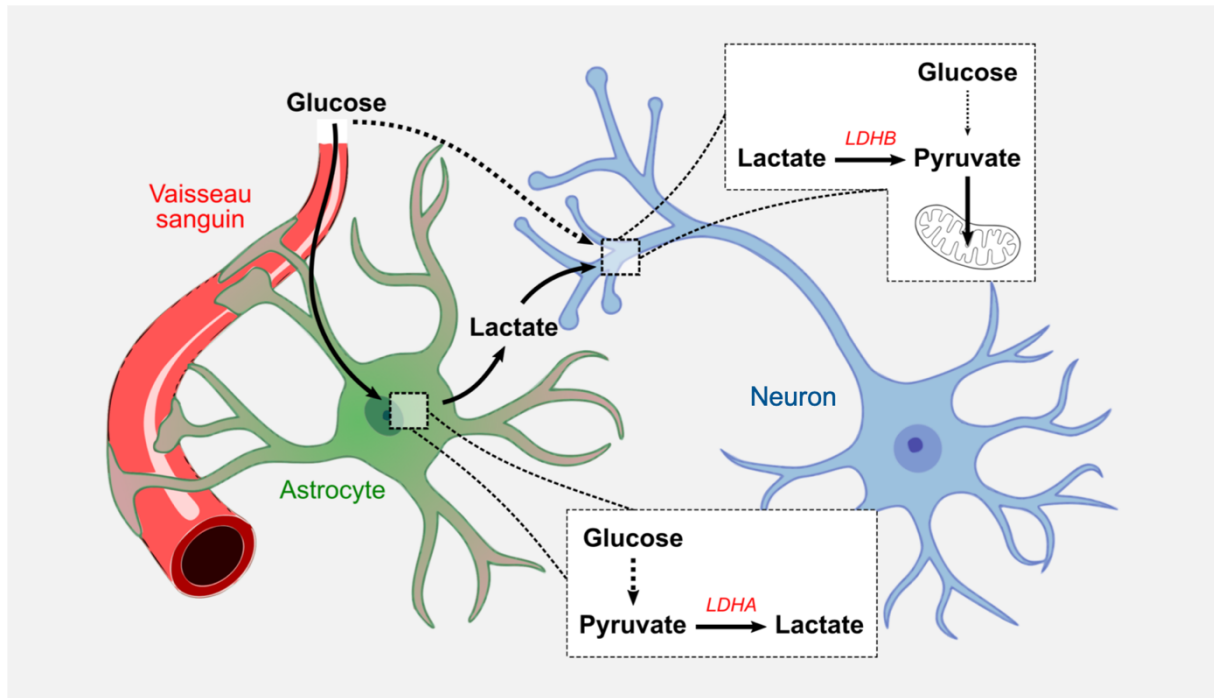


Figure 8 : Schéma de la navette lactate entre astrocytes et neurones

Le glucose provenant des capillaires sanguins est capté par les astrocytes qui vont l'oxyder en pyruvate. Le pyruvate sera réduit en lactate par LDHA puis exporté dans le milieu extracellulaire. Les neurones assimilent le lactate, le réoxyde en pyruvate *via* LDHB et alimentent le cycle de Krebs dans la mitochondrie pour produire de l'énergie. Les neurones peuvent également utiliser le glucose comme source énergétique.

1.4.3 Dérégulation énergétique et reprogrammation métabolique des tumeurs

La reprogrammation du métabolisme énergétique des cellules tumorales est l'une des caractéristiques des cancers (145). Dans la première partie du XX^{ème} siècle, le docteur Otto Warburg observait que le métabolisme énergétique des cellules cancéreuses différait anormalement de celui des cellules saines. Les cellules tumorales consommaient et sécrétaient plus de glucose et de lactate et, ce, indépendamment du niveau d'oxygène (146). L'accumulation de lactate dans le microenvironnement tumoral induisant son acidification est un facteur de mauvais pronostic associé aux métastases et aux récives (147–150). Cependant, le concept général est bien plus complexe que ce shift métabolique glycolytique, aussi connu sous le nom d'« Effet Warburg ». La signalisation oncogénique est souvent en faveur d'une augmentation de l'expression et d'une stabilisation du facteur de transcription HIF-1 alors qu'il est normalement dégradé sous l'action de l'oxygène (151). Ce facteur active la transcription de nombreux gènes impliqués dans la prolifération (TGF α et IGF), l'angiogenèse (VEFG et PDGF) et l'expression d'enzyme de la glycolyse (HK, PKM, LDHA) (152–154). D'un autre côté, HIF-1 promeut l'expression de la pyruvate déshydrogénase kinase 1 qui,

par phosphorylation, inhibe le complexe pyruvate déshydrogénase (155). L'OxPhos ralentit la croissance tumorale alors HIF-1 α s'oppose à cet effet en diminuant la synthèse de l'acétyl-CoA pour réduire l'activité du cycle de Krebs et le métabolisme oxydatif des cellules (156).

Comme toutes cellules tumorales, les cellules de GBM sont capables d'adapter leurs capacités métaboliques à leurs besoins, comme pour favoriser leur survie ou maintenir leur prolifération, mais également en fonction de leur environnement. A l'instar des navettes d'échange physiologique du lactate, il existe une symbiose métabolique entre les cellules tumorales glycolytiques des zones hypoxiques qui le produisent et les cellules tumorales oxydatives des zones oxydatives qui le consomment (157). Ces zones ne sont pas statiques, elles fluctuent dans le temps et l'espace obligeant les cellules tumorales à reprogrammer constamment leurs flux glycolytique et oxydatif (158,159).

Pour des raisons thermodynamiques, les cellules utilisent l'une ou l'autre voie métabolique pour maximiser soit le rendement énergétique (énergie produite par molécule de substrat), soit le débit énergétique (énergie produite par unité de temps) (160). Au cours de l'évolution, l'acquisition de la mitochondrie lors de l'augmentation des niveaux d'oxygène dans l'atmosphère a permis d'accroître considérablement la production d'énergie (161,162). L'augmentation du rendement énergétique est une stratégie de coopération chez les organismes multicellulaires afin de réduire la concurrence vis-à-vis d'un substrat commun (160). Cependant les cellules cancéreuses suivent une stratégie de compétition pour proliférer rapidement (163), elles présentent souvent des altérations mitochondriales (164,165) et utilisent préférentiellement la glycolyse (146). La glycolyse est une voie énergétique considérablement plus rapide que l'OxPhos et dépend principalement de la disponibilité du glucose et de l'équilibre rédox de la cellule (représenté par le couple NAD⁺/NADH/H⁺). En supposant l'apport en glucose illimité, elle produira beaucoup plus d'ATP que l'OxPhos pour un même laps de temps (50 à 100 fois plus).

Les HKs sont les enzymes catalysant la toute première réaction de la glycolyse, la phosphorylation du glucose en G6P, métabolite initial des voies des pentoses phosphates et de la synthèse des nucléotides. L'isoforme 1 (HK1) est principalement associé au catabolisme du glucose alors que l'HK2 intervient à la fois dans le catabolisme et dans l'anabolisme (166). Un knock-down de HK1 induit une augmentation d'expression de HK2, une diminution de l'OxPhos et accélère les mécanismes de tumorigenèse par le biais d'une transition épithélio-mésenchymateuse (167). Les GBMs présentent une forte expression de HK2 alors que les

gliomes de bas grade expriment principalement HK1. Une déplétion de HK2 restaure le métabolisme oxydatif des GBMs et les sensibilise à la radiation et au témozolomide (166,168).

Le sous-type mésenchymateux des GBMs est celui qui a le plus mauvais pronostic et qui est le plus résistant aux traitements (169). Il présente une signature métabolomique associée à une diminution de l'activité de la PKM et une accumulation du PEP dans la cellule (170). Il existe deux isoformes de PKM qui proviennent de l'épissage alternatif de son gène: PKM1 et PKM2. L'isoforme M1 est stable et active alors que M2, moins active, est régulée allostériquement par différents acteurs (171). Lorsqu'elle est inactive, PKM2 permet l'accumulation d'intermédiaires pouvant être utilisés dans les processus anaboliques et favorisant la prolifération cellulaire (172,173).

La fermentation lactique permet de réguler instantanément l'homéostasie rédox contrairement à l'OxPhos qui dépend de l'oxygène et qui fait intervenir de nombreux intermédiaires, enzymes et systèmes de régulation. Les LDHs jouent donc un rôle majeur, si ce n'est indispensable dans le métabolisme tumoral. La surexpression de l'isoforme LDHA est souvent retrouvée dans les cancers (174) et apparaît comme un facteur de mauvais pronostic chez les patients (175), associée à l'angiogenèse (176) et à la radiorésistance (177). Lorsque l'angiogenèse est inhibée dans les GBMs, le bévacizumab induit une augmentation de l'expression de LDHA le long des bordures invasives (178). La diminution d'expression de LDHA augmente la consommation d'oxygène qui favorise le stress oxydatif (179) et qui réduit la croissance tumorale (180,181). Une moins forte expression de LDHA est également de meilleur pronostic dans certains gliomes (182). L'isoforme LDHB est moins étudiée dans les cancers et aucune donnée n'est retrouvée pour les GBMs. Sa diminution d'expression par hyperméthylation de son promoteur est corrélée positivement avec l'agressivité des cancers de la prostate et des carcinomes hépatocellulaires (183,184). Une perte d'expression de LDHB promeut la prolifération et l'invasion des cancers pancréatiques (185). LDHB joue aussi un rôle dans la modulation de l'autophagie des adénocarcinomes du col utérin (186). Lorsque les deux isoformes sont étudiées simultanément, la double extinction de LDHA et LDHB abolie la fermentation lactique dans des modèles 2D humain d'adénocarcinome du colon et murin de mélanome. Cet effet a pour conséquence de diminuer la croissance de la tumeur (187).

Le métabolisme tumoral est un déterminant majeur du développement des GBMs. Les nombreuses mutations modulant ce métabolisme favorisent la survie, la prolifération et résistance aux traitements des GBMs (173,188). Il peut également être utilisé comme un

marqueur diagnostic, pronostic et même thérapeutique puisque la reprogrammation métabolique des cellules tumorales génère des vulnérabilités pouvant être ciblées. Des analogues de métabolites tels que le 2-deoxyglucose ou l'oxamate ont déjà été testés dans le GBM. Le 2-deoxyglucose entre en compétition avec le glucose, il est phosphorylé par l'HK puis s'accumule dans la cellule ne pouvant pas être isomérisé par la GPI. Seul son effet est limité mais lorsqu'il est associé avec la metformine, inhibant l'OxPhos, la croissance et l'invasion des GBMs est ralentie (189). L'oxamate est une forme isostérique du pyruvate qui inhibe LDHA et permet de diminuer la migration des cellules de GBM de manière dose dépendante (190). Un agent spécifique de LDHA et LDHB pourrait augmenter l'OxPhos des cellules (187), favoriser la production de plus d'espèces réactives à l'oxygène et rendre la cellule plus sensible aux approches de radiothérapie.

1.5 Lignées cellulaires

Les modèles cellulaires sont des outils essentiels et indispensables pour la compréhension d'un phénomène, d'un processus ou d'une maladie. Ils permettent de miniaturiser un système pour mieux le comprendre, ils ont une très grande durée de vie et permettent d'obtenir des résultats reproductibles. Chaque modèle présente des avantages et des inconvénients, il est donc nécessaire de valider soigneusement son modèle (191).

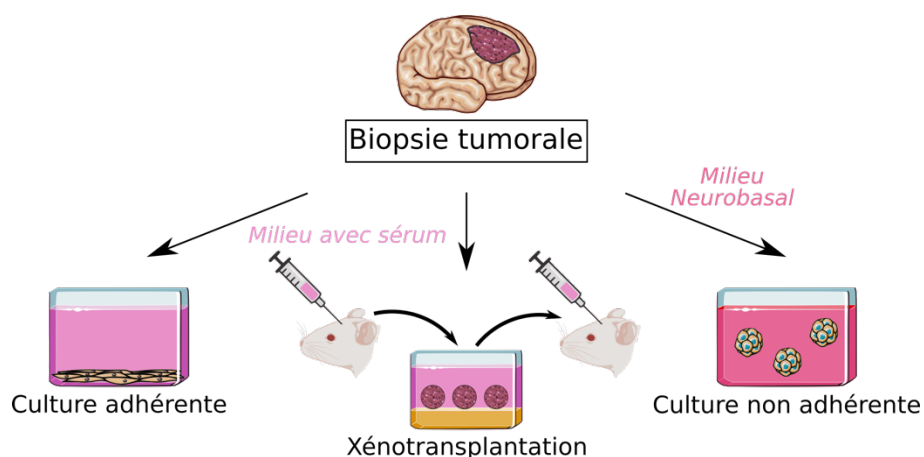


Figure 9 : Modèles cellulaires issus d'une biopsie tumorale

Aperçu des trois modèles expérimentaux dérivés de patients : la culture en milieu supplémenté avec du sérum comprenant les lignées adhérentes ainsi que celles avec xénotransplantation successives et la culture en milieu neurobasal sans sérum pour le maintien des lignées non adhérentes. Adaptée d'après (192).

1.5.1 Lignées cellulaires établies

Pendant des années, les cellules de GBM ont été cultivées de manière adhérentes dans un milieu complété avec du sérum. Ces lignées, comme les U87MG ou les U-251, ont permis d'étudier certains mécanismes et aspects du développement des GBM. Cependant, elles ne reproduisent pas finement toutes les caractéristiques des GBM (193) et dérivent rapidement de leur phénotype original (194). Lorsqu'elles sont implantées chez l'animal, les tumeurs divergent également de ce qui est observé chez l'homme. Bien qu'elles soient angiogéniques (195), elles ne présentent pas de cœur nécrotique (196) et n'infiltrent pas le parenchyme sain du cerveau (197).

1.5.2 Xénogreffes dérivées de patient (PDX)

Ce modèle est basé sur la xénotransplantation séquentielle chez l'animal de petites pièces de matériel tumoral humain, comprenant tissus et cellules tumorales (198,199). L'intérêt de ce modèle réside dans l'hypothèse que les PDX conservent les caractéristiques originales de la tumeur. Les cellules tumorales ne subissent pas de changements génétiques ou mutations significatives sur plusieurs générations murines (200). En contraste du modèle précédent, elles présentent une hétérogénéité cellulaire et conservent une signature biomoléculaire clinique. De plus, elles reproduisent l'architecture tumorale des GBM ainsi que leur phénotype invasif (192). Les PDX permettent d'obtenir des renseignements cliniques prédictifs plus pertinents lors de l'utilisation de traitements ciblant la tumeur (201). Elles ne sont donc jamais en contact avec du plastique et lorsqu'un passage *in vitro* est nécessaire, elles sont cultivées sur une gélose d'agar. Parmi les limitations de ce modèle, le temps de culture entre deux implantations est relativement court, ce qui restreint les procédures expérimentales *in vitro* envisageables. Il nécessite également une utilisation continue et importante d'animaux, représentant un coût non négligeable.

1.5.3 Lignées non-adhérentes

L'utilisation de cellules cultivées non adhérentes en milieu neurobasal sans sérum est un bon compromis entre les deux précédant modèles. Ces lignées poussent spontanément sous forme de neurosphères ou sphéroïdes (202). Cette structure tridimensionnelle mime

partiellement les conditions *in vivo* d'une tumeur, à savoir la différence de disponibilité de l'oxygène et des nutriments selon l'endroit où se situent les cellules. Le cœur du sphéroïde apparaît comme plus hypoxique et le glucose y diffuse plus difficilement alors que la périphérie est plus oxygénée et les nutriments ou facteurs de croissance directement disponibles (193). Ce modèle de culture préserve les échanges entre les cellules et maintient aussi les interactions symbiotiques normalement trouvés au sein de la tumeur *in vivo*. En outre, lorsque ces cellules sont implantées chez l'animal, elles reproduisent plus finement les caractéristiques retrouvées chez les patients (angiogenèse, nécrose, invasion localisée) (203).

Au cours de cette thèse, plusieurs lignées issues de patients ont été utilisées. Du fait de l'accès aux données de caractérisation de la biopsie de GBM (199), la lignée P3 a été le plus fréquemment utilisée. Elle a été isolée à l'hôpital universitaire de Bergen (Norvège) à partir d'une biopsie d'un patient mâle âgé de 64 ans atteint d'un GBM de sous-type mésenchymal. L'analyse par CGH a montré que la tumeur présente des aberrations chromosomiques comme un gain sur les chromosomes 7, 19 et 20q, une perte sur les chromosomes 1q42-43, 9, 10 et 20p ainsi qu'une perte de *PIK3R* et de *CDKN2A/B*. La lignée cellulaire présente un phénotype intermédiaire, à la fois invasif et angiogénique (199).

1.6 Infiltration tumorale

L'une des caractéristiques des GBMs est sa capacité à envahir le parenchyme cérébral sans métastases extra-cérébrales (204). L'infiltration diffuse apparaît comme un facteur de mauvais pronostic chez les patients atteints de GBM (205). Les cellules tumorales peuvent envahir individuellement ou collectivement pour former des GBMs multifocaux (206). L'invasion se fait préférentiellement le long de structures préexistantes comme les axones de la substance blanche et les vaisseaux sanguins (207,208). Si l'invasion péri-vasculaire est un processus très étudié et ses mécanismes moléculaires commencent à être élucidés, l'invasion le long des fibres nerveuses reste très peu connue. Certaines chimiokines et leurs récepteurs, comme SDF1 α (Facteur 1 dérivant des cellules stromales) et CXCR4 (Récepteur 4 de la chimiokine à motif C-X-C) semblent être impliqués dans l'invasion le long des fibres nerveuses (209). L'axe transcellulaire NOTCH1-SOX2 semble également être une voie importante pour l'invasion des GBMs le long des fibres nerveuses (210). Les cellules de GBM

envahissent le parenchyme sur des neurones partiellement démyélinisés suggérant la destruction de la gaine de myéline par les cellules GBM.

Plus récemment, plusieurs études ont souligné le rôle de l'activité électrique dans le développement des GBMs (211,212). Les connections entre les CSCs par le biais de microtubes ou les interactions avec les neurones par le biais de synapses neurogliales sont cruciales dans les étapes invasives des GBMs. D'autres facteurs ont été identifiés comme étant important dans l'invasion des GBMs comme CXCR3, TGF β ou la thrombospondine-1 (213,203,214).

1.7 Objectifs

Les GBMs sont des tumeurs agressives associées à un très mauvais pronostic dont leur prise en charge a très peu évolué depuis 2007. Les travaux de ce projet de thèse visent à étudier de nouveaux mécanismes impliqués dans la croissance et l'invasion des GBMs.

La première partie s'est consacrée au développement de modèle *in vitro* de croissance et d'infiltration pour étudier et tester des cibles d'intérêt afin de mieux comprendre les phénomènes du développement des GBMs et d'essayer de prédire l'efficacité clinique. **(articles 1, 2 et 3).**

La deuxième partie s'est intéressée à l'étude de cibles impliquées dans l'infiltration et le métabolisme énergétique des GBMs.

L'invasion des cellules dans le parenchyme est un obstacle majeur aux traitements des GBMs ainsi qu'un élément qui contribue dans la mort des patients. Une analyse protéomique entre les zones invasive et centrale a été réalisée révélant des candidats potentiels impliqués dans les processus invasifs. **(article 4)**

Le GBM est une tumeur hautement glycolytique pouvant adapter son métabolisme. Les LDHs apparaissent comme des candidats majeurs dans son développement puisqu'elles possèdent plusieurs rôles, elles interviennent dans le métabolisme énergétique, la navette lactate cérébrale ainsi que dans la régulation du potentiel rédox de la cellule. L'objectif était d'étudier les effets du blocage des LDHs dans le GBM et d'en dégager les vulnérabilités grâce à la combinaison d'analyses transcriptomique et métabolomique. **(article en révision)**

2

Modélisation expérimentale

2.1 Liste des articles relatifs à ce chapitre

- (1) Glioblastoma patient-derived cell lines: Generation of non-adherent cellular models from brain tumors (215) – *Neuromethods* (10.1007/978-1-0716-0856-2_5)
- (2) A 3D Spheroid Model for Glioblastoma (216) – *Journal of Visualized Experiments* (10.3791/60998)
- (3) Co-culture of Glioblastoma Stem-like Cells on Patterned Neurons to Study Migration and Cellular Interactions (217) - *Journal of Visualized Experiments* (10.3791/62213)

2.2 Réglementation

L'utilisation de matériel biologique humain est soumise à une réglementation assurant le respect et la protection du corps humain (218). Cette réglementation éthique s'appuie sur les règles du Code civil et du Code de la santé publique dont les principes majeurs sont (1) l'inviolabilité du corps humain, (2) la non patrimonialité du corps humain et de ses matériels biologiques ainsi que (3) l'anonymat de la personne (218). Il est également stipulé que le prélèvement de matériel biologique ne peut se faire que dans un but thérapeutique ou scientifique (219) avec le consentement préalable du donneur (220).

Suite à l'accord libre et éclairé du patient et l'anonymisation du prélèvement, le matériel biologique peut donc être utilisé à des fins scientifiques.

2.3 Extraction, établissement et entretien

Après exérèse de la tumeur cérébrale, la biopsie de GBM est directement placée dans un tube contenant du milieu de culture avant d'être acheminée au laboratoire. Après être découpées en pièce à l'aide d'un scalpel, l'échantillon est digéré avec de la trypsine, une peptidase hydrolysant les liaisons des protéines membranaires. Enfin, les cellules et particules

dissociées sont mécaniquement filtrées à travers un tamis de 40 μm puis déposées dans une flasque avec du milieu neurobasal. Ce milieu est complété avec du supplément B27, de l'héparine (100 U/mL), du FGF basique (20 ng/mL) et de la pénicilline – streptomycine (1000 U/mL).

Les cellules sont lavées chaque jour et le milieu remplacé jusqu'à élimination des déchets. La formation spontanée de microsphères tumorales en absence de sérum est le reflet du caractère souche des cellules tumorales (221). Des microsphères tumorales non adhérentes (sphéroïdes) poussent spontanément, et l'obtention de microsphères tumorales caractéristiques appelées sphéroïdes (**Figure 10**).

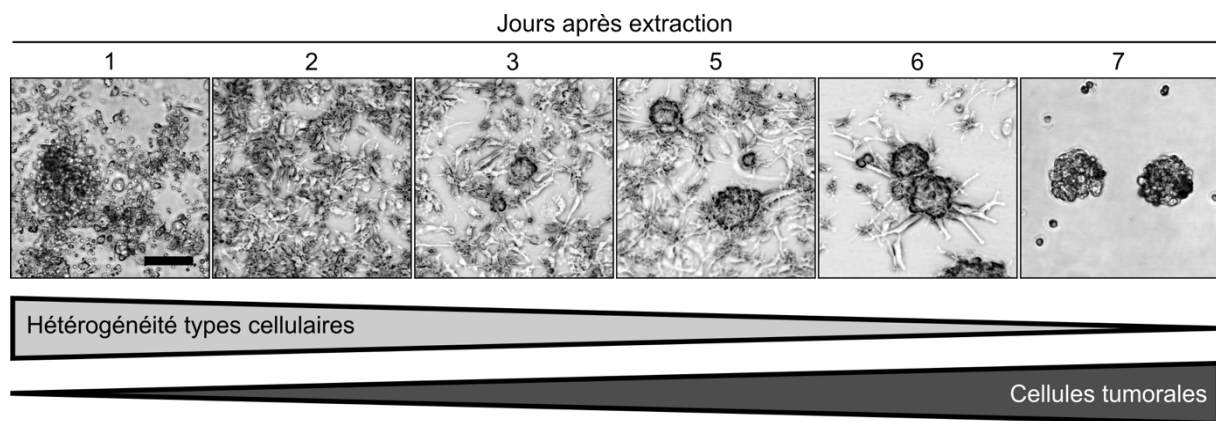


Figure 10 : Établissement d'une lignée cellulaire issue de patient

Les cellules sont extraites à partir d'une biopsie de GBM et cultivées en milieu neurobasal sans sérum.

L'entretien de la lignée GBM issue de patient se réalise par un repiquage qui se distingue des lignées cellulaires adhérentes où la trypsine est utilisée pour détacher les cellules de la flasque. Dans le cas présent, les sphéroïdes sont dissociés avec de l'acutase, moins toxique et moins agressive pour les cellules (222). Après comptage, les cellules sont replacées dans du milieu neurobasal frais.

Les cellules extraites conservent l'expression de marqueurs à caractères souches comme la nestine ou Sox2 (**Figure 11**). La nestine est une protéine filamenteuse assurant une fonction régulatrice essentielle de la neurogenèse (63). Sox2 est un facteur de transcription retrouvé lors de l'embryogenèse qui permet le renouvellement des cellules souches indifférenciées (62). L'expression de marqueurs de différenciation neuronale demeure faible (CD90) ou absente (NeuN).

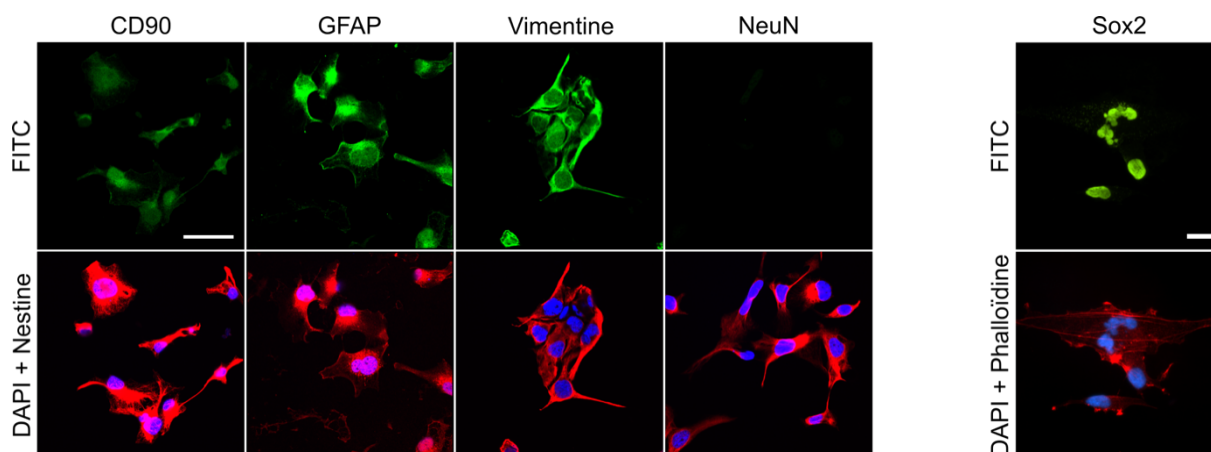


Figure 11 : Marquage de cellules adhérentes provenant de sphéroïdes dissociés

Les cellules sont marquées pour la nestine et Thy-1 (CD90), GFAP, vimentine et NeuN (*gauche*) ainsi que pour le cytosquelette et Sox2 (*droite*). Échelle = 25 μ m.

2.4 Expérimentations *in vitro*

2.4.1 Introduction

Un nombre considérable d'expériences utilisant des lignées cellulaires commerciales ont été réalisées sur une simple couche de cellules. La prolifération se quantifie par un comptage direct du nombre de cellules ou par une réaction colorimétrique. L'invasion et la migration, difficilement séparables ici, correspondent au déplacement des cellules à travers un insert de culture contenant une membrane poreuse (chambre de Boyden) ou le long d'une surface exempt de cellules. Malgré la simplicité d'utilisation et le moindre coût de ces techniques, elles présentent un désavantage majeur vis-à-vis des expériences tridimensionnelles (3D) : elles ne reproduisent pas l'architecture complexe d'une tumeur (223). Ce point est critique pour plusieurs raisons, la surface de contact en monocouche avec le milieu de culture est maximale exagérant la biodisponibilité des nutriments et des traitements. De plus, l'adhésion des cellules sur des surfaces non physiologiques impacte les processus de différenciation (224).

Les cultures 3D ont été développées pour surmonter ces défauts et mieux mimer l'architecture multicellulaire et l'hétérogénéité tumorale (223). La structure du sphéroïde contribue à une meilleure évaluation de la pharmacocinétique des médicaments et des mécanismes physiques à l'origine des résistances aux traitements (225). La densité cellulaire et la taille du sphéroïde impacte sur la diffusion des nutriments et des gaz (**Figure 12a et b**). Ainsi, l'environnement au centre du sphéroïde devient plus hypoxique (**Figure 12c**) et

nécessite une reprogrammation métabolique pour s'adapter à cette condition plus défavorable (226). Un centre nécrotique apparaît avec des sphéroïdes de plus en plus volumineux, se rapprochant au plus près de ce qui est retrouvé dans beaucoup de cancers et particulièrement les GBMs (227). Les cultures 3D représentent donc un modèle relevant pour étudier les mécanismes de croissance et d'invasion des tumeurs solides (228).

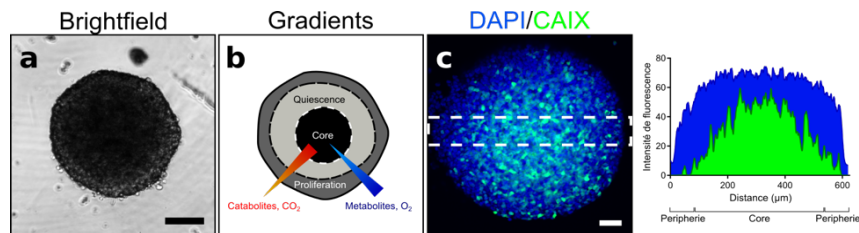


Figure 12 : Le sphéroïde est un modèle intermédiaire pour mimer les tumeurs solides

a. Image en fond clair d'un sphéroïde P3 avec une zone centrale dense. **b.** Représentation schématique montrant les gradients de métabolites et de gaz au sein du sphéroïde, adaptée de Hirschhaeuser *et al.* (229) **c.** Image confocale d'un sphéroïde marqué pour les noyaux (DAPI) et pour l'anhydrase carboxique IX (CAIX) (*gauche*) et quantification de l'intensité de fluorescence de la zone sélectionnée (*droite*). Échelle = 100 µm.

2.4.2 Préparation de sphéroïdes de taille homogène

Les sphéroïdes sont préparés sur des plaques 96 puits à fond incurvé. Après dissociation avec de l'acutase, les cellules sont comptées à raison de 10 000 cellules par puits et sont diluées dans un milieu de suspension (milieu neurobasal complet contenant 0.4 mg/mL de méthylcellulose). La méthylcellulose est une forme synthétique de la cellulose, son coût est faible, elle a peu d'influence sur le pH et n'est pas toxique (230). Son intérêt en culture réside dans sa capacité à forcer rapidement l'agrégation cellulaire due à sa faible réactivité avec les cellules. Les cellules sont incubées à 37°C, 5% de CO₂, 95% d'humidité et s'agglomèreront progressivement pour former des sphéroïdes utilisables au bout de 72 h (**Figure 13A**).

2.4.3 Expériences de croissance

Le sphéroïde formé est prélevé avec une pipette dont la pointe du cône a été coupée afin d'éviter l'endommagement de la structure. Il est rincé puis replacé en puits à fond incurvé dans du milieu de suspension frais avec ou non des molécules d'intérêts (agents chimiques, inhibiteurs). Une image est prise à T₀ puis à intervalles réguliers. La croissance du sphéroïde est le reflet de la prolifération cellulaire.

La roténone est un composé très lipophile qui inhibe le complexe I de la chaîne respiratoire induisant ainsi la production d'espèces réactives à l'oxygène et un dysfonctionnement mitochondrial (231). L'ajout de roténone dans le milieu de culture ralentit la croissance des sphéroïdes tumoraux (**Figure 13B**).

2.4.4 Expériences d'invasion

L'invasion tumorale est la première étape clé de la cascade métastatique. Son mécanisme met en jeu la capacité des cellules de GBM à interagir, remodeler et se mouvoir à travers la matrice extracellulaire (MEC) du système nerveux central. La MEC est un réseau complexe principalement composés de protéines fibrillaires comme le collagène, la laminine, la fibronectine et le protéoglycane. Pour se déplacer, la cellule de GBM émet une protrusion (invadopode) et crée des points focaux d'adhérence dans la MEC. Elle synthétise des protéases pour dégrader la MEC, réorganise son cytosquelette, se contracte et se détache des autres cellules pour avancer (232).

Ainsi pour mimer ce microenvironnement tumoral, reproduire plus fidèlement la morphologie de la tumeur et les processus d'invasion, les sphéroïdes sont placés dans une matrice tridimensionnelle. Celle-ci est composée de collagène de type 1, principal représentant de la classe des collagènes fibrillaires. Le collagène sert principalement de point d'ancrage pour les cellules tumorales (233). Couramment utilisé dans les essais d'invasion, il s'agit aussi du type de collagène le plus abondant dans l'organisme et est également un élément constitutif du stroma cérébral.

L'acidification du microenvironnement tumoral est un facteur qui favorise l'infiltration (234). L'ajout d'acide chlorhydrique (HCl) dans le milieu de culture a permis d'augmenter l'invasion des cellules en matrice de collagène (**Figure 13C**).

Les phosphodiésterases des nucléotides cycliques (PDE) sont des enzymes régulant le couplage excitation – contraction cellulaire en dégradant l'AMP et le GMP cyclique (AMPc et GMPc) (235). Des concentrations élevées d'AMPc réduisent la migration cellulaire (236,237). Dans les gliomes, un faible niveau d'AMPc est corrélée avec une plus grande malignité des tumeurs (238). De plus, l'expression des PDE est retrouvée augmentée dans les GBMs (239,240). La PDE3 hydrolyse préférentiellement l'AMPc, elle a initialement été étudiée dans le cœur et les muscles lisses vasculaires qui possèdent des cellules hautement contractiles

(241). L'utilisation du cilostamide, inhibiteur de PDE3, réduit les capacités invasives des cellules de GBMs (**Figure 13D**). Ces résultats sont concordant avec un autre cancer agressif, celui du pancréas (242).

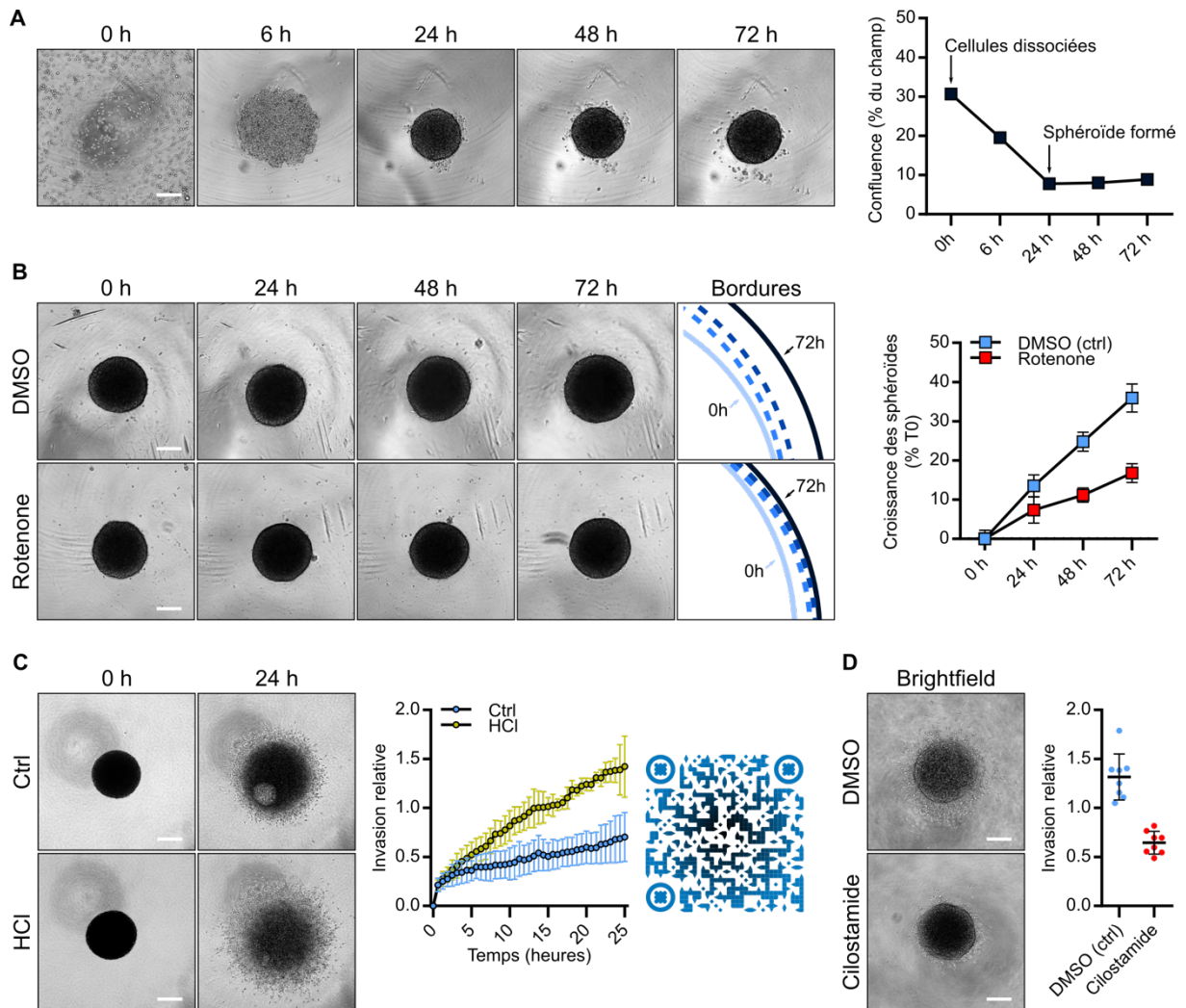


Figure 13 : Aperçu des expérimentations réalisables avec des sphéroïdes

A. Formation de sphéroïdes à partir de cellules dissociées en puits à fond incurvés. **B.** Expérience de croissance en présence de roténone. **C-D.** Expériences d'invasion en présence d'acide chlorhydrique (C) ou de cilostamide (D). Échelle = 100 μ m.




2.4.5 Analyse des expériences

La microscopie optique est l'un des moyens les plus simples d'étudier les phénomènes de croissance, d'invasion ainsi que d'autres phénomènes cellulaires. Dans ce cadre, l'image numérisée correspond à une représentation planaire d'un objet dans un espace tridimensionnel et transcrite en niveau de gris ou en couleur (**Tableau 2**). Il s'agit d'une matrice dont l'unité est le pixel (provenant de l'anglais *picture element*), chaque pixel est défini par

une valeur correspondant à une couleur. La création des images résulte de la volonté de figer un instant dans le temps afin de pouvoir analyser et interpréter l'évènement observé à tout moment.

Notre système visuel est capable de détecter des variations d'intensité lumineuse qui correspondent le plus souvent à des contours d'objets. Cette étape du traitement d'image, instantanée et automatique, nous permet de décomposer l'image en plusieurs régions homogènes ou de délimiter des zones hétérogènes. Cependant la quantification manuelle des paramètres pouvant être extraits (longueur, périmètre, aire, morphologie...) est énormément chronophage.

Tableau 2 : Valeurs des couleurs

| Type d'image | Valeurs des pixels | Exemples |
|----------------|--------------------------------------|---|
| Binaire (BIN) | [0 à 1] |  |
| Niveau de gris | 8 bits [0 à 255] |  |
| | 16 bits [0 à 2 ¹⁶ - 1] | |
| | 32 bits [0 à 2 ³² - 1] | |
| Couleur (RVB) | [0 à 255] ³ |  |

Le traitement informatique d'image est alors apparu pour remplacer l'observateur humain par une machine et de permettre l'automatisation des analyses. Les images sont d'abord prétraitées via une réduction du bruit de fond ou une augmentation de contraste à l'aide de filtres ou d'algorithmes puis sont traitées pour en extraire les paramètres d'intérêt. Ici, nous nous intéresserons brièvement à l'un des traitements qui opèrent sur des grandeurs calculées à partir des valeurs de chaque pixel de l'image : la détection de contour par segmentation ou approche frontière. Les variations d'intensité de pixels sont des informations importantes représentant des modifications de propriétés physiques et/ou géométriques (densité, distance, ombres, orientation...). Un contour se présente généralement comme une zone présentant une variation locale d'intensité. En considérant l'image comme un échantillonnage d'une fonction scalaire, cette variation peut être calculée sous la forme d'un

gradient pour chaque pixel en fonction des pixels voisins. Ainsi, les contours correspondront aux pixels de fort gradient (243).

Des outils ont été développés pour automatiser l'enchaînement de ces étapes mais rarement sur des plateformes libres et gratuites (244–246). Ils débutent généralement avec (1) un algorithme de soustraction de bruit fond où pour chaque pixel, une valeur moyenne est déterminée à partir des valeurs des pixels compris dans un cercle autour de ce pixel. Cette valeur moyenne est ensuite soustraite à la valeur du pixel de l'image originale supprimant ainsi les variations des intensités (247). (2) Un filtre de détection de contour est appliqué (classiquement un filtre de Sobel) pour calculer le gradient en chaque pixel de l'image. Il existe d'autres types de filtres similaires comme celui de Prewitt, ou bien ceux utilisant des systèmes de convolution comme les filtres de Canny et de Deriche. L'étape finale est de sélectionner ces pixels à fort gradient par (3) des algorithmes de seuillage pour obtenir une image binaire et d'en délimiter le contour avec une sélection composite. De manière générale, il est nécessaire d'ajuster les paramètres de chacune de ces étapes d'une image à l'autre en prenant également compte de la résolution et/ou du niveau de gris de l'image.

Dans l'optique de réduire ce paramétrage et d'optimiser l'utilisation sur plusieurs de type d'image, nous avons modifié certaines parties en développant un outil sur le logiciel libre et gratuit ImageJ (**Figure 14**). L'image brute est représentée en **Figure 14Ai** avec son diagramme de profil basé sur l'intensité de valeur des pixels. A ce stade, seul le centre du sphéroïde est déterminable par seuillage avec une valeur très contrasté des pixels comparé à ceux du reste de l'image. L'algorithme de soustraction du bruit de fond est remplacé par une opération d'images calculée à partir de l'image originale soumise à un filtre de convolution (3x3) d'intensité 1 soustraite de l'image originale soumise à un masque flou. Le filtre floute légèrement l'image alors que le masque améliore sa piquée. Pour les zones ne comprenant pas de fortes variations d'intensité (centre du sphéroïde et la matrice de collagène sans cellules), les valeurs de pixels sont ramenées à 0. Le décalage produit par les deux transformations qui ont été soustraites a permis de mettre en évidence des irrégularités d'intensité et donc de donner une information sur la présence de bords. Ainsi, cette étape permet de générer une image générique d'un unique format et d'éliminer le bruit de fond (**Figure 14Aii**). Un filtre de Sobel est appliqué pour détecter les contours de l'image prétraitée (**Figure 14Aiii**). Une image binaire est obtenue grâce à un seuillage avec un algorithme Triangle (248) suivi d'étapes d'extraction, de remplissage et d'élimination de petites particules. Les

zones d'intérêts peuvent ensuite être extraites, vérifiées et enregistrées (**Figure 14Aiv**). L'invasion se calcule à *posteriori* par la soustraction du total par le centre. Le panel B de la **Figure 14** montre le résultat du contourage des objets sur différents types d'images sans ajustement préalable des paramètres.

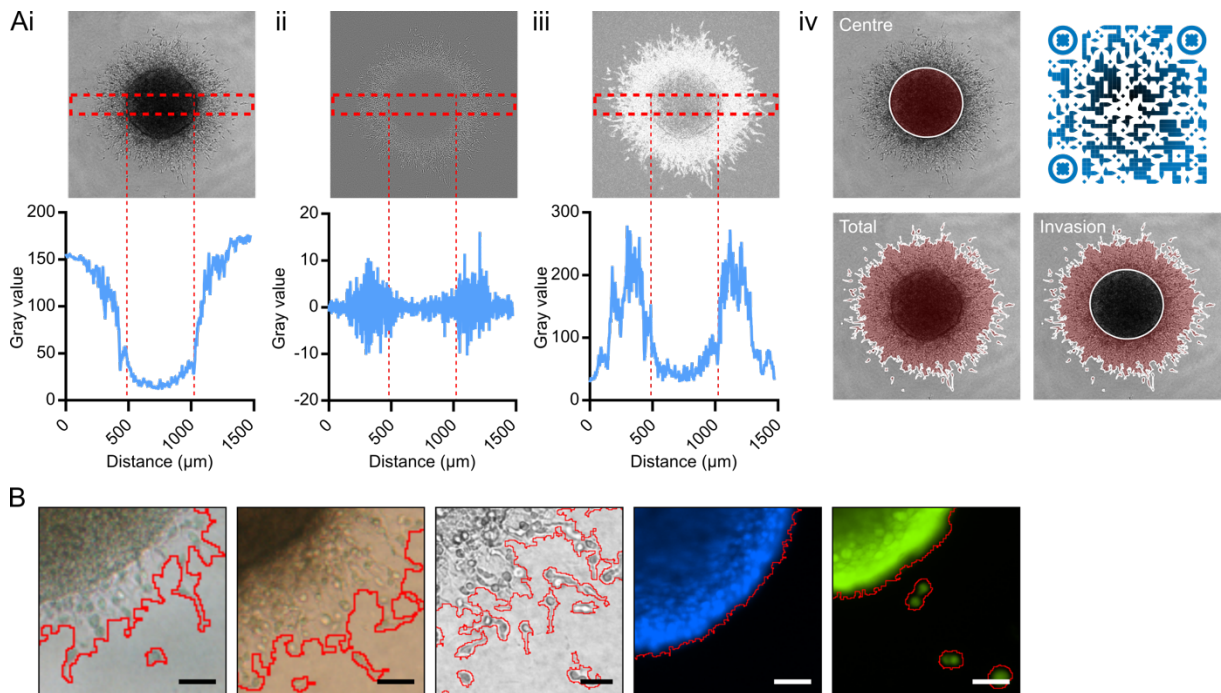


Figure 14 : Présentation de l'algorithme de segmentation

A. Présentation de la segmentation étape par étape. **(i)** Image brute. **(ii)** Image obtenue de la soustraction de l'image filtrée par l'image avec un masque. **(iii)** Contour de l'image avec filtre Sobel. **(iv)** Délimitation des différentes zones du sphéroïde. **B.** Exemples de segmentation avec les paramètres de base. Échelle = 50 µm.

Cet outil relativement simple reste cependant limité dans son utilisation lorsque des paramètres non pris en compte venait à apparaître comme par exemple la présence de plusieurs objets dans le même champ (pas de séparation automatique de ceux-ci), une résolution trop faible, un très mauvais contraste ou bien une image ayant subi une compression irréversible avec pertes. Des outils plus performants, basés sur l'intelligence artificielle, peuvent être alors utilisés (245).

Un autre intérêt de la microscopie est l'utilisation de sondes fluorescentes (comme la calcéine, l'ethidium homodimer ou l'hoechst) directement placées dans le milieu renseignent sur la viabilité (cellules positives à la calcéine) ou sur mortalité cellulaire (cellules positives à l'ethidium homodimer). Cependant, la capacité de pénétration de ces sondes peut être un point limitant selon la taille du sphéroïde, ce qui sera traduit par une absence de signal au

niveau du centre de la structure. De plus, l'acquisition d'images fluorescentes est beaucoup plus longue qu'en microscopie classique (des centaines de millisecondes *versus* quelques millisecondes) et génère de grandes quantités de données.

2.4.6 Coupe coronale d'un sphéroïde envahissant une matrice de collagène

Cette technique d'histologie à base de paraffine présente plusieurs intérêts. Tout d'abord, découper un sphéroïde invasif sur plusieurs lames permet l'utilisation de nombreux marqueurs sur le même échantillon et de diminuer la quantité utilisée. Des coupes fines de quelques micromètres d'épaisseur réduisent l'effet de saturation (concentration plus importante de cellules fluorescentes) ou l'absence de signal (faible pénétration du marqueur) qui peuvent être observés au centre des sphéroïdes 3D (246). Elle permet également d'analyser des informations à l'échelle cellulaire comme les interactions cellules/cellules et cellules/matrice (249). Enfin, l'imprégnation à la paraffine permet la conservation à long terme des échantillons à température ambiante.

Les phases de manipulation d'un sphéroïde invasif dans une la matrice de collagène à l'aide d'un enrobage d'agarose se basent sur un protocole validé pour des cellules isolées dans un hydrogel (249). A notre connaissance, une coupe coronale d'un tel sphéroïde n'a pas encore été réalisée. L'ensemble du processus est schématisé dans la **Figure 15**. Les sphéroïdes sont inclus dans un insert de culture de 8.0 µm format 24 puits. Après 24 heures d'invasion, les sphéroïdes sont fixés 4 heures avec du PFA 4% puis lavés trois fois avec du PBS avant d'être déshydratés dans deux bains d'éthanol 70%. L'éthanol est éliminé puis de l'agarose liquide 2% non bouillant est déposé au-dessus de l'échantillon dans l'insert. Après solidification, la membrane de l'insert est retirée ce qui facilite le démoulage du gel d'agarose comprenant le sphéroïde dans le collagène sur sa partie supérieure. L'échantillon est ensuite entièrement enrobé avec de l'agarose liquide puis laissé à température ambiante. Il est ensuite déshydraté dans deux bains d'éthanol 96%, deux bains d'éthanol 100% puis par deux bains de toluène. L'échantillon est enfin placé dans deux bains de paraffine liquide (60°C). L'insertion se fait verticalement dans un bloc d'inclusion.

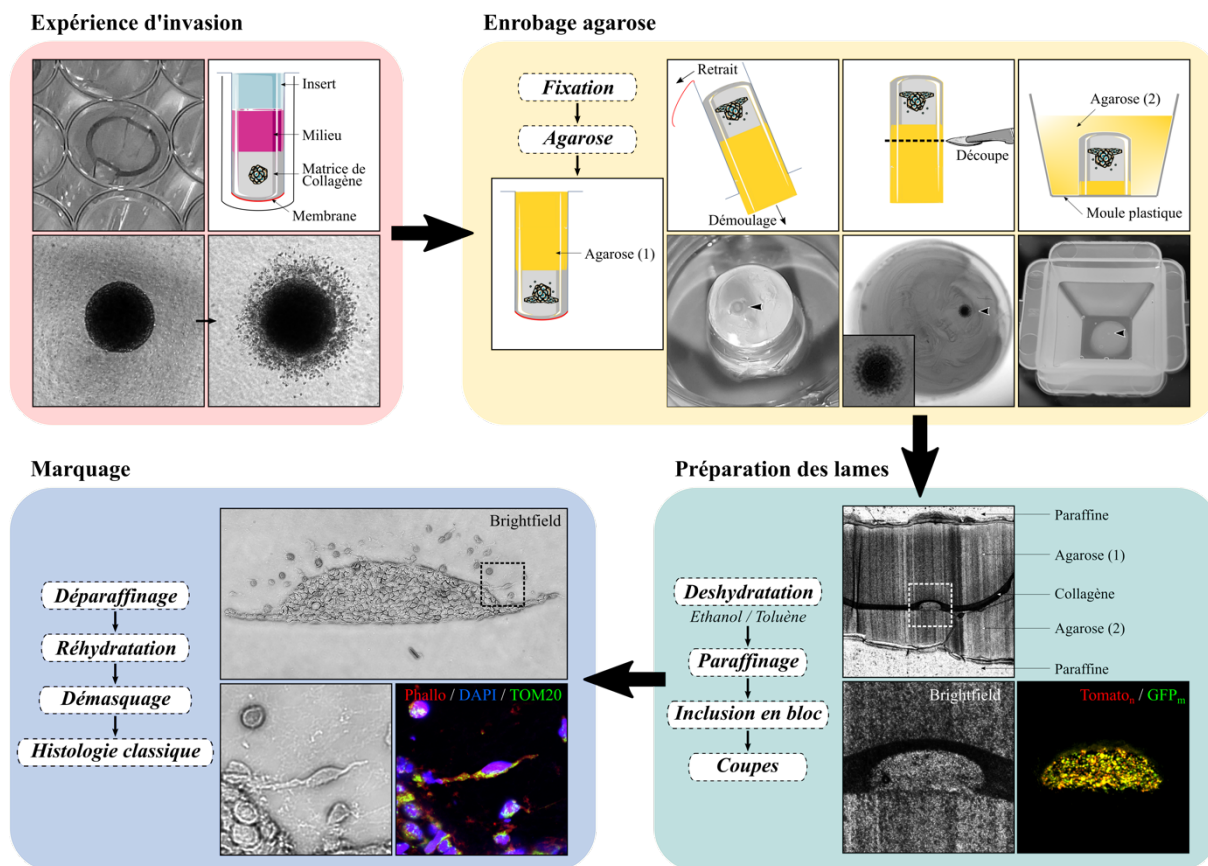


Figure 15 : Processus pour manipuler, paraffiner et marquer des sphéroïdes invasifs en matrice de collagène
Expérience d'invasion : les sphéroïdes sont inclus dans une matrice de collagène de type I en insert de culture puis sont incubés 24h. Enrobage agarose (adapté selon (249)) : Après fixation au PFA et lavage au PBS, l'agarose 2% est coulé au-dessus de la matrice. La membrane de l'insert est retirée permettant le démoulage de l'échantillon, il est ensuite coupé puis à nouveau enrobé avec de l'agarose 2%. Préparation des lames : l'échantillon est déshydraté dans des bains d'éthanol puis de toluène, paraffiné et inclus en bloc de paraffine pour être coupé avec un microtome. Marquage : les lames sont déparaffinées dans des bains de toluène puis d'éthanol, les antigènes sont démasqués dans un bain de citrate. Le sphéroïde est marqué pour le cytosquelette (phalloïdine), les noyaux (DAPI) et les mitochondries (TOM20).

2.4.7 Co-culture avec des neurones

Ici, nous décrivons un modèle simplifié pour étudier l'invasion des GBM à travers un recouvrement de neurones adhérent sur des fibres de laminine. Les cellules étant disséminées dissociées ou sous forme de sphéroïdes. Ces deux conditions visent à récapituler l'invasion sur des neurones tel que c'est observé chez des patients atteints de GBM (203,217,250). Ce modèle permettra d'étudier l'échappement des cellules de GBM à travers les fibres nerveuses et d'étudier les nouvelles voies moléculaires impliquées dans ce processus.

a. Protocole

Les étapes du protocole sont schématisées dans la **Figure 16A**.

Des lamelles circulaires en verre de 18 mm sont traitées par un mélange d'air/plasma activé pendant 5 minutes. Elles sont ensuite placées en chambre fermée avec 100 μL de (3-aminopropyl)triéthoxysilane et un dessiccateur pendant 1 heure. Les lamelles sont incubées avec du poly(éthylène glycol)-succinimidyl valérate (PEG SVA) dans un tampon carbonate de 10 mM et de $\text{pH} > 8$ pendant 1 heure. Elles sont ensuite rincées avec de l'eau ultrapure et séchées sous une hotte chimique. Le photoinitiateur 4-benzoylbenzyl-triméthylammonium chlorure (PLPP) est dissous à 14,7 mg/mL dans du PBS. Un mélange de 3 μL de gel de PLPP et 50 μL d'éthanol absolu est déposé au centre de la lamelle. L'échantillon est placé sous une hotte chimique pour favoriser l'évaporation complète de l'éthanol absolu. La lamelle est ensuite montée dans une chambre de Ludin et placée sur un microscope équipé d'un système d'autofocus. Les images qui correspondent au motif visionné sont chargées sur le logiciel. Les paramètres suivants sont appliqués : réplication 4 x 4 temps, espace de 200 μm , dose d'UV de 1000 mJ/mm^2 . Après l'illumination automatique aux UV, le PLPP décollé est retiré à l'aide de plusieurs rinçages au PBS. La laminine (50 $\mu\text{g}/\text{mL}$ de PBS) est ensuite incubée pendant 30 minutes. La chambre est lavée avec du PBS.

Les neurones proviennent de la dissection de l'hippocampe d'embryons de rats (E18 Sprague-Dawley) qui est transféré dans une solution saline balancée d'Hank's (HBSS)/1 mM 4-(2-hydroxyéthyl)-&-piperazineéthanesulfonate (HEPES) contenant une solution de 15 mL de pénicilline-streptomycine. L'excès de la solution est éliminé sans que l'hippocampe soit séché. Puis est ajouté 5 mL de trypsine-éthylène diamide tétraacétique (EDTA), supplémenté en pénicilline (10000 unités/mL), en streptomycine (10000 $\mu\text{g}/\text{mL}$) avec 1 mM d'HEPES. L'échantillon est incubé 15 minutes à 37°C puis rincé deux fois avec la solution d'HBSS/HEPES/pénicilline-streptomycine. Le tissu est laissé 2 à 3 minutes dans cette solution avant d'être dissocié précautionneusement avec une pipette Pasteur. Les cellules sont finalement comptées et la viabilité est évaluée. Les neurones sont ensuite semés sur la lamelle précédemment préparée à raison de 50 000 cellules par cm^2 dans du NBM enrichi avec 3% de sérum de cheval. Après 48 h d'incubation à 37°C, les cellules dissociées ou les sphéroïdes sont ajoutés sur les neurones. L'échantillon est immédiatement placé sur un microscope équipé d'une chambre thermostatée à 37°C et 5% de CO_2 . Les images sont acquises toutes les 5 minutes sur 12 heures avec un objectif X20.

b. Résultats représentatifs

Les cellules de GBM migrent de manière aléatoire le long des extensions neuronales (**Figure 16B - vidéo**). Elles peuvent être distinguées des cellules neuronales par leur fluorescence, ce qui permet le suivi des mouvements cellulaires. Ainsi, la capacité migratoire des cellules de GBM sur le tapis de neurones est plus grande que celles déposées sur la laminine (**Figure 16B i et ii**). La motilité cellulaire est quantitativement estimée avec le déplacement carré moyen (MSD) et sa transformation logarithmique représente une fonction linéaire (251), elle est également plus importante pour les cellules de GBM semées sur les neurones (**Figure 16B iii**). Le ratio directionnel (ou persistance) est aussi calculé pour les deux conditions, il permet de comparer la direction du parcours de la cellule (réel entre le point de départ et d'arrivée) par rapport à la direction idéale de la migration (ligne droite entre le point de départ et d'arrivée) (252) (**Figure 16B iv**).

La migration des sphéroïdes est également suivie via la détection de l'aire de fluorescence au cours du temps sur les neurones ou sur le recouvrement de laminine (**Figure 16C i**). Après 500 minutes, la moitié du tapis de neurones est recouvert par les cellules de GBM alors que les sphéroïdes n'adhèrent pas au recouvrement de laminine (**Figure 16C ii**).

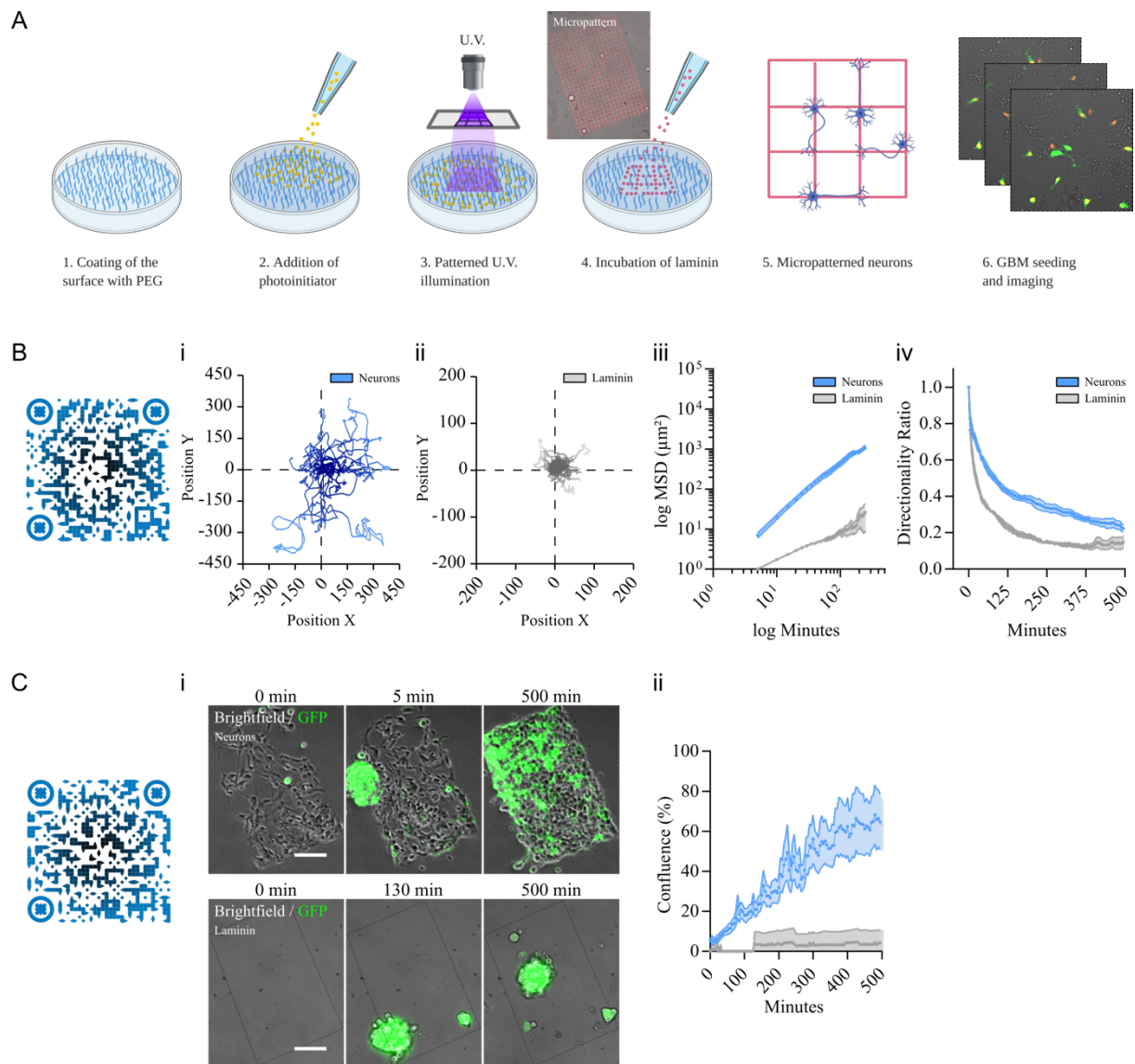


Figure 16 : Coculture des cellules de GBM sur un tapis de neurones

A. Setup expérimental. **(1)** La surface de la plaque est recouverte par une couche de PEG. **(2)** Ajout de l'agent photo-inhibiteur. **(3)** Un rayon UV projette une image à travers l'objectif du microscope, ce qui active localement l'agent photo-inhibiteur et clive les molécules de PEG. **(4)** La laminine est ajoutée puis s'adsorbe sur les zones clivées. **(5)** Les neurones sont déposés et adhèrent uniquement sur le recouvrement de laminine. **(6)** Les cellules fluorescentes ($GFP_{\text{membranaire}}/Tomato_{\text{nucléaire}}$) de GBM P3 sont déposées sur les neurones et les images sont acquises toutes les 5 minutes. **B.** Analyse du déplacement des cellules P3. Graphique de déplacement des cellules sur un recouvrement **(i)** de neurones ou **(ii)** de laminine. **(iii)** Déplacement carré moyen (Mean Square Displacement ou MSD) et **(iv)** Ratio directionnel des cellules P3 sur neurones ou sur laminine. **C.** Analyse de migration des sphéroïdes. **(i)** Image représentative à différents temps des sphéroïdes sur neurones et sur laminine. Échelle = 100 μm . **(ii)** Migration des sphéroïdes représenté par la confluence de l'aire de fluorescence. Pour chaque expérience : 4 zones indépendantes, les données sont représentées par la moyenne \pm S.E.M. Abréviations : PEG = polyéthylène glycol, UV = ultraviolet, GFP = protéine fluorescente verte.

2.5 Expérimentations *in vivo*

La greffe de cellules tumorales humaines chez les animaux permet d'étudier la tumorigenèse et l'efficacité d'un traitement dans un contexte *in vivo*. Les sphéroïdes sont directement implantés dans le cerveau d'une souris immunodéficiences RAG2/ γ à l'aide d'un appareillage stéréotaxique. Cette implantation est préférée à celle sous-cutanée car elle permet à tumeur l'expression de composants de la MEC cérébrale, non retrouvée au niveau de la peau. La tumeur se trouve également dans un microenvironnement plus proche et donc plus représentatif de celui observé chez l'homme. L'implantation se réalise sur des souris anesthésiées dont le crâne a été perforé pour faciliter l'insertion d'une seringue Hamilton. Cinq sphéroïdes sont inoculés à gauche de 2,2 mm du point de rencontre des sutures de l'os frontal et des pariétaux (bregma) et à 3.4 mm de profondeur. La croissance tumorale peut être observée deux à trois semaines après l'implantation. A la fin de l'expérience, les souris sont euthanasiées et les cerveaux prélevés pour être ensuite étudiés avec des techniques d'immunohistologie renseignant des informations sur la tumeur (nestine) mais également d'autres paramètres comme la vascularisation (CD31) (**Figure 17**). Plusieurs des caractéristiques des GBM sont observées comme une large invasion controlatérale par le biais des corps calleux (**Figure 17** panel haut droit), une augmentation de la densité vasculaire dans la tumeur par rapport à la partie saine (**Figure 17** milieu droit) et des cellules qui envahissent de manière isolée (**Figure 17** bas droit).

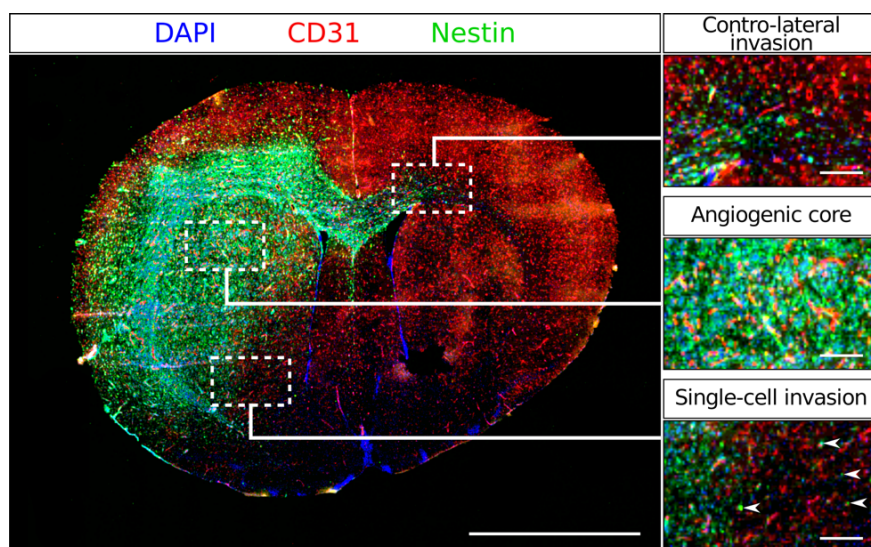


Figure 17 : Immunohistologie sur une coupe coronale d'un cerveau de souris

Les cellules sont marquées pour le DAPI (bleu), CD31 (rouge) et la nestine (vert). Échelles = 2,5 mm (gauche) et 250 μ m (droite)

3.1 The invasive proteome of glioblastoma revealed by laser-capture microdissection

Le phénotype invasif et diffus des GBMs est à l'origine du mauvais pronostic de ces tumeurs (253). C'est aussi pourquoi la résection chirurgicale, bien que la plus large possible, n'englobe pas l'intégralité de la tumeur. Les cellules tumorales envahissent préférentiellement le long des corps calleux, composé de fibres nerveuses, mais également le long des vaisseaux sanguins et dans l'espace interstitiel pour former des tumeurs secondaires cérébrales (208). Les analyses « omics » sont généralement basées sur la biopsie même, comprenant simultanément plusieurs zones de la tumeur ou une seule zone... Il n'existe pas de traitement efficace selon les sous-types de GBMs déterminés par transcriptomique, excepté les GBMs présentant une mutation du promoteur MGMT avec une amélioration de la survie des patients lors de l'utilisation du TMZ (8,169). La transcriptomique repose sur la quantification des ARN issus de la transcription du génome, témoin des réponses adaptatives des cellules. Cependant, entre 80 et 90% des ARN messagers produits sont dégradés avant d'être traduits en protéines (254,255). L'effet génotypique (synthèse des ARN messagers) ne reflète donc pas forcément l'effet phénotypique (synthèse et activité des protéines).

Dans cette étude, nous avons utilisé la lignée P3 de GBM issue de patients et implantée dans le cerveau de souris pour étudier le changement d'expression de protéines entre les zones centrales et invasives. Les zones ont été récoltées par microdissection laser puis analysées par une étude de protéomique afin d'identifier de nouvelles signatures tumorales. Enfin les cibles trouvées ont été validées *in vitro*.

Principaux résultats :

- L'analyse a montré une augmentation d'expression de 34 protéines et une diminution d'expression de 118 protéines dans la zone invasive par rapport à la zone centrale.
- PLP1 et DMN1 sont les candidats majeurs retrouvés parmi les protéines surexprimées.
- L'utilisation *in vitro* d'inhibiteurs de PLP1 (PLP1i) ou de DNM1 (dynasore) à doses non cytotoxiques réduit les capacités invasives des cellules tumorales.

The invasive proteome of glioblastoma revealed by laser-capture microdissection

Thomas Daubon, Joris Guyon, Anne-Aurélien Raymond, Benjamin Dartigues, Justine Rudewicz, Zakaria Ezzoukhry, Jean-William Dupuy, John M. J. Herbert, Frédéric Saltel, Rolf Bjerkvig, Macha Nikolski, and Andreas Bikfalvi

INSERM U1029, Pessac, France (T.D., J.G., J.R., A.B.); LAMC, University of Bordeaux, Bordeaux, France (T.D., J.G., J.R., A.B.); KG Jebsen Brain Tumour Research Center, University of Bergen, Bergen, Norway (T.D., R.B.); University Bordeaux, INSERM UMR1053, BaRITOn Bordeaux Research in Translational Oncology, F-33000 Bordeaux, France (F.S.); Oncoprot, TBM Core US005 University of Bordeaux, France (A.-A.R., Z.E., F.S.); Bordeaux Bioinformatics Center, CBiB University of Bordeaux, France (B.D., J.R., M.N.); Plateforme Protéome, University of Bordeaux, Bordeaux, France (J.-W.D.); Disease Gene Discovery Limited, 27 Old Gloucester Street, London, UK (J.M.J.H.); NorLux Neuro-Oncology, Department of Biomedicine University of Bergen, Norway (R.B.); Oncology Department, Luxembourg Institute of Health 84, Val Fleuri, Luxembourg (R.B.); LaBRI, UMR5800 University of Bordeaux, Talence, France (M.N.)

Corresponding Authors: Andreas Bikfalvi and Thomas Daubon, U1029 INSERM-Angiogenesis and Cancer Lab, Université Bordeaux – Campus Pessac, Bat. B2, RDC, Allée Geoffroy St-Hilaire, 33615 Pessac, France (andreas.bikfalvi@u-bordeaux.fr; thomas.daubon@u-bordeaux.fr).

Abstract

Background. Glioblastomas are heterogeneous tumors composed of a necrotic and tumor core and an invasive periphery.

Methods. Here, we performed a proteomics analysis of laser-capture micro-dissected glioblastoma core and invasive areas of patient-derived xenografts.

Results. Bioinformatics analysis identified enriched proteins in central and invasive tumor areas. Novel markers of invasion were identified, the genes proteolipid protein 1 (PLP1) and Dynamin-1 (DNM1), which were subsequently validated in tumors and by functional assays.

Conclusions. In summary, our results identify new networks and molecules that may play an important role in glioblastoma development and may constitute potential novel therapeutic targets.

Key Points

- Proteomics analysis on central and invasive areas reveals molecular heterogeneity.
- Membrane trafficking, cytoskeleton, and metabolism pathways are particularly enriched.
- Identification of new players in glioblastoma development.

Glioblastomas (GBM) are the most common and aggressive tumors from the central nervous system. Patient survival rate, despite therapeutic improvements, is about 15 months after tumor detection.^{1,2} GBM derive mainly from astrocytes but may contain oligodendrocytic components as well. They are characterized by increase in vascular growth, but also by tortuous blood vessels, that are poorly perfused and thrombose, resulting in hypoxia and, in turn, necrosis.³ Furthermore, single or contro-lateral invasion is observed.⁴ The Stupp protocol, commonly used as first-line therapy, is based on large tumor

mass resection, local irradiation, and temozolomide treatment. Tumor recurrence is a constant feature and observed after a few months at which point patients may undergo second line surgery and antiangiogenic therapy (bevacizumab).⁵ However, evasive resistance to antiangiogenic treatment is observed with tumor recurrence in most of the cases, mainly due to secondary tumors formed from invasive cells. We have recently performed RNA sequencing for both central and invasive areas and identified a gene regulatory network with high connectivity.⁶

Importance of the Study

Our study deals with the identification of molecular players and regulatory circuits in glioblastoma development. Since glioblastomas are heterogeneous tumors composed of a tumor core and an invasive periphery, we have chosen

a proteomics approach which takes into account this regional heterogeneity. We used laser-capture microdissection and state-of-the-art proteomics analysis of core and invasive tumor areas to identify molecular players and signatures.

In this study, we performed laser-capture microdissection of core and invasive areas from patient-derived GBM xenografts followed by high-throughput proteomic analysis. We identified novel protein signatures including proteolipid protein 1 (PLP1) and Dynamin-1 (DNM1) and validated them in additional tumor samples. Finally, a functional validation was carried out *in vitro*. Thus, our results report novel unexpected proteins that are involved in glioblastoma development and may constitute novel therapeutic targets for preventing invasion following surgery.

snap-frozen samples. The sections were then dehydrated in a series of pre-cooled ethanol baths (40 s in 95% and twice 40 s in 100%) and air-dried. Laser microdissection of samples was performed using a PALM MicroBeam microdissection system version 4.6 equipped with the P.A.L.M. RoboSoftware (P.A.L.M. Microlaser Technologies AG, Bernried, Germany). Laser power and duration were adjusted to optimize the capture efficiency. Microdissection was performed at 5x magnification. Three tumors were analyzed for each condition, and five caps were collected for each tumor type. Three replicates were generated on serial sections for each brain tumor.

Materials and Methods

Ethical Issues

Male RAG γ 2C^{-/-} mice were housed and treated in the animal facility of Bordeaux University (“Animalerie Mutualisée Bordeaux”). All animal procedures were performed as according to the institutional guidelines and approved by the local ethics committee (agreement number: 5522).

Patients gave their consent prior tissue analysis according to the clinical guidelines. Informed written consent was obtained from all subjects (Department of Neurosurgery, Humanitas, Milan according to Humanitas ethical committee regulations).

Intracranial Tumor Xenografts

P3 spheroids were prepared 3 days before implantation by seeding 10⁴ P3 cells in neurobasal medium with 0.4% methylcellulose (Sigma) in a U-bottom 96 wells plate (Falcon). After PBS washing, five P3 spheroids were stereotactically implanted into the brains of randomly chosen three Rag γ 2C^{-/-} mice (8–12 weeks old). P3 cells have been extensively characterized and have molecular profile of the mesenchymal subgroup (from male patient, age 64; chromosomal aberrations + [Chr 7, Chr19, 20q], -[1q42-q43, Chr9, Chr10, 20p] - [PIK3R, CDKN2A/B]⁷). Briefly, GBM spheroids (5 spheroids of 10⁴ cells per mouse) were implanted into the right cerebral hemisphere using a Hamilton syringe fitted with a needle (Hamilton, Bonaduz, Switzerland), following the procedure already described,⁸ which consisted in an injection at Bregma 0, 2 mm left, 3 mm deep.

Laser-Capture Microdissection

Coronal brain sections (10 μ m thickness) were made using a CM3050-S microtome (Leica, Wetzlar, Germany) from

Sample Preparation for Mass Spectrometry

Microdissected tissues were first incubated in RIPA buffer supplemented with inhibitor cocktail (Complete, Roche). They were then treated by sonication for 10 s, supplemented with Laemmli buffer, heated at 95°C during 5 min and finally loaded onto a 10% acrylamide SDS-PAGE gel. Migration was stopped when samples entered into the first centimeter of the resolving gel and proteins were visualized by Colloidal Blue staining. Each SDS-PAGE band was cut into 1 × 1 mm gel pieces. Gel pieces were destained in 25 mM ammonium bicarbonate (NH₄HCO₃), 50% Acetonitrile (ACN), and shrunk in ACN for 10 min. After ACN removal by evaporation or pipetting, gel pieces were dried at room temperature. Proteins were first reduced in 10 mM dithiothreitol, 100 mM NH₄HCO₃ for 30 min at 56°C, then alkylated in 100 mM iodoacetamide, 100 mM NH₄HCO₃ for 30 min at room temperature, and shrunken in ACN for 10 min. After ACN removal, gel pieces were rehydrated with 100 mM NH₄HCO₃ for 10 min at room temperature. Before protein digestion, gel pieces were shrunken in ACN for 10 min and then dried at room temperature. Proteins were digested by incubating each gel slice with 10 ng/ μ l of trypsin (T6567, Sigma-Aldrich) in 40 mM NH₄HCO₃, 10% ACN, rehydrated at 4°C for 10 min, and finally incubated overnight at 37°C. The resulting peptides were extracted from the gel by three steps: a first incubation in 40 mM NH₄HCO₃, 10% ACN for 15 min at room temperature and two incubations in 47.5% ACN, 5% formic acid for 15 min at room temperature. The three collected extractions were pooled with the initial digestion supernatant, dried in a SpeedVac, and resuspended in 0.1% formic acid before nanoLC-MS/MS analysis.

nanoLC-MS/MS Analysis

Online nanoLC-MS/MS analyses were performed using an Ultimate 3000 RSLC Nano-UPHLC system (Thermo

Scientific, USA) coupled to a nanospray Q-Exactive hybrid quadrupole-Orbitrap mass spectrometer (Thermo Scientific, USA). Each peptide extract were loaded onto a 300 μm ID \times 5 mm PepMap C₁₈ precolumn (Thermo Scientific, USA) at a flow rate of 20 $\mu\text{l}/\text{min}$. After 3 min desalting, peptides were online separated on a 75 μm ID \times 25 cm C₁₈ Acclaim PepMap RSLC column (Thermo Scientific, USA) with a 4–40% linear gradient of solvent B (0.1% formic acid in 80% ACN, solvent A: 0.1% formic acid in H₂O) in 108 min. The separation flow rate was set at 300 nl/min. The mass spectrometer was operated in positive ion mode at a 1.8 kV needle voltage. Data were acquired using Xcalibur 3.1 software in a data-dependent mode. Full MS scans in the range from m/z 300 to 1600 were recorded at a resolution of 70,000 at m/z 200 and the target value for the automatic gain control (AGC) algorithm was set to 3×10^6 ions collected within 100 ms. Dynamic exclusion was set to 30 s and top 12 ions were selected from fragmentation in HCD mode. MS/MS spectra were acquired with a resolution of 17,500 at m/z 200, and the maximum ion injection time and the AGC target were set to 100 ms and 1×10^5 ions, respectively. Only precursors with assigned charges states +2 and +3 were selected for fragmentation. Molecules that are not proteins are generally charged with only one proton, hence the interest of sequencing only multicharged ions, which are generally peptides. Furthermore, peptide anion analysis remains little practiced because of challenges with high-pH reversed-phase separations and a lack of robust fragmentation methods suitable for peptide anion characterization. Others settings were as follows: no sheath and no auxiliary gas flow; heated capillary temperature of 270°C; normalized HCD collision energy of 27%; and an isolation width of 2 m/z .

MS Data Processing and Quantification

Mascot 2.5 algorithm through Proteome Discoverer 1.4 Software (Thermo Fisher Scientific Inc.) was used for protein identification in batch mode by searching against a *Mus musculus* database (Proteome ID UP000000589; release date November 15, 2018; 54,188 proteins) merged to a *Homo sapiens* database (Proteome ID UP000005640; release date November 17, 2018; 73,931 proteins) from <http://www.uniprot.org/> website.⁸ Two missed enzyme cleavages were allowed. Mass tolerances in MS and MS/MS were set to 10 ppm and 0.02 Da. Oxidation of methionine, acetylation of lysine, and deamidation of asparagine and glutamine were searched as dynamic modifications. Carbamidomethylation on cysteine was searched for as a static modification. For protein quantification, raw LC-MS/MS data were imported in Proline Studio (<http://proline.profipteomics.fr/>) for feature detection, alignment, and quantification. Protein identification was only accepted when at least 2 specific peptides had a pretty rank = 1 and had a protein false discovery rate value < 1.0% calculated using the “decoy” option in Mascot.⁸ Label-free quantification of MS1 level by extracted ion chromatograms was carried out using the parameters indicated in [Supplementary Table 1](#). Protein ratios were normalized to the median ratio. A missing values inference method was applied, and we used a variant when there is a minimum of 1.5-fold change with an adjusted P value below .05.

Experimental Reproducibility Between Triplicates

Protein quantifications were analyzed using a bespoke pipeline of python scripts. For human data set, there were 743 proteins in each brain sample and 517 proteins for the mouse data set. We estimated the dispersion of protein quantification values between technical replicates (3 per sample) for each condition (angiogenic and invasive) by computing the coefficient of variation $CV = \frac{\sigma}{\mu}$, where σ and μ are the standard deviation and mean. Histograms of CV values were built for each sample separately for each condition. Based on the analysis of these histograms, we chose $CV = 0.8$ as the threshold for eliminating proteins whose values were not sufficiently reproducible between triplicates. Proteins were retained only if the CV was below the 0.8 threshold for both conditions, resulting in 574, 691, and 714 proteins for each of the brain samples for Human and in 372, 468, and 484 proteins for each of the brain samples for mouse. To compare central and invasive conditions, we have generated aggregated tables with protein quantifications for all samples and replicates, resulting in 18 column tables (9 columns per condition) for Human and mouse; a protein was retained to be part of these tables only if it was present in 6 out of 9 columns for each condition. These resulting aggregated data set contain in total 730 proteins for the Human-annotated data set and 510 for the mouse-annotated data set ([Supplementary Tables 2 and 3](#)). Furthermore, for certain downstream analyses, we considered only proteins common to all replicates, reducing the aggregated data sets to 544 and 331 proteins for Human and mouse, respectively.

Differential Expression Analysis

To reveal potential biomarkers which distinguish between invasive and angiogenic conditions, we applied the Welch's t -test to the corresponding replicate value vectors. The resulting P -values were further adjusted using the Benjamini–Hochberg multiple test correction algorithm⁹ resulting in padj values for each protein. We set the threshold for the significance of the padj at 0.01, yielding (i) for the aggregated data sets 152 and 284 potential biomarkers for Human and mouse, respectively; and (ii) for the common data sets 119 and 206 potential biomarkers for Human and mouse, respectively. These significantly differentially expressed proteins are further filtered by computing the log-fold change between protein quantifications for invasive and angiogenic replicates as $\log FC = \log \frac{\mu(I)}{\mu(A)}$, where I and A are vectors of values for invasive and angiogenic conditions, respectively. Proteins having $\text{padj} < 0.01$ and $|\log FC| > 2$ for the Human data set and $\text{padj} < 0.01$ and $|\log FC| > 5$ for the mouse data set are retained to generate the clustermaps. Clustermaps were generated using pheatmap package v.1.0.12¹⁰ with the Euclidean distance and Ward D2 clustering method parameters.

Functional Enrichment Analysis

For the enrichment analysis, the significantly differentially expressed proteins ($\text{padj} < 0.01$) in the aggregated

data sets were further filtered by the logFC criterion. We have retained proteins having the $|\log_{2}FC| > 1$ for both Human- and mouse-aggregated data sets. In order to find pathways deregulated between the two conditions of interest, we subsequently performed a Gene Set Enrichment Analysis (GSEA) on these subsets. We used Gseapy python package (<https://pypi.python.org/pypi/gseapy>), which is a wrapper to the functionalities provided by the Broad's institute GSEA suite (<http://www.broad.mit.edu/gsea/>). We used the enrichment function, applying a 0.05 adjusted P-value cutoff, and ran the analysis using the GO biological process and GO cellular component knowledgebases. KEGG package was also used for defining cellular pathways enriched in invasive areas.

AngioScore

The AngioScore was calculated as done previously.¹¹ Briefly, for each gene, the AngioScore is the percentage of publications that contain one or more relevant angiogenesis keywords in the abstracts from all publications assigned to a gene by the Entrez Gene database. A *t*-test comparison of AngioScores between the core and the invasive GBM areas was performed.

Antibodies and Reagents

PLP inhibitor peptide was purchased from Peprotech (100–21), and DNM1 inhibitor, Dynasore (RD Systems, 201-LB/C). Cells were treated at concentrations indicated concentrations in the legend section.

Histological and Immunohistological Analyses

For immunofluorescence on histological sections, frozen sections were processed as described previously.⁶ Patient paraffin-embedded sections were deparaffinised in xylene and hydrated serially in 100%, 95%, and 80% ethanol. Endogenous peroxidase was quenched in 3% H₂O₂ in PBS for 10 min. Slides were then incubated with anti-DNM1 (Invitrogen PA1660), anti-PLP1 (Sigma SAB2101830), or anti-Nestin (ThermoFisher PA5-11887) antibodies overnight at 4°C. Sections were washed three times in PBS, and secondary fluorescent antibodies were applied (Anti-mouse or anti-rabbit fluorescent antibodies). After mounting, DNM1 or PLP1 expression localizations were analyzed using IHC profiler from Fiji Software. IHC profiler uses the DAB signal in images and the results are expressed as a ratio the DAB area to the total area.

Proliferation and Viability Experiments

A 96 wells plate (Falcon) was coated with 0.2 mg/ml of Matrigel in NBM for 30 min. Then, 2000 P3 cells were placed into the wells with 10 ng/ml of Hoechst stain in NBM and incubated for 24 h. When adherent cells appeared, supernatant were removed and substituted by 100 μ l of NBM with treatment. Pictures of each well were taken at T0, 24 h, 48 h, and at 72 h. LIVE/DEAD (Invitrogen) assays were also realized through the addition of Calcein into the wells. The

number of living (in blue) and/or dead (in red) cells was quantified with the FIJI software.

Invasion Assays in Collagen I Gels

P3 spheroids were prepared 3 days, respectively, before inclusion by the seeding of 10⁴ cells in neurobasal medium with 0.4% methylcellulose (Sigma) in a U-bottom 96 wells plate (Falcon). A solution of 1 mg/ml of collagen I (Fisher Scientific) was prepared in PBS with 7.2mM NaOH. Treatments were mixed directly into the collagen gels. After 30 min incubation on ice, spheroids were individually picked, washed in PBS, and included in the collagen solution. After 45 min at 37°C in a cell incubator, neurobasal medium with the different treatments was added. P3 spheroid invasion areas were measured after 24 h with FiJI software, with a home-made macro. Briefly, total area was automatically quantified and the core area was manually measured. The core area was then subtracted from the total area for obtaining the invasive area. For each independent experiment, the mean of 7 to 8 invasive areas was calculated and compared with controls.

Statistical Analysis for In Vitro Experiments

Statistical analysis was performed using the Graphpad software. Multiple comparisons were performed with one-way analysis of variance, followed by Tukey post hoc tests and with one-way ANOVA Bonferroni multiple comparison test. Statistical comparison between two groups was performed by using the Mann–Withney test.

Data Availability

The mass spectrometry proteomics data have been deposited to the ProteomeXchange Consortium via the PRIDE (Deutsch et al., 2017) partner repository, with the data set identifier PXD012791. All data are available within the Article and [Supplementary Files](#), or available from the authors upon request.

Results

Laser Capture and Mass Spectrometry of Glioblastoma Core and Invasive Areas

For this study, we have used patient-derived P3 tumors. These tumors are of mesenchymal phenotype and have the following characteristics: male patient, age 64; chromosomal aberrations + [Chr 7, Chr19, 20q], – [1q42-q43, Chr9, Chr10, 20p] – [PIK3R, CDKN2A/B]. Five P3 spheroids were injected in the right hemisphere in the striatum.⁶ Laser-capture microdissection (LCM) was performed on patient-derived glioblastoma xenografts from P3 cells transduced with GFP vectors from core and invasive areas and the proteins extracted ([Figure 1A](#) and [B](#)). Tumor core and invasive areas from three different mice were laser-microdissected and processed for proteomic analysis. Proteins were digested and analyzed by liquid chromatography/tandem

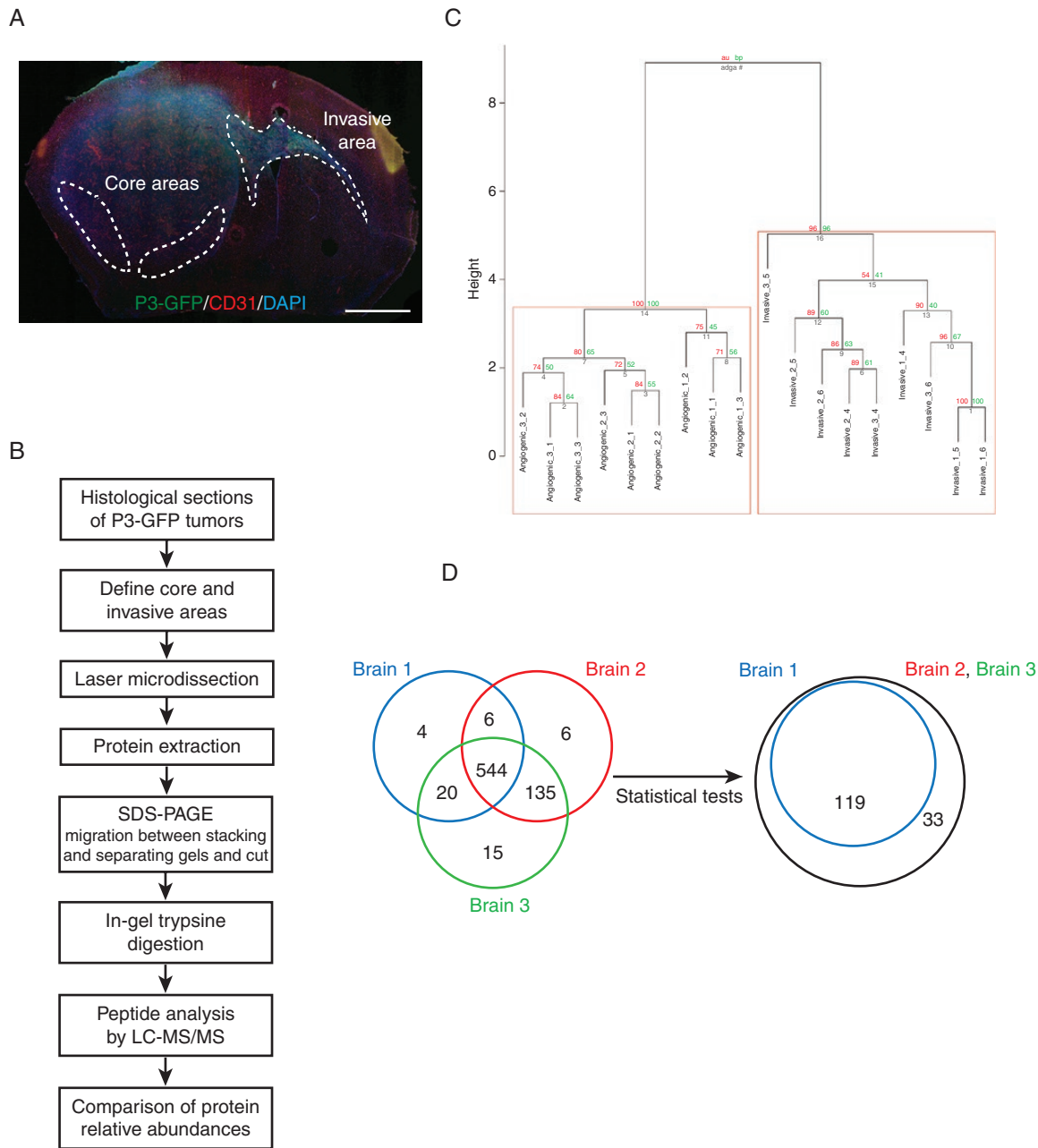


Figure 1. Laser-capture microdissection and proteomics analysis for comparing central and invasive glioblastoma areas. (A) Schematic representation of P3 tumor core and invasive areas. P3-GFP cells were stereotactically injected into mouse hemisphere and were visualized using fluorescence microscopy with CD31 and DAPI staining (P3 in green, CD31 in red, and DAPI in blue). Scale bar = 500 μ m. (B) Technical flow chart of P3 tumors analysis by combining laser microdissection and mass spectrometry analysis. (C) Hierarchical clustering of paired samples obtained from the analysis of the log-ratio values of the 544 proteins common for all samples. Values at the left represent approximately unbiased P values (AU) and values at the right correspond to boot-strap probability (BP). (D) Venn diagrams of Human proteins expressed in the three different tumors analyzed by proteomics. 544 proteins are common between the three tumors (left diagram). After Welch test P -values by FDR and setting the significance threshold at 0.01, 152 Human proteins were found differentially regulated between the core and the invasive areas (right diagram).

mass spectrometry (LC-MS/MS). Relative abundances of specific Human and mouse peptides were compared and then grouped to analyze the differential protein expression levels. The dendrogram showed a distinct pattern of arborescence for invasive and core proteins (Figure

1C and Supplementary Figure 1A). A total of 730 Human and 510 mouse proteins were detected. A Venn diagram shows a comparison of the number of proteins found for three different mouse brains, where 544 Human proteins were found common with all (Figure 1D). After adjusting

the Welch test *P*-values by FDR and setting the significance threshold at 0.01, 152 Human proteins were found significantly differentially regulated between the core and the invasive areas (Figure 1D), and 284 mouse proteins (Supplementary Figure 1B). Thirty-four Human proteins were found upregulated in the invasive area and 118 in core area (Supplementary Table 4). For Human proteins, metabolic pathways were enriched, notably gluconeogenesis (GO:0006094), mitochondrion (GO:0005739), and fatty acid metabolism (GO:019395 and GO:0006635) (Figure 2A). Furthermore, categories relating to cytoskeleton proteins (focal adhesion GO:0005925, cell cortex part GO:0044448, and or cytoskeleton GO:0005856) and trafficking were also enriched (Figure 2A). Two hundred seventy-six mouse proteins were found upregulated in the invasive area and eight in core area (Supplementary Table 5). For mouse proteins, metabolic pathways were also enriched, such as gluconeogenesis (GO:0006094), glucose catabolic to pyruvate (GO:0061718), canonical glycolysis (GO:0061621), and mitochondrion (GO:0005739) (Supplementary Figures 1C and 2). Analysing invasive and central protein hits with KEGG database, PI3K-Akt signaling pathway (hsa04151), and synaptic vesicle cycle (hsa04721) were highly represented (Supplementary Table 6).

Enrichment of New Marker Proteins in Invasive Glioblastoma Area

For the subsequent analyses, we focused our attention on the Human specific proteins. Volcano plot for proteins overexpressed in the invasive part and/or the tumor core demonstrated a clear enrichment of proteins in the core area, but with higher log-fold change ($|\log FC|$) found in the invasive area (Figure 2B and Supplementary Table 4). A 2D cluster heatmap of proteins with $\text{padj} < 0.01$ and $\log FC > 2$ and which are in common in three mouse brains showed a highly significant overexpression of Proteolipid Protein-1 (PLP1, log-fold change of 3.19), Dynamin-1 (DNM1, log-fold change of 4.02), and RHOB (log-fold change of 3.14) in the invasive area (Figure 2C). Among the most upregulated proteins in the core area were Glial Fibrillary Astrocytic Protein (GFAP, log-fold change of -2.38), Isocitrate Dehydrogenase 2 (IDH2, log2 fold change of -2.04), and glutamine synthetase (GLUL, log-fold change of -2.99) (Figure 2C). An interaction network of proteins from the invasive area showed a main node where DNM1 and PLP1 were linked (Figure 2D). Among the highest upregulated genes, VSNL1 (Visinin Like 1, log-fold change of 6.38) and STXBP1 (syntaxin binding protein, log-fold change of 4.31) were identified. However, functional analysis of these molecules is difficult since no specific inhibitors exist.

To provide further evidence of the difference between the invasive area and the angiogenic tumor core, we calculated an "AngioScore," as described previously.¹¹ The AngioScore is derived by searching angiogenesis and tumor angiogenesis keywords against total publications using Pubmed and reflects in our analysis angiogenic signaling provided by the tumor (Figure 2E). The average AngioScore was 1.5 times higher in the angiogenic tumor core when compared with the invasive area, by taking the 30 best hits from each area. This is globally in agreement

with the proteomic expression analysis. By filtering the 20 highest AngioScores, most of the identified protein potential biomarkers were expressed in the core area (Supplementary Table 7). In the invasive part, some proteins (RHOB or fumarate hydratase) also exhibited an elevated AngioScore but these proteins have been indeed extensively studied in the context of tumor angiogenesis (Supplementary Table 7).

Analysis of PLP1 and DNM1 Expression in Patient Samples

Little is known about the role of PLP1 in tumor development¹² and only few publications identify DNM1 as glioblastoma marker.^{13,14} Therefore, we focused our attention on these proteins since they were significantly overexpressed in the invasive area. Immunostaining with anti-PLP1 or anti-DNM1 antibodies showed higher expression of both proteins in invasive areas in patient-derived xenografts (Figure 3A and B). PLP1 was detected in the extracellular space and on the plasma membrane, and DNM1 was expressed in the cytoplasm (Figure 3A and B). This was confirmed in paraffin-embedded patient samples (Figure 3C).

PLP1 and DNM1 Inhibition Decreases Cell Invasion

To functionally study the role of PLP1 and DNM1, invasion experiments were performed. We used the patient-derived cell line P3 for these experiments. To interfere with PLP1- and DNM1-dependent invasion, specific inhibitors were used in a collagen type I invasion assay (Figure 4). Both inhibitors showed inhibitory activity on invasion (29% of inhibition for PLP1 inhibitor; 36%/71%/97% of inhibition for Dynasore at 78/155/310 μM , respectively) (Figure 4A and B). The specific inhibitor of DNM1 (Dynasore) demonstrated a very strong and dose-dependent inhibition of tumor cell invasion (Figure 4B). To rule out cell toxicity, we used the Dead/Live kit assay. At a maximum inhibitory Dynasore concentration of cell invasion (310 μM), cytotoxicity was indeed observed but not at 155 μM , which inhibited invasion at 71% (Figure 5A). In addition, Dynasore at 155 μM also inhibited proliferation of P3 cells (Figure 5B). We also verified the effect of PLP inhibitor on cytotoxicity and proliferation. No difference in comparison to untreated cells was found (Figure 5C and D).

Discussion

In this article, we undertook a systematic study to unravel molecular signatures related to glioblastoma development and, in particular, invasion. To this aim, we performed a proteomics analysis on patient-derived tumors implanted in immunodeficient mice. It has been previously shown that the molecular characteristics of patient tumors remain stable when xenografted in mice.¹⁵ We performed our analysis on laser-capture microdissected material obtained from invasive and central tumor areas. The scientific pipeline used in this study was validated in previous publications in

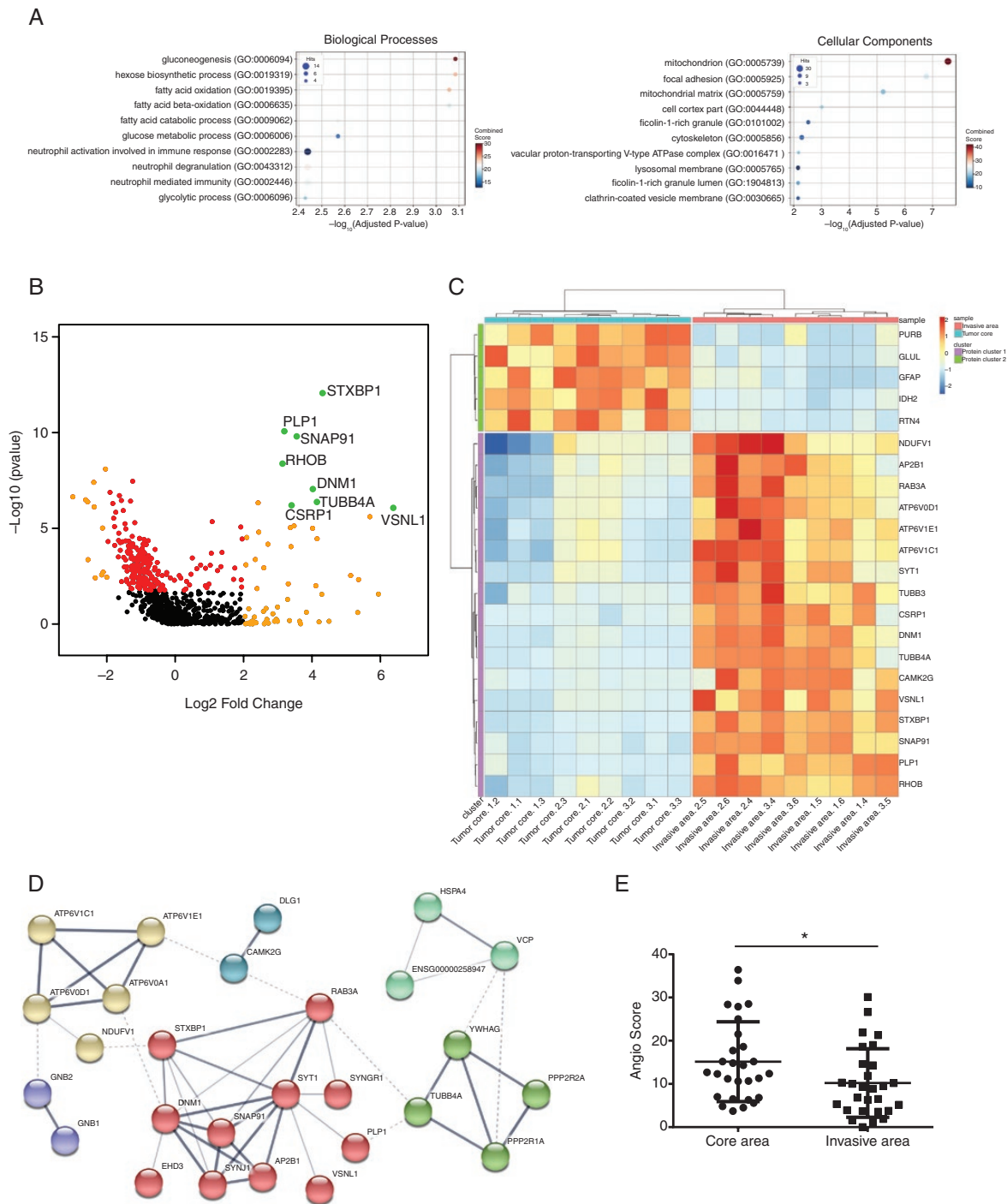
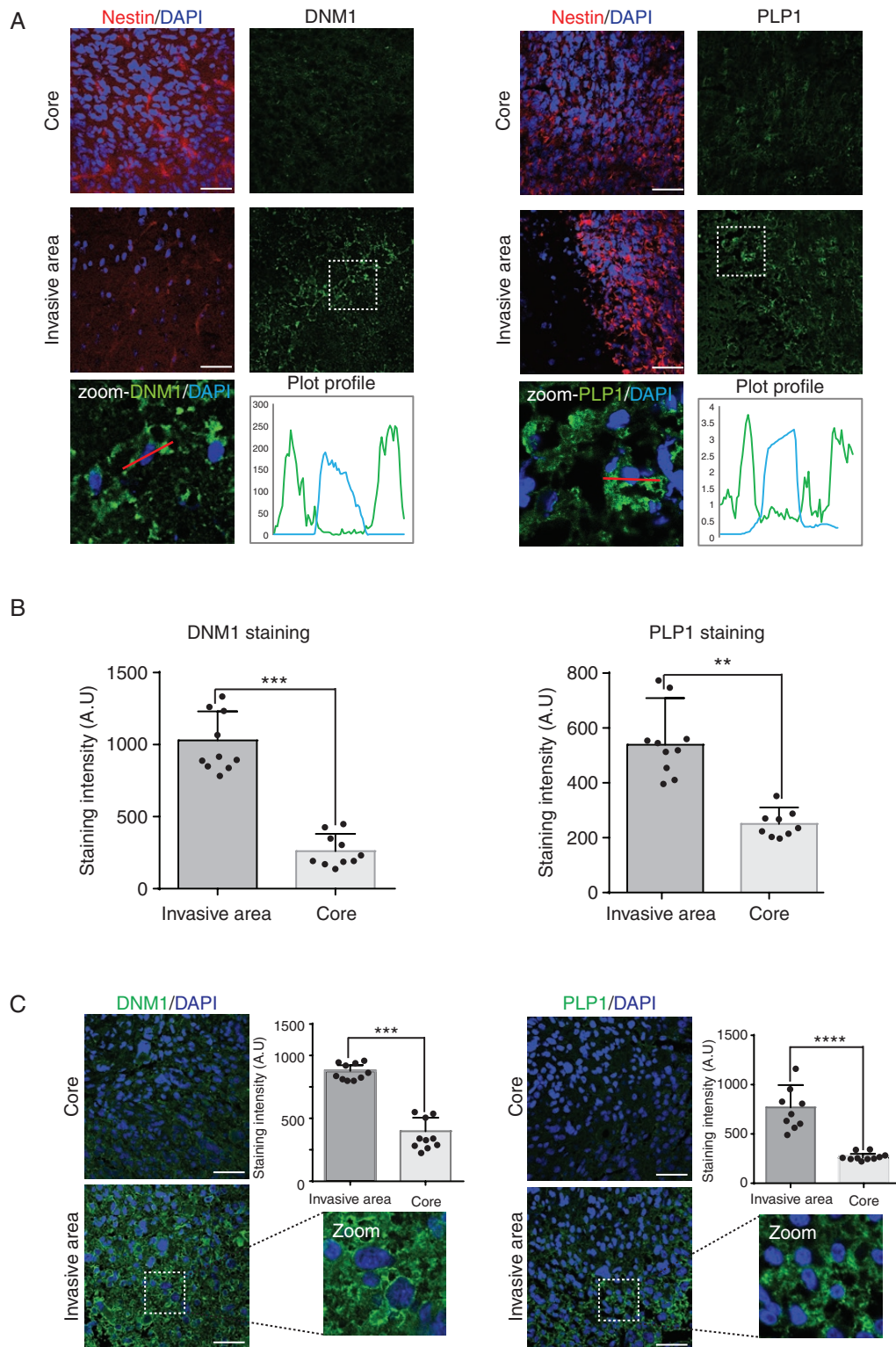


Figure 2. Protein enrichment of tumor invasive area (A) Gene Set Enrichment Analysis results. Gene Ontology (GO) biological processes (BP) and cellular components (CC) enrichment of the top 152 proteins that are significantly differentially expressed between core and invasive areas ($p_{adj} < 0.01$ and $|\log_{2}FC| > 2$), and which are represented here for the three tumors. The x-axis represents the negative \log_{10} P -adjusted value. The size of each spot (Ratio) corresponds to the fraction of proteins within our set of proteins that have the corresponding GO function. (B) Graphical representation of quantitative proteomics data for the three P3 tumors. Proteins are ranked in a volcano plot according to P value for technical reproducibility, calculated from a one-tailed paired t -test ($-\log_{10}$ [P value]) (y-axis) and their relative abundance ratio (log ratio) between core and invasive areas (x-axis). The line indicates the $P < 0.05$ threshold. Off-centered spots are those that vary the most between core and invasive areas. (C) Heatmap of the top 22 of the 152 proteins that are significantly differentially expressed for P3 tumor core and invasive areas ($p_{adj} < 0.01$ and $|\log_{2}FC| > 2$). (D) Network of human tumor invasive proteins. Each node represents a protein and interactions with medium confidence >0.4 are shown. Proteins are clustered using the Markov Cluster Algorithm and colors represent clusters. Dashed lines represent intercluster edges and width represent edge confidence (medium: >0.4 , high: >0.7 , and highest: 0.9). Disconnected proteins are removed from the analysis. (E) AngioScore of the top 30 hits from P3 tumor core and invasive areas. Student t -test, * $P < .05$.



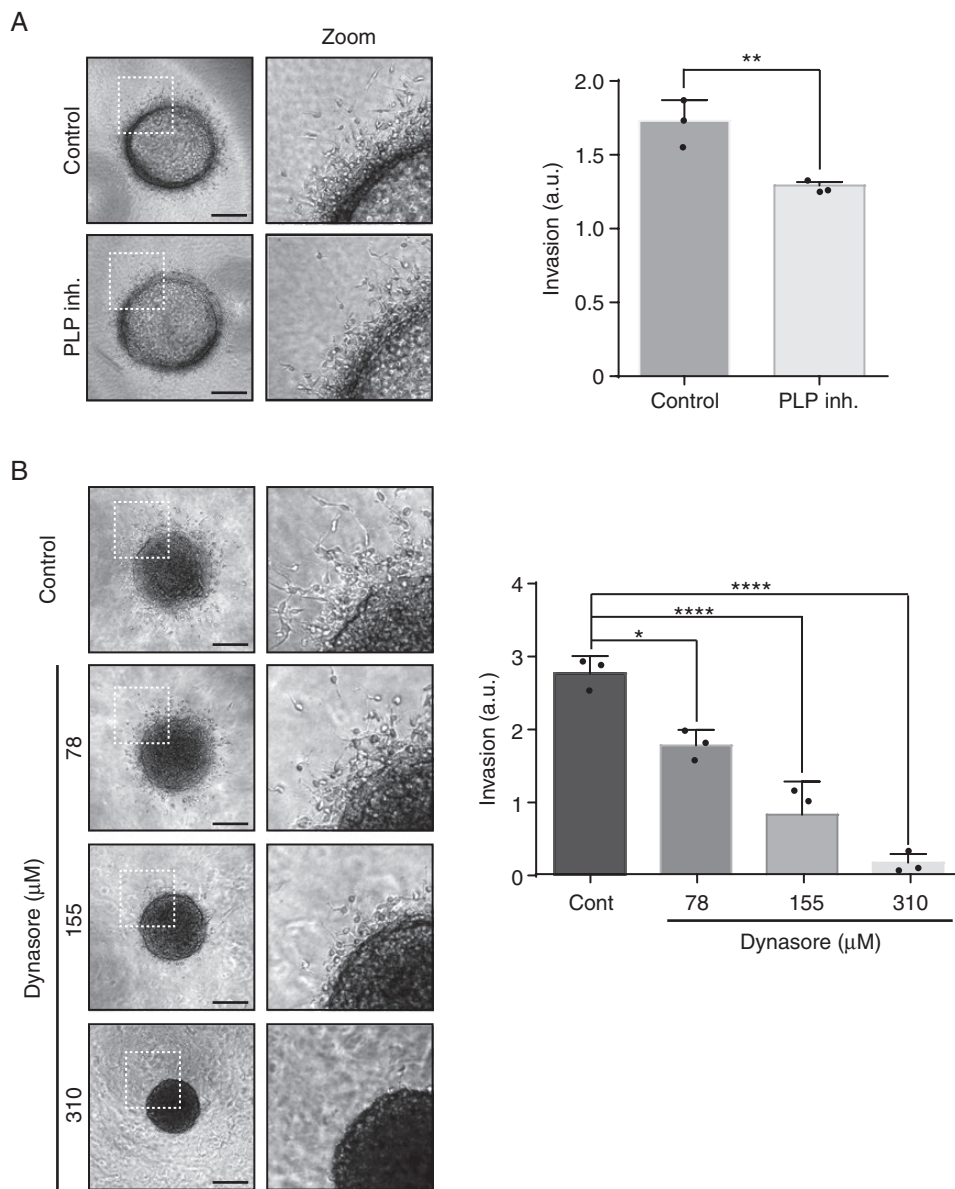


Figure 4. DNM1 and PLP1 control P3 cell invasion. (A) P3 cells were included into Collagen I gels and then incubated with control or PLP1 inhibitor (80 µg/ml). P3 spheroid invasion was measured in collagen I gels after 24 h. Scale: 50 µm. The graph represents the results as means ± SD of three independent experiments, each done in eight replicates for each condition. ** $P < .01$ (Student *t*-test). (B) P3 cells were included into Collagen I gels and then incubated with control or DNM1 inhibitor Dynasore at several concentrations (78, 155, or 310 µM). P3 spheroid invasion was measured in collagen I gels after 24 h. Scale: 50 µm. The graph represents the results as means ± SD of three independent experiments, each done in eight replicates for each condition. * $P < .05$; **** $P < .0001$ (ANOVA).

which unidentified protein candidates were discovered for tumor classification¹⁶ or for invadopodia structure.¹⁷ When stringent statistical conditions were applied ($\text{padj} < 0.01$ and $\text{logFC} > 2$), 34 Human proteins were overexpressed and 118 were downregulated in invasive areas (out of 152 proteins present in the aggregated dataset).

Our analysis also included the estimation of an AngioScore. This latter approach was already successfully used in a previous publication from our team.¹¹ In the AngioScore, we compared the 30 best hits between core and

invasive areas, and confirmed enrichment angiogenesis-related proteins in the core area. Furthermore, the AngioScore was significantly reduced in the invasive area.

To reinforce the validity of our analysis, we only selected proteins which were overexpressed in the different tumor areas of three different animals. PLP1 and DNM1 were among the top candidates. PLP1 is a proteolipid protein expressed in the myelinated neurons, which was recently found in glioblastoma by scRNAseq.¹⁸ However, this article did not discriminate between the

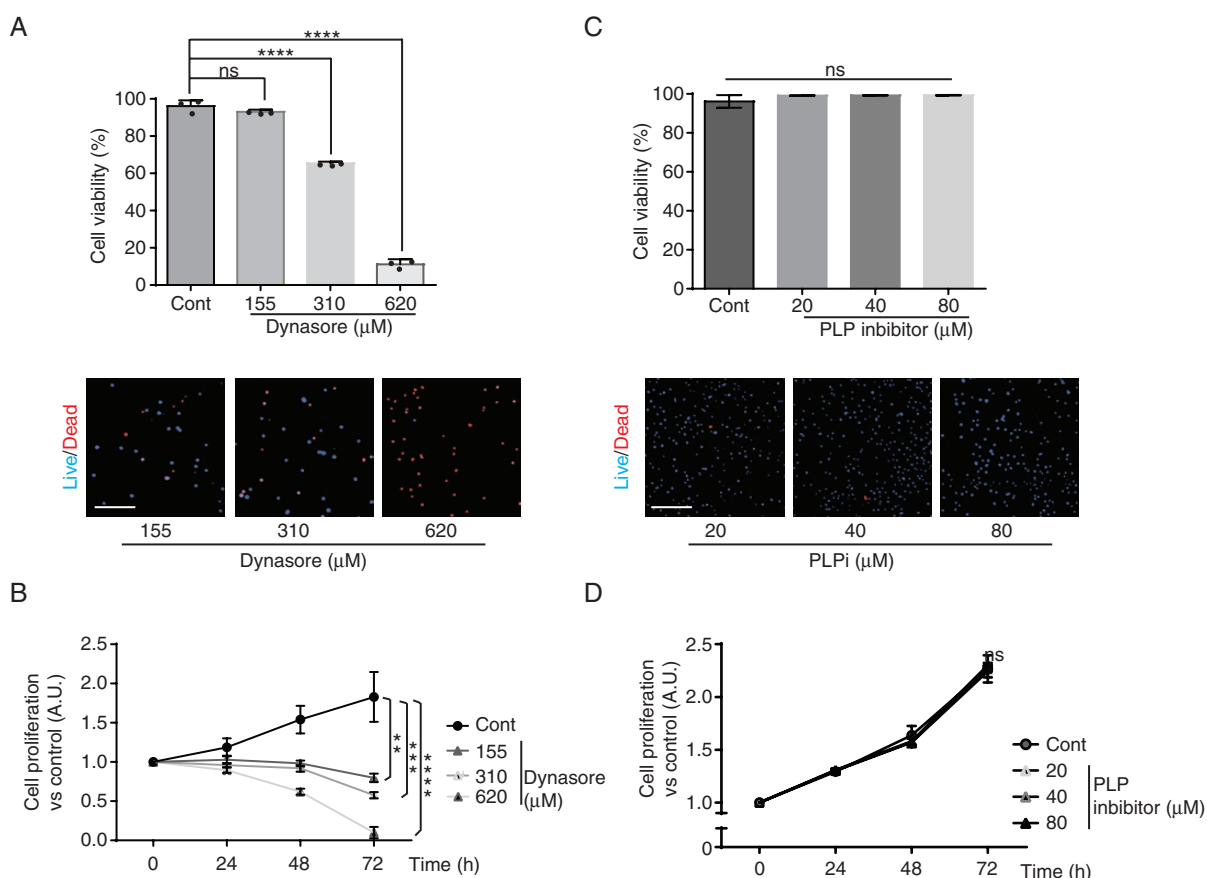


Figure 5. DNM1 inhibitor Dynasore reduces cell viability and proliferation at high doses. (A) Cell viability was recorded in live microscopy with Dead/Live kit (Invitrogen) as represented in lower panels (blue for living cells and red for dead cells). Dynasore was used at 155, 310, or 620 μM as indicated. The graph represents the percentage of living cells at the time of 72 h, and the results as means \pm SD of three independent experiments, each done in 10 replicates for each condition. ns, nonsignificant; **** $P < .0001$ (ANOVA). (B) Cell proliferation was recorded in live microscopy at time 24, 48, and 72 h. Dynasore was used at 155, 310, or 620 μM as indicated. The graph represents cell proliferation at different time points, and the results as means \pm SD of three independent experiments, each done in 10 replicates for each condition. ns, nonsignificant; ** $P < .01$; *** $P < .001$; **** $P < .0001$ (ANOVA). (C) Cell viability was recorded in live microscopy with Dead/Live kit (Invitrogen) as represented in lower panels (blue for living cells and red for dead cells). PLP1 inhibitor (PLPi) was used at 20, 40, or 80 μM as indicated. The graph represents the percentage of living cells at the time of 72 h, and the results as means \pm SD of three independent experiments, each done in 10 replicates for each condition. ns, nonsignificant (ANOVA). (D) Cell proliferation was recorded in live microscopy at time 24, 48, and 72 h. PLP1 inhibitor (PLPi) was used at 20, 40, or 80 μM as indicated. The graph represents cell proliferation at different time points, and the results as means \pm SD of three independent experiments, each done in 10 replicates for each condition. ns, nonsignificant (ANOVA).

viable core and the invasive areas. PLP was shown to be expressed in glioblastoma without isoform distinction¹² but more recently, the PLP1 isoform was reported as oligodendrocytic marker.¹⁹ We reinforced our analysis by immunohistology using a specific anti-PLP1 antibody, to ascertain its overexpression in the invasive area. Furthermore, we performed functional analysis using a specific PLP inhibitor and found that tumor cell invasion was inhibited. A similar analysis was performed on DNM1. DNM1 has been studied in acute myeloid leukaemia, lung, and colon adenocarcinomas but not in glioblastoma.²⁰ In glioblastoma, DNM1 was recently characterized as a marker of long-term patient survival in a computational analysis.²¹ At a biological level, DNM1 was found to form a complex with Cortactin in glioma cells.¹⁴ Our data are not in agreement with a publication which

reported a role of DNM2 in glioblastoma invasion using the standard glioblastoma cell lines LN444 and SNB19.²² DNM2 is highly expressed in all cancer types contrary to the expression of DNM1, which is mainly expressed in glioma, as referenced in TCGA. Furthermore, DNM2 is not a good prognosis marker for glioblastoma patient survival (TCGA database). Dynamin 2 was also recently described as a potential therapeutic target for glioblastoma development.²³ In our analysis, 2',3'-cyclic-nucleotide 3'-phosphodiesterase (CNP, log₂ fold change of 1.28) was significantly overexpressed in the core area in agreement with a previously published study.²⁴ CNP is not well studied in glioblastoma development and can be of interest for further studies. Furthermore, as indicated by the enrichment analysis, metabolic pathways were highly represented in both Human and mouse protein data sets.

We validated the regional expression of PLP1 and DNMI1 by analyzing their RNA expression in the Ivy Glioblastoma Atlas Project database. Both candidates were found upregulated in the infiltrative tumor (IT), and the leading edge (LE) when compared with core areas (Cellular Tumor—CT). These areas were defined by histological characteristics, by evaluating the number of tumor cells in the sections. This correlation indicates that both tumor genes and proteins are involved in glioblastoma invasion.

Our study differs from the previous proteomics analysis where two different PDX glioblastoma models (angiogenic or invasive) were compared.²⁵ In the latter analysis, Annexin A2 (ANXA2) and Calnexin (CNX) were found upregulated in the angiogenic model. A second proteomics study, from the same group, investigated effects of bevacizumab, which significantly modulated the tumor proteome.²⁶ Bevacizumab induces a switch from angiogenic to invasive tumors, largely documented in the literature.^{5,27} Our study is completely different from these studies above since they did not take into account regional heterogeneity. Thus, the results from the proteomics cannot be compared, except for Isocitrate dehydrogenases 1 and 2 (IDH1, IDH2), ANXA5, and alpha-Enolase (ENO1) which were found upregulated in the angiogenic tumor model²⁶ and in the core area in our study. All together, we highlight in this study underexplored proteins, which show evidence of a role in cell invasion.

Supplementary Material

Supplementary material is available online at *Neuro-Oncology* (<http://neuro-oncology.oxfordjournals.org/>).

Keywords

glioblastoma | intratumor heterogeneity | invasion | patient-derived xenograft | proteomics analysis.

Authors' Contributions

T.D. and J.G. performed biological experiments; B.D., J.R., and J.H. performed bioinformatics analysis; A.-A.R. and J.W.D. performed proteomics experiments; Z.E. performed LCM experiments; T.D., A.-A.R., F.S., R.B., M.N., and A.B. discussed the results; M.N. supervised the bioinformatics analysis; T.D. and A.B. designed and supervised research; T.D., M.N., and A.B. wrote the manuscript.

Acknowledgments

This work was supported by grants from Institut National de la Santé et de la Recherche Médicale (INSERM) (recurrent funding), and from the “Ligue contre le Cancer” and the “Conseil Régional Nouvelle Aquitaine” to A.B., by Helse Vest, Haukeland Hospital, The Norwegian Research Council and Stiftelsen Kristian Gerhard Jebsen Research Foundation for R.B. and by the “Plan Cancer” for

J.R.. The Oncoprot platform was supported by Nouvelle-Aquitaine Region with European Regional Development Fund.

Conflict of interest statement. None declared.

References

- Louis DN, Perry A, Reifenberger G, et al. The 2016 World Health Organization classification of tumors of the central nervous system: a summary. *Acta Neuropathol.* 2016;131(6):803–820.
- Stupp R, Mason WP, van den Bent MJ, et al. Radiotherapy plus concomitant and adjuvant temozolomide for glioblastoma. *N Engl J Med.* 2005;352(10):987–996.
- Das S, Marsden PA. Angiogenesis in glioblastoma. *N Engl J Med.* 2013;369(16):1561–1563.
- Kotliarova S, Fine HA. SnapShot: glioblastoma multiforme. *Cancer Cell.* 2012;21(5):710–710 e711.
- Keunen O, Johansson M, Oudin A, et al. Anti-VEGF treatment reduces blood supply and increases tumor cell invasion in glioblastoma. *Proc Natl Acad Sci U S A.* 2011;108(9):3749–3754.
- Daubon T, Léon C, Clarke K, et al. Deciphering the complex role of thrombospondin-1 in glioblastoma development. *Nat Commun.* 2019;10(1):1146.
- Bougnaud S, Golebiewska A, Oudin A, et al. Molecular crosstalk between tumour and brain parenchyma instructs histopathological features in glioblastoma. *Oncotarget.* 2016;7(22):31955–31971.
- Perkins DN, Pappin DJ, Creasy DM, Cottrell JS. Probability-based protein identification by searching sequence databases using mass spectrometry data. *Electrophoresis.* 1999;20(18):3551–3567.
- Benjamini Y, Hochberg Y. Controlling the false discovery rate: a practical and powerful approach to multiple testing. *Journal of the Royal Statistical Society, Series B.* 1995;57(1):289–300.
- Kolde R. *Heatmap: pretty heatmaps. R Package Version 61, 1–7* 2012.
- Soulet F, Kilarski WW, Roux-Dalvai F, et al. Mapping the extracellular and membrane proteome associated with the vasculature and the stroma in the embryo. *Mol Cell Proteomics.* 2013;12(8):2293–2312.
- Golfinos JG, Norman SA, Coons SW, et al. Expression of the genes encoding myelin basic protein and proteolipid protein in human malignant gliomas. *Clin Cancer Res.* 1997;3(5):799–804.
- Patel AP, Tirosh I, Trombetta JJ, et al. Single-cell RNA-seq highlights intratumoral heterogeneity in primary glioblastoma. *Science.* 2014;344(6190):1396–1401.
- Abe T, La TM, Miyagaki Y, et al. Phosphorylation of cortactin by cyclin-dependent kinase 5 modulates actin bundling by the dynamin 1-cortactin ring-like complex and formation of filopodia and lamellipodia in NG108-15 glioma-derived cells. *Int J Oncol.* 2019;54(2):550–558.
- Wang J, Miletic H, Sakariassen PØ, et al. A reproducible brain tumour model established from human glioblastoma biopsies. *BMC Cancer.* 2009;9:465.
- Henriet E, Abou Hammoud A, Dupuy JW, et al. Argininosuccinate synthase 1 (ASS1): a marker of unclassified hepatocellular adenoma and high bleeding risk. *Hepatology.* 2017;66(6):2016–2028.
- Ezzoukhry Z, Henriet E, Cordelières FP, et al. Combining laser capture microdissection and proteomics reveals an active translation machinery controlling invadosome formation. *Nat Commun.* 2018;9(1):2031.

18. Filbin MG, Tirosh I, Hovestadt V, et al. Developmental and oncogenic programs in H3K27M gliomas dissected by single-cell RNA-seq. *Science*. 2018;360(6386):331–335.
19. Kong J, Cooper LA, Wang F, et al. Machine-based morphologic analysis of glioblastoma using whole-slide pathology images uncovers clinically relevant molecular correlates. *PLoS One*. 2013;8(11):e81049.
20. Haferlach T, Kohlmann A, Wiczorek L, et al. Clinical utility of microarray-based gene expression profiling in the diagnosis and subclassification of leukemia: report from the International Microarray Innovations in Leukemia Study Group. *J Clin Oncol*. 2010;28(15):2529–2537.
21. Patel VN, Gokulrangan G, Chowdhury SA, et al. Network signatures of survival in glioblastoma multiforme. *PLoS Comput Biol*. 2013;9(9):e1003237.
22. Feng H, Liu KW, Guo P, et al. Dynamin 2 mediates PDGFR α -SHP-2-promoted glioblastoma growth and invasion. *Oncogene*. 2012;31(21):2691–2702.
23. Luwor R, Morokoff AP, Amiridis S, et al. Targeting glioma stem cells by functional inhibition of dynamin 2: a Novel treatment strategy for glioblastoma. *Cancer Invest*. 2019;37(3):144–155.
24. Zorniak M, Clark PA, Leeper HE, et al. Differential expression of 2',3'-cyclic-nucleotide 3'-phosphodiesterase and neural lineage markers correlate with glioblastoma xenograft infiltration and patient survival. *Clin Cancer Res*. 2012;18(13):3628–3636.
25. Rajcevic U, Petersen K, Knol JC, et al. iTRAQ-based proteomics profiling reveals increased metabolic activity and cellular cross-talk in angiogenic compared with invasive glioblastoma phenotype. *Mol Cell Proteomics*. 2009;8(11):2595–2612.
26. Demeure K, Fack F, Duriez E, et al. Targeted proteomics to assess the response to anti-angiogenic treatment in human glioblastoma (GBM). *Mol Cell Proteomics*. 2016;15(2):481–492.
27. Obad N, Espedal H, Jirik R, et al. Lack of functional normalisation of tumour vessels following anti-angiogenic therapy in glioblastoma. *J Cereb Blood Flow Metab*. 2018;38(10):1741–1753.

3.2 Specific expression of lactate dehydrogenases in glioblastoma controls intercellular lactate transfer to promote tumor growth and invasion

Les cellules de GBMs présentent un fort métabolisme glycolytique permettant d'accroître la production de biomasse et de maintenir une forte prolifération tumorale (146). Ce phénomène s'accompagne d'une augmentation de la sécrétion du lactate acidifiant le microenvironnement tumoral et favorisant l'invasion des cellules (256).

La production de lactate est médiée par les LDHs. Les enzymes LDHA et LDHB catalysent la conversion du pyruvate en lactate et inversement. Cette réaction est couplée à l'oxydoréduction du couple $\text{NAD}^+/\text{NADH}/\text{H}^+$, indispensable à l'homéostasie rédox de la cellule. L'isoforme LDHA ayant une plus forte affinité pour le pyruvate est souvent surexprimée dans les cancers (174) et est un facteur de mauvais pronostic chez les patients (175). L'isoforme LDHB est peu étudiée dans les cancers. De plus, ces deux enzymes n'ont pas encore été simultanément étudiées dans le GBM.

Sur deux lignées cellulaires différentes de GBM, nous nous sommes d'abord intéressés à l'effet *in vitro* du lactate sur la croissance et l'invasion des GBMs. Nous avons ensuite étudié l'impact de la perte complète d'expression des enzymes LDHA (sgLDHA), LDHB (sgLDHB) ou des deux simultanément (sgLDHA/B). Une approche couplant analyses métabolomique et transcriptomique a mis en évidence l'adaptation des GBMs et leur reprogrammation métabolique vis-à-vis de la perte des LDH. Cette approche a permis de détecter des vulnérabilités cellulaires qui ont été exploitées pour altérer le développement *in vivo* des GBMs. Enfin, le blocage des LDHs apparaissant comme une stratégie thérapeutique prometteuse, nous proposons une approche pharmacologique avec le stiripentol (médicament antiépileptique) pour inhiber ces enzymes.

Principaux résultats :

- Le lactate seul alimente le cycle de Krebs et promeut l'invasion des GBMs.
- La double délétion de LDHA et LDHB est nécessaire pour abolir complètement la sécrétion du lactate et inhiber la croissance et l'invasion tumorale.
- La mise en relation d'analyses métabolomique et transcriptomique révèle un métabolisme OxPhos plus important pour les sgLDHA/B sensibilisant la lignée à la radiothérapie et prolongeant significativement la survie des souris.
- Le stiripentol réduit l'activité des LDHs et augmente la survie des souris en combinaison avec un traitement antiangiogénique.

Specific expression of lactate dehydrogenases in glioblastoma controls intercellular lactate transfer to promote tumor growth and invasion

Joris Guyon¹, Ignacio Fernandez-Moncada^{2,11}, Claire Larrieu^{3,11}, Cyrielle Bouchez^{3,11}, Tiffanie Chouleur¹, Heidi Espedal⁴, Gro Rosland³, Boutaina Daher³, Aurélien Barre⁵, Benjamin Dartigues⁵, Aurélien Coffe⁵, Justine Rudewicz⁵, Irati Romero-Garmendia³, Barbara Klink^{6,7,8}, Konrad Grützmann⁸, Marie-Alix Derieppe⁹, Thibaut Molinié³, Nina Obad⁴, Céline Léon¹, Hrvoje Miletic^{4,10}, Giovanni Marsicano², Macha Nikolski^{3,5}, Rolf Bjerkvig⁴, Andreas Bikfalvi^{1,*}, and Thomas Daubon^{1,3,#,*}.

1- University of Bordeaux, INSERM U1029, University Bordeaux, Pessac, France;

2- University Bordeaux, INSERM, U1215 Neurocentre Magendie, Bordeaux, France

3- University Bordeaux, CNRS, IBGC, UMR 5095, Bordeaux, France

4- NorLux Neuro-Oncology, Department of Biomedicine, University of Bergen, Norway

5- Bordeaux Bioinformatic Center CBiB, University of Bordeaux, France

6- Department of Oncology, Luxembourg Institute of Health, 1526, Luxembourg, Luxembourg.

7- German Cancer Consortium (DKTK), 01307, Dresden, Germany.

8- Core Unit for Molecular Tumor Diagnostics (CMTD), National Center for Tumor Diseases (NCT), 01307, Dresden, Germany.

9- Animal Facility, University Bordeaux, 33615, Pessac, France.

10- Department of Pathology, Haukeland University Hospital, Bergen, Norway.

11- Authors contributed equally to this work.

*Corresponding authors and co-principles investigators: thomas.daubon@u-bordeaux.fr and andreas.bikfalvi@u-bordeaux.fr

Lead author: thomas.daubon@u-bordeaux.fr

Key words: Glioblastoma, lactate dehydrogenases, energy metabolism, invasion, antiepileptic drug.

Short title: lactate dehydrogenases in GBM development

Abbreviations:

3D, three dimensional; Bev, bevacizumab; Ivy GAP, Ivy Glioblastoma Atlas Project GBM, glioblastoma; GFP, green fluorescent protein; KO, knock-out; LA, lactic acid; LDH, lactate dehydrogenase; MCT, monocarboxylate transporter; OxPhos, oxidative phosphorylation; PDX, patient-derived xenografts; ROS, reactive oxygen species; sgRNA, single guide RNA; TCA, tricarboxylic acid; TCGA, Tissue Cancer Genome Atlas.

ABSTRACT

Lactate is a central metabolite in brain physiology, involved in the astrocyte-neuron lactate shuttle, but also contributes to tumor development. Glioblastoma (GBM) is the most common and malignant primary brain tumor in adults, recognized by angiogenic and invasive growth, in addition to its altered metabolism. By adapting their glycolytic or oxidative metabolism, GBM stem-like cells are able to resist chemo- and radiotherapy. We show herein that lactate fuels GBM anaplerosis by replenishing the TCA cycle in absence of glucose. Lactate dehydrogenases (LDH) catalyze the interconversion of pyruvate and lactate. Deletion of either LDHA or LDHB did not alter significantly GBM growth and invasion. However, ablation of both LDH isoforms led to a reduction of tumor growth, and, consequently, to an increase in mouse survival. Comparative transcriptomics and metabolomics revealed metabolic rewiring involving high oxidative phosphorylation (OxPhos) in the double LDHA/B KO group which sensitized tumors to cranial irradiation, massively improving mouse survival. Survival was also increased when control mice were treated with the antiangiogenic treatment, bevacizumab, and the antiepileptic drug, stiripentol which targets LDH activity.

Taken together, this highlights the complex metabolic network in which both LDH A and B are integrated and underscores that combined inhibition of LDHA and B is necessary to impact tumor development. Targeting of these enzymes in combination with anti-angiogenic and repurposed drugs may be of therapeutic benefit, especially when associated with radiotherapy.

INTRODUCTION

GBM is the most common malignant primary brain tumor in adults. Major hallmarks of GBM are high proliferation rate, pronounced angiogenesis, and local invasion¹. GBM is a highly heterogeneous tumor that exhibit astrocytic-, oligodendrocytic-, neural progenitor-, and mesenchymal features². The current treatment of GBM consists in surgical tumor resection, followed by concomitant radio-chemotherapy. However, this strategy invariably leads to tumor recurrence due the inability to fully eradicate invasive cells and results in poor prognosis³. This highlights the need for alternative therapeutic targets to improve this tumor management and treatment. Glioblastoma invasion impacts three types of brain structures: blood vessels, white matter tracts, and the interstitial space⁴. Expression of hypoxia-inducible factor 1 α (HIF1 α) expression induced by hypoxia or following anti-angiogenic treatment, significantly impacts GBM invasion⁵ and metabolism⁶.

Unlike non-neoplastic cells that rely on mitochondrial oxidative phosphorylation (also known as “mitochondrial respiration”) to produce energy, a common property of solid cancers, is enhanced glucose metabolism⁷. Even under aerobic condition, tumor cells have a high glycolytic rate and production of lactate⁸. This particularity, known as the Warburg effect, is an efficient way to increase biomass production for maintaining a high proliferation rate, and to facilitate invasion by microenvironment acidosis^{7,9}. Production of lactate, an end product of glycolysis, is catalysed by lactate dehydrogenase (LDH), a tetrameric enzyme composed by two subunits, LDHA and/or LDHB, both encoded by separate genes. In the human body, LDH exists in five different isozymes composed of four subunits, LDH1 is composed of only LDHB subunits and LDH5 of LDHA subunits, LDH2/3/4 express differently one or the other subunit¹⁰. Depending on the lactate/pyruvate flux, LDHA and LDHB can both catalyse the conversion of pyruvate into lactate or its retroconversion, both reactions coupled to oxidoreduction of NAD⁺/NADH. This leads to increased lactate production (for LDHA) and consumption (for LDHB). Lactate and protons are then extruded from cells by monocarboxylate transporters (MCTs). Other subunits of LDH exist, LDHC and LDHD, but are not highly expressed in brain tissue in contrary to LDHA or LDHB¹¹.

Many cancers display high LDHA levels¹², which is associated with poor patient survival^{13,14}. Several pre-clinical studies have demonstrated that LDHA inhibition shows anti-proliferative effects^{15,16}. One proposed explanation is that LDHA inhibition induces mitochondrial reactive oxygen species (ROS) production and oxidative damage^{15,17,18}.

Moreover, several studies have shown that LDHA activity and lactate secretion promote invasion and metastasis^{19,20}. In GBM, a relationship between lactate and *in vitro* migration has also been established²¹⁻²³. LDHA has been found at GBM invasive borders of antiangiogenic-treated tumors⁶. Isocitrate-dehydrogenase (IDH)-mutated gliomas, which are of better prognosis than IDH1wt gliomas, express lower levels of LDHA²⁴. Of note, LDHB has not yet been explored in the GBM context, unlike in uterine cancer where LDHB activity modulates autophagy²⁵. However, no study to date has examined the role of both LDHA/LDHB in promoting GBM development and invasion.

We therefore aimed to study the impact of LDHA and LDHB activity in GBM development using patient-derived GBM stem-like cells cultured as spheroids to maintain parental DNA genotype and tumor phenotype while implanted into rodents²⁶.

We show herein that GBM stem-like cells starved from carbon sources and fed with lactate can compensate for the absence of glucose to sustain the TCA cycle to drive proliferation and invasion. Single CRISPR-cas9 LDHA or LDHB knock-out have limited effects on glioblastoma development, but major biological adaptations are observed in double LDHA/B KO cells. Even under low O₂ concentration, double LDHA/B KO cells still rely on TCA and mitochondrial respiration to support tumor growth, which could be further inhibited by irradiation. Finally, treatment with stiripentol (Diacomit[®], Biocodex), a known antiepileptic drug that also block LDH activity²⁷, inhibits lactate production and decreases GBM invasion and growth. Collectively, these results demonstrate a central role of LDHA/LDHB and lactate production to support energy metabolism which has a major impact on GBM invasion and growth.

RESULTS

Expression of LDHA and LDHB are restricted to specific glioblastoma areas

We have previously showed that regional expression of specific molecules define GBM hallmarks^{5,28}. Regional expression of the lactate dehydrogenase isoforms was first analyzed in a patient-derived xenograft mouse model by immunohistochemistry. Both LDH isoforms were more express in the tumor when compared to healthy tissue (**Fig 1a**). However, LDHA was found mainly expressed in the central hypoxic area of the tumor and in some invasive cells, while LDHB was mainly expressed in peripheral tumor areas but also in invasive cells in contact to neurons of the corpus callosum (**Fig 1a**). Thus, LDHA and LDHB showed a distinct spatially-restricted expression pattern in the tumor core but were found both expressed in invasive cells (**Fig 1a**). Next, we generated an original setup in which spheroids invading in a 3D collagen matrix in paraffin, a model that recapitulates GBM oxygenation regional heterogeneity²⁹, were included in paraffin to analyse LDHA and LDHB expression in coronal sections (**Fig 1b**). LDHA was found highly expressed in the central hypoxic area but also in some single invasive cells, while LDHB was highly expressed at spheroid borders and invasive areas (**Fig 1c**). Of note, only few cells expressed both enzymes. *In silico* analysis on a single-cell RNAseq database from invasive and central GBM areas demonstrated a similar pattern, with preferential expression of *LDHA* in the central area and *LDHB* in the peripheral area albeit mRNA of both enzymes were found in a portion of invasive tumor cells (**Supplementary Fig 1a**). When using data extracted from the IVYGAP database, distinct regional *LDHA* and *LDHB* expression was observed, as well as a positive correlation between LDHA and the hypoxic transcription factor HIF1a in invasive and microvascular areas (**Supplementary Fig 1b**). *LDHB* and *HIF1a* expression were not found as correlated (**Supplementary Fig 1b**). When analyzed in the GBM-TCGA data set, LDHA was found to be a marker of poor prognosis. LDHB expression was, on the contrary, linked to favourable prognosis (**Supplementary Fig 1c**). In summary, LDHA and LDHB expression is restricted to hypoxic or peripheral areas respectively.

Lactate modulates glioblastoma invasion by fuelling energy metabolism pathways

On physiological conditions, brain tissue is exposed to low level of oxygen, *i.e.* physiological hypoxia, that ranges from 0.5 to 7 % depending on the distance from blood vessels³¹. Local O₂ concentration can be even lower in brain tumors, reaching around 0.1% in the core area. We, therefore, investigated whether stem-like cells (P3 or BL13 cells) in culture

express LDHA and/or LDHB, and whether expression of these enzymes can be modified by incubating cells at 0.1% O₂. We observed that LDHA expression was upregulated from 48 hours under hypoxic conditions (3x fold induction at 72 hours), while LDHB expression did not change (**Fig 2a** for P3 cells and **Supplementary Fig 2a** for BL13 cells). Lactate production was also increased under hypoxia 0.1%, correlating with higher LDH activity in P3 and in BL13 cells (**Fig 2b-d** and **Supplementary Fig 2b-d**). Lactate has been reported to sustain tumor growth *via* monocarboxylate transporters (MCT1/4)³². We then tested the effect of lactate on tumor cell proliferation and invasion. To rule out a lactate-induced cytotoxic effect, lactate was added to the medium of P3 cells and cytotoxicity was measured by fluorescence assay. Lactate concentrations starting at 30 mM induced cytotoxicity at 24 hours (**Supplementary Fig 2e**). The effect of non-cytotoxic lactate concentrations was then tested and spheroid growth and invasion measured. Spheroid growth was significantly inhibited by 20 mM lactate (**Fig 2e**), while cell invasion increased in the presence of lactate from 10 mM onwards (**Fig 2f**). Lactate treatment also induced changes in cell morphology, promoting an elongated cell shape, reminiscent of a mesenchymal phenotype (**Supplementary Fig 2f**). In absence of glucose, lactate by itself increased cell invasion (**Fig 2g**). To rule out an effect of acidification, we tested cell invasion at the same pH of lactate treatment (pH 6.8) by using HCl, and no effect was observed (**Fig 2g**). Rotenone, a respiratory chain complex I inhibitor, completely blocked lactate-induced invasion. This suggests that lactate is fuelling mitochondria activity to promote invasion (**Fig 2g**). Pyruvate, the main LDH substrate was then tested in invasion experiments, and invasion rates was increased in comparison to control conditions but remained lower than under lactate stimulation (**Supplementary Fig 2g**). Of note, the respiration capacity of P3 cells was similar in complete medium, with glucose or lactate (**Fig 2h**). Lactate consumption by GBM mitochondrial activity was followed by [¹³C₃]lactate infusion in glucose-starved P3 cells, wherein labelled TCA intermediates (citrate, oxoglutarate) and amino acids (alanine, glutamate, glutamine) were detected in the endometabolome but also in the exometabolome after 1 hour (**Fig 2i** and **Supplementary Fig 3**). Intracellular abundance of lactate and pyruvate was found unchanged along the experiment (**Figure 2i** and **Supplementary Figure 3**), but the amount of [¹³C₃]lactate and [¹³C₃]pyruvate immediately reached their maximum level (**Supplementary Figure 3**). The appearance of [¹³C₂]citrate from the beginning indicated a fast reaction from acetyl-CoA, and higher isotopologues increased quickly after, indicating an active TCA cycle (**Supplementary Figure 3**). These results shed light

on the pathways involved in lactate metabolism of GBM cells and is a direct demonstration that lactate is used as an energy source *via* the TCA cycle. Only a slight increase or almost no labelling of amino-acids not associated with the TCA cycle or gluconeogenesis was observed and, thus, this was not included in the analysis.

Double LDHA/B KO impairs *in vitro* and *in vivo* GBM growth and invasion

First, we transduced P3 and BL13 cells with lentiviral CRISPR-Cas9 constructs to fully eliminate LDHA and/or LDHB expressions (sgControl, sgLDHA, sgLDHB, and sgLDHA/B). Knock-out (KO) was validated by Western-blot in single LDHA or LDHB KO cells, and in double LDHA/B KO cells at 21 or 0.1% O₂ (**Fig 3a** and **Supplementary Fig 4a**). Next, we performed functional experiments to further validate knockout strategy. Lactate secretion was only abolished on double LDHA/B KO cells (**Fig 3b**). LDH activity was decreased in LDHA and slightly decreased in LDHB single KO cells, but massively decreased in double KO cells (**Supplementary Fig 4b**). LDHB activity was not detected in LDHB or LDHA/B KO cells (**Supplementary Fig 4c**). Next, we transduced the lactate-sensitive FRET biosensor into all P3 cells to detect intracellular lactate levels (**Supplementary Fig 4d**)³³. Basal lactate concentrations were higher in control, LDHA or LDHB KO cells than in double LDHA/B KO cells (**Fig 3c**). Adding oxamate, a potent LDH inhibitor that also induces lactate efflux by MCT trans-acceleration³⁴, followed by a MCT blocker cocktail (diclofenac and AR-C155858) unveil that basal lactate concentrations are higher in control, LDHA or LDHB KO cells compared to double LDHA/B KO cells, are result explained by decreased lactate production (**Fig 3c**). Spheroid growth was next monitored over one week at 1% O₂ and showed that double LDHA/B KO strongly reduced spheroid growth, unlike LDHA KO that moderately decreased spheroid growth and LDHB KO that had no effect (**Fig 3d**, left panel). This was associated with a strong ethidium homodimer-1 staining for visualization of apoptotic events (**Fig 3d**, right panel). This cell death signature was also supported by a high Annexin-V staining in double KO cells detected by cytometry (**Supplementary Fig 4e**). The invasion capacity was analyzed in all cell lines and a moderate but significant decrease in invasion was observed in LDHA KO in both P3 (**Fig 3e**) and BL13 cells (**Supplementary Fig 4f**). Nevertheless, LDHB KO P3 but not LDHB KO BL13 cells had higher invasive capacities (**Fig. 3e** and **Supplementary Fig 4f**). For LDHA/B KO cells, under 0.1 % O₂, the invasive capacity dropped by 75% for P3 cells (**Fig 3e**), and by 50% for BL13 cells (**Supplementary Fig 4f**).

Spheroids from single and double LDHA/B KO cells were injected into immunodeficient mice to evaluate *in vivo* tumor development and survival. No histopathological differences were observed between control and single LDH KO (LDHA KO or LDHB KO) tumors (**Fig 3f**). However, double LDHA/B KO tumors were much smaller and less invasive than control tumors (**Fig 3g**), which correlated with an increase in mouse survival, in both, the P3 (**Fig 3h**) and the BL13 model (**Supplementary Fig 4i**). Only a small but significant increase in mouse survival was observed in the LDHA KO group, and, surprisingly, a drastic decrease in survival in LDHB KO group (**Fig 3h**), the latter was most likely due to haemorrhages at the tumor site. Vascular endothelial growth factor (VEGF), the main inducer of neoangiogenesis by tumor cells, was quantified by ELISA and an increase was only observed in LDHB KO cells (**Supplementary Fig 4g**). The VEGF inhibitor bevacizumab (bev) was then injected in mice bearing single or double LDHA/LDHB KO P3 tumors. An increase in survival was observed in mice implanted with LDHB KO tumors and treated with bev, reaching a similar survival curve than for control animals (**Supplementary Fig 4h**). Increased survival was also seen in mice with double LDHA/B KO tumors, while no difference was observed in mice with control or LDHA KO tumors (**Supplementary Fig 4h**).

Metabolic switch in double LDHA/B KO cells under hypoxia delineates vulnerabilities

To trace metabolic fluxes at 0.1% O₂, cells were starved and infused with [¹³C₆]glucose for 24 or 48 hours. Principal component analysis (PCA), defining global RNA regulation, showed that metabolism of double LDHA/B KO cells switched after 48 hours at 0.1% O₂ when compared to control or single KO tumors (**Fig 4a**). Exometabolome of double LDHA/B KO cells strongly differed from other cells, by a decrease in glucose consumption and an absence of lactate production (**Fig 4b**). In addition, pyruvate and its derivatives (acetate and formate) were only secreted in double LDHA/B KO cells (**Fig 4b**).

RNA sequencing was then performed on the same cells under 21 or 0.1 % O₂, and confronted with metabolomics data. Metabolograms were used to integrate transcriptomics and metabolomics data as previously described³⁵. The changes of each metabolite/transcript pair were determined and average metabolome/transcriptome variations of a metabolic pathways were visualized by comparing two conditions (**Fig 4c**). Based on global results showed previously (**Fig 4a**), metabolograms were built by analyzing total metabolite abundances in P3 control cells at 21% and while adapting at 0.1% O₂ (**Fig 4c**, left panels, and

supplementary Fig 5), and compared to P3 control and P3 double LDHA/B KO cells at 21% (**Fig 4c**, middle panels, and **supplementary Fig 5**) or at 0.1% O₂ (**Fig 4c**, right panels, and **supplementary Fig 5**). When changes in consensus gene expression were analyzed, differences in glycolysis or oxidative phosphorylation for all comparisons were seen, but only negligible variations for amino acid synthesis (**Fig 4c**). Significant variations in the majority of pathways from the metabolome perspective were observed for most of the comparisons (**Fig 4c**). For P3 control cells, the majority of transcripts were related to glycolysis and showed increases in expression at 0.1% O₂ when compared to 21% O₂ (18 up, 12 down), whereas the majority of metabolites significantly decreased at 0.1% O₂ (0 up, 4 down) (**Fig 4c**, left panels). Metabolograms were heterogeneous when comparing changes between P3 control and double LDHA/B KO cells at (1) 21% and (2) at 0.1% O₂ (**Fig 4c**, middle and right panels). P3 double LDHA/B KO cells had a strongly modified metabolism, as seen by the increase in all metabolites and transcripts related to glycolysis and oxidative phosphorylation, especially under 0.1% O₂ (**Fig 4c**).

Since metabolograms are based on the total metabolite abundances, metabolite abundance was calculated after [¹³C₆]glucose labelling using the fractional contribution and was incorporated into the central pathway of the carbon metabolic network map obtained from previous comparisons (**Fig 4c**). To explore the relationship between transcriptomic and metabolomic data, transcript levels of metabolism-related genes were incorporated into the central carbon metabolic network pathway map (**Fig 4d** and **supplementary Fig 6**) and comparisons were generated between P3 control cells after 48 h under 0.1% O₂ or between P3 control and double LDHA/B KO cells when cultured under 21% O₂ (**supplementary Fig 6**). At 0 h, the difference between P3 double LDHA/B KO versus control cells was low to non-significant (**Supplementary Fig 6**). The detailed metabolic map depicts the increase in abundance for the majority of metabolites after [¹³C₆]glucose labelling in double KO LDHA/B cells versus control cells for the glycolytic and the oxidative phosphorylation pathways (**Fig 4d**). Fourteen transcripts from the glycolytic pathway (HK1, HK2, GPI, PFKB3, PFKB4, ALDOC, TPI1, PGK1, ENO1, ENO2 and PKM), and from the Krebs cycle (ACO2, SUCLG1 and SDHB) were upregulated, while 6 were downregulated (GAPDHS, LDHA, LDHB, DLAT, SDHD, CS) (**Fig 4d**). These findings indicate that, under hypoxia, double LDHA/B KO deregulates cell metabolism at many levels. Global transcripts at 0.1% O₂ were increased in P3 control cells when compared to 21% O₂ (**Supplementary Fig 7**, upper panels), impacting metabolism, and in particular

glycolysis (HK2, ENO1, ENO2, GAPDH, PKM, LDHA). At 21 % O₂, major biological pathways are related to membrane and organelle dynamics during cell division and cell cycle regulation, at the contrary, in more unfavorable condition at 0.1% O₂, pathways are involved to low oxygen adaptation and maintenance of energy production (**Supplementary Fig 7**, upper panels). Hypoxic stress has been found to decrease the nucleotide pool³⁶. Indeed, the abundance of nucleotides was lower while fractional contribution was enriched suggesting a continuous but limited turnover (**Supplementary Fig 6**). Under 0.1% O₂, the transcription profiles were more enriched in double LDHA/B KO cells when compared to P3 sgControl cells (**Supplementary Fig 7**, lower panels). This was also seen at 21% O₂ (**Supplementary Fig 7**, middle panels). The differences in abundance and isotopolog contribution between control and double KO LDHA/B cells were less pronounced in 21% O₂. In hypoxia, the abundance in nucleotide monophosphates (AMP, GMP and UMP) was also higher in double KO LDHA/B cells (**Supplementary Fig 8**). The fractional contribution of purines and pyrimidines mainly consisted in m+5 labeling in double KO LDHA/B cells whereas m+5, m+7 and m+8 labeling was seen in control cells.

Double LDHA/B KO cells reorganize their mitochondrial respiratory chain to support growth under 0.1% O₂ concentration

To corroborate the RNA sequencing results (**Fig 4c-d** and **supplementary Fig 6**), we exposed P3 cells to 21 or 0.1% O₂ and analyzed the subunits of the mitochondrial respiratory chain by Western blot. NDUFB8, SDHA, UQCRC2, COXII protein levels increased upon 0.1% O₂ in double LDHA/B KO cells, but only NDUFB8 and COXII at 21% O₂ (**Fig 5a**). Expression of the subunit V ATP5A complex did not change in high or low oxygen conditions (**Fig 5a**). For single LDHB or LDHA KO cells, only minor changes were observed (**Fig 5a**). Immunostaining of mitochondria networks revealed an increase in the mitochondrial mass and modifications in network shape, defined as aspect ratio, only in double LDHA/B KO cells (**Fig 5b**). Under uncoupling conditions, double LDHA/B KO cells possess higher respiratory capacity than the other cells (**Fig 5c**). Two *in vivo* strategies were employed to inhibit these metabolic adaptations. The double LDHA/B KO tumors were challenged either with the respiratory complex I inhibitor phenformin or by irradiation (**Fig 5d**). Phenformin treatment improved survival of control tumor-bearing mice while did not improve survival of KO LDHA/B tumor-

bearing mice (**Fig 5e**). Furthermore, cranial irradiation massively increased overall survival in mice, with a higher efficiency for mice bearing double LDHA/B KO tumors (**Fig 5e**).

Use of anti-epileptic drug targeting LDH activity efficiently reduces GBM development

Mice were next treated with the anti-epileptic drug stiripentol, which inhibits LDH activity and is capable to cross the blood-brain barrier³⁷. Importantly, this drug has already been used in preclinical therapy studies *in vivo* in mice²⁷ (**Fig 6a**). We first validated LDH inhibition *in vitro* in P3 GBM cells by intracellular lactate recording with the FRET biosensor *Laconic*, finding that lactate level decreased and its production was inhibited 50% after 24 hrs treatment with 500 μ M of stiripentol (**Fig 6b**). This was correlated with a drastic decrease of basal and uncoupled respiration in pre-treated P3 cells (**Fig 6c**). Furthermore, stiripentol significantly reduced P3 spheroid proliferation (**Fig 6d**) and invasion at 0.1% O₂ (**Fig 6e**). To test stiripentol anti-cancer properties *in vivo*, intraperitoneally injection of either 100 mg/kg of stiripentol (stiri) or 10 mg/kg of bevacizumab (bev) alone, or in combination (combo) in animals implanted with P3 cells were then carried out (**Fig 6f**). Stiripentol treatment had positive effect on mouse survival when administered alone but its combination with bevacizumab treatment significantly increased survival (**Fig 6f**). Immunohistochemistry analysis showed reduction in tumor size and invasion when treated with the combinatory regimen (**Fig 6g**).

DISCUSSION

A common property of many solid cancers including GBMs, is upregulation of glycolysis¹⁻³ and it has been postulated that blocking glycolysis could be a useful target against this aggressive disease. Our study pinpoints lactate as one of the main metabolic drivers in glioblastoma, through both LDHA and LDHB activities to support tumor development and invasion.

Histological analysis of LDHA and LDHB expression demonstrated a clear pattern with LDHA predominantly expressed in the central hypoxic area, confirming our previous data³⁸, whereas LDHB was expressed in peripheral and invasive tumor areas. Only a few cells were found positive for LDHA in peripheral and invasive areas in the corpus callosum. This pattern was also confirmed in the collagen-embedded invasive spheroid model where LDHA was mainly found in the hypoxic core of spheroid²⁹ and in a few invasive cells. LDHB is exclusively localized at spheroid borders and in invasive cells. This observed differential spatial distribution was reinforced by analyzing a single-cell database which include RNAseq data from central and invasive GBM regions³⁰. These results demonstrate that LDHA or LDHB spatial distribution echoes the expression of the lactate transporters MCT1 and MCT4³², supporting the hypothesis of lactate shuttle between cells, as described in the astrocyte-neuron lactate shuttle (ANLS).

We evidenced that lactate, as a single carbon source being retro-converted into pyruvate, is able to fuel the TCA cycle *via* upregulation of oxidative phosphorylation, an observation that become evident when inhibiting the respiratory chain complex I with rotenone. Our data also show that lactate alone can regulate tumor invasion in cells starved for most carbon sources, over proliferation, by quickly fuelling TCA cycle. When glucose is present, lactate and acidification (by HCl) regulate GBM invasion²³. Acidification of the microenvironment participates to cell invasion by upregulating many factors such as TGF β ²³. Labelling of starved GBM stem-like cells with [¹³C₃]lactate quickly generated pyruvate which fuels the TCA cycle, or converted into alanine which is secreted into the extracellular space. The TCA cycle plays a central role in energy metabolism through acetyl-CoA oxidation but has also functions in biosynthetic pathways (*e.g.* non-essential amino acids or fatty acids)³⁹. As the TCA cycle cannot fully oxidize all intermediates, known as cataplerosis, these were removed from the cycle and secreted by the cells mainly in the form of glutamine and asparagine.

Moreover, exogenous lactate provides an important and rapid carbon pool for citrate-mediated fatty acid biosynthesis^{40,41}. Consistent with a previous study⁴⁰, we observed a smaller m+2 isotopolog contribution of α -ketoglutarate and succinate compared to citrate. Oddly enough, m+2 isotopolog contribution of glutamate and malate tend to be similar to citrate.

Single KO of LDHA does not have significant impact on the stem-like GBM cell models used in this study, which is different to LDHA KO neuroblastoma cells described in another publication⁴². When LDHA is absent, compensatory mechanisms are observed in our study, even under low oxygen conditions. Surprisingly, KO LDHB cells were more aggressive on *in vitro* and *in vivo* experiments, an observation that may be partially explained by an accumulation of extracellular lactate and higher production of VEGF, inducing a strong vascular response and lower survival of implanted animals. VEGF is of the strongest signal for neoangiogenesis and was shown to be activated *via* lactate and tumor acidosis, increasing endothelial cell proliferation^{43,44}. LDHB knockout was previously characterized to be linked to autophagy, and reduction of cell proliferation²⁵, which was not observed in our study. Double LDHA/B KO decreased both proliferation and invasion and was also linked to an increase in apoptosis, thus improving mouse survival *via* reduction of the tumor mass. While complementary roles of LDHA and LDHB in brain tumor development have been reported in a neuroblastoma model⁴², double LDHA/B KO in GBM stem-like cells induced a strong decrease on tumor development *via* lactate production and consumption. In an elegant publication, Zdravcic and colleagues showed that LDHA/B ablation impairs melanoma and colon adenocarcinoma growth⁴⁵, but with less difference for melanoma between single LDHA KO and LDHA/B KO when compared to our study. Cerebral tumors rely on low oxygen concentrations, which can partially explain these differences between the models. As lactate has been shown to be immunosuppressive⁴⁶, we are, at present, investigating macrophages/microglia activation in our *in vivo* models, as they represent the main immune cells in glioblastoma⁴⁷. GBM stem-like cells evolve in a different microenvironment than melanoma cells or adenocarcinoma cells and, thus, metabolic regulations during tumor growth may be different.

Accumulation and excretion of incompletely catabolized intermediates could reflect hyperactive metabolism⁴⁸ or a blockade of essential pathways. The best example is the Warburg effect, where a high glycolytic rate lead to pyruvate excess that cannot be consumed

by mitochondria, resulting in significant lactate production and secretion. In addition, GBM LDHA/B KO cells lost the ability to maintain the redox balance under anaerobic conditions. Therefore, the double knock-out globally impacts the cellular metabolism and this is associated with a decrease of glucose consumption, an accumulation of the majority of intermediates from glycolysis and TCA and excretion of formate or acetate. One possible explanation for fermentative by-product overflow is that the pyruvate-derived acetate is produced to maintain a lower redox potential to compensate LDH KO⁴⁹. We also observed an increase in the expression of the respiratory complex in LDHA/B KO cells in hypoxia to counteract the metabolic stress in these extreme conditions. To increase apoptosis of double LDHA/B KO tumor, phenformin was used as an inhibitor of respiratory complex I. This treatment failed to increase double LDHA/B KO tumor apoptosis which is possibly due to the compensation by other respiratory complexes or alternative metabolic pathways such as fatty acid oxidation. Of note, control tumors were found sensitive to phenformin treatment, as suggested by other groups⁵⁰. After cranial irradiation, on the contrary, a strong increase in mouse survival was globally observed.

In a recent study, the use of anti-epileptics as anticancer drugs has been proposed, and this could be beneficial for the treatment of GBM patients⁵¹. We therefore took advantage of the use of stiripentol, an antiepileptic drug approved by FDA for the treatment of Dravet Syndrome because it also potently inhibits both LDHA and LDHB activity²⁷. Our results demonstrate that stiripentol coupled with an antiangiogenic drug induced a significant therapeutic response with inhibition of tumor growth and tumor cell invasion.

All in all, we conducted herein a detailed analysis of the metabolic consequences of the deletion or inhibition of LDH enzymes in GBM cells and demonstrated that targeting of both LDHA and LDHB is required for efficient inhibition of tumor growth. These results are of great translational significance because these enzymes may represent interesting candidates for further therapeutic development in GBM.

Author contributions:

JG, IFM, CL, CB, GR, BD, TM, CLéon and TD performed experiments; TC, HE, IRG, NO performed preliminary experiments. ABarre, BD, AC, JR and MN performed bioinformatics RNA sequencing and metabolomics analysis; MAD implanted animals and performed in vivo experiments; BB and JG performed RNA sequencing; JG, HM, GM, MN, RB, AB and TD discussed the results; TD and AB supervised the work; JG, IFM, AB and TD wrote the manuscript. All authors have read and agreed to the published version of the manuscript.

Acknowledgements

This work was supported by grants from CNRS and INSERM (recurrent fundings), and from the “Ligue contre le Cancer” and the Fondation ARC, ARTC, PLBIO INCA and the SIRIC-BRIO to TD and AB and by Helse Vest, Haukeland Hospital, The Norwegian Research Council and Stiftelsen Kristian Gerhard Jebsen Research Foundation for RB. CB is a recipient of SIRIC BRIO funding for here postdoctoral position. The authors thank Jubayer A Hossain, Matthias Preussler, and Matteo Gambarreti for preliminary experiments, Arnaud Villacreces and Jean-Max Pasquet from the « Celloxia, modeling the hypoxic niche » facility for their technical assistance (Univ. Bordeaux, INSERM U1035, F-33000 Bordeaux, France), the VIB-CCB Metabolomics Expertise Center for the ¹³C-lactate metabolic analyses, with Bart Ghesquiere, and MetaToul facility for ¹³C-glucose analysis and their expertise (Lindsay Peyriga, Florian Bellvert, Jean-Charles Portais et Maud Heuillet), Biocodex for providing stiripentol (Marc Verleye), Florence Cavalli for advising the use of bioinformatics tools, and Arnaud Mourier for the constructive criticism of the manuscript and performed experiments. We are also grateful about the work done Marcia Campistron and Marie-Paule Algeo from Animalerie Mutualisee de Talence. The microscopy was done in the Bordeaux Imaging Center a service unit of the CNRS-INSERM and Bordeaux University, member of the national infrastructure France BioImaging supported by the French National Research Agency (ANR-10-INBS-04).

MATERIALS AND METHODS

Ethical issues

Male RAG γ 2C^{-/-} mice were housed and treated in the animal facility of Bordeaux University. All animal procedures have been done according to the institutional guidelines and approved by the local ethics committee (agreement number: A5522). The collection of biopsy tissue was approved by the regional ethical committee at Haukeland University Hospital, Bergen, Norway (REK 013.09), and by Humanitas Hospital (Milan, Italy).

Antibodies and reagents

The detailed information of primary and secondary antibodies used in this study is listed in Reagent List. For immunofluorescence, DAPI was used to stain DNA in blue, Phalloidin Rhodamine was used to stain cytoskeleton in red. Calcein-AM and ethidium homodimer-1 were directly added to cultures in their usual media. Calcein-AM is converted into green fluorescent calcein by intracellular esterase and is an indicator of cell viability. Injured or dead cells take up ethidium homodimer-1 which stained the DNA in red. Spheroids are incubated in these reagents for 45 min at 37°C and then images were directly taken. Others reagents and products are listed in Reagent List.

Cell culture

Patient-derived GBM P3 and BL13 cells were cultured in NeuroBasal medium (NBM) supplemented with B27, heparin (100 U/ μ L), 20 ng/mL basic FGF and Penicillin – Streptomycin (1000 U/mL) at 37°C in 5% CO₂ incubator. Stable cell lines were generated by infecting

lentiviral particles. For generation of lentiviral particles, HEK293T cells were transfected with the lentiCRISPR v2 vector with sgRNA, psPAX2 (packaging construct) and pMD2.G (viral envelope). The culture medium was replaced by Opti-MEM with 20mM HEPES 6 hours after transfection. After 2-3 days of culture, the supernatant was collected, passed through a 0.22 μ m syringe filter. The virus-containing media supplemented with 8 μ g/mL polybrene was used to infect P3 and BL13 cells. The infected cells were selected in media with puromycin (0.75 μ g/mL) or blasticidin (10 μ g/mL) and the LDHA or/and LDHB deletion was assessed by Western blot.

sgRNA constructs

LDHA and LDHB sgRNAs were designed online (<http://crispr.mit.edu/>). The target sequences were 5'-TGCGAATACGCCACGCGATGGG-3' for Control, 5'-CCGATTCCGTTACCTAATGGGGG-3' for LDHA, and 5'-AAGATCACTGTAGTGGGTGT-3' for LDHB. The sgRNAs were then cloned into the lentiCRISPR v2 vector by a BsmBI digestion.

Spheroid experimental assays

Protocols are described into details in a previous article²⁹. Briefly, P3 and BL13 spheroids of uniform size were prepared from 10^4 dissociated cells in NBM with 0.4% methylcellulose in a 96-well round-bottom plate. The spheroids were used after 3 days of formation. For spheroid growth, each spheroid was washed with PBS and individually replaced in fresh complete neurobasal medium with 0.4% methylcellulose supplemented with different treatments in a 96-well round bottom plate. For spheroid invasion, spheroids were washed in PBS and individually included in a 96-well flat-bottom plate in 100 μ L of type I collagen matrix prepared on ice with 1 mg/mL collagen type I and NaOH (initial concentration: 1M, volume added correspond to 0.023 volume of collagen type I). The matrix was incubated at 37°C for 30 minutes and then, complete neurobasal medium with different treatments were added over the matrix.

Intracranial implantation

For *in vivo* experiments, 5 spheroids of P3 or BL13 knock-out for LDHA, LDHB or LDHA/B (only LDHA/B for BL13) and control cell lines were stereotactically implanted into the brains of immunodeficient RAG γ 2C^{-/-} mice ($n = 8$ for survival or $n = 5$ for stop at a given point, 7-9-

week-old) housed and treated in the animal facility of Bordeaux University (“Animalerie Mutualisée Bordeaux”). The animals were anesthetized with ketamine (1.5mg/Kg) and xylazine (150µg/Kg) and a burrhole was drilled 2.2 mm to the left of the bregma, and the spheroids were implanted into the cerebral cortex at 3 mm depth using a 10 µL Hamilton syringe. An analgesic procedure was applied with the subcutaneous injection of buprenorphine (0.1 mg/kg, once 10 min before and once 12 to 24h after implantation). After 4 days, started the bevacizumab injections (10 mg/kg ip), and/or stiripentol (100 mg/kg ip), or phenformin (50 mg/kg ip) injection 3 times a week. The animals were euthanized by cervical dislocation at the end of the experiment and brains removed for further histological and immunohistological analyses.

Histological samples preparation

For frozen process, mice brains were placed in a cryotube after extraction, directly frozen in liquid nitrogen without fixation and stored at -80°C. Sections (10 µm) were prepared using a cryostat (CM1900, Microsystems) and mounted on slides. Before immunolabeling process (see below), cryo-sections were dried at room temperature for 10 minutes. They were fixed with 4% paraformaldehyde (PFA) for 15 min at room temperature, then washed 3-times in phosphate-buffered saline (PBS). For paraffin process, mice brains or other samples were fixed with 4% PFA for 15 min at room temperature, then washed 3-times in PBS. Samples were dehydrated serially in 70, 96, and 100% ethanol then toluene, and paraffinized. Sections (10 µm) were prepared using a microtome (Leica) and mounted on slides. Before immunolabeling process (see below), paraffin-embedded sections were deparaffinized in toluene and hydrated serially in 100, 96, and 70% ethanol and distilled water then for 1h at 95°C in citrate buffer before staining procedure.

Immunolabeling process

Samples were permeabilized with 0.1% Triton X-100 in PBS for 15 min, quickly washed in PBS, blocked with 1% bovine serum albumin and 2% fetal donkey serum (FDS) in PBS (blocking buffer) for 1 h. Samples were incubated with primary antibodies in blocking buffer overnight at 4°C, followed by 3-time PBS wash and incubation with secondary antibodies in blocking buffer for 1 h, for staining DNA or/and cytoskeleton, samples were treated with DAPI

or/and Phalloidin Rhodamine, respectively. Samples were washed 3-times in PBS and were mounted using Prolong Gold antifade reagent.

Western blot

Cells were washed twice in PBS and, depending on the analysis, two procedures were used for protein lysis. (1) Cells were lysed in RIPA buffer (10 mM Tris-HCl, pH 7.4, 150 mM NaCl, 0.5% NP-40, 1% TritonX-100, 1 mM EDTA) containing proteases and phosphatases inhibitors. Protein concentrations were determined using bicinonic acid assay. Cell lysates were resuspended in Laemmli Buffer (LB - 62.5 mM Tris, 10% glycerol, 2.5% SDS, 5% β -mercaptoethanol, pH 6.8). (2) Cells were directly lysed in LB. All protein extracts (1 and 2) were separated on an acrylamide gel (10% for LDHA and B, 4-12% precasted gels (Invitrogen) for OxPhos proteins) and transferred to a nitrocellulose membrane. After blocking in blocking buffer for 1 hour at room temperature, membranes were incubated with different primary antibodies overnight at 4°C. After 3 washes in TBST (20 mM Tris, 0.5 N NaCl, 0.1% Tween-20, pH = 8) and 1 in TBS (20 mM Tris, 0.5 N NaCl, pH = 8), membranes were incubated with IR-Dye 680 or 800 labelled secondary antibodies, or secondary antibodies coupled with HRP.

Image acquisition and analysis

For Western Blot analysis, membranes were imaged using Odyssey infra-red scanner (LI-COR). The densitometry of proteins was quantified using Image Studio Lite Software with normalization against tubulin or vinculin. Uncropped immunoblot are depicted in Supplementary Figure 8. For cell or spheroid experiment assays, images were acquired with an Eclipse Ti Nikon microscope equipped with NIS (Nikon imaging element) software based on x4, x10 or x20 objective lens (Nikon), a Hamamatsu Digital CCD C10600-10B camera. Images were acquired in brightfield or/and color filters (red/green) at the plane level where the contrast is the most pronounced. Fiji software with different open-access macros was used for image analysis ([GitHub](#)). Images of the spheroid growth were acquired at 0h and every 24 h (total duration dependent on the experiments), growth was quantified as the percent of change of the spheroid area relative to 0 h. Images of the spheroid invasion were acquired at 24 h, invasion was quantified as the invasive area (total area – core area) normalized to the core area, and expressed as a fold change relative to the control group for each independent experiment. For samples from immunolabeling process, images were acquired with confocal

microscope (Nikon Elipse Ti) or epifluorescence microscope (Nikon). The pipeline analysis of mitochondrial morphology and mass was adapted in Fiji software from Koopman et al⁵². The slide scanner was a Nanozoomer 2.0HT with fluorescence imaging module (Hamamatsu Photonics France) using objective UPS APO 20X NA 0.75 combined to an additional lens 1.75X, leading to a final magnification of 35X. Virtual slides were acquired with a TDI-3CCD camera. Fluorescent acquisitions are done with a mercury lamp (LX2000 200W - Hamamatsu Photonics, Massy, France) and the set of filters adapted for DAPI, and/or GFP/Alexa 488, and/or Alexa 568 and or Alexa 647/Cy5 fluorescence.

Sample preparation and transcriptomic profiling

Transcriptomic sequencing was performed in collaboration with Core Unit for Molecular Tumor Diagnostics (CMTD), National Center for Tumor Diseases (NCT), Dresden-Germany. Details are included in the Supplemental Experimental Procedures. The R package DESeq2⁵³ was used to identify differentially expressed genes using a stringent threshold: absolute value of Log2 Fold Change (LFC) >1 and p-value adjusted for multiple testing (p-adjust) <0.01. KEGG pathways enrichment analysis was done with the R package ClusterProfiler⁵⁴. Gene Ontology (GO) terms enrichment analysis was done with the R package BACA with the EASE score set at 0.01. Only GO terms from Biological Pathways level 5 were used for this analysis. GO terms were clustered to get annotation clusters with a similarity of genes greater than 0.85. Finally, read counts were transformed using variance stabilizing transformations (VST).

Sample preparation and metabolic profiling

Metabolomic profiling was performed in collaboration with MetaboHUB-MetaToul (¹³C₆ Glucose) and VIB Metabolomics (¹³C₆ Lactate). Details are included in the Supplemental Experimental Procedures. The Principal Component Analysis (PCA) was done on the total geometric mean abundance of each metabolite in each condition. PCA is realized with the `dudi.pca` function from the R package « `ade4` » and visualized with `ggplot`. Metabolite abundance between two conditions was analyzed using the non-parametric Mann-Whitney test with a Benjamini-Hochberg correction for multiple comparisons. For visualisation purposes, comparisons between two conditions may be Log2-transformed.

Metabolomic and transcriptomic representation

Metabolome and transcriptome were independently analyzed (see above). Due to the difficulty in examining detailed metabolic networks using several cell lines and conditions, two representations are proposed. The first one, called metabologram⁵³, have the ability to visualize data at pathway level relative to the second one, which is the classical detailed network map of central carbon. In order to avoid redundancy of data, the metabologram showed all the isotope abundances in metabolites and the network map showed only the [¹³C]-labelled abundance in metabolite in order to trace the pathway of [¹³C]-initial metabolite. For each pathway and after the stringent threshold based on log₂ FC and p-value (p<0.05), transcripts are selected according to the KEGG pathway database.

Intracellular lactate recording

Cultured P3 spheroids were gently dissociated and seeded on 18 mm glass coverslips treated with Matrigel. Constructs coding for the lactate-sensitive FRET biosensor Laconic³³ have been described previously and are available through Addgene (Plasmid #44238). Adenoviral vectors encoding the FRET biosensor was custom made by Vector Biolabs. The lactate-sensitive biosensor Laconic was expressed by exposing cells to 1x10⁶ PFU of adenoviral particles (serotype 5) overnight. After 48-72 hrs post infection, cells were imaged on wide-field mode with an inverted LEICA DMI6000B microscope (Leica Microsystems, Germany) equipped with a motorized stage Scan IM (Märzhäuser, Germany), a 40X oil-immersion objective (NA 1.25), a excitation system Lumencor spectra 7 (Lumencor, US) and a Coolsnap HQ2 CDD camera (Photometrics, US). Cells were superfused with an imaging solution consisting of (in mM): 10 HEPES, 112 NaCl, 24 NaHCO₃, 3 KCl, 1.25 MgCl₂, 1.25 CaCl₂, 10 glucose and bubbled with air/5% CO₂ at 37 °C with a constant flow of 3 ml/min. For fluorescent ratio measurements, cells expressing Laconic were excited at 430 nm for 0.05–0.1 s and emission collected with band pass filters mounted on a motorized filter wheel, at 465-485 nm for mTFP and 542-556 nm for Venus, with image acquisition every 10 s. The ratio between mTFP and Venus was computed and is proportional to the intracellular lactate level. To quantify differences in lactate level, biosensor occupancy was computed as a proxy of intracellular lactate level with the following equation: Occupancy = (R-R_{min})/(R_{max}-R_{min}), in which R: basal mTFP/Venus ratio (before any drug treatment), R_{min}: steady state mTFP/Venus ratio induced by oxamate (6 mM), R_{max}: steady state mTFP/Venus ratio induced by MCTs

block (1 μ M AR-C155858 and 1 mM diclofenac). Lactate production rate was computed by fitting a linear rate to the first minutes of lactate accumulation during MCTs block. Fluorescence ratios were normalized to Rmin before quantifications.

LDH and LDHB activities

In the LDH assay (ab102526), LDH reduces NAD to NADH, which then interacts with a specific probe to produce a color (OD max = 450 nm) based on whole lysates (LDHA + LDHB isozymes) while LDHB activity is measured on LDHB enzyme which was immune-captured within the wells of the microplate (ab140361) and determined by following the production of NADH catalyzed by the enzyme (LDHB isozymes, alone). Recommendations from manufacturer were followed for optimal procedure.

Statistical analysis

No statistical methods were used to predetermine sample size. The experiments were not randomized and investigators were not blinded to allocation during experiments and outcome assessment. GraphPad Prism software and RStudio was used for analyses. Equality of variances was made with a *F*-test for two groups and Brown-Forsythe test for at least three groups. According to the homoscedasticity, comparisons of two groups were made by an unpaired two-tailed *t*-test or a Mann-Whitney test. Comparisons of at least three groups were performed using a one-way ANOVA followed by a Dunnett's or Tukey's multiple comparisons test or Kruskal-Wallis test followed by a Dunn's multiple comparisons test. A two-way ANOVA test was used to compare two or more than two groups with two variables or more than two variables (*e.g.* 21% and 0.1% O₂) or repeated measures at different times followed by a Tukey's multiple comparisons test. Survival analyses were made using log-rank Mantel-Cox test. All the tests used were indicated in the figure legends. *P values* <0.05 were considered statistically significant.

Data availability

All data are available within the Article and Supplementary Files, or available from the corresponding authors on reasonable request. Transcriptomics data are available from the European Nucleotide Archive: PRJEB45718.

REFERENCES

1. Giese, A., Bjerkvig, R., Berens, M. E. & Westphal, M. Cost of Migration: Invasion of Malignant Gliomas and Implications for Treatment. *J. Clin. Oncol.* 21, 1624–1636 (2003).
2. Neftel, C. *et al.* An Integrative Model of Cellular States, Plasticity, and Genetics for Glioblastoma. *Cell* 178, 835–849.e21 (2019).
3. Vollmann-Zwerenz, A., Leidgens, V., Feliciello, G., Klein, C. A. & Hau, P. Tumor Cell Invasion in Glioblastoma. *Int. J. Mol. Sci.* 21, (2020).
4. Scherer, H. J. THE FORMS OF GROWTH IN GLIOMAS AND THEIR PRACTICAL SIGNIFICANCE. *Brain* 63, 1–35 (1940).
5. Daubon, T. *et al.* Deciphering the complex role of thrombospondin-1 in glioblastoma development. *Nat. Commun.* 10, 1146 (2019).
6. Fack, F. *et al.* Bevacizumab treatment induces metabolic adaptation toward anaerobic metabolism in glioblastomas. *Acta Neuropathol. (Berl.)* 129, 115–131 (2015).
7. Gatenby, R. A. & Gillies, R. J. Why do cancers have high aerobic glycolysis ? *Nat. Rev. Cancer* 4, 891–899 (2004).
8. Warburg, O. On the Origin of Cancer Cells. *Science* 123, 309–314 (1956).
9. Liberti, M. V & Locasale, J. W. The Warburg Effect : How Does it Benefit Cancer Cells ? *Trends Biochem. Sci.* 41, 211–218 (2016).
10. Drent, M., Cobben, N. A. M., Henderson, R. F., Wouters, E. F. M. & van Dieijen-Visser, M. Usefulness of lactate dehydrogenase and its isoenzymes as indicators of lung damage or inflammation. *Eur. Respir. J.* 9, 1736–1742 (1996).
11. Bittar, P. G., Charnay, Y., Pellerin, L., Bouras, C. & Magistretti, P. J. Selective Distribution of Lactate Dehydrogenase Isoenzymes in Neurons and Astrocytes of Human Brain. *J. Cereb. Blood Flow Metab.* 16, 1079–1089 (1996).
12. Altenberg, B. & Greulich, K. O. Genes of glycolysis are ubiquitously overexpressed in 24 cancer classes. *Genomics* 84, 1014–1020 (2004).
13. Koukourakis, M. I. *et al.* Lactate dehydrogenase-5 (LDH-5) overexpression in non-small-cell lung cancer tissues is linked to tumour hypoxia, angiogenic factor production and poor prognosis. *Br. J. Cancer* 89, 877–885 (2003).
14. Koukourakis, M. I., Giatromanolaki, A., Simopoulos, C. & Sivridis, E. Lactate dehydrogenase 5 (LDH5) relates to up-regulated hypoxia inducible factor pathway and metastasis in colorectal cancer. 5, 25–30 (2005).
15. Sheng, S. L. *et al.* Knockdown of lactate dehydrogenase A suppresses tumor growth and metastasis of human hepatocellular carcinoma. *FEBS J.* 279, 3898–3910 (2012).
16. Xie, H. *et al.* Targeting Lactate Dehydrogenase-A Inhibits Tumorigenesis and Tumor Progression in Mouse Models of Lung Cancer and Impacts Tumor-Initiating Cells. *Cell Metab.* 19, 795–809 (2014).
17. Fantin, V. R., St-Pierre, J. & Leder, P. Attenuation of LDH-A expression uncovers a link between glycolysis, mitochondrial physiology, and tumor maintenance. *Cancer Cell* 9, 425–434 (2006).
18. Le, A. *et al.* Inhibition of lactate dehydrogenase A induces oxidative stress and inhibits tumor progression. *Proc. Natl. Acad. Sci.* 107, 2037–2042 (2010).
19. Goetze, K., Walenta, S., Ksiazkiewicz, M., Kunz-Schughart, L. A. & Mueller-Klieser, W. Lactate enhances motility of tumor cells and inhibits monocyte migration and cytokine release. *Int. J. Oncol.* 39, 453–463 (2011).
20. Rizwan, A. *et al.* Relationships between LDH-A, Lactate and Metastases in 4T1 Breast Tumors. *Clin Cancer Res* 19, 5158–69 (2013).
21. Baumann, F. *et al.* Lactate promotes glioma migration by TGF- β 2-dependent regulation of matrix metalloproteinase-2. *Neuro-Oncol.* 368–380 (2009) doi:10.1215/15228517-2008-106.
22. Colen, C. B. *et al.* Metabolic Targeting of Lactate Efflux by Malignant Glioma Inhibits Invasiveness and Induces Necrosis : An In Vivo Study 1. *Neoplasia* 13, 620–632 (2011).
23. Seliger, C. *et al.* Lactate-Modulated Induction of THBS-1 Activates Transforming Growth Factor (TGF) - β 2 and Migration of Glioma Cells In Vitro. *PLoS One* 8, e78935 (2013).
24. Chesnelong, C. *et al.* Lactate dehydrogenase A silencing in IDH mutant gliomas. *Neuro-Oncol.* 16, 686–695 (2014).
25. Brisson, L. *et al.* Lactate Dehydrogenase B Controls Lysosome Activity and Autophagy in Cancer. *Cancer Cell* 30, 418–431 (2016).
26. Wang, J. *et al.* A reproducible brain tumour model established from human glioblastoma biopsies. 13, 1–13 (2009).
27. Sada, N., Lee, S., Katsu, T., Otsuki, T. & Inoue, T. Targeting LDH enzymes with a stiripentol analog to treat epilepsy. *Science* 347, 1362–1367 (2015).

28. Daubon, T. *et al.* The invasive proteome of glioblastoma revealed by laser-capture microdissection. *Neuro-Oncol. Adv.* 1, vdz029 (2019).
29. Guyon, J. *et al.* A 3D Spheroid Model for Glioblastoma. *J. Vis. Exp. JoVE* (2020) doi:10.3791/60998.
30. Darmanis, S. *et al.* Single-Cell RNA-Seq Analysis of Infiltrating Neoplastic Cells at the Migrating Front of Human Glioblastoma. *Cell Rep.* 21, 1399–1410 (2017).
31. Sakadžić, S. *et al.* Two-photon high-resolution measurement of partial pressure of oxygen in cerebral vasculature and tissue. *Nat. Methods* 7, 755–759 (2010).
32. Allen, E. *et al.* Metabolic Symbiosis Enables Adaptive Resistance to Anti-angiogenic Therapy that Is Dependent on mTOR Signaling. *Cell Rep.* 15, 1144–1160 (2016).
33. San Martín, A. *et al.* A genetically encoded FRET lactate sensor and its use to detect the Warburg effect in single cancer cells. *PLoS One* 8, e57712 (2013).
34. Contreras-Baeza, Y. *et al.* Monocarboxylate transporter 4 (MCT4) is a high affinity transporter capable of exporting lactate in high-lactate microenvironments. *J. Biol. Chem.* 294, 20135–20147 (2019).
35. Hakimi, A. A. *et al.* An Integrated Metabolic Atlas of Clear Cell Renal Cell Carcinoma. *Cancer Cell* 29, 104–116 (2016).
36. Hisanaga, K., Onodera, H. & Kogure, K. Changes in levels of purine and pyrimidine nucleotides during acute hypoxia and recovery in neonatal rat brain. *J. Neurochem.* 47, 1344–1350 (1986).
37. Sada, N., Lee, S., Katsu, T., Otsuki, T. & Inoue, T. Targeting LDH enzymes with a stiripentol analog to treat epilepsy. *Science* 347, 1362–1367 (2015).
38. Talasila, K. M. *et al.* The angiogenic switch leads to a metabolic shift in human glioblastoma. *Neuro-Oncol.* 19, 383–393 (2017).
39. Owen, O. E., Kalhan, S. C. & Hanson, R. W. The Key Role of Anaplerosis and Cataplerosis for Citric Acid Cycle Function. *J. Biol. Chem.* 277, 30409–30412 (2002).
40. Chen, Y.-J. *et al.* Lactate metabolism is associated with mammalian mitochondria. *Nat. Chem. Biol.* 12, 937–943 (2016).
41. Minami, N. *et al.* Lactate Reprograms Energy and Lipid Metabolism in Glucose-Deprived Oxidative Glioma Stem Cells. *Metabolites* 11, 325 (2021).
42. Dornenburg, C. *et al.* LDHA in Neuroblastoma Is Associated with Poor Outcome and Its Depletion Decreases Neuroblastoma Growth Independent of Aerobic Glycolysis. *Clin. Cancer Res.* 24, 5772–5783 (2018).
43. Sonveaux, P. *et al.* Targeting the Lactate Transporter MCT1 in Endothelial Cells Inhibits Lactate-Induced HIF-1 Activation and Tumor Angiogenesis. *PLoS ONE* 7, e33418 (2012).
44. Vegran, F., Boidot, R., Michiels, C., Sonveaux, P. & Feron, O. Lactate Influx through the Endothelial Cell Monocarboxylate Transporter MCT1 Supports an NF- κ B/IL-8 Pathway that Drives Tumor Angiogenesis. *Cancer Res.* 71, 2550–2560 (2011).
45. Ždravlević, M. *et al.* Double genetic disruption of lactate dehydrogenases A and B is required to ablate the ‘Warburg effect’ restricting tumor growth to oxidative metabolism. *J. Biol. Chem.* 293, 15947–15961 (2018).
46. Fischer, K. *et al.* Inhibitory effect of tumor cell-derived lactic acid on human T cells. *Blood* 109, 3812–3819 (2007).
47. Müller, S. *et al.* Single-cell profiling of human gliomas reveals macrophage ontogeny as a basis for regional differences in macrophage activation in the tumor microenvironment. *Genome Biol.* 18, 234 (2017).
48. Meiser, J. *et al.* Increased formate overflow is a hallmark of oxidative cancer. *Nat. Commun.* 9, 1368 (2018).
49. Liu, X. *et al.* Acetate Production from Glucose and Coupling to Mitochondrial Metabolism in Mammals. *Cell* 175, 502–513.e13 (2018).
50. Jiang, W. *et al.* Repurposing phenformin for the targeting of glioma stem cells and the treatment of glioblastoma. *Oncotarget* 7, 56456–56470 (2016).
51. Jung, E. *et al.* Emerging intersections between neuroscience and glioma biology. *Nat. Neurosci.* 22, 1951–1960 (2019).
52. Koopman, W. J. H., Visch, H.-J., Smeitink, J. A. M. & Willems, P. H. G. M. Simultaneous quantitative measurement and automated analysis of mitochondrial morphology, mass, potential, and motility in living human skin fibroblasts. *Cytometry A* 69A, 1–12 (2006).
53. Hakimi, A. A. *et al.* An Integrated Metabolic Atlas of Clear Cell Renal Cell Carcinoma. *Cancer Cell* 29, 104–116 (2016).
54. Yu, G., Wang, L.-G., Han, Y. & He, Q.-Y. clusterProfiler: an R Package for Comparing Biological Themes Among Gene Clusters. *OMICS J. Integr. Biol.* 16, 284–287 (2012).

Figure legends

Figure 1

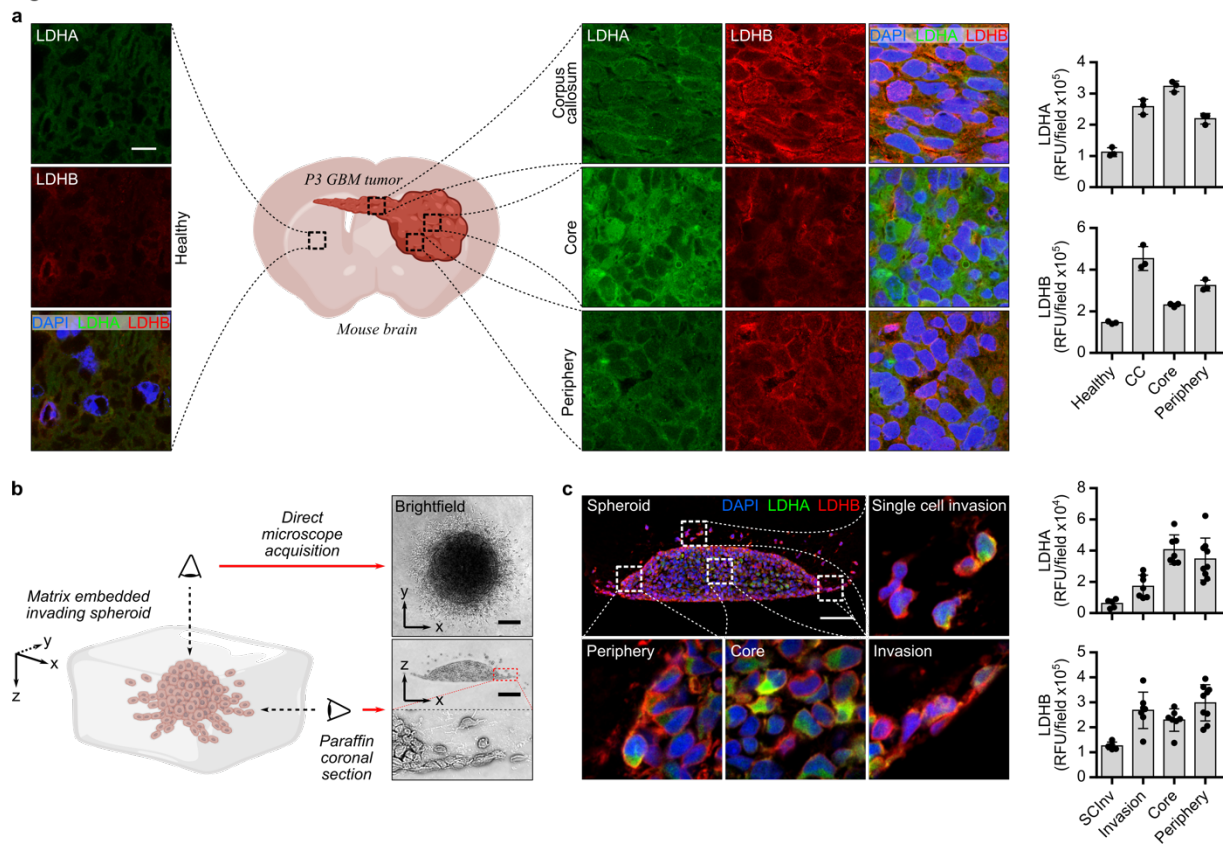


Figure 1: Distinctive expression of lactate dehydrogenase A and B in GBM.

a. Coronal section of P3 spheroids implanted in mouse brain, embedded with paraffin and stained with DAPI (blue), LDHA (green) and LDHB (red). Magnification shows areas as depicted in the central illustration. Quantification of LDHA and LDHB staining was performed on the tumor areas as indicated in the graphs. Scale: 15 μm . **b.** Left, 3D representation of an invading P3 spheroid embedded in a collagen matrix. Right, upper view: brightfield microscope image, lower view: coronal section of an invading spheroid. Scale: 100 μm . **c.** Coronal section of a P3 spheroid embedded with paraffin and stained with DAPI (blue), LDHA (green) and LDHB (red). Magnification boxes show different areas as depicted in the main image. Quantification of LDHA and LDHB staining was performed on the spheroid areas as indicated in the graphs. Scale: 100 μm .

Figure 2

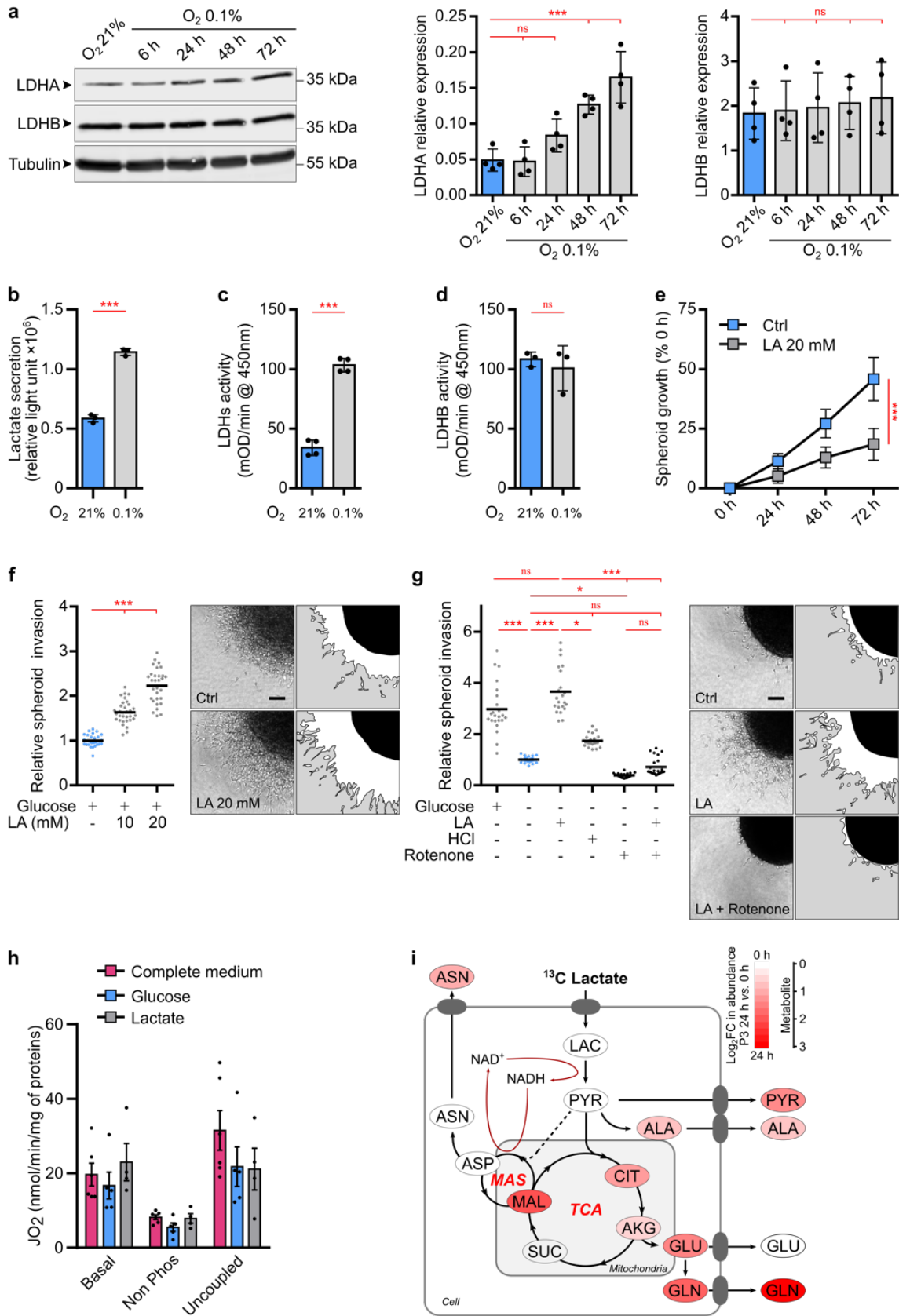


Figure 2: Increased lactate production by hypoxia, fuels TCA cycle, and drives cell invasion.

a. Western blot analysis of LDHA and LDHB from P3 cells upon exposure to 21% or 0.1% O₂ for 6, 24, 48 and 72 h. The graphs represent densitometry quantification of immunoblots normalized to tubulin ($n = 4$). **b.** Lactate secretion of P3 cells exposed to 21 or 0.1% O₂ measured with a bioluminescent assay using a pro-luciferin reductase substrate converted to luciferin in the presence of NADH ($n = 3$). **c, d.** Colorimetric assays for the activity of (c) total LDH enzymes ($n = 4$) or (d) immune-captured LDHB enzyme in P3 cells ($n = 3$). **e.** P3 spheroid growth recorded over 72 h during incubation with or without 20 mM lactate. Area of spheroids were measured at 0, 24, 48 and 72 h and growth is represented as a percentage of spheroid area compared to time 0 (8–10 spheroids per condition, $n = 3$). **f.** P3 spheroid invasion in collagen I gel incubated 24 h at 21% O₂ and incubated with 10 or 20 mM lactate. Invasion rate is expressed as a fold change to the control. (6–8 spheroids per condition, $n = 4$). Images of representative invasive spheroids in each condition. Scale: 100 μm . **g.** P3 spheroid invasion in collagen I gel incubated 24 h at 0.1% O₂ and incubated with 20 mM lactate, 20 μM rotenone, and 1.5 mM HCl. Invasion rate is expressed as a fold change of the control (6–8 spheroids per condition, $n = 4$). Images of representative invasive spheroids in each condition. Scale: 100 μm . **h.** P3 cell mass-specific respiration obtained by oxygraphy analysis (left) and inhibitors sensitivity ratio standardized for their respective maximal respiratory capacity (right). Cells were cultured in (1) complete medium or in medium without glucose and pyruvate supplemented with either (2) 10 mM glucose or (3) 20 mM lactate ($n = 4$). JO₂ Basal: baseline respiratory capacity, JO₂ non-phosphorylating (non phos): minimal respiratory capacity and JO₂ uncoupled: maximal respiratory capacity. **i.** Metabolic changes of central carbon metabolism on P3 cells infused with [¹³C]lactate for 24 h. Metabolites are labelled with a colored oval whose color corresponds to log₂ fold changes between 24 h and 0 h (red, increase in 24 h). The values m+0 to m+6 indicate: m+0 stands for the fraction of metabolite without ¹³Carbon and m+n ($n > 0$) stands for fraction of metabolite with n ¹³Carbon. The sum of (m+0, m+1, ..., m+10, ...) equals to 1. TCA, TriCarboxylic Acid cycle; MAS, Malate-Aspartate Shuttle; LAC, lactate; PYR, pyruvate; CIT, citrate; AKG, alpha-ketoglutarate; SUC, succinate; MAL, malate; ALA, alanine; GLU, glutamate; GLN, glutamine; ASP, aspartate; ASN, asparagine. See also **Suppl Figure 3**. Data are represented as mean \pm s.d (**a, b, c, d, e**), as mean (f, g) or as mean \pm s.e.m (h). n represents independent experiments. P values were calculated using One-Way ANOVA following by Dunnett's multiple comparisons test (a), unpaired t test (**b, c, d, e**), Kruskal-Wallis test following by Dunn's multiple comparisons test (**f, g**), Two-way ANOVA following by Tukey's multiple comparisons test (h); * $P < 0.05$; ** $P < 0.01$; *** $P < 0.001$; ns, not significant. Exact P values are provided in the Source Data.

Figure 3

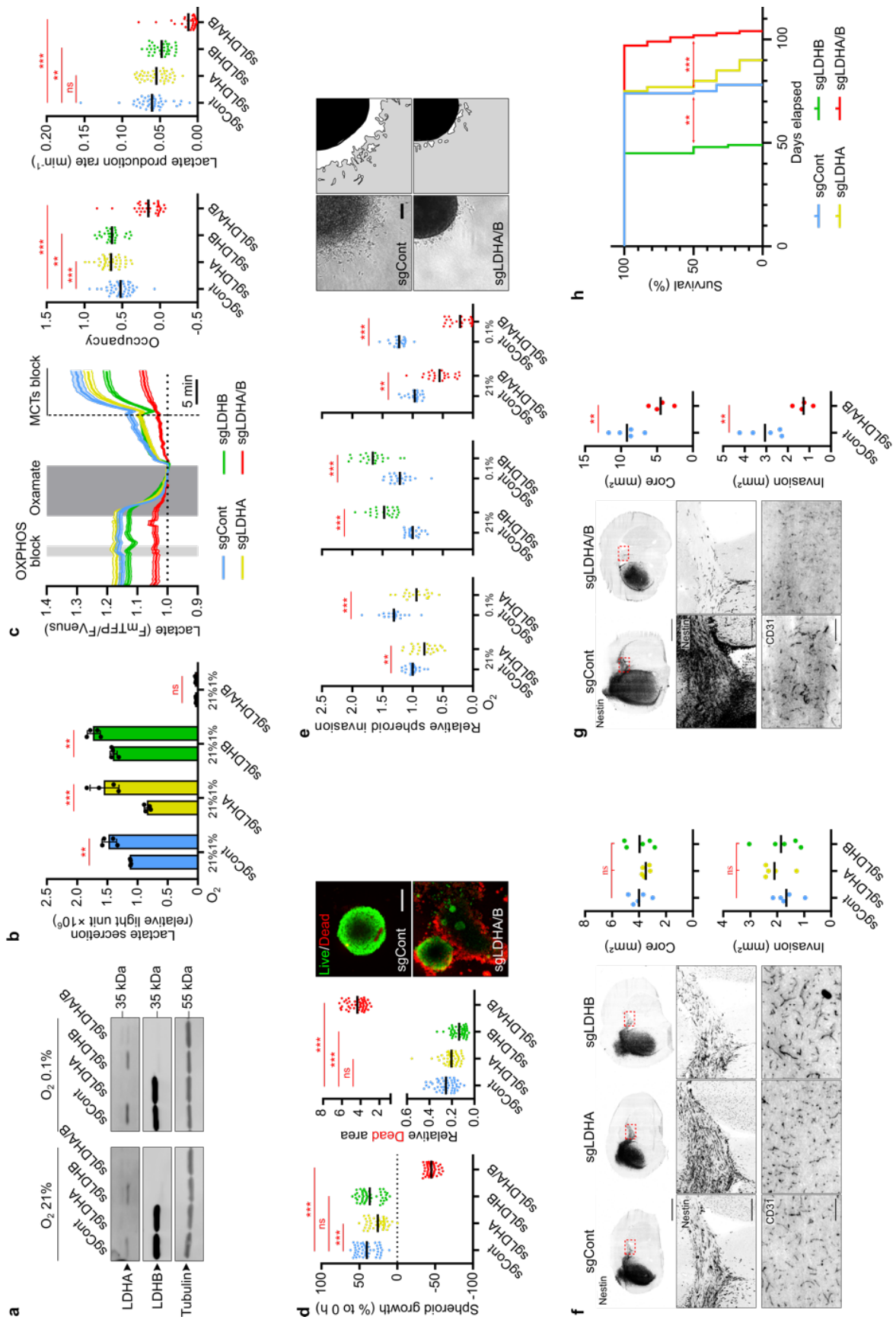


Figure 3: Double knockout of LDHA and LDHB impairs GBM lactate metabolism, viability, and invasion

a. Western blot analysis of LDHA and LDHB expression in P3 cells transduced with CRISPR-Cas9 lentiviral vectors with scramble sequence (sgControl) or against LDHA (sgLDHA), LDHB (sgLDHB) or both (sgLDHA/B). Knockout (KO) cells were exposed to 21% or 1% O₂ for 48 h. **b.** Lactate secretion of P3 cells KO for LDHA, LDHB or both, exposed to 21% or 1% (n = 3). **c.** Intracellular lactate level analyzed with a fluorescent biosensor in P3 cells (control, KO for LDHA, LDHB or both). *Left*, lactate level monitored in basal condition, followed by sequential exposure to OXPHOS block (5 mM sodium azide), 6 mM oxamate and MCTs blockers (1 μM AR-C1558585 + 1 mM diclofenac). The response to oxamate and MCTs blockers was used to determine, *Middle*, the basal lactate level (expressed as biosensor occupancy) and, *Right*, the lactate production rate (n=4, 33-44 cells analyzed per condition). See material and methods for analysis details and see also Supplementary Figure 4. **d.** *Left*: P3 spheroid growth recorded over one week at 1% O₂ (8–10 spheroids per condition, n = 3). *Right*: Viability of spheroids at one week, incubated with calcein (green) or ethidium homodimer-1 (red). Scale: 200 μm. **e.** P3 spheroid invasion in collagen I gel, incubated 24 h at 21% or 0.1% O₂. Invasion rate is expressed as fold change from controls (6-8 spheroids per condition, n = 4). Images of representative of control or LDHA/B KO spheroids. Scale: 100 μm. **f-g.** A first cohort of mice was sacrificed when one mouse reached a limit point, brains was extract, snap frozen in liquid nitrogen, sliced and stained. For the second cohort, each mouse was sacrificed when it reached a limit point allowing the draw of survival curves. *Left*: Immunofluorescence staining of Nestin (*top* and *middle*) and CD31 (*bottom*) of control and LDHA/B KO P3 tumor section. Scales: 2 mm (*top*), 250 μm (*middle*) and 100 μm (*bottom*). *Right*: Graphs represent tumor core and invasion area of control and LDHA/B KO P3 tumors in mm² (average of 5-6 sections per tumor, n = 5 mice per group). **h.** Kaplan-Meier survival curves of xenotransplanted mice with P3 cells KO for LDHA (yellow), LDHB (green), LDHA/B (red) or control (blue) (n = 8 mice per group). Data are represented as mean ± s.d (b), as mean ± s.e.m (c – left part) or as mean (c, d, e, f, g). n represents independent experiments or biological replicates. P values were calculated using Two-way ANOVA following by Tukey's multiple comparisons test (**b**, **e**), Kruskal-Wallis test following by Dunn's multiple comparisons test (**c**, **d**), One-Way ANOVA following by Dunnett's multiple comparisons test (**f**), unpaired t test (**g**) or Log-rank (Mantel-Cox) test (**h**); *P<0.05; **P<0.01; ***P<0.001; ns, not significant; exact P values are provided in the Source Data.

Figure 4

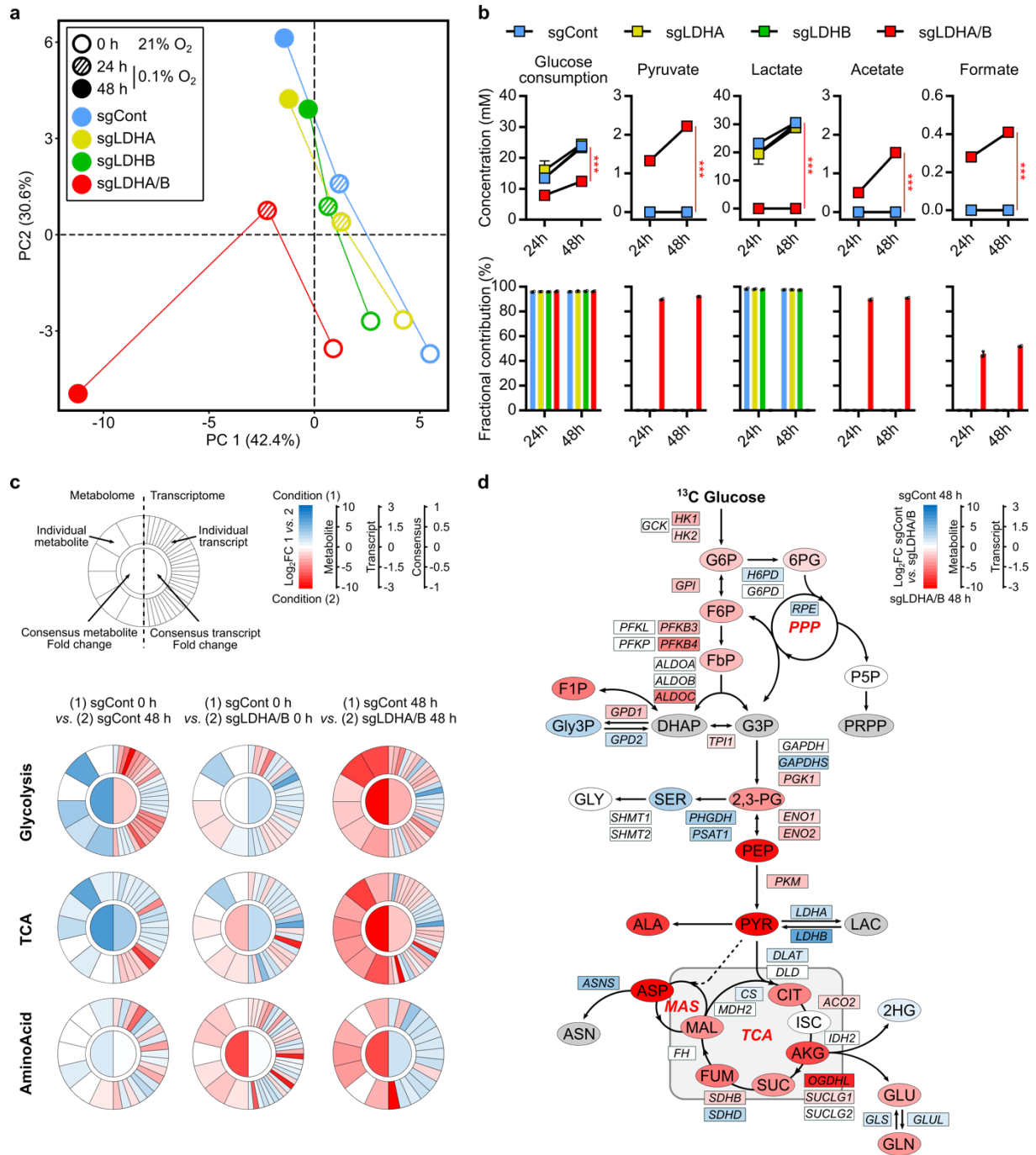


Figure 4: Correlation between transcriptomic and metabolomic analysis reveals dysregulated metabolic pathways in double knock out LDHA/B.

LDH KO P3 cells were infused 0, 24 and 48 h with [¹³C]glucose at 0.1% O₂. **a.** Principal component analysis of metabolomic data from cell extracts. **b.** Metabolites from cell medium. *Top*, concentration of metabolite consumed ([¹³C]glucose) or secreted (pyruvate, lactate, acetate, formate) by cells. *Bottom*, amount of labeled isotopes relative to the total amount of this element, expressed as a percentage (fractional contribution). **c.** Circular metabologram illustrating metabolic and transcriptomic differences in metabolite pathways between LDH KO P3 cells. The metabologram is divided in two parts, the left corresponds to metabolomic analysis and the right to the transcriptomic analysis. The outer circle corresponds to the log₂ fold change for each metabolite (*left*) and transcripts (*right*). The central circle displays the average fold change of all analytes. **d.** Metabolic changes of central 13-labeled-carbon metabolism in LDH KO P3 cells infused with [¹³C]glucose at 1% O₂ for 48 h. Metabolites are labelled with a colored-oval and enzyme transcripts with a colored-square, whose color corresponds to the log₂ fold changes between sgControl and sgLDHA/B (blue, increase in sgControl; red, increase in sgLDHA/B; gray, not measured or not computable). For legend, see also **Figure 2i**; PPP: Pentose Phosphate Pathway; G6P: Glucose-6-Phosphate; 6PG: 6-Phosphogluconate; F6P: Fructose-6-Phosphate; FbP: Fructose-bisPhosphate; P5P: Pyridoxal-5-Phosphate; F1P: Fructose-1-Phosphate; Gly3P: Glycerol-3-Phosphate; DHAP: Dihydroxyacetone Phosphate; G3P: Glyceraldehyde-3-Phosphate; PRPP: Phosphoribosylpyrophosphate; GLY: Glycine, SER: Serine; 2,3-PG: 2,3-Phosphoglycerate; PEP: Phosphoenolpyruvate; 2HG: 2-Hydroxyglutarate. See also **Suppl Figure 5**.

Figure 5

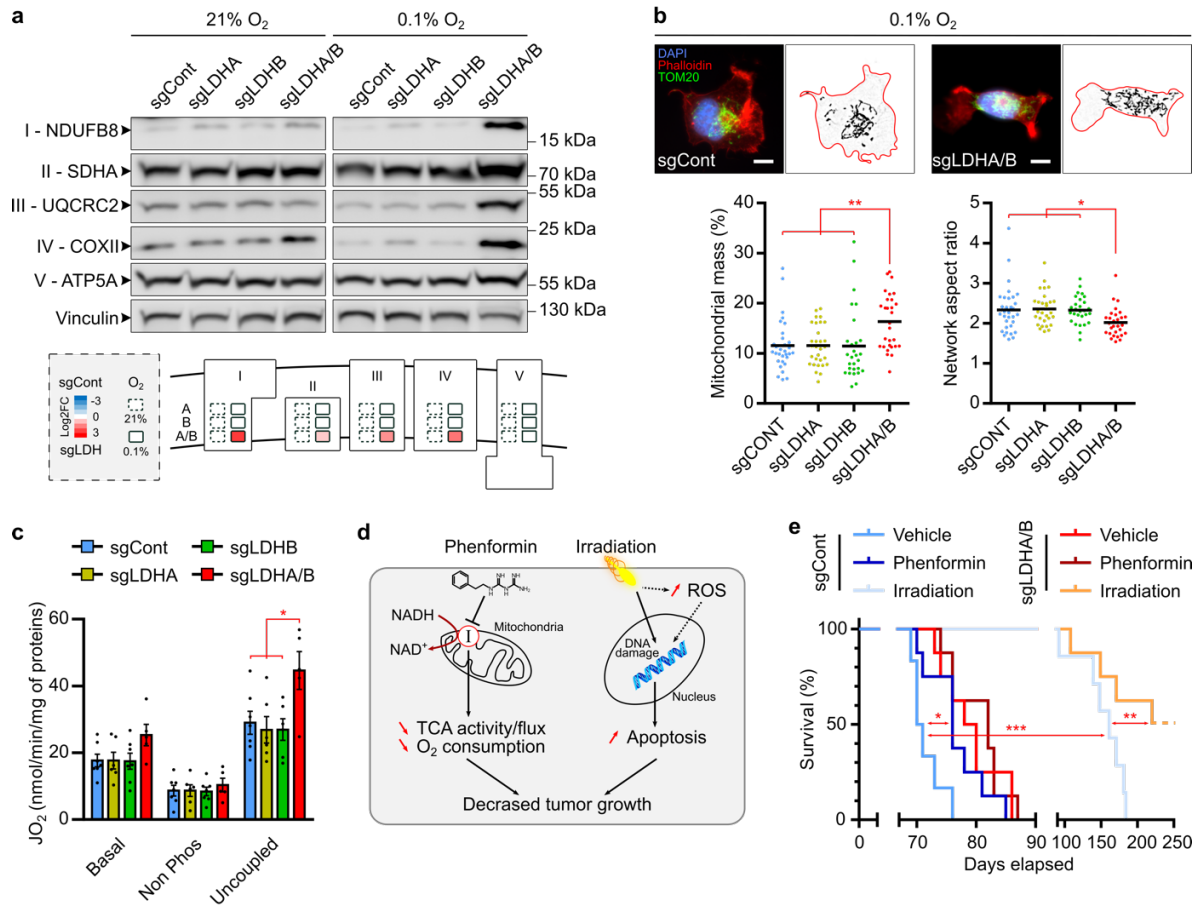


Figure 5: Knock out LDHA/B affect mitochondrial functions and sensitize tumors to radiation.

a. Western blot analysis of mitochondrial respiratory chain subunits from LDH KO P3 cells upon exposure to 21% or 0.1% O₂. Roman numbers indicate the respiratory complex number. The diagram below represents densitometry quantification of the immunoblots normalized to vinculin and expressed as log₂ foldchange to control cells in 21% and 0.1% O₂ ($n = 3$). **b.** Epifluorescence (*top*) and quantitative image analysis (*bottom*) of immune stained mitochondria (TOM20, green) from LDH KO P3 cells (Phalloidin, red; DAPI, blue) upon exposure to 0.1% O₂ (28-32 cells per group). Mitochondrial mass corresponds to the area covered by the mitochondria relative to the entire cell area. Network aspect ratio is the ratio of the major axis to minor axis of the mitochondrial network. Scale: 10 μ m. **c.** LDH KO P3 cell mass-specific respiration obtained by oxygraphy analysis ($n = 4$). For details, see **Figure 2h**. **d.** Schematic representation of phenformin or irradiation effects on tumor cells. **e.** Kaplan-Meier survival curves of xenotransplanted mice with LDHA/B KO (red) or control (blue) P3 cells, treated with phenformin or irradiated with 10 Gy. Data are represented as mean (**b**) or as mean \pm s.e.m (**c**). n represents independent experiments or biological replicates. P values were calculated using Two-way ANOVA following by Tukey's multiple comparisons test (**a**, **c**), One-way ANOVA following by Tukey's multiple comparisons test (**b**) or Log-rank (Mantel-Cox) test (**e**); * $P < 0.05$; ** $P < 0.01$; *** $P < 0.001$; ns, not significant; exact P values are provided in the Source Data.

Figure 6

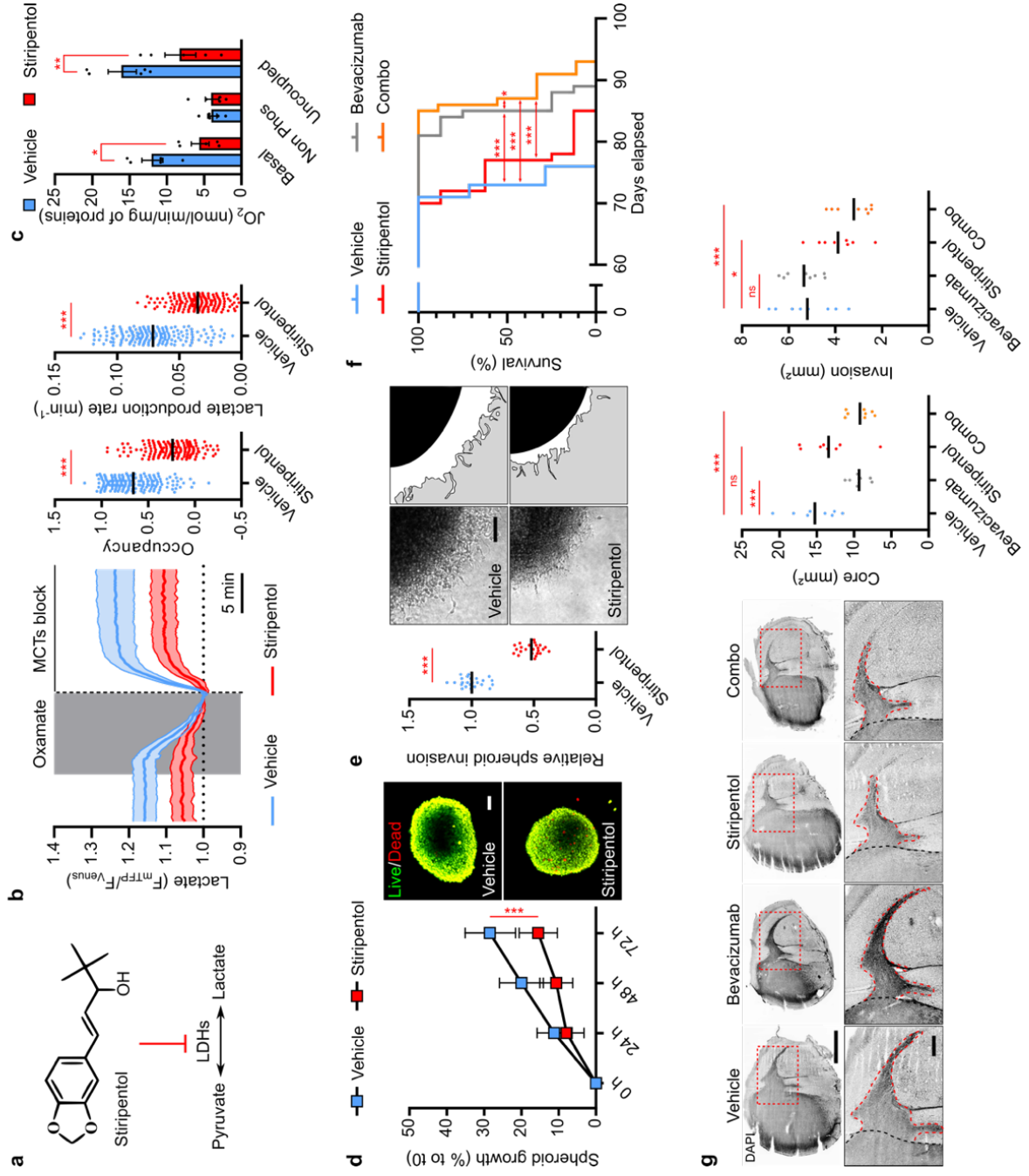
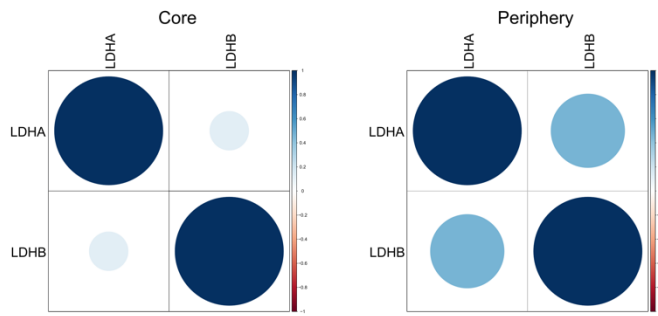


Figure 6: Combination of antiepileptic and antiangiogenic drugs reduce GBM growth

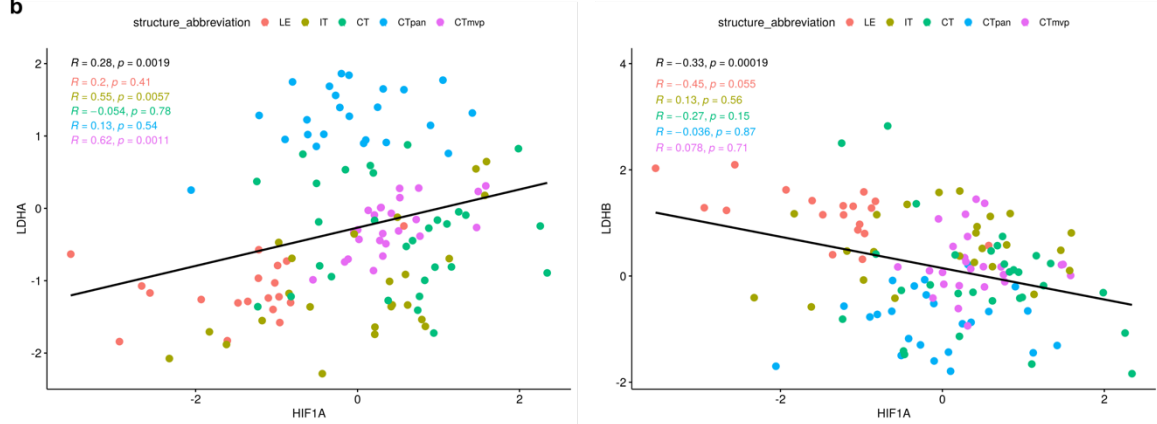
a. Stiripentol, an aromatic allylic alcohol drug that inhibits LDH. **b.** Intracellular lactate level analyzed with a fluorescent biosensor in P3 cells treated with vehicle or 500 μ M stiripentol. *Left*, lactate level monitored in basal condition, followed by sequential exposure to 6 mM oxamate and MCTs block (1 μ M AR-C1558585 + 1 mM diclofenac). The response to oxamate and MCTs block was used to determine, *Middle*, the basal lactate level (expressed as biosensor occupancy) and, *Right*, the lactate production rate ($n=4$, 33-45 cells analyzed per condition). **c.** P3 cell mass-specific respiration in cells treated with 500 μ M stiripentol, obtained by oxygraphy analysis ($n = 4$). For details, see **Figure 2h**. **d.** *Left*: P3 spheroid growth recorded over 72 h during incubation with stiripentol at 0.1% O_2 (8–10 spheroids per condition, $n = 3$). *Right*: Viability of spheroids at 72 h, incubated with calcein (green) or ethidium homodimer-1 (red). Scale: 100 μ m. **e.** *Left*: P3 spheroid invasion in collagen I gel, incubated 24 h with 500 μ M stiripentol at 0.1% O_2 . Invasion rate is expressed as fold change from control (6-8 spheroids per condition, $n = 3$). *Right*: Representative images of invasive spheroids for each condition. Scale: 100 μ m. **f.** Kaplan-Meier survival curves of xenotransplanted mice with P3 cells. Mice were treated either with vehicle (blue), bevacizumab (gray), stiripentol (red) or both drugs (orange) ($n = 8$ mice per group). **g.** *Left*: Immunofluorescence staining of DAPI of treated P3 tumor section. Scales: 500 μ m. *Right*: The graphs represent the tumor core and invasion area of double LDH KO P3 tumor in mm^2 (average of 5-6 sections per tumor, $n = 4-5$ mice per group).

Supplementary Figure 1

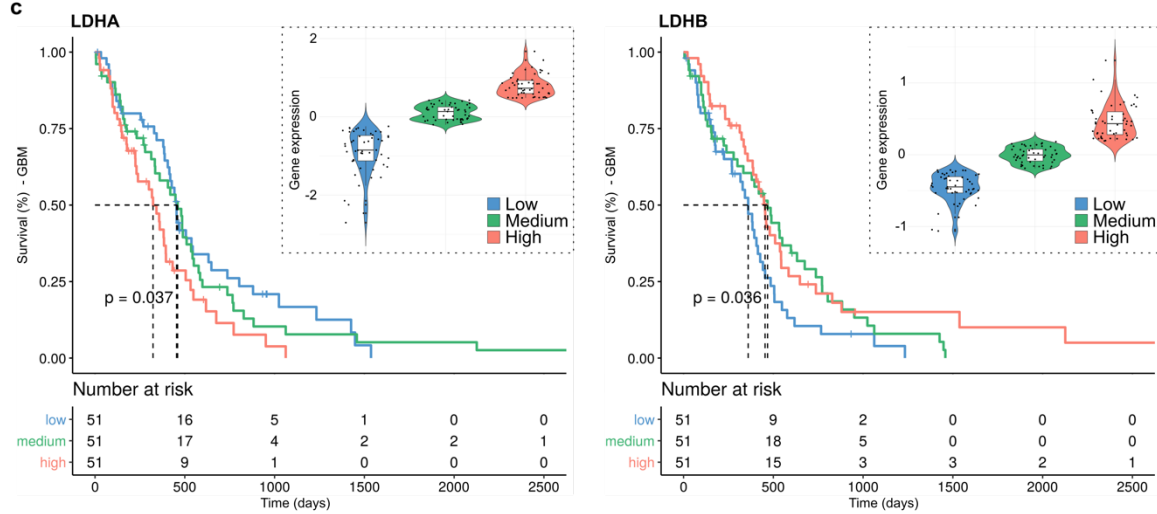
a



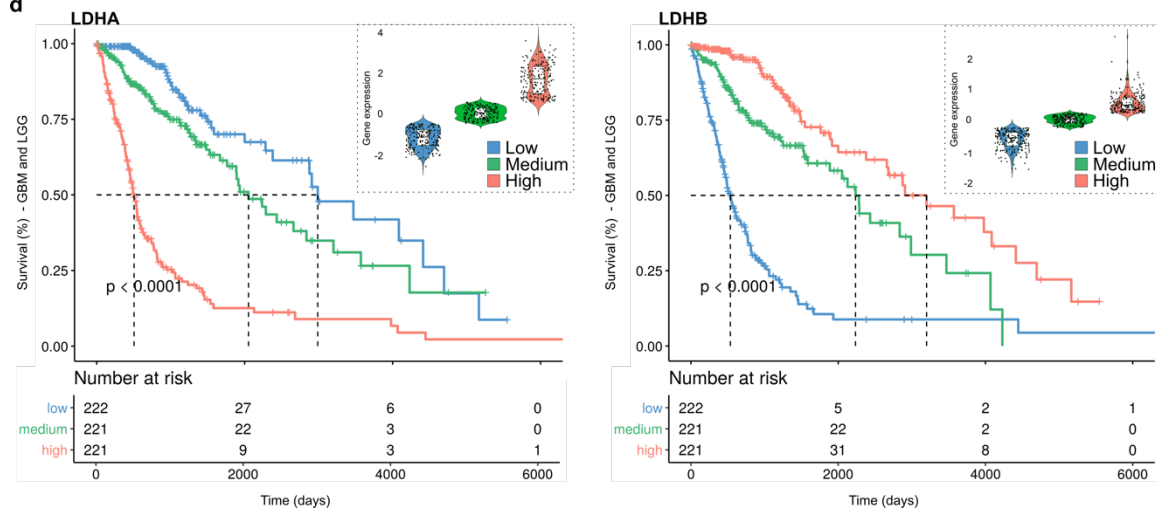
b



c



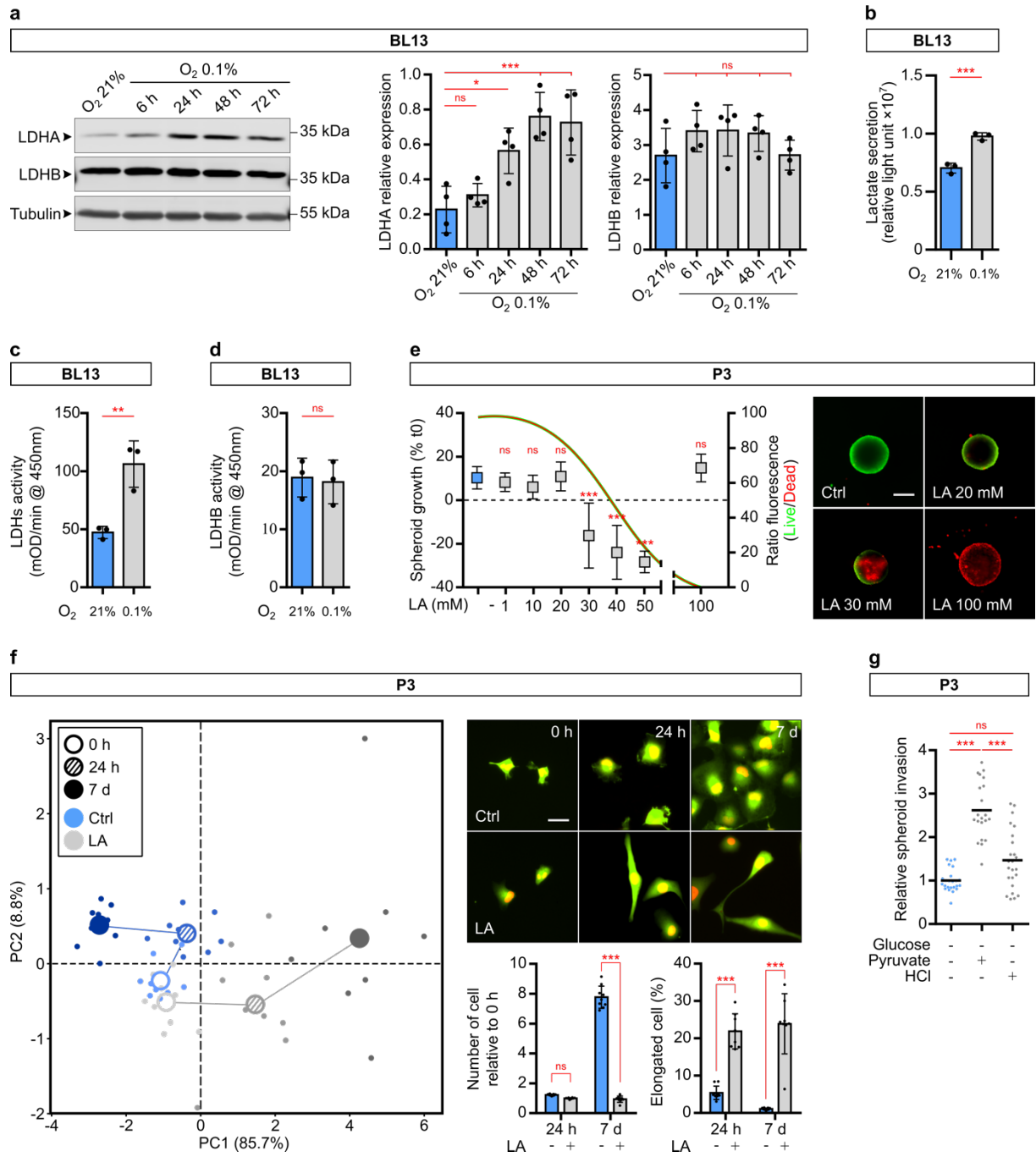
d



Supplementary Figure 1: Expression of LDHA and LDHB in publicly available databases

a. Correlation between gene expression of LDHA and LDHB and cell localization based on single cell RNA sequencing data extracted from Darmanis et al.(257) (1010 tumor cells and 62 periphery cells). **b.** *LDHA* and *LDHB* gene expression relative to HIF1A gene expression according to their anatomical origin (data extracted from Ivy Glioblastoma Atlas Project). LE, Leading Edge; IT, Infiltrating Tumor; CT, Cellular Tumor; CTpan, Cellular Tumor pseudopalisading cells around necrosis; CTmvp, Cellular Tumor microvascular proliferation. **c-d.** Survival analysis based on *LDHA* (*left*) or *LDHB* (*right*) gene expression level in glioblastoma (**c**) and on low grade gliomas (**d**). Data were extracted from TCGA.

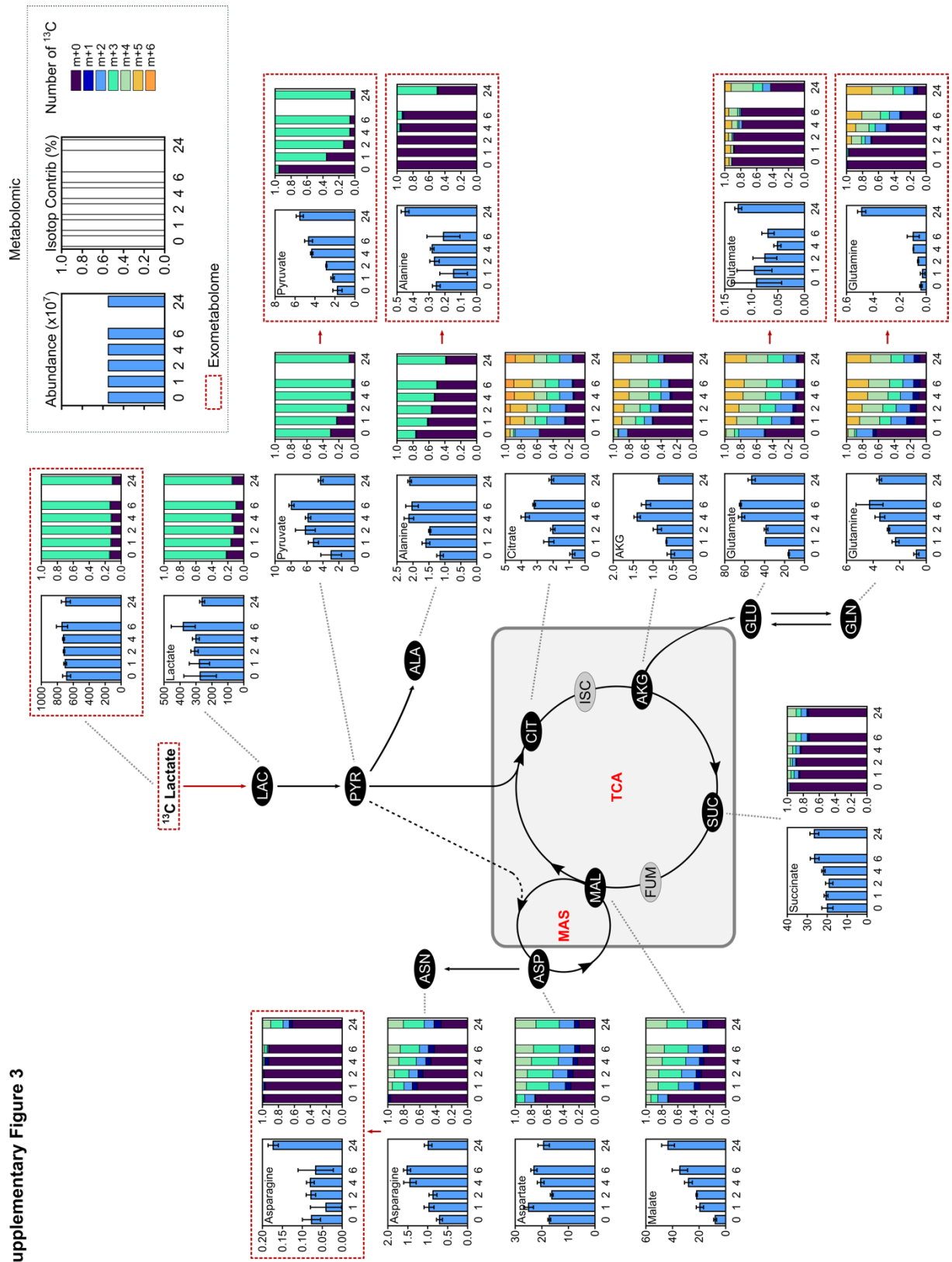
Supplementary Figure 2



Supplementary Figure 2: Independent stem-like cell line BL13 confirms results obtained in P3 stem-like cells

a. Western blot analysis of LDHA and LDHB from BL13 cells upon exposure to 21% or 0.1% O₂ during 6, 24, 48 and 72 h. The graphs represent densitometry quantification of the immunoblots normalized to tubulin ($n = 4$). **b.** Lactate secretion of BL13 cells exposed to 21% or 0.1% O₂ measured by bioluminescent assay using a pro-luciferin reductase substrate converted to luciferin in the presence of NADH ($n = 3$). **c, d.** Colorimetric assays related to the activity of **(c)** LDH enzymes ($n = 4$) or **(d)** immune-captured native LDHB enzyme ($n = 3$) in BL13 cells by measuring the absorbance at 450 nm. **e.** P3 spheroid cytotoxicity assay recorded over 24 h when incubated with or without lactic acid at different concentrations (1, 10, 20, 30, 40, 50, and 100 mM). Area of spheroids were measured at 0 and 24 h. Growth is represented as a percentage of spheroid area when compared to time 0 and viability is estimated with Live/Dead fluorescence ratio at 24 h and represented as a fitted curve (8–10 spheroids per condition, $n = 3$). Images of representative spheroids in each condition (in green, calcein ; in red, ethidium homodimer-1). Scale: 250 μm . **f.** Principal component analysis of morphologic data on P3 cells incubated 7 days with or without lactate (20 mM). Cell number and morphology were measured at 0 h, 24 h and 7 days. Images of representative adherent cells in each condition (in green, GFP; in red, nuclear Tomato). Scale: 40 μm . The graphs represent quantification of the cell number and elongated cells (Aspect ratio > 2,5; $n = 3$). **g.** P3 spheroid invasion in collagen I gel incubated 24 h at 21% O₂ and treated with 20 mM pyruvate or 1.5 mM HCl. Invasion rate is expressed as a fold change of the control (6-8 spheroids per condition, $n = 3$). Data are represented as mean \pm s.d. n represents independent experiments. P values were calculated using One-Way ANOVA following by Dunnett's multiple comparisons test **(a)**, unpaired t test **(b, c, d)**, Kruskal-Wallis test following by Dunn's multiple comparisons test **(e, g)**; Two-Way ANOVA following by a Sidak's multiple comparisons test **(f)**; * $P < 0.05$; ** $P < 0.01$; *** $P < 0.001$; ns not significant; exact P values are provided in the Source Data.

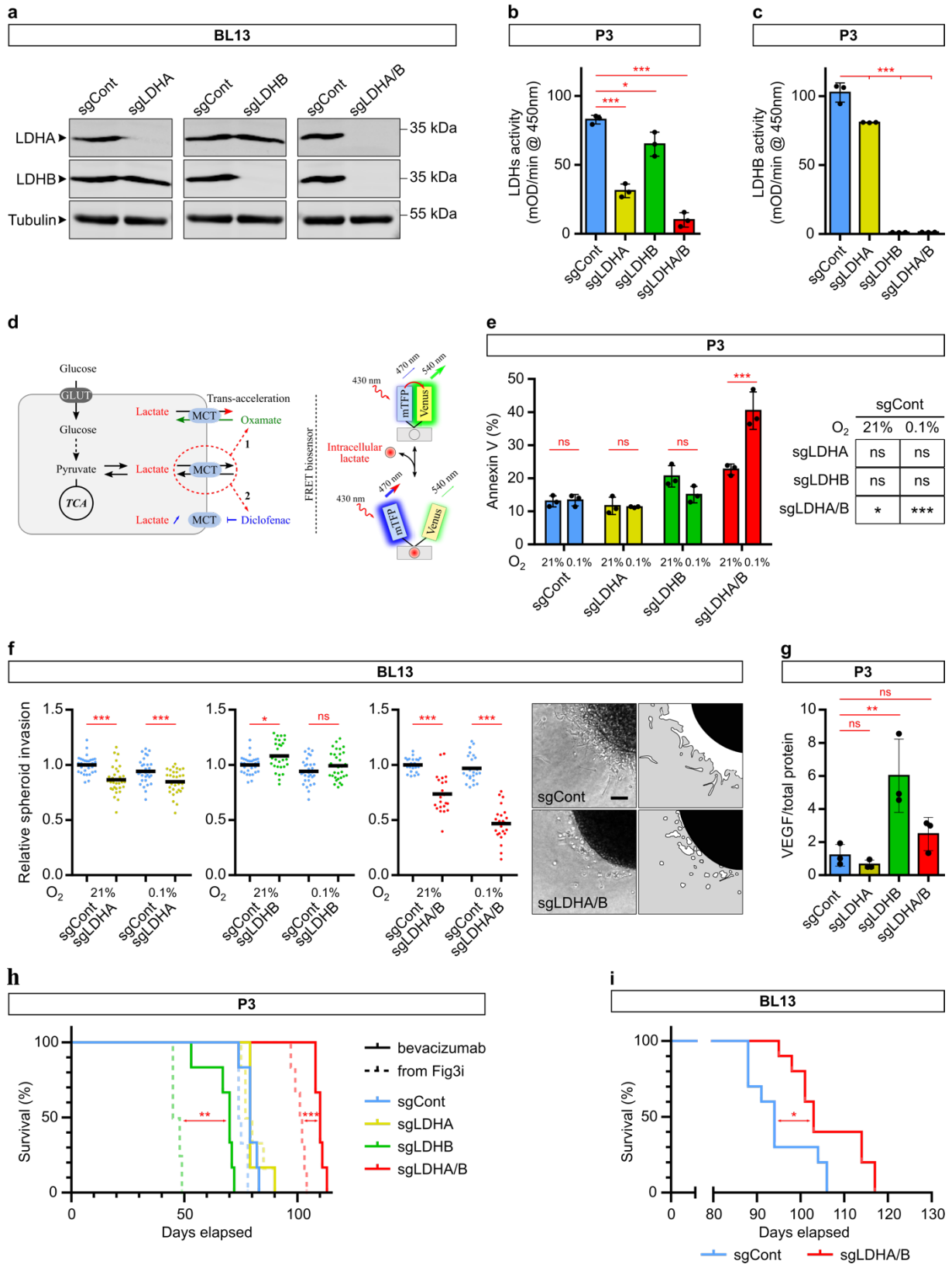
Supplementary Figure 3



Supplementary Figure 3: Metabolic tracing using [¹³C₃]lactate (Extended data Figure 2i)

P3 cells were infused during 0, 1, 2, 4, 6 and 24 h with [¹³C₃]lactate at a concentration of 5 mM. Metabolites from cell extracts (endometabolome) or cell medium (exometabolome) measured by gas chromatography-mass spectrometry. Metabolite abundance of some intermediates of metabolic pathway of interest. Quantification of the [¹³C₃]lactate carbon incorporation into intermediates of the carbon metabolism (isotopologue contribution). m+0 stands for the fraction of metabolite without ¹³Carbon and m+n (n > 0) stands for fraction of metabolite with n ¹³Carbon. The sum of (m+0, m+1,..., m+10,...) equals to 1.

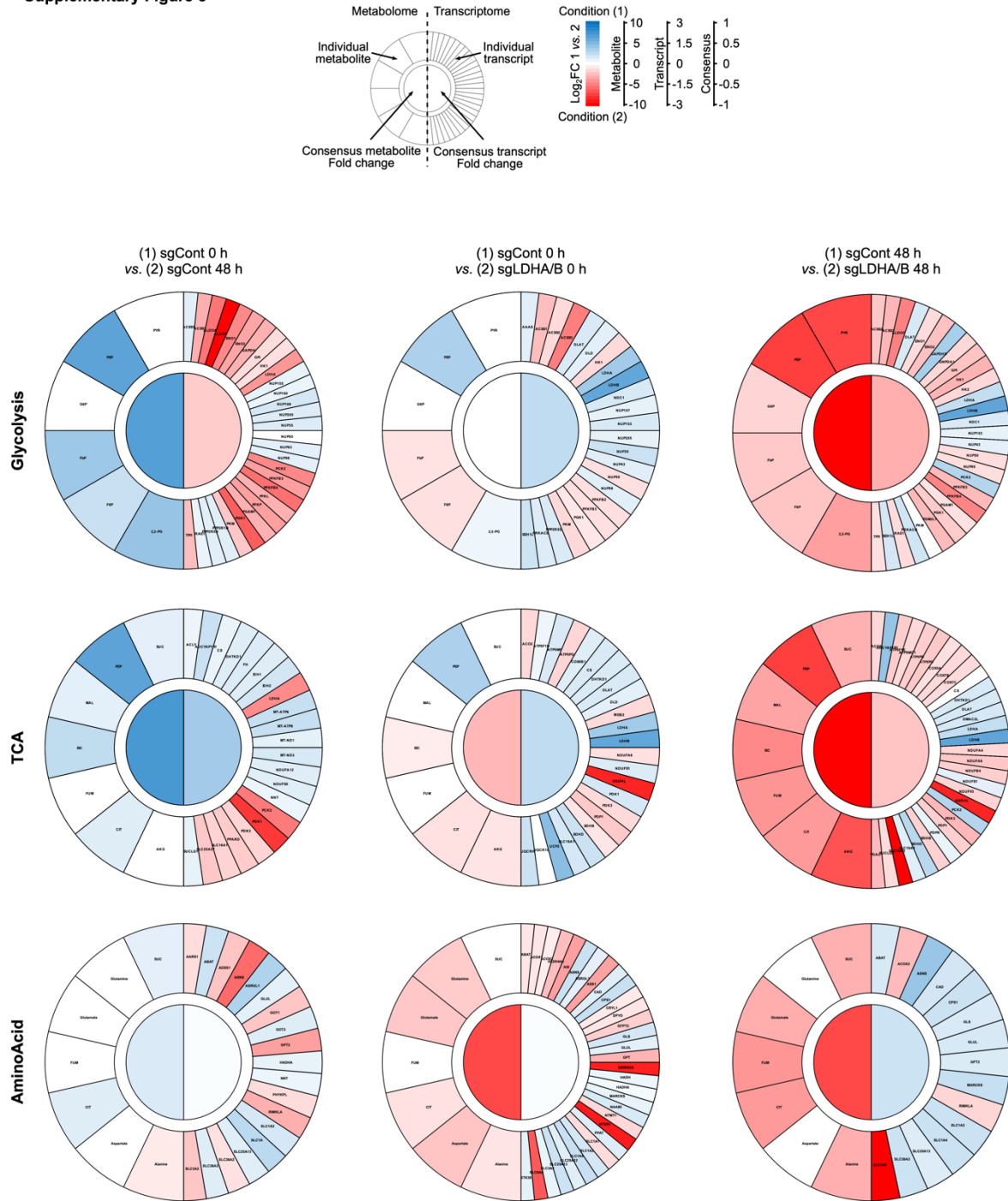
Supplementary Figure 4



Supplementary Figure 4: LDHA/B KO in BL13 cells and bevacizumab treatment in P3 tumors.

a. Western blot analysis of LDHA and LDHB from BL13 cells knockout by Crispr-Cas9 lentiviral vectors against LDHA, LDHB or both, and upon exposure to 21% O₂. **b, c.** Colorimetric assays related to the activity of **(b)** LDH enzymes ($n = 4$) or **(c)** immune-captured native LDHB enzyme ($n = 3$) by measuring the absorbance at 450 nm in KO P3 cells. **d.** Schematic representation of the intracellular lactate level monitoring with a fluorescent biosensor. The presence of the lactate changes the conformation of the biosensor and fluorescence emission. Known as an accelerated-exchange transport (trans-acceleration), oxamate was used to quickly release the lactate out of the cells for the determination of the lactate basal level. Then, diclofenac was used to block the lactate transporter for the quantification of the lactate production rate. **e.** Cells incubated during 48 h at 21% or 0.1% O₂, labeled with Annexin V-FITC and analyzed by cytometry. Table of statistical comparisons of annexin-V signal in sgLDHA, sgLDHB and sgLDHA/B cells with respective control (either 21 or 0.1% O₂). **f.** BL13 spheroid invasion in collagen I gel incubated 24 h at 21 or 0.1 % O₂. Invasion rate is expressed as a fold change of the control (6-8 spheroids per condition, $n = 4$). Images of representative invasive sgControl or sgLDHA/B spheroids. Scale: 100 μ m. **g.** Supernatants were collected from each cell line and analyzed by using ELISA to detect VEGF. **h.** Kaplan-Meier survival curves complement of **Figure 3i** where xenotransplanted mice with LDHA/B KO P3 spheroids were treated by bevacizumab. **i.** Kaplan-Meier survival curves of xenotransplanted mice with BL13 cells KO for LDHA/B (red) or control (blue) ($n = 10$ mice per group). Data are represented as mean \pm s.d **(b, c, e, g)**. n represents independent experiments. P values were calculated using Two-way ANOVA following by Tukey's multiple comparisons test.

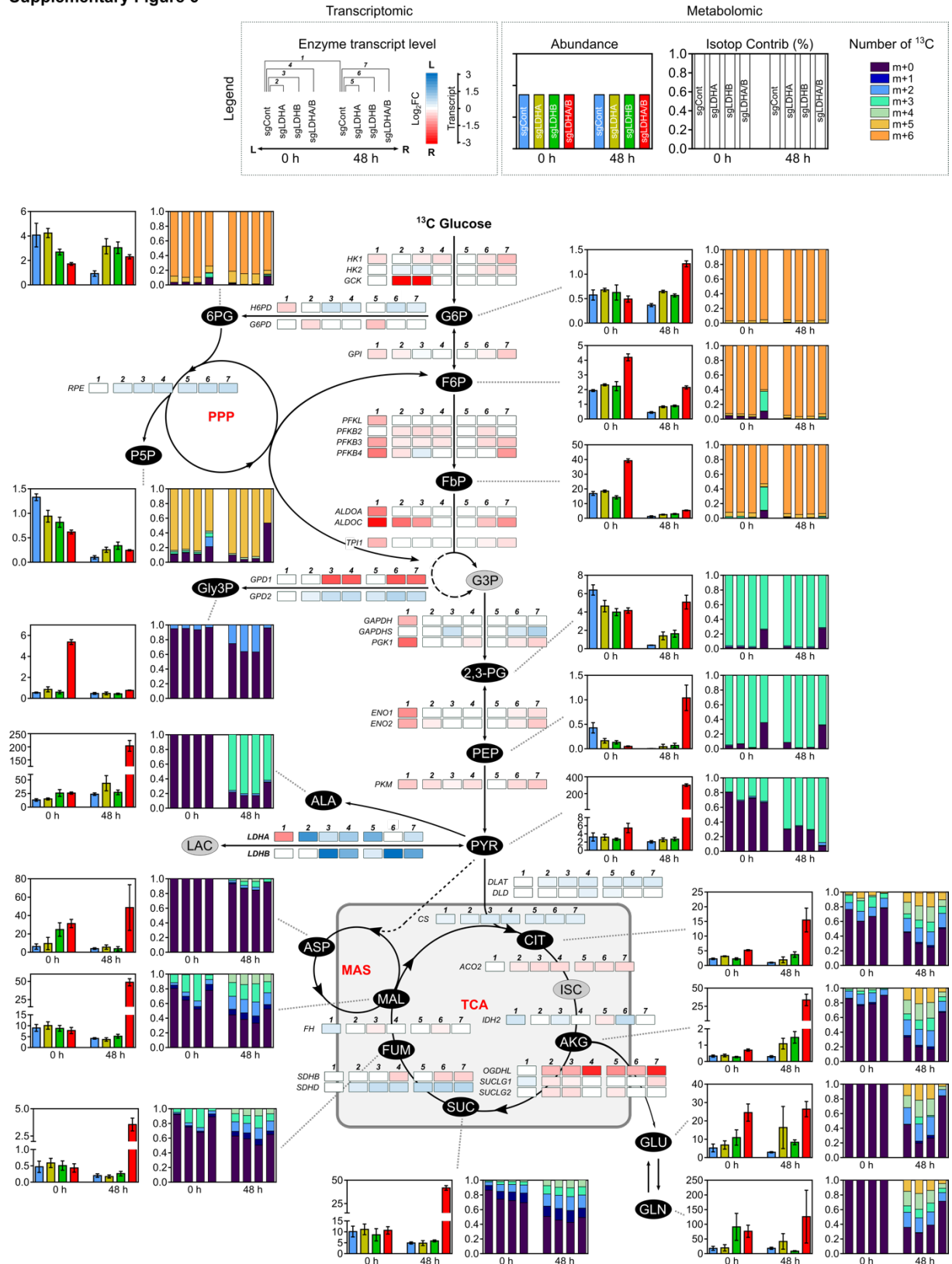
Supplementary Figure 5



Supplementary Figure 5: Detailed metabolograms

Circular metabologram illustrating metabolic and transcriptomic differences in metabolite pathways between LDH KO P3 cells. The metabologram is divided in two parts, the left corresponds to metabolomic analysis and the right to the transcriptomic analysis. The outer circle corresponds to the log₂ fold change for each metabolite (*left*) and transcripts (*right*). The central circle displays the average fold change of all analytes. Metabolites and gene names were added into these metabolograms.

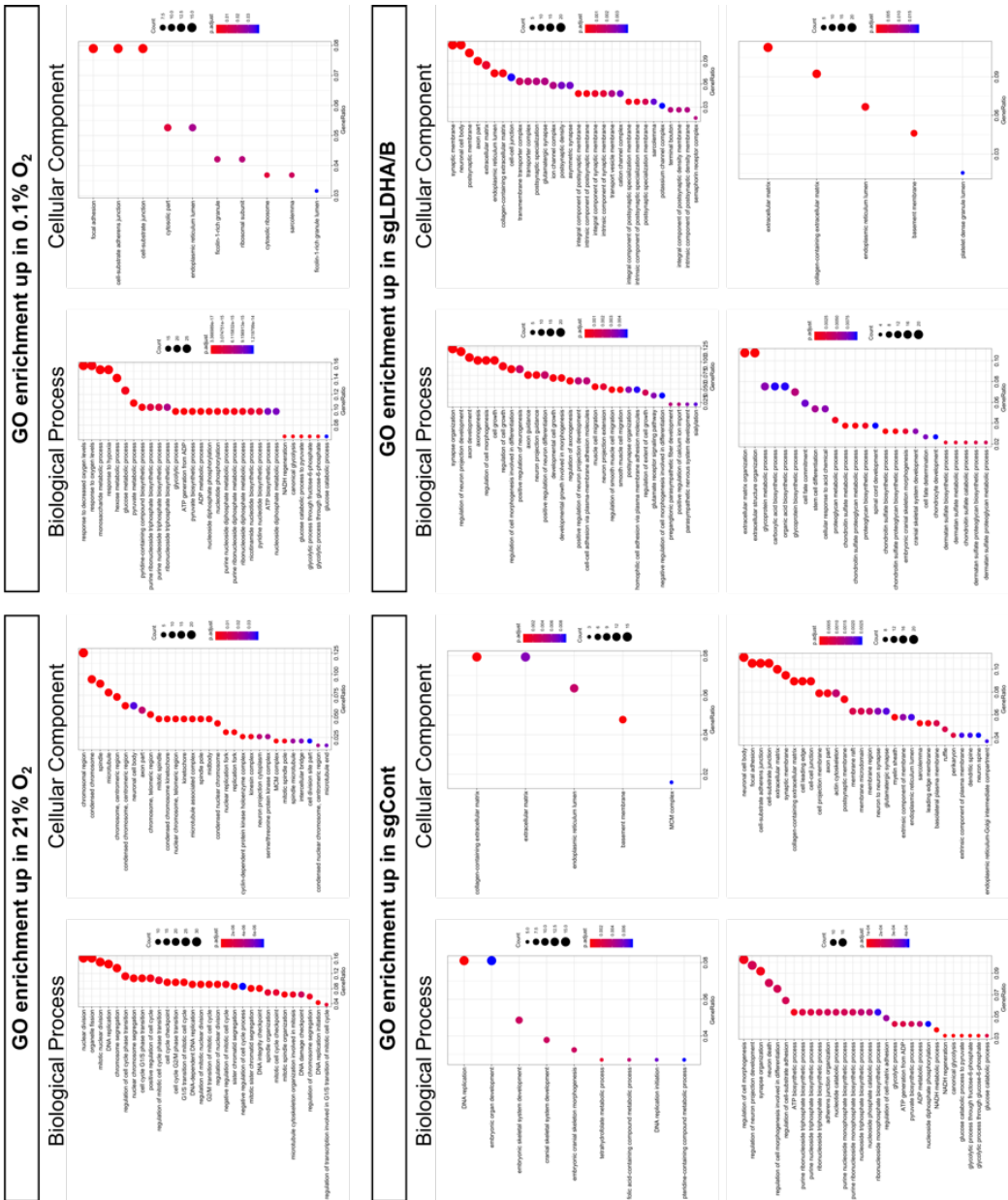
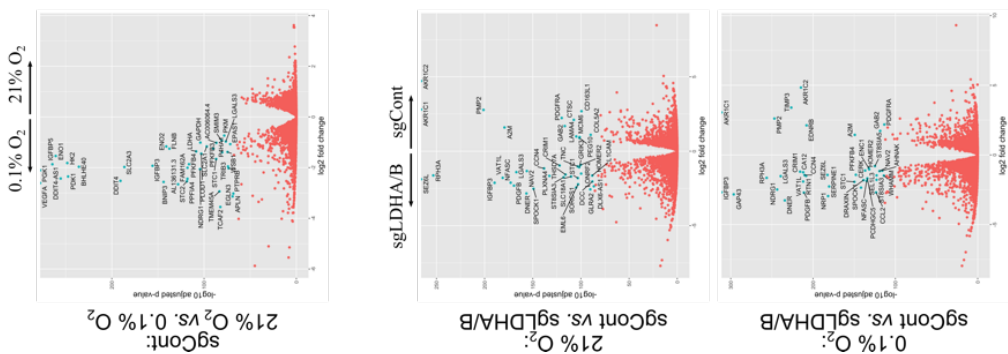
Supplementary Figure 6



Supplementary Figure 6: RNAseq/metabolomics profiles of P3 CRISPR adaptations to hypoxia or basal differences between P3 sgControl, P3 sgLDHA, P3 sgLDHB and P3 sgLDHA/B cells

P3 sgControl, sgLDHA, sgLDHB and sgLDHA/B were infused during 0, 24 and 48 h at 0.1% O₂ with [¹³C₆]glucose. Metabolites from cell extracts (endometabolome) or cell medium (exometabolome) measured by gas chromatography-mass spectrometry. Abundance and isotopolog contribution of all metabolite isotopes contribution of direct isotopes are showed. m+0 stands for the fraction of metabolite without ¹³Carbon and m+n (n > 0) stands for fraction of metabolite with n ¹³Carbon. For example, m+5 correspond to a metabolite with 5 labeled ¹³Carbon. The sum of (m+0, m+1,..., m+10,...) equals to 1. Enzyme transcripts with colored-square whose colour corresponds to the log₂ fold changes between two conditions : **1** : sgCont 0 h and sgCont 48 h, **2** : sgCont 0 h and sgLDHA 0 h, **3** : sgCont 0 h and sgLDHB 0 h, **4** : sgCont 0 h and sgLDHA/B 0 h, **5** : sgCont 48 h and sgLDHA 48 h, **6** : sgCont 48 h and sgLDHB 48 h, **7** : sgCont 48 h and sgLDHA/B 48 h.

Supplementary Figure 7



Supplementary Figure 7: Bioinformatics analysis based on RNAseq data from all cell lines

Left: Volcano plots for visualizing gene expression in described comparisons. Right: Enrichment analysis using Gene Ontology with filtered terms “biological process” and “cellular component”.

Supplemental Experimental Procedures

TCGA Glioblastoma cohort

The TCGA Glioblastoma (GBM) RNAseqV2 normalized data (level 3, $\log_2(x+1)$ transformed RSEM normalized count, version 2017-10-13), the associated clinical data and complementary clinical data from GDC pancan were downloaded from the xenabrowser website datapages (<https://xenabrowser.net/datapages/>).

For the genes LDHA and LDHB, primary tumor samples from the GBM cohort were split into three groups of equivalent size defined by the level of their expression. Overall survival (in months) was used to estimate survival distributions using the Kaplan–Meier method and the three distributions were compared using the log-rank test.

Ivy-GAP cohort

The expression of HIF1A, LDHA and LDHB were downloaded from the IVY-GAP website (<https://glioblastoma.alleninstitute.org/rnaseq/search/index.html>) with associated clinical data. Spearman correlation was computed between HIF1A and LDHA and between HIF1A and LDHB for all samples and for each anatomic structure separately.

RNA sequencing

- Sample preparations and RNA sequencing

P3 sgControl, sgLDHA, sgLDHB and sgLDHA/B were cultivated under 0.1% or 21% oxygen for 48h. Total RNA was extracted from fresh frozen cells with the Qiagen RNeasy Mini Kit according to the manufacturer's protocol. Quality and quantity of RNA was checked using a Fragment Analyzer (Agilent) with the company's Standard Sensitivity RNA Kit (DNF-471). Libraries were prepared using the TruSeq stranded mRNA Kit (Illumina). All barcoded samples were pooled and sequenced together in 75nt paired-end mode with an Illumina NextSeq500 in 2 runs to reach sufficient coverage. Runs were demultiplexed with bcl2fastq (v2.20.0.422, Illumina).

- Bioinformatics analysis

Quality of obtained fastq files was initially checked by FastQC v0.11.4² followed by adapter removal and quality trimming using Trim Galore v0.4.2. Mapping of reads to the human reference genome (GRCh38 Ensembl release 95) was done using STAR v2.5.3a with standard settings³ and duplicates were marked using Picard tools v1.141.

Quality analysis of mapped reads was done using RSeQC v3.0.0⁴ to analyze read distributions across gene bodies. Raw read counts per gene were determined by counting gene-specific reads in exons of protein-coding genes using FeatureCounts v1.5.3⁵. Finally, a gene expression data matrix was created by removing genes without any reads and lowly expressed genes (less than 1 read per million in more than 50% of samples) followed by cyclic loess normalization resulting in normalized log2-counts per million for 14,111 protein-coding genes that were measured in each sample.

The R package DESeq2⁶ v1.22.2 was used to identify differentially expressed genes. Enrichment analysis was performed using the ClusterProfiler⁷ R package v3.10.1. Gene Ontology (GO) terms enrichment analysis was visualized using Bubble Chart to Compare Annotations (BACA) using the p-value threshold at 0.01. Only GO terms from Biological Pathways level 5 were used for this analysis. GO terms were clustered to get annotation clusters with a similarity of genes greater than 0.85. PathView R package v.1.22.3 was used to visualize KEGG metabolic pathways.

Metabolomics Supplemental Method 1: [¹³C]₆ Glucose – ¹³C isotopic profiling

- Sample preparations

For cells in suspension (fast filtration method), 1 mL of cell culture are dropped on a filter (Sartolon Polyamide 0.2µm) in order to eliminate cultivation medium. The filter is then rinsed with washing solution, quickly removed from the filtration unit, putted on an aluminum foil and frozen in liquid nitrogen. Every filter is then extracted into a centrifuge tube containing the 5 mL of cold sampling solution (see table below). The centrifuge tubes are then vortexed and placed 1 hour at -20°C. After one hour, the tubes are centrifuged 5 min at 2000 g and the supernatant is putted in a new tube for evaporation.

| Types of metabolites | Sampling solution composition | Temperature of extraction | Duration of extraction | Evaporation | Solution of resuspension |
|---------------------------|--|---------------------------|------------------------|-------------|---|
| Central metabolites | ACN(4)/MeOH(4)/H ₂ Omq (2) 125 mM formic acid | -20°C | 1 h minimum | Speedvac | Water |
| Intracellular amino acids | ACN(4)/MeOH(4)/H ₂ Omq (2) 125 mM formic acid | -20°C | 1 h minimum | Speedvac | Water |
| Coenzyme A | ACN(4)/MeOH(4)/H ₂ Omq (2) 125 mM formic acid | -20°C | 1 h minimum | Speedvac | 2% methanol, 98% water, 25 mM formic acid, pH adjusted at 3.5 |

For cell supernatants, the sampling procedure is based on the separation of the cells from the medium thanks to the combination of filtration and centrifugation. This give access only to the exometabolome content for metabolomics or fluxomics studies. The supernatant can be stored at -80°C before shipment and analysis evaporated. Then samples are prepared either for NMR or MS analysis manually or automatically using a robotic station.

To control the quality of the analysis, blank samples are done for each type of samples (culture medium, conditions, treatment...). These blank samples are obtained from “cell-free” culture made in parallel and sampled in the same way and time as the culture with cells.

- Nuclear Magnetic Resonance (NMR) profiling

The acquisition of 1D 1H NMR Avance II 800MHz equipped with a 5mm CQPCI Z-Gradient cryoprobe. Following parameters were used for the acquisition: Pulse program: zgpr30; Pulse angle 30°; Time Domain (TD) 64k; Number of dummy scan: 4; Number of scan: 32; Acquisition time: 2.04 sec; Pulse P1 length: 7.70 µsec; Pulse P1 power: -12.39 dB; Pulse P9 power: 43.79 dB; Acquisition temperature: 280°K. Raw data obtained after acquisition are FID. A Fourier transform were applied for each spectrum with a specific smoothing (efp with LB = 0.3 and SI = 128K). Phase and baseline correction were also performed using automatic tools form TopSpin 3.5 software before the automatic integration of specific signals belonging to exometabolites present in the samples. Absolute quantification of metabolites of interest was performed using the internal standard TSP-d4 as reference. The quality of the analysis is based on the good resolution of the spectrum: width at half height for TSP-d4 signal < 2.5Hz.

- Liquid chromatography / Mass Spectrometry analysis

Central metabolites were separated on an ionic chromatography column IonPac AS11 (250 × 2 mm i.d.; Dionex, CA, USA). Solvent used was KOH at a flow rate of 350 µL/min. Solvent was varied as follows: 0 min: 2 %, 2 min: 2 %, 10 min: 5 %, 16 min: 35 %, 20 min: 100 % and 24 min: 100%. The column was then equilibrated for 6 min at the initial conditions before the next sample was analyzed. The volume of injection was 15 µL. High-resolution experiments were performed with an ICS5000+, ion chromatography system (Dionex, CA, USA) coupled to an LTQ Orbitrap Velos mass spectrometer (Thermo Fisher Scientific, Waltham, MA, USA) equipped with a heated electrospray ionization probe. MS analyses were performed in negative FTMS mode at a resolution of 60 000 (at 400 m/z) in full-scan mode, with the following source parameters: the capillary temperature was 350 °C, the source heater temperature, 300 °C, the sheath gas flow rate, 50 a.u. (arbitrary unit), the auxiliary gas flow rate, 5 a.u., the S-Lens RF level, 60 %, and the source voltage, 3.5 kV.

Amino acids were separated on a PFP column (150 × 2.1 mm i.d., particle size 5 µm; Supelco Bellefonte, PEN, USA). Solvent A was 0.1 % formic acid in H₂O and solvent B was 0.1 % formic acid in acetonitrile at a flow rate of 250 µL/min. Solvent B was varied as follows: 0 min: 2 %, 2 min: 2 %, 10 min: 5 %, 16 min: 35 %, 20 min: 100 % and 24 min: 100%. The column was then equilibrated for 6 min at the initial conditions before the next sample was analyzed. The volume of injection was 5 µL. High-resolution experiments were performed with a Vanquish HPLC system coupled to an Orbitrap Qexactive+ mass spectrometer (Thermo Fisher Scientific, Waltham, MA, USA) equipped with a heated electrospray ionization probe. MS analyses were performed in positive FTMS mode at a resolution of 70 000 (at 400 m/z) in full-scan mode, with the following source parameters: the capillary temperature was 320 °C, the source heater temperature, 300 °C, the sheath gas flow rate, 40 a.u. (arbitrary unit), the auxiliary gas flow rate, 10 a.u., the S-Lens RF level, 40 %, and the source voltage, 5 kV.

All the metabolites were determined by extracting the exact mass with a tolerance of 5 ppm. For central metabolites isotopic profile analysis and amino acids isotopic profile analysis, their concentrations have to be included in the dynamic range of the method, respectively. This range was determined during the method validation with the PA-PT sample and corresponds to the total area of the cluster / number of isotopologues with a bias of less than 5 %.

- Data Quality

Filters and supernatants were received on 03.04.19 and analyzed on 10.04.19 (MS) and 11.04.19 (NMR). All the acceptability criteria were satisfied, values meet MetaToul's acceptance as shown in the table below.

| | | Acceptability criteria |
|--|-----------------------------|------------------------|
| MS calibration \leq 7 days | Day of injection (11.04.19) | Passed |
| Bias on Pascal Triangle sample \leq 5% | PEP -1.4% max | Passed |
| | FruBP -2.5% max | Passed |
| | ATP 2.4% max | Passed |

- Data extraction and Quality

The data extraction of the raw mass spec data files yielded information that could be loaded into a relational database. Peaks were identified using IsoCor peak integration software⁸.

- Normalization

Data correction was performed to correct variation resulting from the difference of cell number into each condition. For abundance interpretation, sample P3 LDHA/B at 24 h and 48 h were 2-times concentrated.

Metabolomics Supplemental Method 2: [¹³C]₆ Lactate – ¹³C isotopic profiling

- Sample preparations

Metabolite extraction was performed using 80% methanol and 0.2% of myristic acid d27 (internal standard). After 5 minutes of incubation cells were scraped and collected in a new tube. Following a centrifugation at 20'000 G for 10 minutes at 4°C, the supernatant was transferred to a new vial for MS analysis. Pellet was used for protein quantification.

- Liquid chromatography / Mass Spectrometry analysis

10 μ l of each sample was loaded into a Dionex UltiMate 3000 LC System (Thermo Scientific Bremen, Germany) equipped with a C-18 column (Acquity UPLC -HSS T3 1.8 μ m; 2.1 x 150 mm, Waters) coupled to a Q Exactive Orbitrap mass spectrometer (Thermo Scientific) operating in negative ion mode. A step gradient was carried out using solvent A (10 mM TBA and 15 mM acetic acid) and solvent B (100% methanol). The gradient started with 0% of solvent B and 100% solvent A and remained at 0% B until 2 min post injection. A linear gradient

to 37% B was carried out until 7 min and increased to 41% until 14 min. Between 14 and 26 minutes the gradient increased to 100% of B and remained at 100% B for 4 minutes. At 30 min the gradient returned to 0% B. The chromatography was stopped at 40 min. The flow was kept constant at 250 μ L/min at the column was placed at 25°C throughout the analysis. The MS operated in full scan mode (m/z range: [70–1050]) using a spray voltage of 3.2 kV, capillary temperature of 320 °C, sheath gas at 10.0, auxiliary gas at 5.0. The AGC target was set at 3e6 using a resolution of 140.000, with a maximum IT fill time of 512ms. Data collection was performed using the Xcalibur software (Thermo Scientific). The data analyses were performed by integrating the peak areas (EI-Maven – Polly - Elucidata).

ELISA VEGF

Supernatants were collected from all cell lines and a VEGF Human ELISA Kit (Thermo Fisher) and procedure was followed based on manufacturer instructions.

Supplementary references

1. Darmanis, S. *et al.* Single-Cell RNA-Seq Analysis of Infiltrating Neoplastic Cells at the Migrating Front of Human Glioblastoma. *Cell Rep.* **21**, 1399–1410 (2017).
2. Wingett, S. W. & Andrews, S. FastQ Screen: A tool for multi-genome mapping and quality control. *F1000Research* **7**, 1338 (2018).
3. Dobin, A. *et al.* STAR: ultrafast universal RNA-seq aligner. *Bioinforma. Oxf. Engl.* **29**, 15–21 (2013).
4. Wang, L., Wang, S. & Li, W. RSeQC: quality control of RNA-seq experiments. *Bioinforma. Oxf. Engl.* **28**, 2184–2185 (2012).
5. Liao, Y., Smyth, G. K. & Shi, W. featureCounts: an efficient general purpose program for assigning sequence reads to genomic features. *Bioinforma. Oxf. Engl.* **30**, 923–930 (2014).
6. Hakimi, A. A. *et al.* An Integrated Metabolic Atlas of Clear Cell Renal Cell Carcinoma. *Cancer Cell* **29**, 104–116 (2016).
7. Yu, G., Wang, L.-G., Han, Y. & He, Q.-Y. clusterProfiler: an R Package for Comparing Biological Themes Among Gene Clusters. *OMICS J. Integr. Biol.* **16**, 284–287 (2012).
8. Millard, P., Letisse, F., Sokol, S. & Portais, J.-C. IsoCor: correcting MS data in isotope labeling experiments. *Bioinforma. Oxf. Engl.* **28**, 1294–1296 (2012).

4

Conclusion - Discussion

Les GBMs sont les tumeurs cérébrales les plus fréquentes chez l'adulte qui se caractérisent notamment par un fort métabolisme glycolytique et une infiltration diffuse dans le parenchyme cérébral. Leur prise en charge thérapeutique associant la chirurgie avec la radiothérapie et la chimiothérapie (8,9) a permis d'augmenter la médiane de survie des patients à 17 mois. Cependant, peu d'évolutions ont été effectuées depuis une quinzaine d'années. De plus, une récurrence proche de la cavité tumorale est invariablement observée dans les semaines suivant le traitement (9). Ceci serait principalement dû à la présence de CSCs qui aurait résisté à la radiothérapie et à la chimiothérapie (258). Lors de la rechute, il n'existe pas de recommandations établies. Le choix du traitement se décide en RCP en fonction de certains critères comme l'état général du patient, son âge ou de l'évolution de sa maladie. L'inclusion des patients en essais cliniques est privilégiée pour vérifier l'efficacité de nouvelles approches thérapeutiques. Les thérapies ciblées, comme l'inhibition de l'angiogenèse ou l'inhibition de la voie de signalisation de l'EGFR, ainsi que l'immunothérapie stimulant l'immunité à réponse cellulaire n'ont pas vraiment montré de bénéfice par rapport au traitement standard. Il apparaît donc évident que la clé d'un traitement efficace repose sur le fait de trouver de nouvelles cibles et des alternatives thérapeutiques.

4.1 Pertinence des modèles d'expérimentation

L'étude d'une tumeur se fait à plusieurs niveaux : *in vitro* avec les cultures cellulaires, *in vivo* chez le petit animal et *in situ* chez les patients lors des essais cliniques. Avant les essais chez l'homme, il est indispensable d'évaluer l'activité d'une molécule candidate chez l'animal compte tenu des risques non connus pouvant apparaître lors de son administration. La molécule est étudiée sur les plans pharmacologiques pour valider son mécanisme d'action, pharmacocinétique pour modéliser son devenir dans l'organisme et toxicologique pour établir ses doses toxiques. Bien que cette approche essaye de prédire les effets chez l'homme, son

recours tend à diminuer (259,260). Ainsi, des méthodes alternatives *in vitro* doivent être mises au point pour se rapprocher aux mieux de ce qui est observé *in vivo*. Les tests *in vitro* sont principalement réalisés en culture cellulaire et sont facilement adaptables selon le mécanisme étudié : prolifération, migration, invasion...

Le choix du modèle cellulaire est un élément crucial pour étudier les phénomènes tumoraux. D'un côté, les lignées établies qui sont cultivées en 2D dans un milieu supplémenté en sérum permettent d'étudier facilement et de manière reproductible les voies de signalisation mises en place par les cellules ou l'effet d'un traitement sur une population cellulaire peu hétérogène. Cependant, elles ne reproduisent pas l'architecture complexe d'une tumeur et faussent l'appréciation de l'effet pharmacologique d'un traitement, toutes les cellules étant exposées à la même concentration de la molécule. En outre, les cellules dérivent rapidement de leur génotype initial ce qui les éloigne de la représentation de la tumeur originale (261).

Un peu plus complexe à manipuler, les lignées dérivées de patients cultivées en 3D et sans sérum représentent un modèle tumoral plus pertinent. Elles conservent l'hétérogénéité et les caractéristiques tumorales comme la présence d'un cœur hypoxique, d'une zone de quiescence et de prolifération, des gradients d'échange de gaz et nutriments. Leur taille est maîtrisée pour éviter l'apparition d'un cœur nécrotique (< 400 μm de diamètre). Toutefois, elles ne miment pas spontanément la tumeur dans son environnement biologique complexe mais peuvent être insérées dans une matrice artificielle pour se rapprocher de cette situation. Le collagène est la protéine la plus abondante chez les mammifères (262). Il permet de fournir un hydrogel transparent qui sert d'ancrage aux cellules tumorales influençant peu la différenciation cellulaire (263). Ce modèle permet de distinguer le processus d'invasion, où les cellules émettent des protrusions et sécrètent des métalloprotéases digérant la matrice, du processus de migration où elles se déplacent par simple extension cytoplasmique (264). De plus, il est possible d'adapter la rigidité de la matrice en modulant la concentration du gel.

La volonté de cette partie était de développer un outil simple d'utilisation, reproductible, facilement analysable et ayant une meilleure prédiction thérapeutique. Pour améliorer le niveau de ressemblance de la complexité tumorale, les directions futures s'orientent vers l'implémentation de la matrice avec des cellules du microenvironnement telles que les cellules de la microglie, les cellules endothéliales vasculaires ou les neurones.

L'infiltration des GBMs le long des fibres nerveuses est un mode d'invasion très peu décrit dans la littérature à cause de la difficulté à trouver de bon modèles (265). Nous proposons un modèle simple, en cultivant des neurones de rat sur un recouvrement de laminine, sur lesquels sont déposés des cellules de GBMs. Il s'agit d'un système flexible pour analyser les échanges moléculaires entre GBM et neurones. Cette méthode peut également être applicable dans un hydrogel 3D sensible aux U.V. (266).

Les cellules de GBMs adhèrent sur les neurones en étendant leur surface cellulaire et augmentant leur points contacts et migrent efficacement, ce qui ne peut pas être observé sur un recouvrement de laminine (267). Cette attraction pour les neurones pourrait être partiellement expliquée par l'activation de la voie de signalisation Notch1/Sox2 (210) ou encore par la présence de facteurs sécrétés par les neurones. Il a récemment été montré que les cellules de GBMs forment des synapses avec les neurones permettant au glutamate sécrété par les neurones d'activer le récepteur AMPAR localisé sur les membranes des cellules de GBM (211).

Une des limites majeures de cette méthode est l'utilisation cellules provenant d'espèces différentes. Pour éviter la cross-réactivité entre les espèces, il est possible d'utiliser des neurones issus de cellules souches pluripotentes humaines (268) ou bien des nano-fibres pour étudier la migration (269). Cependant, ces dernières sont inertes et limitent les contacts cellule-cellule. Une autre stratégie consiste à utiliser des organoïdes complexes (mini cerveaux) et faire des cultures de confrontation pour évaluer le potentiel invasif des cellules de GBM (265,270).

En outre, ces modèles ne peuvent pas encore totalement se substituer aux expérimentations animales mais les approches biomimétiques pourraient réduire leur nombre en recherche biomédicale.

4.2 Étude de l'infiltration des GBMs

L'analyse protéomique sur des tumeurs dérivées de patient implantées dans des souris immunodéprimées a permis de décrypter les signatures moléculaires liées à l'invasion des GBMs. Le matériel des zones invasive et centrale de la tumeur a été obtenu *via* capture par microdissection laser. Pour renforcer la validité de cette analyse, nous avons sélectionné deux protéines fortement surexprimées dans la zone invasive et communes à trois animaux différents : la protéine protéolipide 1 (PLP1) et la dynamine 1 (DNM1).

PLP1 est un constituant structural de la gaine de myéline qui permet de maintenir l'intégrité axonale (271). Dans les gliomes, elle apparaît comme un marqueur de différenciation oligodendrocytaire (272) qui favorise l'adhésion cellulaire et la gliogenèse (273). Le marquage immunohistochimique a également appuyé la surexpression de PLP1 pour les cellules de GBMs situés dans les corps calleux. Dans cette étude, nous avons montré que son inhibition *in vitro* réduisait l'invasion des GBMs.

La même approche a été réalisée pour DNM1. Cette protéine est essentielle pour l'endocytose de vésicules synaptiques et nécessaire pour une forte activité neuronale (274). Une forte expression de DNM1 apparaît comme un marqueur de mauvais pronostic chez les patients atteints de GBM (275). Elle intervient aussi dans le processus de fission mitochondriale (276), qui, lorsqu'il est excessif, contribue au développement (277), permet la maintenance des cellules souches (278) et favorise la migration des GBMs (279). Dans notre étude, lorsque DNM1 est inhibée, l'invasion *in vitro* des cellules de GBM est réduite de manière dose dépendante.

L'analyse de l'expression des ARNs de PLP1 et de DNM1 dans la base IVYGap a montré que ces deux candidats sont régulés positivement dans la partie infiltrative (« infiltrative tumor ») et dans la bordure tumorale (« leading edge »). Ces zones ont été définies par des caractéristiques histologiques en évaluant le nombre de cellules tumorales par section.

A notre connaissance, cette étude est la première à montrer l'importance du rôle des protéines PLP1 et DNM1 dans les processus invasifs du GBM. Si ces résultats étaient répliqués, cela pourrait ouvrir de nouvelles perspectives de compréhension mécanistique et thérapeutique du GBM.

4.3 Blocage du métabolisme fermentatif des GBMs.

Les cancers solides reprogramment leur métabolisme pour maintenir leur prolifération, se déplacer et s'adapter à leur microenvironnement. Ces phénomènes jouent un rôle dans la progression tumorale. La glycolyse est la voie d'entrée principale du métabolisme énergétique des tumeurs. Elle est accrue dans les cancers et l'inhiber serait un moyen efficace de réduire l'agressivité des GBMs. Notre étude identifie le lactate comme l'un des principaux facteurs métaboliques à travers l'activité des deux enzymes LDHA et LDHB pour favoriser le développement et l'invasion des GBMs.

L'analyse histologique de la tumeur *in vivo* corrobore avec celle du sphéroïde invasif où LDHA apparait plus exprimée dans les zones centrales hypoxiques et LDHB en périphérie. Cette configuration d'expression est renforcée avec les données de transcriptomique issue du projet IVYGap (280). Ces résultats démontrent que la distribution spatiale de LDHA et LDHB fait écho à l'expression des transporteurs de lactate MCT1 et MCT4 (281), supportant l'hypothèse de la navette lactate entre les cellules, comme celle décrite entre les astrocytes et les neurones (132).

L'approche métabolomique où le [$^{13}\text{C}_3$]lactate est infusé dans les cellules montre que celui-ci est utilisé comme source carbonée pour alimenter le TCA, produire de l'énergie et favoriser l'invasion des GBMs. Il est rapidement converti en pyruvate qui a trois devenir possibles : (1) être décarboxylé en acétyl-CoA pour être oxydé dans le TCA, (2) être transaminé en alanine pour les réactions d'anaplérose ou (3) être directement sécrété (**Figure 18**). Le TCA joue un rôle central dans le métabolisme énergétique à travers l'oxydation des métabolites, il possède aussi des fonctions dans les voies de biosynthèse (282). Comme il ne peut pas oxyder complètement tous les intermédiaires, ils sont retirés du cycle et principalement sécrétés sous la forme de glutamine et d'asparagine (**Figure 18**). Le lactate exogène est une source importante pour la biosynthèse des acides gras (283,284).

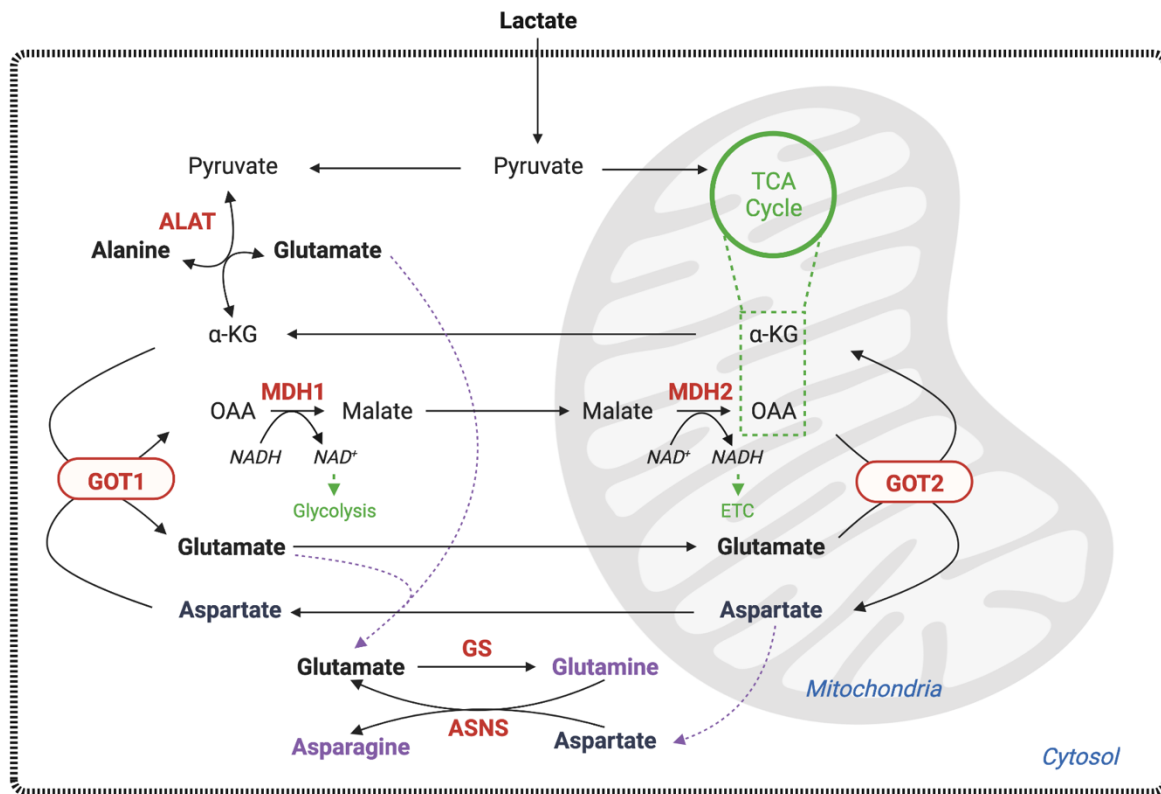


Figure 18 : Voie du métabolisme du lactate

Représentation du métabolisme du lactate dans une CSC. Le lactate pénètre dans la cellule et est converti en pyruvate. Le pyruvate peut entrer dans la mitochondrie pour alimenter le TCA ou il peut être transformé en alanine *via* l’alanine transaminase (ALAT). Les métabolites générés en aval sont impliqués dans la navette malate-aspartate permettant le transfert net d’électron à travers la membrane mitochondriale. Les métabolites ne pouvant plus être oxydés par la mitochondrie sont transformés en glutamine ou en asparagine. ASNS, asparagine synthétase ; GOT, glutamate oxaloacétate transaminase ; GS, glutamine synthase ; MDH, malate deshydrogénase.

Comme les deux LDHs sont capables de catalyser la réaction de conversion du pyruvate et lactate dans les deux sens, seule la double extinction de LDHA/B réduit efficacement la prolifération et l’invasion des GBMs. Elle est également liée à une augmentation de l’apoptose, réduisant la masse tumorale et améliorant le temps de survie des souris. La seule autre étude utilisant une double extinction de LDHA/B montre aussi que la double perte d’expression compromet peu la croissance des mélanomes et des adénocarcinomes du colon (187). Les cellules de GBM évoluent dans un microenvironnement différent des cellules de mélanome ou d’adénocarcinomes et, par conséquent les régulations métaboliques pendant la croissance tumorale peuvent être différentes.

L’accumulation et l’excrétion de métabolites incomplètement catabolisés peut refléter un métabolisme hyperactif ou un blocage des voies essentielles (285). Le meilleur exemple est celui de l’effet Warburg où le fort taux de glycolyse entraîne un excès de pyruvate qui ne peut

être entièrement oxydé dans la mitochondrie, il en résulte une production importante de lactate et est directement sécrété par la cellule. Les cellules KO pour LDHA/B ont perdu leurs enzymes ayant un rôle majeur dans le maintien du rédox sous des conditions hypoxiques. Elles consomment moins de glucose et il y a une accumulation de la majorité des intermédiaires de la glycolyse et du TCA avec l'excrétion de formate et d'acétate. La sécrétion de formate proviendrait d'une augmentation du catabolisme de la sérine, témoin de l'activité oxydative des cellules et favorisant l'invasion *in vitro* des GBMs (285). Il est possible que la production d'acétate à partir du pyruvate (*via* l'acétyl-CoA) soit réalisé pour maintenir le potentiel rédox (286). A l'instar du lactate, l'acétate peut être utilisé comme source énergétique quand les conditions d'oxygénation redeviennent normales (287). Les cellules KO pour LDHA/B augmentent l'expression de leurs complexes respiratoires pour compenser le stress métabolique dans les conditions extrêmes d'hypoxie. La phenformine, inhibiteur du complexe 1, a été utilisée pour augmenter l'apoptose des cellules KO pour LDHA/B. Ce traitement n'a pas réussi à augmenter l'apoptose de cette lignée, ce qui est possiblement dû à une compensation par un autre complexe respiratoire. Par contre, les tumeurs contrôles ont été sensibles au traitement à la phenformine comme le suggèrent d'autres études (288). En effet, après irradiation crâniale, une très forte augmentation de la survie a été observée dans le groupe contrôle.

Dans une étude récente, l'utilisation d'antiépileptiques semblent être prometteuse pour les patients atteints de GBM (289). Nous avons choisi d'utiliser le stiripentol, déjà approuvé par les agences du médicament, car il inhibe l'activité de LDHA et LDHB (290). Nous avons montré qu'il est aussi capable d'inhiber la croissance et l'invasion *in vitro* des GBMs. En combinaison avec le bevacizumab, il augmente la survie des souris, en réduisant notamment l'invasion des cellules tumorales dans le parenchyme cérébral.

Dans cette étude, nous avons réalisé une analyse détaillée des conséquences métaboliques de la délétion des LDHs et démontré que seule la double extinction de LDHA et LDHB est requise pour ralentir le développement tumoral. Cependant, le stiripentol seul n'a pas réussi à obtenir un effet similaire à l'extinction génétique totale des LDHs. Pour se rapprocher de la clinique, une autre stratégie basée sur le protocole de Stupp sans résection chez la souris est en cours. Elle consiste à administrer le stiripentol juste avant l'irradiation

dans le but d'augmenter l'efficacité de cette dernière. La diminution de production de lactate devrait induire une augmentation de la sensibilité aux espèces réactives à l'oxygène.

En outre, la recherche de nouvelles molécules candidates est aussi nécessaire puisque le blocage de la fermentation lactique représente une cible intéressante. Ces molécules doivent pouvoir passer la BHE et inhiber les deux LDHs à la fois. Cependant, il est indispensable de se rappeler que l'inhibition des LDHs peut avoir un impact sur les cellules saines à l'origine d'effets indésirables, qui resteront à évaluer.

4.4 Conclusion générale

L'échec des thérapies conventionnelles et ciblées est généralement attribué à l'hétérogénéité moléculaire intratumorale omniprésente du GBM, qui se produit aux niveaux génétique, épigénétique, transcriptionnel et fonctionnel. La prise en charge des tumeurs s'oriente de plus en plus vers une approche personnalisée et donc adaptée aux caractéristiques de celles-ci.

Dans ce travail de thèse, nous avons établi un système standardisé d'extraction et de culture de lignées de GBM, véritables avatars des patients. Nous avons proposé des méthodes simples et reproductibles pour étudier les phénomènes de croissance et d'invasion tridimensionnelle. Nous avons également développé des outils informatiques pour faciliter l'analyse et réduire le temps de quantification. Nous avons mis au point une toute nouvelle technique histologique permettant de réaliser des coupes coronales de sphéroïdes invasif dans une matrice de collagène.

L'approche protéomique a mis en évidence le rôle *in vivo* de certaines protéines impliquées dans les processus invasifs et leur ciblage *in vitro* a permis de le confirmer.

Le ciblage du métabolisme, moteur énergétique de la cellule, est une stratégie prometteuse. L'étude du métabolisme en utilisant des composés marqués au carbone 13 ont souligné l'importance des voies biochimiques dans les processus tumoraux et mis en évidence les adaptations cellulaires lorsque certaines voies étaient bloquées. Ceci permet de mieux comprendre la plasticité métabolique des cellules à l'origine de la résistance et de la survie des GBMs pour ouvrir de nouvelles voies thérapeutiques.

Associer toutes les données d'analyse permettrait d'avoir un point de vue global pour prédire le comportement des tumeurs et d'en dégager ses vulnérabilités.

Bibliographie

1. Rothschild BM, Tanke DH, Helbling M, Martin LD. Epidemiologic study of tumors in dinosaurs. *Naturwissenschaften*. 1 nov 2003;90(11):495-500.
2. Ekhtiari S, Chiba K, Popovic S, Crowther R, Wohl G, Wong AKO, et al. First case of osteosarcoma in a dinosaur: a multimodal diagnosis. *The Lancet Oncology*. 1 août 2020;21(8):1021-2.
3. Aktipis CA, Boddy AM, Jansen G, Hibner U, Hochberg ME, Maley CC, et al. Cancer across the tree of life: cooperation and cheating in multicellularity. *Philos Trans R Soc Lond B Biol Sci*. 19 juill 2015;370(1673):20140219.
4. Albuquerque TAF, Val LD do, Doherty A, Magalhães JP de. From humans to hydra: patterns of cancer across the tree of life. *Biological Reviews*. 2018;93(3):1715-34.
5. Lorenzo FR, Huff C, Myllymäki M, Olenchock B, Swierczek S, Tashi T, et al. A genetic mechanism for Tibetan high-altitude adaptation. *Nat Genet*. sept 2014;46(9):951-6.
6. Ferlay J, Colombet M, Soerjomataram I, Parkin DM, Piñeros M, Znaor A, et al. Cancer statistics for the year 2020: An overview. *Int J Cancer*. 5 avr 2021;
7. Ah-Pine F, Rousseau A. Tumeurs primitives du système nerveux central - Classifications histologique et topographique, et épidémiologie. 17 déc 2018; Disponible sur: [http://dx.doi.org/10.1016/S0246-0378\(18\)83172-4](http://dx.doi.org/10.1016/S0246-0378(18)83172-4)
8. Stupp R, Mason WP, van den Bent MJ, Weller M, Fisher B, Taphoorn MJB, et al. Radiotherapy plus concomitant and adjuvant temozolomide for glioblastoma. *N Engl J Med*. 10 mars 2005;352(10):987-96.
9. Stupp R, Hegi ME, Mason WP, van den Bent MJ, Taphoorn MJB, Janzer RC, et al. Effects of radiotherapy with concomitant and adjuvant temozolomide versus radiotherapy alone on survival in glioblastoma in a randomised phase III study: 5-year analysis of the EORTC-NCIC trial. *Lancet Oncol*. mai 2009;10(5):459-66.
10. Ostrom QT, Cioffi G, Gittleman H, Patil N, Waite K, Kruchko C, et al. CBTRUS Statistical Report: Primary Brain and Other Central Nervous System Tumors Diagnosed in the United States in 2012–2016. *Neuro Oncol*. nov 2019;21(Suppl 5):v1-100.
11. Système nerveux central [Internet]. Institut National du Cancer. 2020 [cité 15 sept 2021]. Disponible sur: <https://www.e-cancer.fr/Expertises-et-publications/Les-donnees-sur-les-cancers/Survie-des-personnes-atteintes-de-cancer-en-France-metropolitaine/Tumeurs-solides/Systeme-nerveux-central>
12. Baldi I, Huchet A, Bauchet L, Loiseau H. Epidemiology of glioblastoma. *Neurochirurgie*. déc 2010;56(6):433-40.
13. Zouaoui S, Rigau V, Mathieu-Daudé H, Darlix A, Bessaoud F, Fabbro-Peray P, et al. Recensement national histologique des tumeurs primitives du système nerveux central : résultats généraux sur 40 000 cas, principales applications actuelles et perspectives. *Neurochirurgie*. 1 févr 2012;58(1):4-13.
14. Louis DN, Ohgaki H, Wiestler OD, Cavenee WK, Burger PC, Jouvet A, et al. The 2007 WHO Classification of Tumours of the Central Nervous System. *Acta Neuropathol*. août 2007;114(2):97-109.
15. Louis DN, Perry A, Reifenberger G, von Deimling A, Figarella-Branger D, Cavenee WK,

- et al. The 2016 World Health Organization Classification of Tumors of the Central Nervous System: a summary. *Acta Neuropathol.* juin 2016;131(6):803-20.
16. Yan H, Parsons DW, Jin G, McLendon R, Rasheed BA, Yuan W, et al. IDH1 and IDH2 mutations in gliomas. *N Engl J Med.* 19 févr 2009;360(8):765-73.
 17. Xu X, Zhao J, Xu Z, Peng B, Huang Q, Arnold E, et al. Structures of human cytosolic NADP-dependent isocitrate dehydrogenase reveal a novel self-regulatory mechanism of activity. *J Biol Chem.* 6 août 2004;279(32):33946-57.
 18. Dang L, White DW, Gross S, Bennett BD, Bittinger MA, Driggers EM, et al. Cancer-associated IDH1 mutations produce 2-hydroxyglutarate. *Nature.* 10 déc 2009;462(7274):739-44.
 19. Grassian AR, Parker SJ, Davidson SM, Divakaruni AS, Green CR, Zhang X, et al. IDH1 mutations alter citric acid cycle metabolism and increase dependence on oxidative mitochondrial metabolism. *Cancer Res.* 15 juin 2014;74(12):3317-31.
 20. Parsons DW, Jones S, Zhang X, Lin JC-H, Leary RJ, Angenendt P, et al. An integrated genomic analysis of human glioblastoma multiforme. *Science.* 26 sept 2008;321(5897):1807-12.
 21. Mizoguchi M, Yoshimoto K, Ma X, Guan Y, Hata N, Amano T, et al. Molecular characteristics of glioblastoma with 1p/19q co-deletion. *Brain Tumor Pathol.* juill 2012;29(3):148-53.
 22. Smith JS, Perry A, Borell TJ, Lee HK, O'Fallon J, Hosek SM, et al. Alterations of chromosome arms 1p and 19q as predictors of survival in oligodendrogliomas, astrocytomas, and mixed oligoastrocytomas. *J Clin Oncol.* févr 2000;18(3):636-45.
 23. Kasthuber ER, Lowe SW. Putting p53 in Context. *Cell.* 7 sept 2017;170(6):1062-78.
 24. Watanabe K, Sato K, Biernat W, Tachibana O, Ammon K von, Ogata N, et al. Incidence and timing of p53 mutations during astrocytoma progression in patients with multiple biopsies. *Clin Cancer Res.* 1 avr 1997;3(4):523-30.
 25. Killela PJ, Reitman ZJ, Jiao Y, Bettegowda C, Agrawal N, Diaz LA, et al. TERT promoter mutations occur frequently in gliomas and a subset of tumors derived from cells with low rates of self-renewal. *PNAS.* 9 avr 2013;110(15):6021-6.
 26. Heaphy CM, de Wilde RF, Jiao Y, Klein AP, Edil BH, Shi C, et al. Altered telomeres in tumors with ATRX and DAXX mutations. *Science.* 22 juill 2011;333(6041):425.
 27. Mackay A, Burford A, Carvalho D, Izquierdo E, Fazal-Salom J, Taylor KR, et al. Integrated Molecular Meta-Analysis of 1,000 Pediatric High-Grade and Diffuse Intrinsic Pontine Glioma. *Cancer Cell.* 9 oct 2017;32(4):520-537.e5.
 28. Esteller M, Garcia-Foncillas J, Andion E, Goodman SN, Hidalgo OF, Vanaclocha V, et al. Inactivation of the DNA-repair gene MGMT and the clinical response of gliomas to alkylating agents. *N Engl J Med.* 9 nov 2000;343(19):1350-4.
 29. Hegi ME, Diserens A-C, Gorlia T, Hamou M-F, de Tribolet N, Weller M, et al. MGMT gene silencing and benefit from temozolomide in glioblastoma. *N Engl J Med.* 10 mars 2005;352(10):997-1003.
 30. Quillien V, Lavenu A, Karayan-Tapon L, Carpentier C, Labussière M, Lesimple T, et al. Comparative assessment of 5 methods (methylation-specific polymerase chain reaction, methylight, pyrosequencing, methylation-sensitive high-resolution melting, and

- immunohistochemistry) to analyze O6-methylguanine-DNA-methyltransferase in a series of 100 glioblastoma patients. *Cancer*. 2012;118(17):4201-11.
31. Brennan CW, Verhaak RGW, McKenna A, Campos B, Noushmehr H, Salama SR, et al. The Somatic Genomic Landscape of Glioblastoma. *Cell*. 10 oct 2013;155(2):462-77.
 32. Alexandru O, Purcaru SO, Tataranu LG, Lucan L, Castro J, Folcuți C, et al. The Influence of EGFR Inactivation on the Radiation Response in High Grade Glioma. *Int J Mol Sci*. 12 janv 2018;19(1):229.
 33. Felsberg J, Hentschel B, Kaulich K, Gramatzki D, Zacher A, Malzkorn B, et al. Epidermal Growth Factor Receptor Variant III (EGFRvIII) Positivity in EGFR-Amplified Glioblastomas: Prognostic Role and Comparison between Primary and Recurrent Tumors. *Clin Cancer Res*. 15 nov 2017;23(22):6846-55.
 34. Fontanilles M, Marguet F, Ruminy P, Basset C, Noel A, Beaussire L, et al. Simultaneous detection of EGFR amplification and EGFRvIII variant using digital PCR-based method in glioblastoma. *Acta Neuropathologica Communications*. 17 avr 2020;8(1):52.
 35. van den Bent MJ, Weller M, Wen PY, Kros JM, Aldape K, Chang S. A clinical perspective on the 2016 WHO brain tumor classification and routine molecular diagnostics. *Neuro Oncol*. 1 mai 2017;19(5):614-24.
 36. Louis DN, Perry A, Wesseling P, Brat DJ, Cree IA, Figarella-Branger D, et al. The 2021 WHO Classification of Tumors of the Central Nervous System: a summary. *Neuro Oncol*. 2 août 2021;23(8):1231-51.
 37. Wen PY, Packer RJ. The 2021 WHO Classification of Tumors of the Central Nervous System: clinical implications. *Neuro-Oncology*. 1 août 2021;23(8):1215-7.
 38. Ohgaki H, Kleihues P. The Definition of Primary and Secondary Glioblastoma. *Clin Cancer Res*. 15 févr 2013;19(4):764-72.
 39. Wen PY, Weller M, Lee EQ, Alexander BM, Barnholtz-Sloan JS, Barthel FP, et al. Glioblastoma in adults: a Society for Neuro-Oncology (SNO) and European Society of Neuro-Oncology (EANO) consensus review on current management and future directions. *Neuro Oncol*. août 2020;22(8):1073-113.
 40. Neftel C, Laffy J, Filbin MG, Hara T, Shore ME, Rahme GJ, et al. An Integrative Model of Cellular States, Plasticity, and Genetics for Glioblastoma. *Cell*. 8 août 2019;178(4):835-849.e21.
 41. Venteicher AS, Tirosh I, Hebert C, Yizhak K, Neftel C, Filbin MG, et al. Decoupling genetics, lineages, and microenvironment in IDH-mutant gliomas by single-cell RNA-seq. *Science*. 31 mars 2017;355(6332):eaai8478.
 42. Couturier CP, Ayyadhury S, Le PU, Nadaf J, Monlong J, Riva G, et al. Single-cell RNA-seq reveals that glioblastoma recapitulates a normal neurodevelopmental hierarchy. *Nat Commun*. 8 juill 2020;11(1):3406.
 43. Chow LML, Endersby R, Zhu X, Rankin S, Qu C, Zhang J, et al. Cooperativity within and among Pten, p53, and Rb Pathways Induces High-Grade Astrocytoma in Adult Brain. *Cancer Cell*. 8 mars 2011;19(3):305-16.
 44. Moon J-H, Kwon S, Jun EK, Kim A, Whang KY, Kim H, et al. Nanog-induced dedifferentiation of p53-deficient mouse astrocytes into brain cancer stem-like cells. *Biochem Biophys Res Commun*. 19 août 2011;412(1):175-81.
 45. Jiang Y, Marinescu VD, Xie Y, Jarvis M, Maturi NP, Haglund C, et al. Glioblastoma

- Cell Malignancy and Drug Sensitivity Are Affected by the Cell of Origin. *Cell Reports*. 24 janv 2017;18(4):977-90.
46. Sadetzki S, Chetrit A, Freedman L, Stovall M, Modan B, Novikov I. Long-term follow-up for brain tumor development after childhood exposure to ionizing radiation for tinea capitis. *Radiat Res*. avr 2005;163(4):424-32.
 47. Smoll NR, Brady Z, Scurrah K, Mathews JD. Exposure to ionizing radiation and brain cancer incidence: The Life Span Study cohort. *Cancer Epidemiology*. 1 juin 2016;42:60-5.
 48. Farrell CJ, Plotkin SR. Genetic Causes of Brain Tumors: Neurofibromatosis, Tuberous Sclerosis, von Hippel-Lindau, and Other Syndromes. *Neurologic Clinics*. 1 nov 2007;25(4):925-46.
 49. Blumenthal DT, Cannon-Albright LA. Familiality in brain tumors. *Neurology*. 23 sept 2008;71(13):1015-20.
 50. Schlehofer B, Hettinger I, Ryan P, Blettner M, Preston-Martin S, Little J, et al. Occupational risk factors for low grade and high grade glioma: results from an international case control study of adult brain tumours. *Int J Cancer*. 1 janv 2005;113(1):116-25.
 51. Dubrow R, Darefsky AS, Park Y, Mayne ST, Moore SC, Kilfoy B, et al. Dietary Components Related to N-Nitroso Compound Formation: A Prospective Study of Adult Glioma. *Cancer Epidemiol Biomarkers Prev*. 1 juill 2010;19(7):1709-22.
 52. Piel C, Pouchieu C, Migault L, Béziat B, Boulanger M, Bureau M, et al. Increased risk of central nervous system tumours with carbamate insecticide use in the prospective cohort AGRICAN. *International Journal of Epidemiology*. 1 avr 2019;48(2):512-26.
 53. Dürst M, Gissmann L, Ikenberg H, zur Hausen H. A papillomavirus DNA from a cervical carcinoma and its prevalence in cancer biopsy samples from different geographic regions. *Proc Natl Acad Sci U S A*. juin 1983;80(12):3812-5.
 54. Marshall BJ, Warren JR. Unidentified curved bacilli in the stomach of patients with gastritis and peptic ulceration. *Lancet*. 16 juin 1984;1(8390):1311-5.
 55. Moore PS, Chang Y. Why do viruses cause cancer? Highlights of the first century of human tumour virology. *Nat Rev Cancer*. déc 2010;10(12):878-89.
 56. Cobbs CS, Harkins L, Samanta M, Gillespie GY, Bharara S, King PH, et al. Human cytomegalovirus infection and expression in human malignant glioma. *Cancer Res*. 15 juin 2002;62(12):3347-50.
 57. Akhtar S, Vranic S, Cyprian FS, Al Moustafa A-E. Epstein–Barr Virus in Gliomas: Cause, Association, or Artifact? *Front Oncol*. 20 avr 2018;8:123.
 58. Rahman M, Dastmalchi F, Karachi A, Mitchell D. The role of CMV in glioblastoma and implications for immunotherapeutic strategies. *Oncoimmunology*. 16 oct 2018;8(1):e1514921.
 59. Nehme Z, Pasquereau S, Haidar Ahmad S, Coaquette A, Molimard C, Monnien F, et al. Polyploid giant cancer cells, stemness and epithelial-mesenchymal plasticity elicited by human cytomegalovirus. *Oncogene*. avr 2021;40(17):3030-46.
 60. Singh SK, Hawkins C, Clarke ID, Squire JA, Bayani J, Hide T, et al. Identification of human brain tumour initiating cells. *Nature*. 18 nov 2004;432(7015):396-401.

61. Gangemi RMR, Griffero F, Marubbi D, Perera M, Capra MC, Malatesta P, et al. SOX2 silencing in glioblastoma tumor-initiating cells causes stop of proliferation and loss of tumorigenicity. *Stem Cells*. janv 2009;27(1):40-8.
62. Boyer LA, Lee TI, Cole MF, Johnstone SE, Levine SS, Zucker JP, et al. Core transcriptional regulatory circuitry in human embryonic stem cells. *Cell*. 23 sept 2005;122(6):947-56.
63. Lendahl U, Zimmerman LB, McKay RD. CNS stem cells express a new class of intermediate filament protein. *Cell*. 23 févr 1990;60(4):585-95.
64. Ishiwata T, Teduka K, Yamamoto T, Kawahara K, Matsuda Y, Naito Z. Neuroepithelial stem cell marker nestin regulates the migration, invasion and growth of human gliomas. *Oncology Reports*. 1 juill 2011;26(1):91-9.
65. Saleem H, Kulsoom Abdul U, Küçükosmanoglu A, Houweling M, Cornelissen FMG, Heiland DH, et al. The TICking clock of EGFR therapy resistance in glioblastoma: Target Independence or target Compensation. *Drug Resistance Updates*. 1 mars 2019;43:29-37.
66. Edition S. ANOCEF - Association des Neuro-Oncologue d'Expression Française [Internet]. [cité 18 sept 2021]. Disponible sur: <https://www.anocef.org/>
67. Sanai N, Polley M-Y, McDermott MW, Parsa AT, Berger MS. An extent of resection threshold for newly diagnosed glioblastomas. *J Neurosurg*. juill 2011;115(1):3-8.
68. Sahm F, Capper D, Jeibmann A, Habel A, Paulus W, Troost D, et al. Addressing diffuse glioma as a systemic brain disease with single-cell analysis. *Arch Neurol*. avr 2012;69(4):523-6.
69. Seystahl K, Wick W, Weller M. Therapeutic options in recurrent glioblastoma—An update. *Critical Reviews in Oncology/Hematology*. 1 mars 2016;99:389-408.
70. Djamel-Eddine Y-C, De Witte O, Mélot C, Lefranc F. Recurrent glioblastomas: Should we operate a second and even a third time? *Interdisciplinary Neurosurgery*. 1 déc 2019;18:100551.
71. Minniti G, Niyazi M, Alongi F, Navarria P, Belka C. Current status and recent advances in reirradiation of glioblastoma. *Radiation Oncology*. 18 févr 2021;16(1):36.
72. McBain C, Lawrie TA, Rogozińska E, Kernohan A, Robinson T, Jefferies S. Treatment options for progression or recurrence of glioblastoma: a network meta-analysis. *Cochrane Database of Systematic Reviews* [Internet]. 2021 [cité 19 sept 2021];(1). Disponible sur: <https://www.cochranelibrary.com/cdsr/doi/10.1002/14651858.CD013579.pub2/full>
73. Westphal M, Hilt DC, Bortey E, Delavault P, Olivares R, Warnke PC, et al. A phase 3 trial of local chemotherapy with biodegradable carmustine (BCNU) wafers (Gliadel wafers) in patients with primary malignant glioma. *Neuro Oncol*. avr 2003;5(2):79-88.
74. Sage W, Guilfoyle M, Luney C, Young A, Sinha R, Sgubin D, et al. Local alkylating chemotherapy applied immediately after 5-ALA guided resection of glioblastoma does not provide additional benefit. *J Neurooncol*. janv 2018;136(2):273-80.
75. Alexander BM, Cloughesy TF. Adult Glioblastoma. *J Clin Oncol*. 20 juill 2017;35(21):2402-9.
76. Arvanitis CD, Ferraro GB, Jain RK. The blood-brain barrier and blood-tumour barrier in brain tumours and metastases. *Nat Rev Cancer*. janv 2020;20(1):26-41.
77. Guyon J. Sécurité cardiovasculaire des médicaments anticancéreux agissant sur

- l'angiogenèse [Internet] [exercice]. Université Toulouse III - Paul Sabatier; 2019 [cité 27 oct 2021]. Disponible sur: <http://thesesante.ups-tlse.fr/3485/>
78. Risau W. Mechanisms of angiogenesis. *Nature*. 17 avr 1997;386(6626):671-4.
 79. Folkman J. Tumor angiogenesis: therapeutic implications. *N Engl J Med*. 18 nov 1971;285(21):1182-6.
 80. Fox SB, Gasparini G, Harris AL. Angiogenesis: pathological, prognostic, and growth-factor pathways and their link to trial design and anticancer drugs. *Lancet Oncol*. mai 2001;2(5):278-89.
 81. Chinot OL, Wick W, Mason W, Henriksson R, Saran F, Nishikawa R, et al. Bevacizumab plus Radiotherapy–Temozolomide for Newly Diagnosed Glioblastoma. *New England Journal of Medicine*. 20 févr 2014;370(8):709-22.
 82. Gilbert MR, Dignam JJ, Armstrong TS, Wefel JS, Blumenthal DT, Vogelbaum MA, et al. A randomized trial of bevacizumab for newly diagnosed glioblastoma. *N Engl J Med*. 20 févr 2014;370(8):699-708.
 83. Wick W, Gorlia T, Bendszus M, Taphoorn M, Sahm F, Harting I, et al. Lomustine and Bevacizumab in Progressive Glioblastoma. *New England Journal of Medicine*. 16 nov 2017;377(20):1954-63.
 84. Recommendations | Brain tumours (primary) and brain metastases in adults | Guidance | NICE [Internet]. NICE; [cité 5 sept 2020]. Disponible sur: <https://www.nice.org.uk/guidance/ng99/chapter/Recommendations>
 85. Sarkaria JN, Hu LS, Parney IF, Pafundi DH, Brinkmann DH, Laack NN, et al. Is the blood-brain barrier really disrupted in all glioblastomas? A critical assessment of existing clinical data. *Neuro Oncol*. 22 janv 2018;20(2):184-91.
 86. Lombardi G, De Salvo GL, Brandes AA, Eoli M, Rudà R, Faedi M, et al. Regorafenib compared with lomustine in patients with relapsed glioblastoma (REGOMA): a multicentre, open-label, randomised, controlled, phase 2 trial. *Lancet Oncol*. 2019;20(1):110-9.
 87. Guyon J, Chapouly C, Andrique L, Bikfalvi A, Daubon T. The normal and brain tumor vasculature: morphological and functional characteristics and therapeutic targeting. *Front Physiol* [Internet]. 2021 [cité 27 févr 2021];12. Disponible sur: <https://www.frontiersin.org/articles/10.3389/fphys.2021.622615/abstract>
 88. Thorne AH, Zanca C, Furnari F. Epidermal growth factor receptor targeting and challenges in glioblastoma. *Neuro Oncol*. juill 2016;18(7):914-8.
 89. Brandes AA, Finocchiaro G, Zagonel V, Reni M, Caserta C, Fabi A, et al. AVAREG: a phase II, randomized, noncomparative study of fotemustine or bevacizumab for patients with recurrent glioblastoma. *Neuro-oncology*. 2016;18(9):1304-12.
 90. Brown NF, Ng SM, Brooks C, Coutts T, Holmes J, Roberts C, et al. A phase II open label, randomised study of ipilimumab with temozolomide versus temozolomide alone after surgery and chemoradiotherapy in patients with recently diagnosed glioblastoma: the Ipi-Glio trial protocol. *BMC Cancer*. 12 mars 2020;20(1):198.
 91. Reardon DA, Brandes AA, Omuro A, Mulholland P, Lim M, Wick A, et al. Effect of Nivolumab vs Bevacizumab in Patients With Recurrent Glioblastoma: The CheckMate 143 Phase 3 Randomized Clinical Trial. *JAMA Oncology*. 1 juill 2020;6(7):1003-10.
 92. Omuro A, Vlahovic G, Lim M, Sahebjam S, Baehring J, Cloughesy T, et al. Nivolumab

- with or without ipilimumab in patients with recurrent glioblastoma: results from exploratory phase I cohorts of CheckMate 143. *Neuro Oncol.* 9 avr 2018;20(5):674-86.
93. de Groot J, Penas-Prado M, Alfaro-Munoz K, Hunter K, Pei BL, O'Brien B, et al. Window-of-opportunity clinical trial of pembrolizumab in patients with recurrent glioblastoma reveals predominance of immune-suppressive macrophages. *Neuro Oncol.* 15 avr 2020;22(4):539-49.
 94. Weathers S-PS, Kamiya-Matsuoka C, Harrison RA, Liu DD, Dervin S, Yun C, et al. Phase I/II study to evaluate the safety and clinical efficacy of atezolizumab (atezo; aPDL1) in combination with temozolomide (TMZ) and radiation in patients with newly diagnosed glioblastoma (GBM). *JCO.* 20 mai 2020;38(15_suppl):2511-2511.
 95. Hodi FS, O'Day SJ, McDermott DF, Weber RW, Sosman JA, Haanen JB, et al. Improved Survival with Ipilimumab in Patients with Metastatic Melanoma. *N Engl J Med.* 19 août 2010;363(8):711-23.
 96. Choi BD, Maus MV, June CH, Sampson JH. Immunotherapy for Glioblastoma: Adoptive T-cell Strategies. *Clin Cancer Res.* 1 avr 2019;25(7):2042-8.
 97. Migliorini D, Dietrich P-Y, Stupp R, Linette GP, Posey AD, June CH. CAR T-Cell Therapies in Glioblastoma: A First Look. *Clin Cancer Res.* 1 févr 2018;24(3):535-40.
 98. Wheeler CJ, Black KL. Vaccines for glioblastoma and high-grade glioma. *Expert Rev Vaccines.* juin 2011;10(6):875-86.
 99. Weller M, Butowski N, Tran DD, Recht LD, Lim M, Hirte H, et al. Rindopepimut with temozolomide for patients with newly diagnosed, EGFRvIII-expressing glioblastoma (ACT IV): a randomised, double-blind, international phase 3 trial. *The Lancet Oncology.* 1 oct 2017;18(10):1373-85.
 100. Meyerson M, Counter CM, Eaton EN, Ellisen LW, Steiner P, Caddle SD, et al. hEST2, the putative human telomerase catalytic subunit gene, is up-regulated in tumor cells and during immortalization. *Cell.* 22 août 1997;90(4):785-95.
 101. Huang FW, Hodis E, Xu MJ, Kryukov GV, Chin L, Garraway LA. Highly recurrent TERT promoter mutations in human melanoma. *Science.* 22 févr 2013;339(6122):957-9.
 102. Liao LM, Ashkan K, Tran DD, Campian JL, Trusheim JE, Cobbs CS, et al. First results on survival from a large Phase 3 clinical trial of an autologous dendritic cell vaccine in newly diagnosed glioblastoma. *Journal of Translational Medicine.* 29 mai 2018;16(1):142.
 103. Ott PA, Hu Z, Keskin DB, Shukla SA, Sun J, Bozym DJ, et al. An Immunogenic Personal Neoantigen Vaccine for Melanoma Patients. *Nature.* 13 juill 2017;547(7662):217-21.
 104. Mueller S, Cao X, Welker R, Wimmer E. Interaction of the Poliovirus Receptor CD155 with the Dynein Light Chain Tctex-1 and Its Implication for Poliovirus Pathogenesis *. *Journal of Biological Chemistry.* 8 mars 2002;277(10):7897-904.
 105. Merrill MK, Bernhardt G, Sampson JH, Wikstrand CJ, Bigner DD, Gromeier M. Poliovirus receptor CD155-targeted oncolysis of glioma. *Neuro-oncol.* juill 2004;6(3):208-17.
 106. Macadam AJ, Pollard SR, Ferguson G, Skuce R, Wood D, Almond JW, et al. Genetic basis of attenuation of the Sabin type 2 vaccine strain of poliovirus in primates. *Virology.* janv 1993;192(1):18-26.

107. Desjardins A, Gromeier M, II JEH, Beaubier N, Bolognesi DP, Friedman AH, et al. Recurrent Glioblastoma Treated with Recombinant Poliovirus. *New England Journal of Medicine* [Internet]. 26 juin 2018 [cité 27 sept 2021]; Disponible sur: <https://www.nejm.org/doi/10.1056/NEJMoa1716435>
108. Smith E, Morowitz HJ. Universality in intermediary metabolism. *PNAS*. 7 sept 2004;101(36):13168-73.
109. Mitchell P, Moyle J. Stoichiometry of Proton Translocation through the Respiratory Chain and Adenosine Triphosphatase Systems of Rat Liver Mitochondria. *Nature*. oct 1965;208(5006):147-51.
110. Scrabble HJ, Johnson DK, Rinchik EM, Cavenee WK. Rhabdomyosarcoma-associated locus and MYOD1 are syntenic but separate loci on the short arm of human chromosome 11. *PNAS*. 1 mars 1990;87(6):2182-6.
111. Steinbach P, Rehder H. Tetrasomy for the short arm of chromosome 12 with accessory isochromosome (+i(12p)) and a marked LDH-B gene dosage effect. *Clinical Genetics*. 1987;32(1):1-4.
112. Markert CL. Lactate dehydrogenase. Biochemistry and function of lactate dehydrogenase. *Cell Biochemistry and Function*. 1984;2(3):131-4.
113. Granchi C, Paterni I, Rani R, Minutolo F. Small-molecule inhibitors of human LDH5. *Future Med Chem*. oct 2013;5(16):1967-91.
114. Edwards YH, Povey S, LeVan KM, Driscoll CE, Millan JL, Goldberg E. Locus determining the human sperm-specific lactate dehydrogenase, LDHC, is syntenic with LDHA. *Dev Genet*. 1987;8(4):219-32.
115. Koslowski M, Türeci Ö, Bell C, Krause P, Lehr H-A, Brunner J, et al. Multiple Splice Variants of Lactate Dehydrogenase C Selectively Expressed in Human Cancer. *Cancer Res*. 15 nov 2002;62(22):6750-5.
116. Hua Y, Liang C, Zhu J, Miao C, Yu Y, Xu A, et al. Expression of lactate dehydrogenase C correlates with poor prognosis in renal cell carcinoma. *Tumour Biol*. 1 mars 2017;39(3):1010428317695968.
117. Flick MJ, Konieczny SF. Identification of putative mammalian d-lactate dehydrogenase enzymes. *Biochemical and Biophysical Research Communications*. 26 juill 2002;295(4):910-6.
118. Schueren F, Lingner T, George R, Hofhuis J, Dickel C, Gärtner J, et al. Peroxisomal lactate dehydrogenase is generated by translational readthrough in mammals. *eLife*. 3:e03640.
119. Valvona CJ, Fillmore HL, Nunn PB, Pilkington GJ. The Regulation and Function of Lactate Dehydrogenase A: Therapeutic Potential in Brain Tumor. *Brain Pathology*. 2016;26(1):3-17.
120. Mink JW, Blumenschine RJ, Adams DB. Ratio of central nervous system to body metabolism in vertebrates: its constancy and functional basis. *Am J Physiol*. sept 1981;241(3):R203-212.
121. Hall CN, Klein-Flügge MC, Howarth C, Attwell D. Oxidative Phosphorylation, Not Glycolysis, Powers Presynaptic and Postsynaptic Mechanisms Underlying Brain Information Processing. *J Neurosci*. 27 juin 2012;32(26):8940-51.
122. Attwell D, Laughlin SB. An Energy Budget for Signaling in the Grey Matter of the Brain.

- J Cereb Blood Flow Metab. 1 oct 2001;21(10):1133-45.
123. Lennie P. The Cost of Cortical Computation. *Current Biology*. 18 mars 2003;13(6):493-7.
 124. Leino RL, Gerhart DZ, van Bueren AM, McCall AL, Drewes LR. Ultrastructural localization of GLUT 1 and GLUT 3 glucose transporters in rat brain. *J Neurosci Res*. 1 sept 1997;49(5):617-26.
 125. Mathiisen TM, Lehre KP, Danbolt NC, Ottersen OP. The perivascular astroglial sheath provides a complete covering of the brain microvessels: an electron microscopic 3D reconstruction. *Glia*. juill 2010;58(9):1094-103.
 126. McCaslin AFH, Chen BR, Radosevich AJ, Cauli B, Hillman EMC. In vivo 3D morphology of astrocyte-vasculature interactions in the somatosensory cortex: implications for neurovascular coupling. *J Cereb Blood Flow Metab*. mars 2011;31(3):795-806.
 127. Jakoby P, Schmidt E, Ruminot I, Gutiérrez R, Barros LF, Deitmer JW. Higher transport and metabolism of glucose in astrocytes compared with neurons: a multiphoton study of hippocampal and cerebellar tissue slices. *Cereb Cortex*. janv 2014;24(1):222-31.
 128. Vilchez D, Ros S, Cifuentes D, Pujadas L, Vallès J, García-Fojeda B, et al. Mechanism suppressing glycogen synthesis in neurons and its demise in progressive myoclonus epilepsy. *Nat Neurosci*. nov 2007;10(11):1407-13.
 129. Bittar PG, Charnay Y, Pellerin L, Bouras C, Magistretti PJ. Selective distribution of lactate dehydrogenase isoenzymes in neurons and astrocytes of human brain. *J Cereb Blood Flow Metab*. nov 1996;16(6):1079-89.
 130. Pierre K, Pellerin L. Monocarboxylate transporters in the central nervous system: distribution, regulation and function. *J Neurochem*. juill 2005;94(1):1-14.
 131. Zhang Y, Chen K, Sloan SA, Bennett ML, Scholze AR, O'Keefe S, et al. An RNA-Sequencing Transcriptome and Splicing Database of Glia, Neurons, and Vascular Cells of the Cerebral Cortex. *J Neurosci*. 3 sept 2014;34(36):11929-47.
 132. Pellerin L, Pellegrini G, Bittar PG, Charnay Y, Bouras C, Martin JL, et al. Evidence supporting the existence of an activity-dependent astrocyte-neuron lactate shuttle. *Dev Neurosci*. 1998;20(4-5):291-9.
 133. Itoh Y, Esaki T, Shimoji K, Cook M, Law MJ, Kaufman E, et al. Dichloroacetate effects on glucose and lactate oxidation by neurons and astroglia in vitro and on glucose utilization by brain in vivo. *Proc Natl Acad Sci U S A*. 15 avr 2003;100(8):4879-84.
 134. Mächler P, Wyss MT, Elsayed M, Stobart J, Gutierrez R, von Faber-Castell A, et al. In Vivo Evidence for a Lactate Gradient from Astrocytes to Neurons. *Cell Metabolism*. 12 janv 2016;23(1):94-102.
 135. Patel AB, Lai JCK, Chowdhury GMI, Hyder F, Rothman DL, Shulman RG, et al. Direct evidence for activity-dependent glucose phosphorylation in neurons with implications for the astrocyte-to-neuron lactate shuttle. *Proc Natl Acad Sci U S A*. 8 avr 2014;111(14):5385-90.
 136. Quistorff B, Secher NH, Van Lieshout JJ. Lactate fuels the human brain during exercise. *FASEB J*. oct 2008;22(10):3443-9.
 137. van Hall G, Strømstad M, Rasmussen P, Jans O, Zaar M, Gam C, et al. Blood lactate is an important energy source for the human brain. *J Cereb Blood Flow Metab*. juin

- 2009;29(6):1121-9.
138. Herzog RI, Jiang L, Herman P, Zhao C, Sanganahalli BG, Mason GF, et al. Lactate preserves neuronal metabolism and function following antecedent recurrent hypoglycemia. *J Clin Invest.* mai 2013;123(5):1988-98.
 139. Goyal MS, Hawrylycz M, Miller JA, Snyder AZ, Raichle ME. Aerobic Glycolysis in the Human Brain Is Associated with Development and Neotenus Gene Expression. *Cell Metabolism.* 7 janv 2014;19(1):49-57.
 140. Gallagher CN, Carpenter KLH, Grice P, Howe DJ, Mason A, Timofeev I, et al. The human brain utilizes lactate via the tricarboxylic acid cycle: a ¹³C-labelled microdialysis and high-resolution nuclear magnetic resonance study. *Brain.* 1 oct 2009;132(10):2839-49.
 141. Emhoff C-AW, Messonnier LA, Horning MA, Fattor JA, Carlson TJ, Brooks GA. Direct and indirect lactate oxidation in trained and untrained men. *Journal of Applied Physiology.* 15 sept 2013;115(6):829-38.
 142. Liu L, MacKenzie KR, Putluri N, Maletić-Savatić M, Bellen HJ. The Glia-Neuron Lactate Shuttle and Elevated ROS Promote Lipid Synthesis in Neurons and Lipid Droplet Accumulation in Glia via APOE/D. *Cell Metab.* 7 nov 2017;26(5):719-737.e6.
 143. Jourdain P, Allaman I, Rothenfusser K, Fiumelli H, Marquet P, Magistretti PJ. L-Lactate protects neurons against excitotoxicity: implication of an ATP-mediated signaling cascade. *Sci Rep.* 19 févr 2016;6(1):21250.
 144. Tauffenberger A, Fiumelli H, Almustafa S, Magistretti PJ. Lactate and pyruvate promote oxidative stress resistance through hormetic ROS signaling. *Cell Death Dis.* 10 sept 2019;10(9):1-16.
 145. Hanahan D, Weinberg RA. Hallmarks of Cancer: The Next Generation. *Cell.* 4 mars 2011;144(5):646-74.
 146. Warburg O. On the origin of cancer cells. *Science.* 24 févr 1956;123(3191):309-14.
 147. Walenta S, Wetterling M, Lehrke M, Schwickert G, Sundfør K, Rofstad EK, et al. High lactate levels predict likelihood of metastases, tumor recurrence, and restricted patient survival in human cervical cancers. *Cancer Res.* 15 févr 2000;60(4):916-21.
 148. Brizel DM, Schroeder T, Scher RL, Walenta S, Clough RW, Dewhirst MW, et al. Elevated tumor lactate concentrations predict for an increased risk of metastases in head-and-neck cancer. *Int J Radiat Oncol Biol Phys.* 1 oct 2001;51(2):349-53.
 149. Baumann F, Leukel P, Doerfelt A, Beier CP, Dettmer K, Oefner PJ, et al. Lactate promotes glioma migration by TGF- β 2-dependent regulation of matrix metalloproteinase-2. *Neuro Oncol.* août 2009;11(4):368-80.
 150. Colen CB, Shen Y, Ghoddoussi F, Yu P, Francis TB, Koch BJ, et al. Metabolic Targeting of Lactate Efflux by Malignant Glioma Inhibits Invasiveness and Induces Necrosis: An In Vivo Study. *Neoplasia.* 1 juill 2011;13(7):620-32.
 151. Marxsen JH, Stengel P, Doege K, Heikkinen P, Jokilehto T, Wagner T, et al. Hypoxia-inducible factor-1 (HIF-1) promotes its degradation by induction of HIF- α -prolyl-4-hydroxylases. *Biochemical Journal.* 1 août 2004;381(Pt 3):761.
 152. Lee K, Zhang H, Qian DZ, Rey S, Liu JO, Semenza GL. Acriflavine inhibits HIF-1 dimerization, tumor growth, and vascularization. *Proc Natl Acad Sci U S A.* 20 oct

- 2009;106(42):17910-5.
153. Womeldorff M, Gillespie D, Jensen RL. Hypoxia-inducible factor–1 and associated upstream and downstream proteins in the pathophysiology and management of glioblastoma. *Neurosurgical Focus*. 1 déc 2014;37(6):E8.
 154. Moldogazieva NT, Mokhosoev IM, Terentiev AA. Metabolic Heterogeneity of Cancer Cells: An Interplay between HIF-1, GLUTs, and AMPK. *Cancers (Basel)*. 2 avr 2020;12(4):862.
 155. Kim J, Tchernyshyov I, Semenza GL, Dang CV. HIF-1-mediated expression of pyruvate dehydrogenase kinase: a metabolic switch required for cellular adaptation to hypoxia. *Cell Metab*. mars 2006;3(3):177-85.
 156. Schulz TJ, Thierbach R, Voigt A, Drewes G, Mietzner B, Steinberg P, et al. Induction of oxidative metabolism by mitochondrial frataxin inhibits cancer growth: Otto Warburg revisited. *J Biol Chem*. 13 janv 2006;281(2):977-81.
 157. Sonveaux P, Végran F, Schroeder T, Wergin MC, Verrax J, Rabbani ZN, et al. Targeting lactate-fueled respiration selectively kills hypoxic tumor cells in mice. *J Clin Invest*. déc 2008;118(12):3930-42.
 158. Hardee ME, Dewhirst MW, Agarwal N, Sorg BS. Novel imaging provides new insights into mechanisms of oxygen transport in tumors. *Curr Mol Med*. mai 2009;9(4):435-41.
 159. Shibao S, Minami N, Koike N, Fukui N, Yoshida K, Saya H, et al. Metabolic heterogeneity and plasticity of glioma stem cells in a mouse glioblastoma model. *Neuro-Oncology*. 19 févr 2018;20(3):343-54.
 160. Pfeiffer T, Schuster S, Bonhoeffer S. Cooperation and Competition in the Evolution of ATP-Producing Pathways. *Science*. 20 avr 2001;292(5516):504-7.
 161. Lake JA. Origin of the eukaryotic nucleus determined by rate-invariant analysis of rRNA sequences. *Nature*. 14 janv 1988;331(6152):184-6.
 162. Yang D, Oyaizu Y, Oyaizu H, Olsen GJ, Woese CR. Mitochondrial origins. *Proc Natl Acad Sci U S A*. juill 1985;82(13):4443-7.
 163. Madan E, Pelham CJ, Nagane M, Parker TM, Canas-Marques R, Fazio K, et al. Flower isoforms promote competitive growth in cancer. *Nature*. août 2019;572(7768):260-4.
 164. Oudard S, Boitier E, Miccoli L, Rousset S, Dutrillaux B, Poupon MF. Gliomas are driven by glycolysis: putative roles of hexokinase, oxidative phosphorylation and mitochondrial ultrastructure. *Anticancer Res*. juin 1997;17(3C):1903-11.
 165. Arismendi-Morillo G. Electron microscopy morphology of the mitochondrial network in human cancer. *Int J Biochem Cell Biol*. oct 2009;41(10):2062-8.
 166. Wolf A, Agnihotri S, Micallef J, Mukherjee J, Sabha N, Cairns R, et al. Hexokinase 2 is a key mediator of aerobic glycolysis and promotes tumor growth in human glioblastoma multiforme. *J Exp Med*. 14 févr 2011;208(2):313-26.
 167. Tseng P-L, Chen C-W, Hu K-H, Cheng H-C, Lin Y-H, Tsai W-H, et al. The decrease of glycolytic enzyme hexokinase 1 accelerates tumor malignancy via deregulating energy metabolism but sensitizes cancer cells to 2-deoxyglucose inhibition. *Oncotarget*. 10 avr 2018;9(27):18949-69.
 168. Wolf A, Agnihotri S, Munoz D, Guha A. Developmental profile and regulation of the glycolytic enzyme hexokinase 2 in normal brain and glioblastoma multiforme. *Neurobiol*

- Dis. oct 2011;44(1):84-91.
169. Verhaak RGW, Hoadley KA, Purdom E, Wang V, Qi Y, Wilkerson MD, et al. Integrated genomic analysis identifies clinically relevant subtypes of glioblastoma characterized by abnormalities in PDGFRA, IDH1, EGFR, and NF1. *Cancer Cell*. 19 janv 2010;17(1):98-110.
 170. Chinnaiyan P, Kensicki E, Bloom G, Prabhu A, Sarcar B, Kahali S, et al. The Metabolomic Signature of Malignant Glioma Reflects Accelerated Anabolic Metabolism. *Cancer Res*. 15 nov 2012;72(22):5878-88.
 171. Yang W, Lu Z. Regulation and function of pyruvate kinase M2 in cancer. *Cancer Lett*. 10 oct 2013;339(2):153-8.
 172. Christofk HR, Vander Heiden MG, Harris MH, Ramanathan A, Gerszten RE, Wei R, et al. The M2 splice isoform of pyruvate kinase is important for cancer metabolism and tumour growth. *Nature*. 13 mars 2008;452(7184):230-3.
 173. Lunt SY, Muralidhar V, Hosios AM, Israelsen WJ, Gui DY, Newhouse L, et al. Pyruvate kinase isoform expression alters nucleotide synthesis to impact cell proliferation. *Mol Cell*. 8 janv 2015;57(1):95-107.
 174. Altenberg B, Greulich KO. Genes of glycolysis are ubiquitously overexpressed in 24 cancer classes. *Genomics*. déc 2004;84(6):1014-20.
 175. Kim J, Han J, Jang Y, Kim SJ, Lee MJ, Ryu MJ, et al. High-capacity glycolytic and mitochondrial oxidative metabolisms mediate the growth ability of glioblastoma. *Int J Oncol*. sept 2015;47(3):1009-16.
 176. Kolev Y, Uetake H, Takagi Y, Sugihara K. Lactate dehydrogenase-5 (LDH-5) expression in human gastric cancer: association with hypoxia-inducible factor (HIF-1 α) pathway, angiogenic factors production and poor prognosis. *Ann Surg Oncol*. août 2008;15(8):2336-44.
 177. Koukourakis MI, Giatromanolaki A, Panteliadou M, Pouliliou SE, Chondrou PS, Mavropoulou S, et al. Lactate dehydrogenase 5 isoenzyme overexpression defines resistance of prostate cancer to radiotherapy. *Br J Cancer*. 29 avr 2014;110(9):2217-23.
 178. Fack F, Espedal H, Keunen O, Golebiewska A, Obad N, Harter PN, et al. Bevacizumab treatment induces metabolic adaptation toward anaerobic metabolism in glioblastomas. *Acta Neuropathol*. janv 2015;129(1):115-31.
 179. Le A, Cooper CR, Gouw AM, Dinavahi R, Maitra A, Deck LM, et al. Inhibition of lactate dehydrogenase A induces oxidative stress and inhibits tumor progression. *Proc Natl Acad Sci U S A*. 2 févr 2010;107(5):2037-42.
 180. Fantin VR, St-Pierre J, Leder P. Attenuation of LDH-A expression uncovers a link between glycolysis, mitochondrial physiology, and tumor maintenance. *Cancer Cell*. 13 juin 2006;9(6):425-34.
 181. Sheng SL, Liu JJ, Dai YH, Sun XG, Xiong XP, Huang G. Knockdown of lactate dehydrogenase A suppresses tumor growth and metastasis of human hepatocellular carcinoma. *FEBS J*. oct 2012;279(20):3898-910.
 182. Chesnelong C, Chaumeil MM, Blough MD, Al-Najjar M, Stechishin OD, Chan JA, et al. Lactate dehydrogenase A silencing in IDH mutant gliomas. *Neuro Oncol*. mai 2014;16(5):686-95.

183. Leiblich A, Cross SS, Catto JWF, Phillips JT, Leung HY, Hamdy FC, et al. Lactate dehydrogenase-B is silenced by promoter hypermethylation in human prostate cancer. *Oncogene*. 11 mai 2006;25(20):2953-60.
184. Chen R, Zhou X, Yu Z, Liu J, Huang G. Low Expression of LDHB Correlates With Unfavorable Survival in Hepatocellular Carcinoma: Strobe-Compliant Article. *Medicine (Baltimore)*. sept 2015;94(39):e1583.
185. Cui J, Quan M, Jiang W, Hu H, Jiao F, Li N, et al. Suppressed expression of LDHB promotes pancreatic cancer progression via inducing glycolytic phenotype. *Med Oncol*. mai 2015;32(5):143.
186. Brisson L, Bański P, Sboarina M, Dethier C, Danhier P, Fontenille M-J, et al. Lactate Dehydrogenase B Controls Lysosome Activity and Autophagy in Cancer. *Cancer Cell*. 12 sept 2016;30(3):418-31.
187. Ždravlević M, Brand A, Di Ianni L, Dettmer K, Reinders J, Singer K, et al. Double genetic disruption of lactate dehydrogenases A and B is required to ablate the « Warburg effect » restricting tumor growth to oxidative metabolism. *J Biol Chem*. 12 oct 2018;293(41):15947-61.
188. Bailleul J, Yazal T, Sung D, Dao A, Palomera D, Sehgal A, et al. Irradiation Reprograms GBM Metabolism Towards an Antioxidant Profile That Drives Radiation Resistance. *International Journal of Radiation Oncology, Biology, Physics*. 1 sept 2019;105(1):S165-6.
189. Kim EH, Lee J-H, Oh Y, Koh I, Shim J-K, Park J, et al. Inhibition of glioblastoma tumorspheres by combined treatment with 2-deoxyglucose and metformin. *Neuro Oncol*. févr 2017;19(2):197-207.
190. Seliger C, Leukel P, Moeckel S, Jachnik B, Lottaz C, Kreutz M, et al. Lactate-Modulated Induction of THBS-1 Activates Transforming Growth Factor (TGF)-beta2 and Migration of Glioma Cells In Vitro. *PLOS ONE*. 1 nov 2013;8(11):e78935.
191. Allen M, Bjerke M, Edlund H, Nelander S, Westermarck B. Origin of the U87MG glioma cell line: Good news and bad news. *Science Translational Medicine*. 31 août 2016;8(354):354re3-354re3.
192. Huszthy PC, Daphu I, Niclou SP, Stieber D, Nigro JM, Sakariassen PØ, et al. In vivo models of primary brain tumors: pitfalls and perspectives. *Neuro Oncol*. août 2012;14(8):979-93.
193. Lenting K, Verhaak R, Ter Laan M, Wesseling P, Leenders W. Glioma: experimental models and reality. *Acta Neuropathol*. févr 2017;133(2):263-82.
194. Torsvik A, Stieber D, Enger PØ, Golebiewska A, Molven A, Svendsen A, et al. U-251 revisited: genetic drift and phenotypic consequences of long-term cultures of glioblastoma cells. *Cancer Med*. août 2014;3(4):812-24.
195. de Vries NA, Beijnen JH, van Tellingen O. High-grade glioma mouse models and their applicability for preclinical testing. *Cancer Treat Rev*. déc 2009;35(8):714-23.
196. Candolfi M, Curtin JF, Nichols WS, Muhammad AG, King GD, Pluhar GE, et al. Intracranial glioblastoma models in preclinical neuro-oncology: neuropathological characterization and tumor progression. *J Neurooncol*. nov 2007;85(2):133-48.
197. Newcomb EW, Lukyanov Y, Alonso-Basanta M, Esencay M, Smirnova I, Schnee T, et al. Antiangiogenic Effects of Noscapine Enhance Radioresponse for GL261 Tumors. *Int*

- J Radiat Oncol Biol Phys. 1 août 2008;71(5):1477-84.
198. Wang J, Miletic H, Sakariassen PØ, Huszthy PC, Jacobsen H, Brekkå N, et al. A reproducible brain tumour model established from human glioblastoma biopsies. *BMC Cancer*. 29 déc 2009;9:465.
 199. Bougnaud S, Golebiewska A, Oudin A, Keunen O, Harter PN, Mäder L, et al. Molecular crosstalk between tumour and brain parenchyma instructs histopathological features in glioblastoma. *Oncotarget*. 25 mars 2016;7(22):31955-71.
 200. Reyat F, Guyader C, Decraene C, Lucchesi C, Auger N, Assayag F, et al. Molecular profiling of patient-derived breast cancer xenografts. *Breast Cancer Research*. 16 janv 2012;14(1):R11.
 201. Lai Y, Wei X, Lin S, Qin L, Cheng L, Li P. Current status and perspectives of patient-derived xenograft models in cancer research. *Journal of Hematology & Oncology*. 12 mai 2017;10(1):106.
 202. Kim S-S, Pirolo KF, Chang EH. Isolation and Culturing of Glioma Cancer Stem Cells. *Curr Protoc Cell Biol*. 1 juin 2015;67:23.10.1-23.10.10.
 203. Daubon T, Léon C, Clarke K, Andrique L, Salabert L, Darbo E, et al. Deciphering the complex role of thrombospondin-1 in glioblastoma development. *Nat Commun*. 8 mars 2019;10(1):1146.
 204. Li C, Wang S, Yan J-L, Torheim T, Boonzaier NR, Sinha R, et al. Characterizing tumor invasiveness of glioblastoma using multiparametric magnetic resonance imaging. *J Neurosurg*. 26 avr 2019;132(5):1465-72.
 205. Drumm MR, Dixit KS, Grimm S, Kumthekar P, Lukas RV, Raizer JJ, et al. Extensive brainstem infiltration, not mass effect, is a common feature of end-stage cerebral glioblastomas. *Neuro-Oncology*. 15 avr 2020;22(4):470-9.
 206. Friedl P, Wolf K. Tumour-cell invasion and migration: diversity and escape mechanisms. *Nat Rev Cancer*. mai 2003;3(5):362-74.
 207. Louis DN. Molecular pathology of malignant gliomas. *Annu Rev Pathol*. 2006;1:97-117.
 208. Cuddapah VA, Robel S, Watkins S, Sontheimer H. A neurocentric perspective on glioma invasion. *Nat Rev Neurosci*. juill 2014;15(7):455-65.
 209. Zagzag D, Esencay M, Mendez O, Yee H, Smirnova I, Huang Y, et al. Hypoxia- and Vascular Endothelial Growth Factor-Induced Stromal Cell-Derived Factor-1 α /CXCR4 Expression in Glioblastomas. *Am J Pathol*. août 2008;173(2):545-60.
 210. Wang J, Xu S-L, Duan J-J, Yi L, Guo Y-F, Shi Y, et al. Invasion of white matter tracts by glioma stem cells is regulated by a NOTCH1–SOX2 positive-feedback loop. *Nat Neurosci*. janv 2019;22(1):91-105.
 211. Venkataramani V, Tanev DI, Strahle C, Studier-Fischer A, Fankhauser L, Kessler T, et al. Glutamatergic synaptic input to glioma cells drives brain tumour progression. *Nature*. sept 2019;573(7775):532-8.
 212. Venkatesh HS, Morishita W, Geraghty AC, Silverbush D, Gillespie SM, Arzt M, et al. Electrical and synaptic integration of glioma into neural circuits. *Nature*. sept 2019;573(7775):539-45.
 213. Boyé K, Pujol N, D Alves I, Chen Y-P, Daubon T, Lee Y-Z, et al. The role of CXCR3/LRP1 cross-talk in the invasion of primary brain tumors. *Nat Commun*. 17 nov

- 2017;8(1):1571.
214. Joseph JV, Magaut CR, Storevik S, Geraldo LH, Mathivet T, Latif MA, et al. TGF- β promotes microtubule formation in glioblastoma through thrombospondin 1. *Neuro-Oncology* [Internet]. 20 sept 2021 [cité 7 nov 2021];(noab212). Disponible sur: <https://doi.org/10.1093/neuonc/noab212>
 215. Guyon J, Chouleur T, Bikfalvi A, Daubon T. Glioblastoma Patient-Derived Cell Lines: Generation of Nonadherent Cellular Models from Brain Tumors. In: Seano G, éditeur. *Brain Tumors* [Internet]. New York, NY: Springer US; 2021 [cité 27 févr 2021]. p. 105-17. (Neuromethods). Disponible sur: https://doi.org/10.1007/978-1-0716-0856-2_5
 216. Guyon J, Andrique L, Pujol N, Røsland GV, Recher G, Bikfalvi A, et al. A 3D Spheroid Model for Glioblastoma. *JoVE (Journal of Visualized Experiments)*. 9 avr 2020;(158):e60998.
 217. Guyon J, Strale P-O, Romero-Garmendia I, Bikfalvi A, Studer V, Daubon T. Co-culture of Glioblastoma Stem-like Cells on Patterned Neurons to Study Migration and Cellular Interactions. *JoVE (Journal of Visualized Experiments)*. 24 févr 2021;(168):e62213.
 218. Article 16 - Code civil - Légifrance [Internet]. [cité 17 sept 2021]. Disponible sur: https://www.legifrance.gouv.fr/codes/article_lc/LEGIARTI000006419320/
 219. Chapitre Ier : Prélèvement et collecte. (Articles L1241-1 à L1241-7) - Légifrance [Internet]. [cité 17 sept 2021]. Disponible sur: <https://www.legifrance.gouv.fr/codes/id/LEGIARTI000039279717/2020-01-01/>
 220. Article L1211-2 - Code de la santé publique - Légifrance [Internet]. [cité 17 sept 2021]. Disponible sur: https://www.legifrance.gouv.fr/codes/article_lc/LEGIARTI000041721146
 221. Galli R, Binda E, Orfanelli U, Cipelletti B, Gritti A, De Vitis S, et al. Isolation and characterization of tumorigenic, stem-like neural precursors from human glioblastoma. *Cancer Res*. 1 oct 2004;64(19):7011-21.
 222. Kim H. Splitting hESC/hiPSC lines on MEF using Accutase. In: *StemBook* [Internet]. Cambridge (MA): Harvard Stem Cell Institute; 2008 [cité 26 oct 2021]. Disponible sur: <http://www.ncbi.nlm.nih.gov/books/NBK133271/>
 223. Ishiguro T, Ohata H, Sato A, Yamawaki K, Enomoto T, Okamoto K. Tumor-derived spheroids: Relevance to cancer stem cells and clinical applications. *Cancer Sci*. mars 2017;108(3):283-9.
 224. Pelissier FA, Garbe JC, Ananthanarayanan B, Miyano M, Lin C, Jokela T, et al. Age-related dysfunction in mechanotransduction impairs differentiation of human mammary epithelial progenitors. *Cell Rep*. 26 juin 2014;7(6):1926-39.
 225. Desoize B, Jardillier J. Multicellular resistance: a paradigm for clinical resistance? *Crit Rev Oncol Hematol*. déc 2000;36(2-3):193-207.
 226. Corbet C, Feron O. Tumour acidosis: from the passenger to the driver's seat. *Nat Rev Cancer*. oct 2017;17(10):577-93.
 227. Patel V, Hathout L. Image-driven modeling of the proliferation and necrosis of glioblastoma multiforme. *Theoretical Biology and Medical Modelling*. 2 mai 2017;14(1):10.
 228. Sutherland RM. Cell and environment interactions in tumor microregions: the multicell spheroid model. *Science*. 8 avr 1988;240(4849):177-84.

229. Hirschhaeuser F, Menne H, Dittfeld C, West J, Mueller-Klieser W, Kunz-Schughart LA. Multicellular tumor spheroids: an underestimated tool is catching up again. *J Biotechnol.* 1 juill 2010;148(1):3-15.
230. Kojima N, Tao F, Mihara H, Aoki S. Chapter 8 - Methods for Engineering of Multicellular Spheroids to Reconstitute the Liver Tissue. In: Zheng Y-W, éditeur. *Stem Cells and Cancer in Hepatology* [Internet]. Academic Press; 2018 [cité 26 oct 2021]. p. 145-58. Disponible sur: <https://www.sciencedirect.com/science/article/pii/B9780128123010000086>
231. Pamies D, Block K, Lau P, Gribaldo L, Pardo CA, Barreras P, et al. Rotenone exerts developmental neurotoxicity in a human brain spheroid model. *Toxicology and Applied Pharmacology.* 1 sept 2018;354:101-14.
232. Kaufman LJ, Brangwynne CP, Kasza KE, Filippidi E, Gordon VD, Deisboeck TS, et al. Glioma expansion in collagen I matrices: analyzing collagen concentration-dependent growth and motility patterns. *Biophys J.* juill 2005;89(1):635-50.
233. Payne LS, Huang PH. The pathobiology of collagens in glioma. *Mol Cancer Res.* oct 2013;11(10):10.1158/1541-7786.MCR-13-0236.
234. Estrella V, Chen T, Lloyd M, Wojtkowiak J, Cornell HH, Ibrahim-Hashim A, et al. Acidity generated by the tumor microenvironment drives local invasion. *Cancer Res.* 1 mars 2013;73(5):1524-35.
235. Osadchii OE. Myocardial phosphodiesterases and regulation of cardiac contractility in health and cardiac disease. *Cardiovasc Drugs Ther.* juin 2007;21(3):171-94.
236. Lang P, Gesbert F, Delespine-Carmagnat M, Stancou R, Pouchelet M, Bertoglio J. Protein kinase A phosphorylation of RhoA mediates the morphological and functional effects of cyclic AMP in cytotoxic lymphocytes. *EMBO J.* 1 févr 1996;15(3):510-9.
237. Zimmerman NP, Kumar SN, Turner JR, Dwinell MB. Cyclic AMP dysregulates intestinal epithelial cell restitution through PKA and RhoA. *Inflamm Bowel Dis.* juin 2012;18(6):1081-91.
238. Furman MA, Shulman K. Cyclic AMP and adenyl cyclase in brain tumors. *J Neurosurg.* avr 1977;46(4):477-83.
239. Rowther FB, Wei W, Dawson TP, Ashton K, Singh A, Madiesse-Timchou MP, et al. Cyclic nucleotide phosphodiesterase-1C (PDE1C) drives cell proliferation, migration and invasion in glioblastoma multiforme cells in vitro. *Mol Carcinog.* mars 2016;55(3):268-79.
240. Cesarini V, Martini M, Vitiani LR, Gravina GL, Di Agostino S, Graziani G, et al. Type 5 phosphodiesterase regulates glioblastoma multiforme aggressiveness and clinical outcome. *Oncotarget.* 21 févr 2017;8(8):13223-39.
241. Hambleton R, Krall J, Tikishvili E, Honegger M, Ahmad F, Manganiello VC, et al. Isoforms of Cyclic Nucleotide Phosphodiesterase PDE3 and Their Contribution to cAMP Hydrolytic Activity in Subcellular Fractions of Human Myocardium *. *Journal of Biological Chemistry.* 25 nov 2005;280(47):39168-74.
242. Zimmerman NP, Roy I, Hauser AD, Wilson JM, Williams CL, Dwinell MB. Cyclic AMP regulates the migration and invasion potential of human pancreatic cancer cells. *Mol Carcinog.* mars 2015;54(3):203-15.
243. Bolon P, Chassery J-M, Cocquerez J-P, Demigny D, Graffigne C, Montanvert A, et al.

- Analyse d'images : Filtrage et segmentation [Internet]. MASSON; 1995 [cité 27 oct 2021]. Disponible sur: <https://hal.archives-ouvertes.fr/hal-00706168>
244. Barbier M, Jaensch S, Cornelissen F, Vidic S, Gjerde K, Hoogt R de, et al. Ellipsoid Segmentation Model for Analyzing Light-Attenuated 3D Confocal Image Stacks of Fluorescent Multi-Cellular Spheroids. *PLOS ONE*. 15 juin 2016;11(6):e0156942.
 245. Arganda-Carreras I, Kaynig V, Rueden C, Eliceiri KW, Schindelin J, Cardona A, et al. Trainable Weka Segmentation: a machine learning tool for microscopy pixel classification. *Bioinformatics*. 1 août 2017;33(15):2424-6.
 246. Boutin ME, Voss TC, Titus SA, Cruz-Gutierrez K, Michael S, Ferrer M. A high-throughput imaging and nuclear segmentation analysis protocol for cleared 3D culture models. *Sci Rep*. 24 juill 2018;8:11135.
 247. Sternberg. *Biomedical Image Processing*. Computer. janv 1983;16(1):22-34.
 248. Zack GW, Rogers WE, Latt SA. Automatic measurement of sister chromatid exchange frequency. *J Histochem Cytochem*. juill 1977;25(7):741-53.
 249. Short AR, Czeisler C, Stocker B, Cole S, Otero JJ, Winter JO. Imaging Cell–Matrix Interactions in 3D Collagen Hydrogel Culture Systems. *Macromolecular Bioscience*. 2017;17(6):1600478.
 250. Gritsenko PG, Atlasy N, Dieteren CEJ, Navis AC, Venhuizen J-H, Veelken C, et al. p120-catenin-dependent collective brain infiltration by glioma cell networks. *Nat Cell Biol*. janv 2020;22(1):97-107.
 251. Qian H, Sheetz MP, Elson EL. Single particle tracking. Analysis of diffusion and flow in two-dimensional systems. *Biophys J*. oct 1991;60(4):910-21.
 252. Gorelik R, Gautreau A. Quantitative and unbiased analysis of directional persistence in cell migration. *Nat Protoc*. août 2014;9(8):1931-43.
 253. Shboul ZA, Alam M, Vidyaratne L, Pei L, Elbakary MI, Iftekharuddin KM. Feature-Guided Deep Radiomics for Glioblastoma Patient Survival Prediction. *Front Neurosci*. 20 sept 2019;13:966.
 254. Boutros M, Kiger AA, Armknecht S, Kerr K, Hild M, Koch B, et al. Genome-Wide RNAi Analysis of Growth and Viability in Drosophila Cells. *Science*. 6 févr 2004;303(5659):832-5.
 255. Conant GC, Wagner A. Duplicate genes and robustness to transient gene knock-downs in *Caenorhabditis elegans*. *Proceedings of the Royal Society of London Series B: Biological Sciences*. 7 janv 2004;271(1534):89-96.
 256. Goetze K, Walenta S, Ksiazkiewicz M, Kunz-Schughart LA, Mueller-Klieser W. Lactate enhances motility of tumor cells and inhibits monocyte migration and cytokine release. *Int J Oncol*. août 2011;39(2):453-63.
 257. Darmanis S, Sloan SA, Croote D, Mignardi M, Chernikova S, Samghababi P, et al. Single-Cell RNA-Seq Analysis of Infiltrating Neoplastic Cells at the Migrating Front of Human Glioblastoma. *Cell Rep*. 31 oct 2017;21(5):1399-410.
 258. Suvà ML, Rheinbay E, Gillespie SM, Patel AP, Wakimoto H, Rabkin SD, et al. Reconstructing and reprogramming the tumor propagating potential of glioblastoma stem-like cells. *Cell*. 24 avr 2014;157(3):580-94.
 259. Textes adoptés - Plans et mesures visant à accélérer le passage à une innovation sans

- recours aux animaux dans la recherche, les essais réglementaires et l'enseignement - Jeudi 16 septembre 2021 [Internet]. [cité 31 oct 2021]. Disponible sur: https://www.europarl.europa.eu/doceo/document/TA-9-2021-0387_FR.html
260. La règle des 3 R : réduire, raffiner, remplacer · Inserm, La science pour la santé [Internet]. Inserm. [cité 7 nov 2021]. Disponible sur: <https://www.inserm.fr/espace-pro/recherche-preclinique/regle-3-r-reduire-raffiner-remplacer/>
 261. Lee J, Kotliarova S, Kotliarov Y, Li A, Su Q, Donin NM, et al. Tumor stem cells derived from glioblastomas cultured in bFGF and EGF more closely mirror the phenotype and genotype of primary tumors than do serum-cultured cell lines. *Cancer Cell*. mai 2006;9(5):391-403.
 262. Ricard-Blum S. The Collagen Family. *Cold Spring Harb Perspect Biol*. janv 2011;3(1):a004978.
 263. Suh HN, Han HJ. Collagen I regulates the self-renewal of mouse embryonic stem cells through $\alpha 2\beta 1$ integrin- and DDR1-dependent Bmi-1. *J Cell Physiol*. déc 2011;226(12):3422-32.
 264. Ridley AJ. Life at the leading edge. *Cell*. 24 juin 2011;145(7):1012-22.
 265. Linkous A, Balamatsias D, Snuderl M, Edwards L, Miyaguchi K, Milner T, et al. Modeling Patient-Derived Glioblastoma with Cerebral Organoids. *Cell Rep*. 19 mars 2019;26(12):3203-3211.e5.
 266. Pasturel A, Strale P-O, Studer V. Tailoring Common Hydrogels into 3D Cell Culture Templates. *Advanced Healthcare Materials*. 2020;9(18):2000519.
 267. Reith A, Bjerkvig R, Rucklidge GJ. Laminin: a potential inhibitor of rat glioma cell invasion in vitro. *Anticancer Res*. juin 1994;14(3A):1071-6.
 268. Dolmetsch R, Geschwind DH. The human brain in a dish: the promise of iPSC-derived neurons. *Cell*. 10 juin 2011;145(6):831-4.
 269. Rao SS, Nelson MT, Xue R, DeJesus JK, Viapiano MS, Lannutti JJ, et al. Mimicking white matter tract topography using core-shell electrospun nanofibers to examine migration of malignant brain tumors. *Biomaterials*. juill 2013;34(21):5181-90.
 270. Han M, Wang S, Fritah S, Wang X, Zhou W, Yang N, et al. Interfering with long non-coding RNA MIR22HG processing inhibits glioblastoma progression through suppression of Wnt/ β -catenin signalling. *Brain*. 1 févr 2020;143(2):512-30.
 271. Wang E, Dimova N, Sperle K, Huang Z, Lock L, McCulloch MC, et al. Deletion of a splicing enhancer disrupts PLP1/DM20 ratio and myelin stability. *Exp Neurol*. déc 2008;214(2):322-30.
 272. Filbin MG, Tirosh I, Hovestadt V, Shaw ML, Escalante LE, Mathewson ND, et al. Developmental and oncogenic programs in H3K27M gliomas dissected by single-cell RNA-seq. *Science*. 20 avr 2018;360(6386):331-5.
 273. Brooks LJ, Clements MP, Burden JJ, Kocher D, Richards L, Devesa SC, et al. The white matter is a pro-differentiative niche for glioblastoma. *Nat Commun*. 12 avr 2021;12(1):2184.
 274. Ferguson SM, Brasnjo G, Hayashi M, Wölfel M, Collesi C, Giovedi S, et al. A selective activity-dependent requirement for dynamin 1 in synaptic vesicle endocytosis. *Science*. 27 avr 2007;316(5824):570-4.

275. Cheng W-Y, Chow K-C, Chiao M-T, Yang Y-C, Shen C-C. Higher Levels of Dynamin-related Protein 1 are Associated with Reduced Radiation Sensitivity of Glioblastoma Cells. *Curr Neurovasc Res.* 2020;17(4):446-63.
276. Kashatus DF, Lim K-H, Brady DC, Pershing NLK, Cox AD, Counter CM. RALA and RALBP1 regulate mitochondrial fission at mitosis. *Nat Cell Biol.* 7 août 2011;13(9):1108-15.
277. Archer SL. Mitochondrial Dynamics — Mitochondrial Fission and Fusion in Human Diseases [Internet]. <https://doi.org/10.1056/NEJMra1215233>. Massachusetts Medical Society; 2013 [cité 1 nov 2021]. Disponible sur: <https://www.nejm.org/doi/10.1056/NEJMra1215233>
278. Xie Q, Wu Q, Horbinski CM, Flavahan WA, Yang K, Zhou W, et al. Mitochondrial Control by DRP1 in Brain Tumor Initiating Cells. *Nat Neurosci.* avr 2015;18(4):501-10.
279. Wan Y-Y, Zhang J-F, Yang Z-J, Jiang L-P, Wei Y-F, Lai Q-N, et al. Involvement of Drp1 in hypoxia-induced migration of human glioblastoma U251 cells. *Oncology Reports.* 1 août 2014;32(2):619-26.
280. Darmanis S, Sloan SA, Croote D, Mignardi M, Chernikova S, Samghababi P, et al. Single-Cell RNA-Seq Analysis of Infiltrating Neoplastic Cells at the Migrating Front of Human Glioblastoma. *Cell Rep.* 31 oct 2017;21(5):1399-410.
281. Contreras-Baeza Y, Sandoval PY, Alarcón R, Galaz A, Cortés-Molina F, Alegría K, et al. Monocarboxylate transporter 4 (MCT4) is a high affinity transporter capable of exporting lactate in high-lactate microenvironments. *J Biol Chem.* 27 déc 2019;294(52):20135-47.
282. Owen OE, Kalhan SC, Hanson RW. The key role of anaplerosis and cataplerosis for citric acid cycle function. *J Biol Chem.* 23 août 2002;277(34):30409-12.
283. Dornenburg C, Fischer M, Barth TFE, Mueller-Klieser W, Hero B, Gecht J, et al. LDHA in Neuroblastoma Is Associated with Poor Outcome and Its Depletion Decreases Neuroblastoma Growth Independent of Aerobic Glycolysis. *Clin Cancer Res.* 15 nov 2018;24(22):5772-83.
284. Minami N, Tanaka K, Sasayama T, Kohmura E, Saya H, Sampetean O. Lactate Reprograms Energy and Lipid Metabolism in Glucose-Deprived Oxidative Glioma Stem Cells. *Metabolites.* 18 mai 2021;11(5):325.
285. Meiser J, Schuster A, Pietzke M, Vande Voorde J, Athineos D, Oizel K, et al. Increased formate overflow is a hallmark of oxidative cancer. *Nat Commun.* 10 avr 2018;9(1):1368.
286. Liu X, Cooper DE, Cluntun AA, Warmoes MO, Zhao S, Reid MA, et al. Acetate Production from Glucose and Coupling to Mitochondrial Metabolism in Mammals. *Cell.* 4 oct 2018;175(2):502-513.e13.
287. Mashimo T, Pichumani K, Vemireddy V, Hatanpaa KJ, Singh DK, Sirasanagandla S, et al. Acetate is a Bioenergetic Substrate for Human Glioblastoma and Brain Metastases. *Cell.* 18 déc 2014;159(7):1603-14.
288. Jiang W, Finniss S, Cazacu S, Xiang C, Brodie Z, Mikkelsen T, et al. Repurposing phenformin for the targeting of glioma stem cells and the treatment of glioblastoma. *Oncotarget.* 30 août 2016;7(35):56456-70.
289. Jung E, Alfonso J, Osswald M, Monyer H, Wick W, Winkler F. Emerging intersections between neuroscience and glioma biology. *Nat Neurosci.* déc 2019;22(12):1951-60.

290. Sada N, Lee S, Katsu T, Otsuki T, Inoue T. Epilepsy treatment. Targeting LDH enzymes with a stiripentol analog to treat epilepsy. *Science*. 20 mars 2015;347(6228):1362-7.

La plupart des figures ont été créés avec BioRender.com

Annexe

The Normal and Brain Tumor Vasculature: Morphological and Functional Characteristics and Therapeutic Targeting

Résumé :

Le GBM est l'une des tumeurs les plus courantes du SNC chez les adultes. La survie globale ne s'est pas améliorée de façon significative au cours de la dernière décennie et ce, même en optimisant les soins thérapeutiques standard.

Dans cette revue de la littérature, nous examinons les caractéristiques de la vascularisation cérébrale dans les tissus sains et dans le GBM. Les cellules non vasculaires telles que les astrocytes ou les cellules de la microglie interagissent également avec le système vasculaire et jouent des rôles importants. Nous discutons aussi des vaisseaux sanguins artificiels *in vitro* qui correspondent à des modèles utiles pour mieux comprendre l'interaction 3D tumeur-vaisseaux. Enfin, nous résumons les résultats d'essais cliniques avec l'utilisation de traitements antiangiogéniques seuls ou en combinaison et discutons de la valeur de ces approches pour cibler le GBM.



The Normal and Brain Tumor Vasculature: Morphological and Functional Characteristics and Therapeutic Targeting

Joris Guyon^{1†}, Candice Chapouly^{2†}, Laetitia Andrique^{1,3}, Andreas Bikfalvi^{1*} and Thomas Daubon^{4**}

¹INSERM, LAMC, U1029, University Bordeaux, Pessac, France, ²INSERM, Biology of Cardiovascular Diseases, U1034, University Bordeaux, Pessac, France, ³VoxCell 3D Plateform, UMS TBMcore 3427, Bordeaux, France, ⁴University Bordeaux, CNRS, IBGC, UMR 5095, Bordeaux, France

OPEN ACCESS

Edited by:

Sara Petrillo,
University of Turin, Italy

Reviewed by:

Maria Rodriguez Aburto,
University College Cork, Ireland
Nicolas Santander,
University of California,
San Francisco, United States

*Correspondence:

Thomas Daubon
thomas.daubon@u-bordeaux.fr
Andreas Bikfalvi
andreas.bikfalvi@u-bordeaux.fr

[†]These authors share first authorship

^{**}Lead Author

Specialty section:

This article was submitted to
Vascular Physiology,
a section of the journal
Frontiers in Physiology

Received: 28 October 2020

Accepted: 25 January 2021

Published: 05 March 2021

Citation:

Guyon J, Chapouly C, Andrique L, Bikfalvi A and Daubon T (2021) The Normal and Brain Tumor Vasculature: Morphological and Functional Characteristics and Therapeutic Targeting. *Front. Physiol.* 12:622615. doi: 10.3389/fphys.2021.622615

Glioblastoma is among the most common tumor of the central nervous system in adults. Overall survival has not significantly improved over the last decade, even with optimizing standard therapeutic care including extent of resection and radio- and chemotherapy. In this article, we review features of the brain vasculature found in healthy cerebral tissue and in glioblastoma. Brain vessels are of various sizes and composed of several vascular cell types. Non-vascular cells such as astrocytes or microglia also interact with the vasculature and play important roles. We also discuss *in vitro* engineered artificial blood vessels which may represent useful models for better understanding the tumor–vessel interaction. Finally, we summarize results from clinical trials with anti-angiogenic therapy alone or in combination, and discuss the value of these approaches for targeting glioblastoma.

Keywords: brain, glioblastoma, blood vessels, astrocyte, antiangiogenic therapy, vascular tissue engineering

INTRODUCTION

In vertebrates, vessels are built of an internal layer made of endothelial cells which are in contact with the blood and of mural cells that are composed of either smooth muscle cells (larger vessels) or pericytes (in capillaries). In the brain, blood vessels are tightly organized and participate in blood and brain tissue exchange via the blood–brain barrier (BBB).

Within the brain tumor vasculature, two different types of vessels are found, vessels formed by angiogenesis (neoangiogenic vessels) and preexisting vessels which may be co-opted by tumor cells (co-opted vessels). Anti-angiogenic strategies have been developed for targeting the brain tumor vasculature (Lakka and Rao, 2008). Unfortunately, clinical trials were not crowned with success (Chinot et al., 2014). A contributing factor is represented by a shift of tumor cells to a co-optive mode induced by anti-angiogenic therapy which contributes to tumor spread and development (Griveau et al., 2018).

In this article, we discuss the characteristics and specific features of the normal and brain tumor vasculature. We will also include in our discussion *in vitro* constructed artificial blood vessels by tissue engineering which represent an interesting tool to study tissue–vessel interactions and may also be useful in the tumor context. Finally, we will review some recent clinical studies using anti-angiogenic drugs in glioblastoma.

THE BLOOD–BRAIN BARRIER

In a healthy individual, the central nervous system (CNS) parenchyma is protected from the peripheral circulation by the BBB. This barrier comprises a network of blood vessels made of endothelial cells with unique features (**Figure 1** – healthy brain). Endothelial cells at the BBB act as gatekeepers to control soluble factors and immune cell trafficking into the vessel wall and underlying tissues, and both the transcellular and paracellular pathways are involved in this process.

The Paracellular Pathway

The paracellular pathway is modulated by the coordinated opening and closure of endothelial cell–cell junctions which involves a complex rearrangement of endothelium-specific transmembrane tight/adherens junction proteins and the related cytoskeleton. CNS tight junctions are primarily formed by Claudin5 and Occludin, and are coupled with the Zonula Occludens intracellular proteins (ZO1, ZO2, and ZO3) which form a scaffold between these transmembrane proteins and the actin cytoskeleton. Other Claudins may be involved in controlling endothelial cell paracellular barrier properties, as Claudin5 downregulation only leads to small size molecule leakage at the BBB (Nitta et al., 2003). Claudin1, Claudin3, and Claudin12 have been identified as potential candidates, but their role still needs to be clarified (Ohtsuki et al., 2008; Daneman et al., 2010a; Kooij et al., 2014). Members of the immunoglobulin superfamily, notably CAMs (PECAM1, ICAM1, and VCAM1), JAMs (JAM1–3), and Nectin proteins, clustered at CNS endothelial intercellular contacts, promote homotypic cell–cell adhesion and regulate inflammatory cell transmigration at the BBB (Del Maschio et al., 1999). Recent literature suggested that tricellular contacts, where the corners of three cells meet, can also be found in CNS endothelial cells. Specifically, tricellulin and angulin-1/lipolysis-stimulated lipoprotein receptor (LSR) were shown to participate to BBB paracellular control of plasmatic protein and immune cell trafficking (Iwamoto et al., 2014; Sohet et al., 2015). Importantly, tight junctions cannot be dissociated from adherent junctions in regulating BBB tightness; CNS endothelial adherent junctions are characterized by homophilic cadherin (VE-cadherin and N-cadherin) interactions controlling cell adhesion. Adherent junctions are linked to the cytoskeleton *via* their binding partner β -catenin and participate to BBB tightness through phosphorylation, cleavage, and internalization, or by modulating Claudin5 expression level (Meng and Takeichi, 2009).

The Transcellular Pathway

Aside from the paracellular pathway, brain nutrient intake and CNS toxin removal are highly regulated by solute transporters and receptor-mediated transcytosis at the BBB, and inflammatory cells are actively prevented from crossing the BBB by low levels of immune receptors that normally permit immune trafficking.

Specifically, the cerebral endothelium expresses a number of specific solute transporters to facilitate the carrier-mediated transport of glucose (glucose transporters: GLUT1), amino

acids (cationic amino acid transporters: CAT1, CAT3), monocarboxylic acids (monocarboxylate transporters: MCT1), hormones (thyroid hormone transporters: MCT8), fatty acids (fatty acid transporters: FATP-1), nucleotides (nucleoside transporters: ENT1, ENT2), ions (organic anion and organic cation transporters), amines, choline, and vitamins, which are otherwise excluded from the brain due to the paracellular pathway (Sweeney et al., 2019). Efflux mechanisms also contribute to barrier functions, with ATP-binding cassette transporters (P-gp: MDR1), breast cancer resistance protein (BCRP), and multidrug resistance-associated proteins (MRP 1–5) hydrolyzing ATP to actively pump drugs and their conjugates, xenobiotics, endogenous metabolites, and nucleosides across the luminal side of blood vessels into the circulation (Mahringer and Fricker, 2016; Sweeney et al., 2019).

Selective peptides and even large proteins can enter the brain by binding to receptors on endothelial cells via endocytosis (receptor-mediated transcytosis) (leptin receptors, transferrin receptors, and insulin receptors) (Preston et al., 2014). The BBB is characterized by extremely low rates of vesicular transport (transcytosis) which limits the transcellular passage across CNS barriers. It has been recently reported that the major facilitator superfamily domain containing 2a (Mfsd2a) is selectively expressed in CNS blood vessels and actively participates to BBB homeostasis by suppressing transcytosis in CNS endothelial cells (Ben-Zvi et al., 2014). Mfsd2a is located upstream of Caveolin-1 (Cav-1) (Chow and Gu, 2017), which is involved in regulating endothelial permeability, angiogenesis, and leukocyte diapedesis (Zhao et al., 2014), and VE-cadherin/catenin complex targets Cav-1 to endothelial cell junctions leading to BBB breakdown under permeability conditions (Kronstein et al., 2012).

These features exist within the majority of the CNS capillary population. However, it is worth noting that some regions of the CNS display a leaky BBB. These regions are grouped together under the term “circumventricular organs” which are regions of the brain sensing blood-borne signals. Morphologically, in the circumventricular organs, the capillaries are fenestrated with discontinuous tight junctions and thinner endothelial cells which contain more vesicles than capillaries of other parts of the CNS (Coomer and Stewart, 1985). This permits the two-way exchange of metabolic information: the delivery of neuro-hormones into the bloodstream by secretory organs and the sensing of blood-borne molecules by neurons in sensory organs. However, within the circumventricular organs, there is no direct passage of blood-borne substances in the parenchyma due to the presence of outer basement membrane but also astrocytes and tanycytes (ependymal cells sharing common features with radial glial cells and astrocytes) which are considered alternative CNS barriers (Langlet et al., 2013). The peculiar organization of the BBB within the circumventricular organs leads us to approach the CNS vascular barrier system from another angle by acknowledging its complex architecture which is not just a vascular endothelium. Indeed, it is more proper to consider it as a multi-cellular neurovascular unit comprising notably astrocytes, pericytes, basement membranes as well as blood vessels.

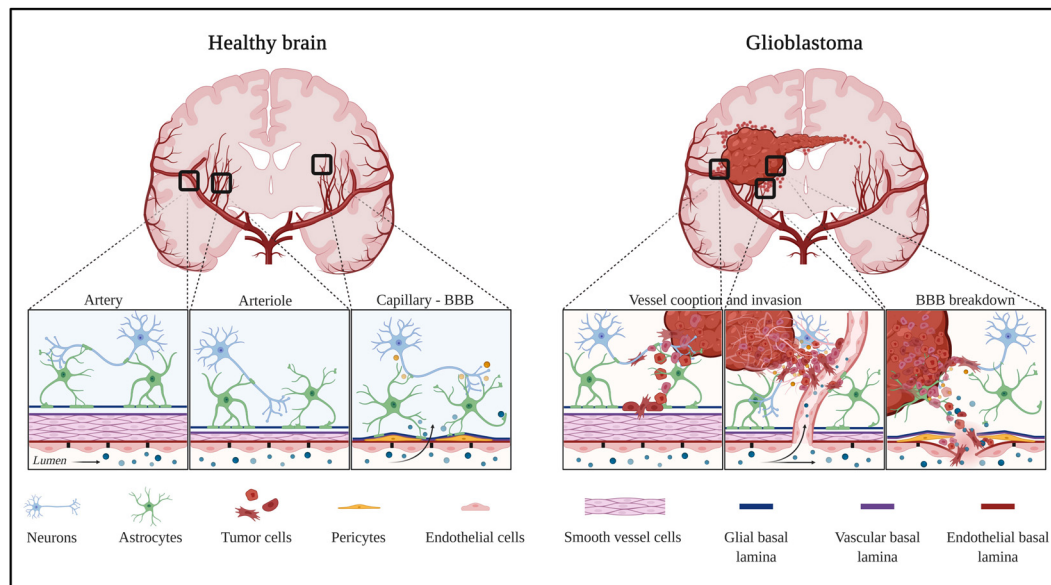


FIGURE 1 | Healthy and tumor brain vascular architecture: focus on artery, arteriole, and capillary. **Left panel:** in a healthy brain vasculature, endothelial cell monolayer is surrounded by a smooth muscle coat in arteries and arterioles, and is replaced by pericytes in the capillaries. The perivascular space is delimited by the vascular basement membrane and glial basement membrane. This space gradually diminished and the two basement membranes enter in direct contact to astrocytes endfeet. Molecules diffuse or are transported at the capillary level. **Right panel:** GBM is a highly angiogenic and infiltrative tumor. Cells invade along blood vessels to support tumor growth (co-option). GBM displaces astrocytes endfeet and alters pericyte stability, leading to perivascular niches and cell evasion. Created with Biorender.com.

THE NEUROVASCULAR UNIT, A MULTI-CELLULAR CNS-BARRIER STRUCTURE

A wealth of literature published during the last decades has enabled a change in the vision of the BBB, leading to the concept of a multi-cellular CNS-barrier structure. Indeed, substantial intercellular communication occurs between vascular cells (endothelial cells and pericytes) and the adjoining glia (Iadecola, 2017). More specifically, to enter the CNS from the vasculature, soluble factors and immune cells must traverse the endothelial BBB and the adjacent pericyte layer. Once soluble factors and immune cells penetrate the BBB, they circulate within the perivascular space, a region surrounding the basal surface of the endothelial cell wall, to reach the CNS parenchyma by passing through the glia limitans composed of the parenchymal basement membrane and the astrocyte endfeet (Engelhardt and Coisne, 2011; Engelhardt and Ransohoff, 2012).

Pericytes

Pericytes, strategically positioned along capillaries, play a critical role in the multi-cellular CNS barrier structure. Indeed, pericytes, sandwiched between endothelial cells and astrocytes, are dynamically and synergistically engaged in interactions with neighboring cells to maintain homeostasis of the CNS (Figure 1 – healthy brain). Pericytes are notably involved in the regulation of cerebral blood flow, neurovascular coupling and BBB homeostasis.

A role for pericytes in the regulation of microcirculatory blood flow has long been suspected (Armulik et al., 2011; Hall et al., 2014; Sweeney et al., 2016). Recent work demonstrated that pericytes synchronize microvascular blood flow dynamics and neurovascular coupling *via* nanotube-like processes called inter-pericyte tunneling nanotubes (IP-TNTs) which connect two pericytes on separate capillaries to form a functional network (Alarcon-Martinez et al., 2020). Pericytes are also part of the neurovascular unit and are most firmly attached to brain capillaries. They are involved in a crosstalk between endothelial cells and the surrounding cerebral tissue. Notably, it has been reported that pericytes interact with endothelial cells via specific adhesion sites that represent peg-and-socket junctions in the presence of *N*-cadherin (Sweeney et al., 2016), the single cell adhesion receptor CD146 (Chen et al., 2017), adhesion plaques containing fibronectin (Courtoy and Boyles, 1983), Connexin43 gap junctions (Cuevas et al., 1984), and even tight junctions (Larson et al., 1987). In a mouse model lacking pericyte coverage at the microvascular level, BBB integrity is compromised because of the transcellular barrier specific dysfunction (Sweeney et al., 2016) but also because of the loss of astrocytic endfeet polarization (Armulik et al., 2010). While pericytes are necessary for maintaining BBB integrity, astrocytic endfeet are also major actors in CNS barrier homeostasis.

Astrocytes

Astrocytes represent an important population of glial cells in the CNS and astrocytic endfeet create a thick continuous layer that covers BBB microvessels called the glia limitans

(Mathiisen et al., 2010) (**Figure 1** – healthy brain). Neural precursor cells represent the primary source of astrocytes which develop at late gestation stages in mammals (Daneman et al., 2010b; Cheslow and Alvarez, 2016). Therefore, it is commonly accepted that if astrocytes do not play a major role in BBB establishment, they strongly impact BBB maturation and maintenance.

Reducing the vascular coverage of the population of astrocytes and astrocytic endfeet in the early postnatal cerebral cortex leads to the formation of microvessels with an abnormally large diameter (Ma et al., 2012). In addition, astrocytes are actively involved in the production of the basement membrane embedding the glia limitans. Knocking down elements of the basement membrane results in the disruption of Aquaporin4 (AQP4) channel enrichment at the astrocytic endfeet membrane (Brightman, 2002; Lien et al., 2012; Menezes et al., 2014). This leads to BBB permeability and associated brain edema (Nagelhus and Ottersen, 2013).

Astrocytes maintain BBB integrity *via* the secretion of soluble factors. Astrocytes improve endothelial barrier function in co-culture or after administration of conditioned medium to CNS endothelial mono-culture (Igarashi et al., 1999; Alvarez et al., 2011; Podjaski et al., 2015). Astrocytes secrete soluble factors notably Sonic Hedgehog (Shh) (Alvarez et al., 2011), retinoic acid (RA) (Mizee et al., 2014), glial-derived neurotrophic factor (GDNF) (Igarashi et al., 1999), and angiopoietin 1 (Ang-1) (Suri et al., 1996; Pfaff et al., 2006) which reduce permeability.

Blood–brain barrier integrity in the cerebellum, spinal cord, and olfactory bulbs relies on astrocyte-derived Wnt-like ligand Norrin which interacts with the endothelial Frizzled4 receptor. Knocking down the Norrin/Frizzled4 signaling leads to BBB defects through β -catenin–dependent transcriptional regulation (Zhou et al., 2014).

Astrocytes also express members of the ephrin receptor (EphR)/ephrin family (Nestor et al., 2007) which may impact BBB homeostasis. Notably, EphA4 receptor is expressed by glial cells especially around blood vessels in the adult marmoset (Goldshmit et al., 2014). EphA4 also plays a role in vascular formation and guidance during CNS development in mice. The proper interaction between the EphA4 receptor and its astrocytic ephrinA5 ligand is necessary for the development of a normal vascular system in the hippocampus of adult mice (Goldshmit et al., 2006; Hara et al., 2010).

Hence, based on these strong arguments, it is now recognized that the vascular component in the CNS is inseparably linked to glial and neuronal partners. Therefore, it is necessary to consider the neurovascular unit as a whole (and not only the BBB) in vascular pathophysiology and targeted therapeutic strategies.

Glioblastoma Disrupts The Normal Brain Architecture And Molecular Interactions

Basic Characteristics of Glioblastoma

Diffuse gliomas are brain tumors classified into IDH1mut and WT tumors (Louis et al., 2016). Glioblastomas (grade IV gliomas) are generally IDH WT tumors and represent the most aggressive form with an extremely poor prognosis. It is now

admitted that glioblastoma (GBM) are mainly derived from neural stem cells, giving rise to transformed cells with astrocytic, neuronal, or oligodendrocytic characteristics (Alcantara Llaguno et al., 2009; Zong et al., 2012). Accumulation of genetic mutations, alterations, and amplifications play a central role in the transformation of healthy neural stem cells. Typical alterations in primary GBM are represented by amplification or mutation of PTEN, NF1, CDKN2A/B, and RB genes, or homozygous deletion or mutation of MDM2, CDK4, EGFR, PDGFR α , and PI3K genes. Typical histopathological features of GBM comprise highly proliferative cells with multinuclei, areas of necrosis surrounded by pseudopalisading cells, and endothelial cell proliferation with numerous clusters of blood vessels forming so-called glomeruloid structures. In 1938, Scherer highlighted several modes of GBM invasion: interstitial invasion, white matter tract invasion, and perivascular invasion (Scherer, 1940). GBM invasion relies on genetic alterations such as overexpression, amplification, deletion, or mutation in focal adhesion kinase (FAK) and phosphatidylinositol 3-kinase (PI3K) pathways. Activation of growth factors and their receptors are mainly involved in promoting invasion. These include CD44, integrins, osteonectin (SPARC), transforming growth factor (TGF) α/β , and receptors for platelet-derived growth factor (PDGF), fibroblast growth factor (FGF-2), and epidermal growth factor (EGF). Extracellular matrix components such as thrombospondins, laminins, or fibronectin are also overexpressed in GBM and their inhibition reduces invasiveness of GBM cells (Serres et al., 2014; Chouleur et al., 2020). Indeed, we and others characterized the role of thrombospondin-1 (which was primarily described as anti-angiogenic molecule) in GBM development and invasion (Daubon et al., 2019).

Glioblastoma is the most common brain tumor in Europe, in the United States, or in China, with more than 50% of glioma cases each year, and with an incidence of 3.2 per 100,000 people each year in the United States. Increasing incidence in populations from several countries were observed, suggested by authors as consequences of environmental or lifestyle factors (Philips et al., 2018). The 5-year overall survival (OS) rate is very low of only 5.1%, even with standard-of-care treatment (large tumor resection, chemo- and radiotherapy, so-called Stupp protocol). GBM are often only diagnosed at an advanced stage of the disease and often only detected when patients present symptoms (headaches, seizures, memory loss, loss of movements, cognitive impairments, and language dysfunctions). The poor response to therapy is partially explained by high intratumor heterogeneity, leaky and tortuous blood vessels in the central part, and intact BBB surrounding invasive cells, which leads to difficulties for therapeutic molecules to reach these sites (**Figure 1** – glioblastoma).

Metabolic Interactions Between GBM Cells and the Endothelium

Glioblastoma is considered as one of the most glycolytic human tumors. High glycolytic flux drive production of pyruvate from glucose, and then pyruvate into lactate by lactate dehydrogenases, to regenerate NAD⁺ to support glycolytic flux by fulfilling the

demand for ATP and other metabolic precursors. As previously described in striated muscles and also in the brain, lactate is, in turn, retro-converted into pyruvate by oxygenated tumor cells to feed oxidative metabolism. This phenomenon was described in the seminal publication of Pellerin et al. (1998) as lactate shuttle between astrocytes and neurons. Vegran et al. (2011) also demonstrated a lactate shuttle between tumor cells and endothelial cells, mainly *via* endothelial monocarboxylate transporter 1 (MCT1). More recently, MCT1 was also identified as a key mediator of lactate signaling between glioma cells and brain endothelial cells (Miranda-Gonçalves et al., 2017). Targeting symbiotic metabolism between GBM and endothelial cells may represent an interesting therapeutic strategy.

Involvement of Pericytes and Astrocytes in Glioblastoma Vascular Pathophysiology

The chronic hyper-permeability of blood vessels is a hallmark of glioblastoma. We focus herein our attention on the role of pericytes and astrocytes in disrupting the BBB in glioblastoma.

Role of Pericytes

Glioblastoma vessels are characterized by numerous structural and functional abnormalities, including altered association between endothelial cells and pericytes. These dysfunctional, unstable vessels contribute to hypoxia, interstitial fluid pressure, and enhanced susceptibility to metastatic invasion (Barlow et al., 2013). An interesting feature of glioblastoma pericytes is that they represent one of the active cell components of the perivascular niche. It has been reported that cancer stem cells, which are closely associated with tumor vessels, trans-differentiate into endothelial cells or pericytes (Wang et al., 2010; Cheng et al., 2013), a phenomenon described as vasculogenic mimicry (VM). VM was also shown to be promoted by tumor-associated macrophages (TAMs) by increasing the expression of cyclooxygenase 2 in the tumor cells (Rong et al., 2016) and has been associated with poor patient prognosis. However, the significance of VM in GBM is still debated and not universally accepted. Furthermore, tumor-derived pericytes exhibit specific genetic alterations that allow for discrimination between them and normal pericytes (Cheng et al., 2013), which may be relevant for diagnosis and therapy. Finally, pericytes were shown to promote evasion from the anti-tumor immune response favoring tumor growth (Figure 1 – glioblastoma). Glioblastoma-dependent immunosuppressive function in pericytes is mediated by the expression of anti-inflammatory molecules such as IL-10, TGF- β , and MHC-II (Valdor et al., 2017).

Role of Astrocytes

Reactive astrocytes are an integral part of the glioblastoma micro-environment and are characterized by hypertrophy, upregulation of intermediate filaments (vimentin and glial fibrillary acidic protein), and increase in proliferation. The role of reactive astrocytes in the pathophysiology of glioblastoma has been widely documented in the literature. Astrocyte–glioma crosstalk was shown to drive migration, proliferation, and invasion of glioblastoma (Guan et al., 2018). However, only few works

focused on the contribution of astrocytes to the aberrant organization of the BBB in these tumors.

The participation of astrocytes to BBB permeability in glioblastoma is documented by the loss of astrocytic endfeet polarity which is characterized by Aquaporin-4 (AQP4) redistribution to membrane domains apart from endfeet areas (Kröger et al., 2004). This re-localization is probably due to the degradation of the proteoglycan agrin by the matrix metalloproteinase 3 (MMP3). Consequently, the water transport is compromised leading to edema. This, in turn, may drive BBB breakdown characterized by disrupted tight junctions leading to the development of vasogenic edema. However, how the loss of polarity is linked to the disturbance of microvascular tight junctions is still not understood (Wolburg et al., 2012). Using a clinically relevant mouse model of glioblastoma, it has been shown that tumor cells populate the perivascular space of preexisting vessels and displace astrocytic endfeet from endothelial or mural cells. This leads to abnormal BBB permeability and loss of astrocyte-mediated gliovascular coupling which pave the way for glioma cells to take control of vascular tone regulation (Watkins et al., 2014). This phenomenon, known as blood vessel co-option, is a strategy for glioblastoma to invade distant sites of the brain parenchyma (Figure 1 – glioblastoma). Vessel co-opting GBM cells directly obtain oxygen and nutrients from the blood. The interactions with the vascular niche stimulate proliferation and self-renewal of GBM cells.

There is still much to explore as reactive astrocytes have already been identified as key players impacting the state of the BBB in various diseases (Liebner et al., 2018). They are likely to also play an important role in vessel hyper-permeability of GBM.

VASCULAR TISSUE ENGINEERING AND ITS POTENTIAL FOR THE STUDY OF GBM–VESSEL INTERACTIONS

The tumor vasculature is critically involved in GBM development. This has led to clinical trials using anti-angiogenic drugs but with mixed results (Chinot et al., 2014). It has been postulated that anti-angiogenic treatment may impact tumor cell behavior by shifting them from an angiogenic to a co-optive behavior (Griveau et al., 2018). Thus, it is important to better understand more rigorously how tumor cells and vessels interact. A number of experimental models have been proposed in this context.

There are two classic and widely used models to study the role of the vasculature in tumor growth: the *in vivo* chick chorio-allantoic membrane (CAM) assay (Lokman et al., 2012) and the *in vivo* mouse/rodent graft model (Eklund et al., 2013). These two models are based on grafting tumor cells on the membrane of a growing chicken or in a specific site in mouse. If the chick model follows to some extent better the 3R rule (replacement, reduction, and refinement; Aske and Waugh, 2017) as considered as less sentient living beings due to not fully active nervous system, it is nevertheless necessary to develop alternative models that are closer to the human situation.

During the last decade, tissue engineering led to the development of artificial vessels which can be used for tissue vascularization in a 3D environment. These *in vitro* models may represent a promising alternative to animal models.

Regarding studies related to tumor–vessel interactions, it is important to note that cancer cells are involved in two phenomena: inducing vessel sprouting (angiogenesis) and transmigrating through the blood vessel wall (endothelial cells, smooth muscle cells, and matrix) for dissemination. The latter phenomenon is difficult to study in both CAM and mouse models. It is therefore necessary to develop *in vitro* models that are closer to the human situation. During the last decade, tissue engineering led to the development of artificial human vessels which can be used for tissue vascularization in a 3D environment. These *in vitro* models, which harbor all the histological components of a blood vessel (lumen, endothelium, smooth muscle cells, and matrix), must also retain its mechanical properties such as liquid-tightness, perfusability, and contractility.

Tissue-Engineered Blood Vessels

Since the 1950s, synthetic tubes were the first choice for vascular reconstruction and grafts in patients with cardiovascular diseases. These conducts were made of polymer materials like expanded polytetrafluoroethylene (ePTFE), polyethylene terephthalate (Dacron), and polyurethane (Kannan et al., 2005), but all the functional characteristics of a blood vessel were not maintained in these tubes: they were not contractile and are not immune to thrombosis or inflammation. Motivated by these limitations, the development of 3D tissue-engineered blood vessels (TEBVs) has progressed significantly over the past two decades. Indeed, TEBVs tend to better match the biomechanical properties and the physiological responses of healthy blood vessels.

Tissue-engineered blood vessels can be not only used for vascular grafts but also for mechanical studies related to the tumor–vessel interaction. For all the aforementioned reasons, engineering of artificial blood vessels is not an easy task and has been for a long time restricted to big diameter arteries (>6 mm) (Niu et al., 2014), and were usually made of synthetic polymers without endothelial of smooth muscle cell. Recently, efforts have been made to produce smaller blood vessels (<2 mm) by the use of various approaches (Song et al., 2018) (Figure 2A).

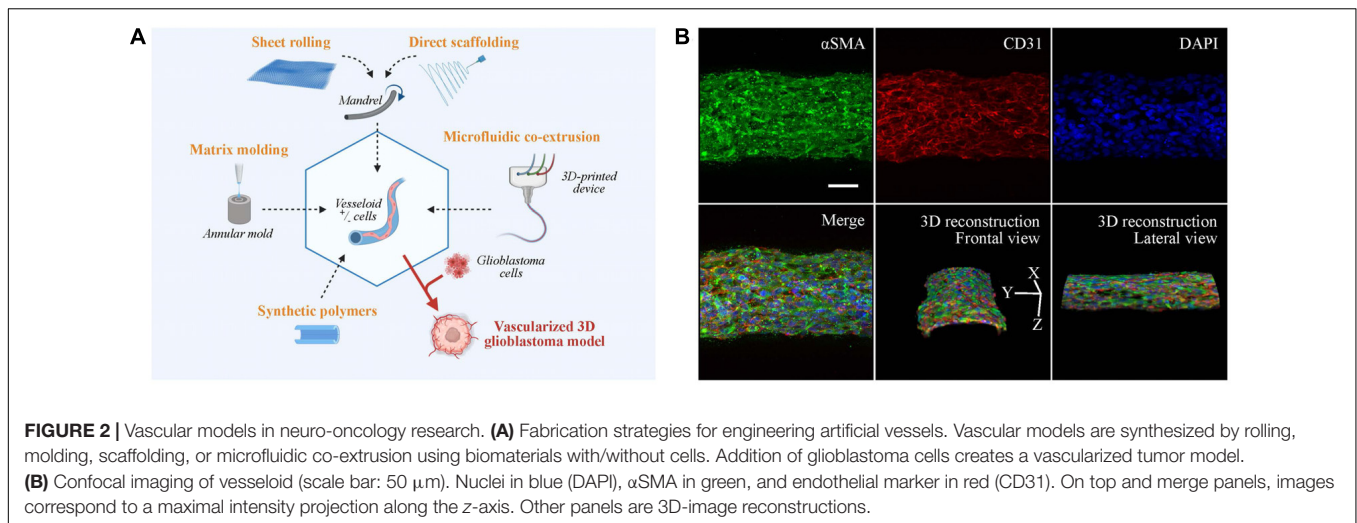
The production of tubular structures is achieved by three commonly used techniques: sheet rolling, tubular molding, and direct scaffolding. The sheet rolling technique is based on the creation of a sheet with the biomaterial of your choice and on the rolling of several sheets together for generating a tubular structure (Peck et al., 2011). Weinberg and Bell (1986) first described the use of a tubular mold that was filled with the desired cells and matrix. Finally, most of the biopolymers can be directly injected in a tubular form by direct scaffolding, but the major issue for all these techniques is the long-term culture of blood vessel. As an example, two pioneered groups (Roger Kamn and Lance Munn) developed in 2011 and 2012 microfluidic channels surrounded by 3D hydrogels using microfabricated silicone molds (Song and Munn, 2011; Shin et al., 2012). The

point was to put endothelial cells in 2D culture on top of these hydrogels to mimic vessel sprouting and invasion inside a tissue. These models were subsequently improved by mixing stroma and tumor cells inside the hydrogel for tumor angiogenesis studies. A recent paper by Andrique et al. (2019) used a co-extrusion microfluidic device to produce small-diameter artificial vessels (<500 μ m) with both endothelial and smooth muscle cells, surrounded by a scaffold made of biocompatible alginate polymer. These “vesseloids” are rapidly formed (only 1 day of culture) easy to handle, perfusable, liquid-tight, and retain their vascular functions (contractility, response to inflammatory stimuli) (Figure 2B). Vesseloids may be used as trunks for angiogenic sprouts to emerge which are useful for organ or tumor vascularization.

Controlled Microenvironment in 3D *in vitro* Models

3D co-culture systems including tumors cells, endothelial cells (blood vessels), and other micro-environmental components have emerged for reproducing tumor–stroma interactions. It was shown that tissue stiffness modulate tumor growth and nutrient transport (Massa et al., 2017). This is critical and must be considered for drug testing in cancer therapy. The major advantage of 3D co-culture models relies on the fact that various parameters can be controlled: type and density of the ECM components (e.g., Matrigel, collagen, PEG, fibronectin, and gelatin methacryloyl), stiffness, hypoxia and gas exchange, and the inclusion of various cell types such as macrophages, astrocytes, or vascular cells.

3D systems, which do not include the vascular component, already improve phenotypic properties, gene expression, and drug response. The importance of the environment in drug delivery testing was already highlighted by Seo et al. (2014). They explained that new anti-cancer drugs are usually tested in 2D tissue culture which neglects the complexity of the 3D micro-environment (Langhans, 2018). The development of 3D *in vitro* tissue-engineered models will help to refine the drug response and contribute to the improvement of anti-cancer therapies. More recently, striking differences in gene expression between 2D and 3D culture of GBM have been reported (Ma et al., 2018) which mirrored the phenotypic differences. This is in agreement with another study (Chaicharoenaudomrung et al., 2020) where GBM cells were cultured in Ca-alginate 3D scaffolds before next-generation sequencing (Illumina), and this uncovered cellular pathways (Map kinase, autophagy, and cell metabolism) for 3D different to 2D cultures. Musah-Eroje and Watson (2019) developed a new 3D model of GBM which seems to more accurately reflect the complexity of the GBM micro-environment. Compared with regular 2D cultures or spheroids, they showed that GBM cells in the 3D model were more resistant to temozolomide and that this resistance was potentiated by hypoxia. One unresolved issue regarding 3D brain organoid models is the lack of functional vascularization. Recently, Cakir et al. (2019) developed with success *in vitro* functional vasculature-like networks in human cortical organoids (hCOs) from human embryonic



stem cells (hESCs). In this work, endothelial reprogramming in hCOs induced the formation of organoids with vascular-like structures. These vascular structures are functional and exhibit BBB characteristics. Close to this work, a recent model of vascularized human cortical organoids (vOrganoids) was developed by Shi et al. (2020) (Vascularized human cortical organoids (vOrganoids) model cortical development *in vivo* 2020 PLOS One). These vOrganoids (human cortical cell types with vasculature structure) presented bidirectional electrical transmission through functional synapses, and their transplantation in the mouse cortex resulted in the survival of the graft. All these innovative 3D models represent useful models for studies related to physiology or pathology and may be useful as a model for therapeutic studies.

3D Co-Culture Models of Tumor and Endothelial Cells

The ultimate step of these 3D tumor models is the inclusion of endothelial and/or pericytes/smooth muscle cells to mimic blood vessels to produce vascularized tissues. A number of these works were done in tumor types other than glioblastoma. For example, Silvestri et al. (2020) developed a tissue-engineered model of a 3D co-culture of microvessels and mammary tumor organoids. They first fabricated a collagen gel scaffold with cylindrical channels filled with endothelial cells as a microvessel device. After perfusion and verification of the microvessels permeability, mammary tumor organoids were introduced inside of the 3D collagen scaffold and tumor cell–endothelial cell interactions were analyzed by live imaging. Others went further and developed a tri-culture metastatic model of breast cancer (Cui et al., 2020). By stereolithography 3D printing, a complex tripartite tissue was created which is composed of bone, vessels, and breast cancer cells. This model was used to study mechanisms of bone metastasis. Wang et al. (2014) have developed a 3D model to observe tumor invasion with high spatial and temporal resolution. Furthermore, intravasation and extravasation were observed at high spatial resolution using microvessels embedded in collagen 3D matrix and mixed with

cancer cells (Langhans, 2018). As for glioblastoma, McCoy et al. (2019) generated GBM spheroids of uniform size distribution, and embedded them into collagen hydrogels to investigate GBM invasion into the ECM of the perivascular niche. They also showed by co-culturing endothelial and GBM cells that GBM cells have a high stemness potential and invasion capacity dependent on IL-8 signaling. Thus, tumor vasculature models may be very useful to shed light into the complex interactions between the vasculature and tumor cells.

REVIVAL OF ANTI-ANGIOGENIC THERAPY: COMBINATION WITH OTHER DRUGS

Anti-Angiogenic Background

To date, bevacizumab is the only anti-angiogenic drug admitted for GBM management. Based on the results of three different clinical studies (Table 1), bevacizumab was approved by the Food and Drug Administration (FDA), the Japanese Ministry of Health, Labour and Welfare (MHLW), and other countries as a combination treatment with standard therapy and as a single agent for relapsed or progressive GBM after previous therapy. However, the OS was not prolonged in these studies; bevacizumab showed nevertheless some benefit in decreasing the use of corticosteroids, the adverse effects of which impair patient's quality of life. However, the European Medicine Agency (EMA) has not approved its indication, estimating that the benefit–risk assessment is not in favor of its prescription in the management of GBM. This is also supported by the National Institute for Health and Care Excellence (NICE) guidelines (NICE, 2018). It is important to emphasize that bevacizumab cannot be used a month before and after brain surgery. This must be considered when using this treatment. Of note, the pharmacokinetics and bioavailability of bevacizumab is limited since it cannot cross the intact BBB which is nevertheless partially disrupted to allow drug penetration to some extent.

TABLE 1 | Pivotal clinical trials supporting the approval indication.

| Study name or ID | Design | Treatment arms | Median PFS (1) vs (2) | Median OS (1) vs (2) |
|--|--|--|--|--|
| AVAglio (NCT00943826) (Chinot et al., 2014) (new dig GBM) | Randomized, double-blinded, placebo-controlled Phase III (N = 921) | (1) RT + TMZ + Placebo (N = 463) (2) RT + TMZ + Bev (N = 458) | *6.2 (6.0–7.5) vs. 10.6 (10.0–11.4) months; HR = 0.64 (0.55–0.74); $p < 0.001$ | *16.7 (15.4–18.4) vs. 16.8 (15.5–18.5) months; HR = 0.88 (0.76–1.02); $p = 0.1$ |
| RTOG0825 (NCT00884741) (new dig GBM) | Randomized, double-blinded, placebo-controlled Phase III (N = 637) | (1) RT + TMZ + Placebo (N = 317) (2) RT + TMZ + Bev (N = 320) | *7.3 (5.6–7.9) vs. 10.7 (10.0–12.2) months; HR = 0.79 (0.66–0.94); $p = 0.004$ | *16.1 (14.8–18.7) vs. 15.7 (14.2–16.8) months; HR = 1.13 (0.93–1.37); $p = 0.11$ |
| EORTC26101 (NCT01290939) (Wick et al., 2017) (recurrent GBM) | Randomized Phase III (N = 437) | (1) Lomustine alone (N = 149) (2) Lomustine + Bev (N = 288) | #1.5 (1.5–2.5) vs. 4.2 (3.7–4.3) months; HR = 0.49 (0.39–0.61); $p < 0.001$ | *8.6 (7.6–10.4) vs. 9.1 (8.1–10.1) months; HR = 0.95 (0.74–1.21); $p = 0.65$ |

RT, radiotherapy; TMZ, temozolomide; Bev, bevacizumab; PFS, progression-free survival; OS, overall survival. *Primary outcome measure. #Secondary outcome measure.

Revival of Bevacizumab and Anti-Angiogenic Therapy

Bevacizumab alone is certainly not a curative treatment for GBM and this raises ethical issues related to the benefit–risk of this treatment between the improvement of the patients' quality of life and frequent occurrence of serious side effects. Security data of clinical trials, as pharmacovigilance studies, have shown frequent and serious cardiovascular effects (hemorrhages, thromboembolic events, and heart failure) and hematological disorders (neutropenia, leukopenia, and thrombocytopenia) (Chinot et al., 2014; Gilbert et al., 2014; Wick et al., 2017). On theoretical grounds, the use of anti-angiogenic drugs may be justified due to physiopathological consideration (high expression of VEGF, BBB dysfunction, edema leading to hemorrhages, cognitive impairment, tumor growth, and cell invasion). Better outcomes may be observed when anti-angiogenic therapy is combined with inhibitors of tumor cell invasion or in combination with immunotherapy as documented in some studies (Kang et al., 2015; Piao et al., 2016; Gravina et al., 2017; Daubon et al., 2019).

A short review of the last-5-years published clinical trials is shown in **Table 2**, using the following parameters from PubMed: key words = Glioblastoma AND Antiangiogenic; filters = Abstract available, Clinical Trial; date = between 2015 and 2020. As no clinical trials of phase III were found, articles related to phase II studies, describing new associations or new indications with bevacizumab or new individual anti-angiogenic drugs, were selected if median progression-free survival (mPFS) or the median overall survival (mOS) outcomes were available and if the trial was referenced in <https://clinicaltrials.gov/>. mPFS and mOS reflect more robust outcomes than response rate. Eighteen clinical trials were found using these inclusion criteria.

New Investigations for Bevacizumab

Certain populations are under-represented in global clinical trials. This has led to the investigation of the efficacy of bevacizumab in newly diagnosed GBM (nGBM) in the elderly (ARTE, Wirsching et al., 2018 and ATAG,

Reyes-Botero et al., 2018 studies) and in pediatric populations (HERBY study, Grill et al., 2018). The ARTE study showed that when radiotherapy associated with bevacizumab, it did not prolong mOS compared with radiotherapy only (12.2 vs 12.1 months; HR = 1.09; $p = 0.75$). However, mPFS was favorable with bevacizumab in restricted *per* protocol analyses (7.6 vs 4.8 months; HR = 0.36; $p = 0.001$) (Wirsching et al., 2018). In combination with temozolomide, bevacizumab seemed active in the ATAG study and had an acceptable adverse effect profile (Reyes-Botero et al., 2018). As for the pediatric population, adjunction of bevacizumab to the current therapy did not improve mOS (18.3 vs 20.3 months; HR = 1.23; $p = 0.46$) (Grill et al., 2018). The results in the pediatric population differ from adults, and, thus, further research is needed.

New Associations With Bevacizumab

Glioblastomas are associated with increased stimulation of different signaling pathways. Trials have been run with bevacizumab combined with molecules interfering with these pathways. The association of bevacizumab with BKM 120–buparlisib, an oral PI3K inhibitor, did not improve outcome (mPFS: 2.8 to 5.3 months; mOS: 6.6 to 10.8 months) and increased the adverse drug effect profile (Hainsworth et al., 2019). In another study, mOS in the arm of bevacizumab combined with dasatinib, a Src signaling inhibitor, is similar to the placebo arm (7.3 vs 7.9 months; HR = 0.92; $p = 0.7$) (Galanis et al., 2019). In two trials, addition with bevacizumab to the histone deacetylase inhibitors vorinostat (Ghiesseddin et al., 2018) and panobinostat (Lee et al., 2015) failed to improve outcome compared with control (mPFS: 3.7 and 5 months; mOS: 10.4 and 9 months, respectively). When bevacizumab is combined with onartuzumab, a monovalent MET inhibitor, it did also not improve patient outcome versus bevacizumab plus placebo alone (mPFS: 3.9 vs 2.9 months; HR = 1.06; $p = 0.74$ and mOS: 8.8 vs 12.6 months; HR = 1.45; $p = 0.14$) (Cloughesy et al., 2017). The GLARIUS trial aimed to study the association of bevacizumab with irinotecan, a topoisomerase 1 inhibitor, comparing with temozolomide alone in nGBM with un-methylated MGMT

TABLE 2 | Phase II clinical trials recently published.

| Study name or ID | Indication | Design | Treatment arms | Outcomes (months) | |
|--|---|---|--|--|--|
| | | | | mPFS | mOS |
| NCT01349660 (Hainsworth et al., 2019) | Relapsed or refractory GBM following first-line therapy | Non-randomized, single group assignment, open label (N = 76) | BKM 120 (buparlisib) <i>per os</i> + Bev (1) Prior anti-angiogenic therapy (N = 19) (2) Without previous anti-angiogenic therapy (N = 57) | * ⁽¹⁾ 2.8 (1.6–5.3) * ⁽²⁾ 5.3 (3.6–9.2) | # ⁽¹⁾ 6.6 (4.0–14.6) # ⁽²⁾ 10.8 (9.2–13.5) |
| NCT01753713 (Sharma et al., 2019) | Recurrent or progressive GBM following first-line therapy | Non-randomized, parallel assignment, open label (N = 33) | (1) Dovitinib <i>per os</i> in anti-angiogenic naïve patients (N = 19) (2) Dovitinib <i>per os</i> in progressed GBM on previous anti-angiogenic therapy (N = 14) | # ⁽¹⁾ 2.0 (1.3–3.7) # ⁽²⁾ 1.8 (0.9–1.8) | # ⁽¹⁾ 8.0 (4.4–11.7) # ⁽²⁾ 4.3 (2.6–6.7) |
| NCT00892177 | Recurrent or progressive GBM | Randomized, parallel assignment, double blinded (N = 12(1)) | (1) Bev + dasatinib <i>per os</i> (N = 83) (2) Bev + placebo (N = 38) | | # ⁽¹⁾ 7.3 (6.2–9.7) vs. # ⁽²⁾ 7.9 (6.6–11.3); HR = 0.92 (0.61–1.4); $p = 0.7$ |
| REGOMA (NCT02926222) (Lombardi et al., 2019) | Relapsed GBM after surgery | Randomized, parallel assignment, open label (N = 119) | (1) Regorafenib <i>per os</i> (N = 59) (2) Lomustine <i>per os</i> (N = 60) | | * ⁽¹⁾ 7.4 (5.8–12.0) vs (2) 5.6 (4.7–7.3); HR = 0.5 (0.33–0.75); $p = 0.0009$ |
| ARTE (NCT01443676) (Wirsching et al., 2018) | Newly diagnosed GBM in elderly patients | Randomized, parallel assignment, open label (N = 75) | (1) RT (N = 25) (2) RT + Bev (N = 50) | # ⁽¹⁾ 4.8 vs (2) 7.6; HR = 0.36 (0.20–0.65); $p = 0.001$ | * ⁽¹⁾ 12.1 vs (2) 12.2; HR = 1.09 (0.63–1.89); $p = 0.75$ |
| ATAG (NCT02898012)(Reyes- Botero et al., 2018) | GBM in elderly patients with a Karnofsky performance status < 70 | Non-randomized, single group assignment, open label (N = 66) | TMZ + Bev (N = 66) | #3.8 (3.2–4.8) | *6 (4.8–6.9) |
| HERBY (NCT01390948) (Grill et al., 2018) | Newly diagnosed GBM in pediatric and adolescent patients | Randomized, parallel assignment, open label (N = 12(1)) | (1) RT + TMZ (N = 59) (2) RT + TMZ + Bev (N = 62) | | # ⁽¹⁾ 20.3 (14.8–33.8) vs. (2) 18.3 (16.2–25.7); HR = 1.23 (0.72–2.09); $p = 0.46$ |
| NRG/RTOG (NCT01609790) (Reardon et al., 2018) | Recurrent GBM | Randomized, parallel assignment, double blinded (N = 115) | (1) Bev + placebo (N = 58) (2) Bev + trebananib (N = 57) | # ⁽¹⁾ 4.8 (3.8–7.1) vs. (2) 4.2 (3.7–5.6); HR = 1.51 (1.02–2.24); $p = 0.04$ | # ⁽¹⁾ 11.5 (8.4–14.2) vs (2) 7.5 (6.8–10.1); HR = 1.46 (0.95–2.27); $p = 0.09$ |
| NCT01738646 (Ghiaseddin et al., 2018) | Recurrent GBM | Non-randomized, single group assignment, open label (N = 40) | Bev + vorinostat (N = 40) | #3.7 (2.9–4.8) | #10.4 (7.6–12.8) |
| NCT00704288 (Cloughesy et al., 2018) | Recurrent or progressive GBM following previous anti-angiogenic therapy | Non-randomized, single group assignment, open label (N = 222) | Cabozantinib <i>per os</i> (N = 70) (1) 140 mg/day (N = 12) (2) 100 mg/day (N = 58) | #2.3 overall (1) 3.3– 2) 2.3 | #4.6 (3.0–5.6) overall (1) 4.1– 2) 4.6 |
| NCT00704288 (Wen et al., 2018) | Recurrent or refractory GBM following non-anti-angiogenic therapy | Non-randomized, single group assignment, open label (N = 222) | Cabozantinib <i>per os</i> (N = 152) (1) 140 mg/day (N = 34) (2) 100 mg/day (N = 118) | #3.7 overall | # ⁽¹⁾ 7.7 # ⁽²⁾ 10.4 |
| GO27819 (NCT01632228) (Cloughesy et al., 2017) | Recurrent GBM | Randomized, parallel assignment, double blinded (N = 129) | (1) Bev + onartuzumab (N = 64) (2) Bev + placebo (N = 65) | * ⁽¹⁾ 3.9 vs. (2) 2.9; HR = 1.06 (0.72–1.56); $p = 0.74$ | # ⁽¹⁾ 8.8 vs. (2) 12.6; HR = 1.45 (0.88–2.37); $p = 0.14$ |
| NCT01846871 (Kalpathy-Cramer et al., 2017) | Recurrent GBM | Non-randomized, single group assignment, open label (N = 10) | Tivozanib | #2.3 (1.5–4) | #8.1 (5.2–12.5) |

(Continued)

TABLE 2 | Continued

| Study name or ID | Indication | Design | Treatment arms | Outcomes (months) | |
|---|--|--|--|---|---|
| | | | | mPFS | mOS |
| NCT01067469 (Weathers et al., 2016) | Recurrent GBM | Randomized, single group assignment, open label (N = 69) | (1) Bev (N = 36) (2) Bev low doses + lomustine (N = 33) | * ⁽¹⁾ 4.11 (2.96–5.55) * ⁽²⁾ 4.34 (2.96–8.34) | # ⁽¹⁾ 8.3 (6.42–11.58) # ⁽²⁾ 9.6 (6.26–16.73) |
| GLARIUS (NCT00967330) (Herrlinger et al., 2016) | Newly diagnosed GBM and a non-methylated MGMT promoter | Randomized, parallel assignment, open label (N = 182) | (1) Bev + irinotecan (N = 122) (2) TMZ (N = 60) | # ⁽¹⁾ 9.7 (8.7–10.8) vs. (2) 6.0 (2.7–6.2); HR = 0.59 (0.42–0.82); <i>p</i> = 0.001 | # ⁽¹⁾ 16.6 (15.4–18.4) vs. (2) 17.3 (14.8–20.4); HR = 0.96 (0.68–1.35); <i>p</i> = 0.83 |
| NCT00667394 | Recurrent GBM | Non-randomized, parallel assignment, open label (N = 41) | Bev + tandutinib | [□] 4.1 | [□] 11 |
| NCT00720356 (Raizer et al., 2016) | Newly diagnosed GBM and a non-methylated MGMT promoter | Non-randomized, single-group assignment, open label (N = 46) | Bev + erlotinib | [□] 9.2 (6.4–11.3) | *13.2 (10.8–19.6) |
| NCT00859222 (Lee et al., 2015) | Recurrent GBM | Non-randomized, single group assignment, open label (N = 24) | Bev + panobinostat | # ⁵ (3–9) | # ⁹ (6–19) |

mPFS, median progression-free survival; mOS, median overall survival; Bev, bevacizumab; RT, radiotherapy; TMZ, temozolomide.

*Primary outcome measure. #Secondary outcome measure. [□]Post hoc analysis.

promoter. This resulted in a superior mPFS with the drug combination (9.7 vs 6.0 months; HR = 0.59; *p* = 0.001) without improving mOS (16.6 vs 17.3 months; HR = 0.96; *p* = 0.83) (Herrlinger et al., 2016).

Another strategy aims at an additive effect by targeting both the vasculature and tumor cells and by combining bevacizumab with inhibitors of other growth factor pathways. Trebananib is a Fc fusion protein that targets Ang1 and Ang2; however, its association with bevacizumab failed to improve outcome when compared with bevacizumab plus placebo alone (mPFS: 4.2 vs 4.8 months, HR = 1.51, *p* = 0.04; and mOS 7.5 vs 11.5 months, HR = 1.46, *p* = 0.09) (Reardon et al., 2018). The association between bevacizumab and tandutinib, an oral FLT3, c-Kit, and PGDFR β inhibitor, showed some benefit (*post hoc* mPFS: 4.1 months; *post hoc* mOS: 11 months) but showed a high toxicity (Odia et al., 2016). One trial with patients presenting a nGBM with an unmethylated MGMT promoter investigated the combination with erlotinib, an EGFR tyrosine kinase inhibitor. This association did not also increase survival (mOS: 13.2 months – estimated mOS should have reached 17.9 months to show an increase in survival) (Raizer et al., 2016). This indicates that, during these last 5 years, no new drug combination with bevacizumab showed substantial clinical benefit and even increased toxicity. Furthermore, when comparing the use of low doses of bevacizumab to standard doses in patients with rGBM, it did not improve survival (mPFS: 4.34 vs 4.11 months; mOS: 9.6 vs 8.3 months) (Weathers et al., 2016).

Combination with immunotherapy also did not provide significant benefit. Recently nivolumab was investigated in a phase III randomized clinical trial with or without bevacizumab in patients with rGBM; nivolumab arm did not improve mOS [9.8 (8.2–11.8) vs 10.0 (9.0–11.8) months; HR = 1.04 (0.83–1.30), *p* = 0.76] and showed a lower mPFS [1.5 (1.5–1.6)

vs 3.5 (2.9–4.6) months; HR = 1.97 (1.57–2.48), *p* > 0.001] (Reardon et al., 2020).

New Anti-Angiogenic Drugs

Bevacizumab is the first representative of a drug family that interfered with the VEGF pathway. Others are represented by VEGF receptor tyrosine kinase inhibitors. A great advantage of these drugs is the oral administration which increases the patient's observance. In 2013, a phase III clinical trial studied the efficacy of cediranib, VEGFR, PDGFR, and c-Kit inhibitor, in combination with lomustine versus lomustine alone in patients with rGBM, but results did not show improvement of PFS (Batchelor et al., 2013). In a trial that compared dovitinib, a FGFR and VEGFR inhibitor, as second-line treatment after prior anti-angiogenic therapy by bevacizumab, no efficacy in prolonging mPFS (1.8 vs 2 months) was seen (Sharma et al., 2019). Tivozanib also showed limited activity in rGBM (mPFS: 2.3 months; mOS: 8.1 months), but the patient number in the trial (N = 10) was low (Kalpathy-Cramer et al., 2017). Two studies on cabozantinib, which inhibits MET and VEGFR2, on a global population did show some positive outcome in the rGBM group not treated previously with anti-angiogenic drugs (mPFS: 2.3 and 3.7 months; mOS: 4.6 and 10.4 months) (Cloughesy et al., 2018; Wen et al., 2018). Furthermore, the REGOMA study showed encouraging therapeutic benefit with regorafenib compared with lomustine alone (mOS: 7.4 vs 5.6 months; HR = 0.5; *p* < 0.001) (Lombardi et al., 2019).

Drug Delivery

Therapy development for GBM is challenging. This is due to resistances to radio- and chemotherapy because of the presence of glioblastoma stem-like cells (Safa et al., 2015). Furthermore, the CNS is composed of natural barriers which impair drug delivery

into the brain. As such, the BBB allows the passive transport of gas and liposoluble molecules. BBB's tight junctions regulate, furthermore, paracellular transport.

Current pharmacological treatments for GBM are administered systemically by intravenous injection or orally. Oral route simplifies patient treatment by proposing several pharmaceutical options. Parenteral route allows a short action period and a controlled dosage. However, tissue diffusion into the brain is hampered and toxic side effects occur because of their systemic action and the possibility to reach the brain tissue only when the BBB is altered. To overcome these problems, permeability of drugs can be enhanced by increasing liposolubility or integrating them into liposomes or nanocarriers. On the other hand, BBB can be temporarily disrupted by therapeutic ultrasound whereas a hyperosmotic disruption did not improve the drug penetration (Kobrinisky et al., 1999; Idbaih et al., 2019).

Another possibility is to administer topically medicinal products using injectable or implantable devices with sustained drug release. Local delivery strategies aim at increasing the concentration of the drug at the tumor site, at decreasing alterations related to enzymatic metabolization, and at reducing the systemic side effects. After surgery, the resection cavity represents an accessible implantation site near non-surgically resectable cells. The only approved strategy by the FDA for nGBM and rGBM is the carmustine-impregnated biodegradable Gliadel wafer. However, these implants did not improve outcomes and presented higher local toxicity (brain edema, seizures) (De Bonis et al., 2012). Hydrogels are a 3D matrix composed of a hydrophilic polymer network. Injectable hydrogel is a reservoir-system similar to soft tissue that can contain a large panel of drugs able to diffuse into the surrounding tissue (Basso et al., 2018). Antineoplastic drugs can be administered directly into the cavity or in the cerebrospinal fluid via an intrathecal injection device (Ommaya reservoir) for therapeutic delivery (Ommaya, 1984). However, the drug concentration decreases as the diffusion distance increases, and thus, this approach is of limited use in highly infiltrating tumors. Moreover, long-term use of these medical devices may cause complications including infections and hemorrhages. Convection-enhanced delivery has been developed to increase local delivery by enhancing diffusion by a bulk flow to maintain a pressure gradient (Bobo et al., 1994). Despite an acceptable safety profile, this method did not improve clinical outcomes of patient with GBM (Oberoi et al., 2016). An alternative method is the use of the intranasal delivery, which is non-invasive because of the anatomical proximity of these structures. Intranasal administration of a telomerase inhibitor in a rat model extended animal survival (Hashizume et al., 2008).

Perspectives for Anti-Angiogenic Drugs

There are new avenues to be explored for anti-vascular therapy. They can be used to enhance the activity of other therapies. For example, local hypoxia induced by bevacizumab could activate evofosfamide, a hypoxia-activated alkylating prodrug (Duan et al., 2008). Evofosfamide was studied on a phase I clinical trial for the treatment of rGBM following previous

bevacizumab therapy, and results appeared to be favorable for being studied in a phase II trial (Brenner et al., 2018). Furthermore, anti-angiogenic therapy could be of more benefit in some GBM subgroups. In a retrospective study of the AVAglio Trial, it has been shown that bevacizumab treatment led to a prolongation of OS of 4.3 months compared with placebo (17.1 vs 12.8 months; multivariable HR = 0.42; $p = 0.001$) in patients with proneural and IDH-1 wild-type nGBM (Sandmann et al., 2015). To date, the use of anti-angiogenic drugs should preferably be part of personalized care for patients.

GENERAL CONCLUSION

The vasculature plays an important role in the brain in normal and pathological conditions. In this article, we reviewed some recent literature on this subject. In a healthy tissue, endothelial cells are considered gatekeepers in all vessel types, for controlling diffusion of soluble factors or immune cells, by using para- or transcellular pathways. In GBM, however, vessels present maturation defect and chronic hyper-permeability, leading to vessel leakage, and poor vessel perfusion and delivery of nutrients. Pericytes and astrocytes have a central role in controlling physiology of normal and GBM NVUs. Pericytes, which are positioned along capillaries, help GBM cells to invade distant sites along blood vessels, as observed for reactive astrocytes. Importantly, GBM cells displace the astrocytic endfeet during co-option, disrupting endothelial cell junctions, and participating in blood leakage and hemorrhage.

The tumor-vessel interaction can also be modeled using *in vitro* bioengineered blood vessels. For now, no perfect 3D co-culture model exists. However, recent efforts have been made at developing 3D artificial vessels and 3D co-culture models using co-cultures of cancer cells and artificial blood vessels. Regarding vascularized 3D GBM models, researchers departed from 2D co-cultures to spheroids and are now able to reproduce small brain organoids with or without a functional vascular network. The main challenge for brain organoids is the co-culture of multiple cell types including neurons, astrocytes, oligodendrocytes, and microglia (Cakir et al., 2019). Another difficulty is the reconstruction of a tissue resembling to the human brain with microglia and six cortical layers (Heide et al., 2018) which exhibits the functional characteristics of the human brain such as neuronal networks and functional synapses (Shi et al., 2020). Moreover, the presence of a stabilized functional vascular network is also critical which requires the improvement of the current models for better recapitulating the physiopathology of these models.

3D co-culture models of blood vessels have been recently developed which may be used as vascularization trunks for tumor models. 3D models are much more relevant to study these interactions because they better recapitulate cell behavior and also better mirror *in vivo* gene expression and signaling. 3D co-culture models represent an attractive alternative to animal models and may be used in drug screening to identify better therapies.

Anti-angiogenic therapy in GBM did not meet the initial high expectations when tested in clinical trials. There was no real clinical benefit in newly diagnosed and recurrent GBM (maybe with exception of regorafenib). However, if clinical trials allow to obtain a global vision of the therapeutic effect, they do not consider patient subgroups. When considered, this may allow a more precise vision of the therapeutic response. Another drawback is variable study design and the criteria for determining progression. Radiologic response criteria such as Macdonald or RANO criteria may be misleading in monitoring clinical responses to anti-angiogenic therapy. Thus, this is still not the end of the road for anti-angiogenic therapy in GBM and more promising data from clinical trials are expected to come.

REFERENCES

- Alarcon-Martinez, L., Villafranca-Baughman, D., Quintero, H., Kacerovsky, J. B., Dotigny, F., Murai, K. K., et al. (2020). Interpericyte tunnelling nanotubes regulate neurovascular coupling. *Nature* 585, 1–5. doi: 10.1038/s41586-020-2589-x
- Alcantara Llaguno, S., Chen, J., Kwon, C. H., Jackson, E. L., Li, Y., Burns, D. K., et al. (2009). Malignant astrocytomas originate from neural stem/progenitor cells in a somatic tumor suppressor mouse model. *Cancer Cell* 15, 45–56. doi: 10.1016/j.ccr.2008.12.006
- Alvarez, J. I., Dodelet-Devillers, A., Kebir, H., Ifergan, I., Fabre, P. J., Terouz, S., et al. (2011). The Hedgehog pathway promotes blood-brain barrier integrity and CNS immune quiescence. *Science* 334, 1727–1731. doi: 10.1126/science.1206936
- Andrique, L., Recher, G., Alessandri, K., Pujol, N., Feyeux, M., Bon, P., et al. (2019). A model of guided cell self-organization for rapid and spontaneous formation of functional vessels. *Sci. Adv.* 5:eau6562. doi: 10.1126/sciadv.aau6562
- Armulik, A., Genové, G., and Betsholtz, C. (2011). Pericytes: developmental, physiological, and pathological perspectives, problems, and promises. *Dev. Cell* 21, 193–215. doi: 10.1016/j.devcel.2011.07.001
- Armulik, A., Genové, G., Mãe, M., Nisancioglu, M. H., Wallgard, E., Niaudet, C., et al. (2010). Pericytes regulate the blood-brain barrier. *Nature* 468, 557–561.
- Aske, K. C., and Waugh, C. A. (2017). Expanding the 3R principles: more rigour and transparency in research using animals. *EMBO Rep.* 18, 1490–1492. doi: 10.15252/embr.2017.44428
- Barlow, K. D., Sanders, A. M., Soker, S., Ergun, S., and Metheny-Barlow, L. J. (2013). Pericytes on the tumor vasculature: jekyll or hyde? *Cancer Microenviron. Off. J. Int. Cancer Microenviron. Soc.* 6, 1–17. doi: 10.1007/s12307-012-0102-2
- Basso, J., Miranda, A., Nunes, S., Cova, T., Sousa, J., Vitorino, C., et al. (2018). Hydrogel-based drug delivery nanosystems for the treatment of brain tumors. *Gels* 4:62. doi: 10.3390/gels4030062
- Batchelor, T. T., Mulholland, P., Neyns, B., Nabors, L. B., Campone, M., Wick, A., et al. (2013). Phase III randomized trial comparing the efficacy of cediranib as monotherapy, and in combination with lomustine, versus lomustine alone in patients with recurrent glioblastoma. *J. Clin. Oncol.* 31, 3212–3218. doi: 10.1200/jco.2012.47.2444
- Ben-Zvi, A., Lacoste, B., Kur, E., Andreone, B. J., Mayshar, Y., Yan, H., et al. (2014). Mfsd2a is critical for the formation and function of the blood-brain barrier. *Nature* 509, 507–511. doi: 10.1038/nature13324
- Bobo, R. H., Laske, D. W., Akbasak, A., Morrison, P. F., Dedrick, R. L., and Oldfield, E. H. (1994). Convection-enhanced delivery of macromolecules in the brain. *Proc. Natl. Acad. Sci. U.S.A.* 91, 2076–2080.
- Brenner, A., Zuniga, R., Sun, J. D., Floyd, J., Part, C. P., Kroll, S., et al. (2018). Hypoxia-activated evofosfamide for treatment of recurrent bevacizumab-refractory glioblastoma: a phase I surgical study. *Neuro-Oncol.* 20, 1231–1239. doi: 10.1093/neuonc/noy015
- Brightman, M. W. (2002). The brain's interstitial clefts and their glial walls. *J. Neurocytol.* 31, 595–603.

AUTHOR CONTRIBUTIONS

All authors listed have made a substantial, direct, and intellectual contribution to the work, and approved it for publication.

ACKNOWLEDGMENTS

This work was supported by Fondation ARC 2020, Ligue Contre le Cancer (Comité de la Gironde), ARTC, Plan Cancer 2021, INCA PLBIO, the Region Nouvelle Aquitaine. JG is a recipient of fellowship from the Toulouse University Hospital (CHU Toulouse).

- Cakir, B., Xiang, Y., Tanaka, Y., Kural, M. H., Parent, M., Kang, Y. J., et al. (2019). Engineering of human brain organoids with a functional vascular-like system. *Nat. Methods* 16, 1169–1175. doi: 10.1038/s41592-019-0586-5
- Chaicharoenaudomrung, N., Kunhorm, P., Promjantuek, W., Rujanapun, N., Heebkaew, N., Soraksa, N., et al. (2020). Transcriptomic profiling of 3D glioblastoma tumouroids for the identification of mechanisms involved in anticancer drug resistance. *In Vivo* 34, 199–211. doi: 10.21873/invivo.11762
- Chen, J., Luo, Y., Hui, H., Cai, T., Huang, H., Yang, F., et al. (2017). CD146 coordinates brain endothelial cell-pericyte communication for blood-brain barrier development. *Proc. Natl. Acad. Sci. U.S.A.* 114, E7622–E7631.
- Cheng, L., Huang, Z., Zhou, W., Wu, Q., Donnola, S., Liu, J. K., et al. (2013). Glioblastoma stem cells generate vascular pericytes to support vessel function and tumor growth. *Cell* 153, 139–152. doi: 10.1016/j.cell.2013.02.021
- Cheslow, L., and Alvarez, J. I. (2016). Glial-endothelial crosstalk regulates blood-brain barrier function. *Curr. Opin. Pharmacol.* 26, 39–46. doi: 10.1016/j.coph.2015.09.010
- Chinot, O. L., Wick, W., Mason, W., Henriksson, R., Saran, F., Nishikawa, R., et al. (2014). Bevacizumab plus radiotherapy-temozolomide for newly diagnosed glioblastoma. *N. Engl. J. Med.* 370, 709–722.
- Chouleur, T., Tremblay, M. L., and Bikfalvi, A. (2020). Mechanisms of invasion in glioblastoma. *Curr. Opin. Oncol.* 32, 631–639. doi: 10.1097/cco.0000000000000679
- Chow, B. W., and Gu, C. (2017). Gradual suppression of transcytosis governs functional blood-retinal barrier formation. *Neuron* 93, 1325–1333.e3.
- Cloughesy, T., Finocchiaro, G., Belda-Iniesta, C., Recht, L., Brandes, A. A., Pineda, E., et al. (2017). Randomized, double-blind, placebo-controlled, multicenter Phase II study of onartuzumab plus bevacizumab versus placebo plus bevacizumab in patients with recurrent glioblastoma: efficacy, safety, and hepatocyte growth factor and O6-Methylguanine-DNA Methyltransferase biomarker analyses. *J. Clin. Oncol. Off. J. Am. Soc. Clin. Oncol.* 35, 343–351. doi: 10.1200/jco.2015.64.7685
- Cloughesy, T. F., Drappatz, J., de Groot, J., Prados, M. D., Reardon, D. A., Schiff, D., et al. (2018). Phase II study of cabozantinib in patients with progressive glioblastoma: subset analysis of patients with prior antiangiogenic therapy. *Neuro-Oncol.* 20, 259–267. doi: 10.1093/neuonc/nox151
- Coomber, B. L., and Stewart, P. A. (1985). Morphometric analysis of CNS microvascular endothelium. *Microvasc. Res.* 30, 99–115. doi: 10.1016/0026-2862(85)90042-1
- Courtoy, P. J., and Boyles, J. (1983). Fibronectin in the microvasculature: localization in the pericyte-endothelial interstitium. *J. Ultrastruct. Res.* 83, 258–273. doi: 10.1016/s0022-5320(83)90133-8
- Cuevas, P., Gutierrez-Diaz, J. A., Reimers, D., Dujovny, M., Diaz, F. G., and Ausman, J. I. (1984). Pericyte endothelial gap junctions in human cerebral capillaries. *Anat. Embryol. (Berl.)* 170, 155–159. doi: 10.1007/bf00319000
- Cui, H., Esworthy, T., Zhou, X., Hann, S. Y., Glazer, R. I., Li, R., et al. (2020). Engineering a novel 3D printed vascularized tissue model for investigating breast cancer metastasis to bone. *Adv. Healthc. Mater.* 9:e1900924.
- Daneman, R., Zhou, L., Galliu, D., Cahoy, J. D., Kaushal, A., and Barres, B. A. (2010a). The mouse blood-brain barrier transcriptome: a new resource for

- understanding the development and function of brain endothelial cells. *PLoS One* 5:e13741. doi: 10.1371/journal.pone.0013741
- Daneman, R., Zhou, L., Kebede, A. A., and Barres, B. A. (2010b). Pericytes are required for blood-brain barrier integrity during embryogenesis. *Nature* 468, 562–566. doi: 10.1038/nature09513
- Daubon, T., Léon, C., Clarke, K., Andrique, L., Salabert, L., Darbo, E., et al. (2019). Deciphering the complex role of thrombospondin-1 in glioblastoma development. *Nat. Commun.* 10:1146.
- De Bonis, P., Anile, C., Pompucci, A., Fiorentino, A., Balducci, M., Chiesa, S., et al. (2012). Safety and efficacy of Gliadel wafers for newly diagnosed and recurrent glioblastoma. *Acta Neurochir. (Wien)* 154, 1371–1378. doi: 10.1007/s00701-012-1413-2
- Del Maschio, A., De Luigi, A., Martin-Padura, I., Brockhaus, M., Bartfai, T., Muscella, P., et al. (1999). Leukocyte recruitment in the cerebrospinal fluid of mice with experimental meningitis is inhibited by an antibody to junctional adhesion molecule (Jam). *J. Exp. Med.* 190, 1351–1356. doi: 10.1084/jem.190.9.1351
- Duan, J.-X., Jiao, H., Kaizerman, J., Stanton, T., Evans, J. W., Lan, L., et al. (2008). Potent and highly selective hypoxia-activated achiral phosphoramidate mustards as anticancer drugs. *J. Med. Chem.* 51, 2412–2420. doi: 10.1021/jm701028q
- Eklund, L., Bry, M., and Alitalo, K. (2013). Mouse models for studying angiogenesis and lymphangiogenesis in cancer. *Mol. Oncol.* 7, 259–282. doi: 10.1016/j.molonc.2013.02.007
- Engelhardt, B., and Coisne, C. (2011). Fluids and barriers of the CNS establish immune privilege by confining immune surveillance to a two-walled castle moat surrounding the CNS castle. *Fluids Barriers CNS* 8:4.
- Engelhardt, B., and Ransohoff, R. M. (2012). Capture, crawl, cross: the T cell code to breach the blood-brain barriers. *Trends Immunol.* 33, 579–589. doi: 10.1016/j.it.2012.07.004
- Galanis, E., Anderson, S. K., Twohy, E. L., Carrero, X. W., Dixon, J. G., Tran, D. D., et al. (2019). A phase 1 and randomized, placebo-controlled phase 2 trial of bevacizumab plus dasatinib in patients with recurrent glioblastoma: alliance/North Central Cancer Treatment Group N0872. *Cancer* 125, 3790–3800. doi: 10.1002/cncr.32340
- Ghaseddin, A., Reardon, D., Massey, W., Mannerino, A., Lipp, E. S., Herndon, J. E. I. I., et al. (2018). Phase II study of bevacizumab and vorinostat for patients with recurrent World Health Organization grade 4 malignant glioma. *Oncologist* 23, 157–e21. doi: 10.1634/theoncologist.2017-0501
- Gilbert, M. R., Dignam, J. J., Armstrong, T. S., Wefel, J. S., Blumenthal, D. T., Vogelbaum, M. A., et al. (2014). A randomized trial of bevacizumab for newly diagnosed glioblastoma. *N. Engl. J. Med.* 370, 699–708. doi: 10.1056/NEJMoa1308573
- Goldshmit, Y., Galea, M. P., Bartlett, P. F., and Turnley, A. M. (2006). EphA4 regulates central nervous system vascular formation. *J. Comp. Neurol.* 497, 864–875. doi: 10.1002/cne.21029
- Goldshmit, Y., Homman-Ludiyi, J., and Bourne, J. A. (2014). EphA4 is associated with multiple cell types in the marmoset primary visual cortex throughout the lifespan. *Eur. J. Neurosci.* 39, 1419–1428. doi: 10.1111/ejn.12514
- Gravina, G. L., Mancini, A., Marampon, F., Colapietro, A., Delle Monache, S., Sferra, R., et al. (2017). The brain-penetrating CXCR4 antagonist, PRX177561, increases the antitumor effects of bevacizumab and sunitinib in preclinical models of human glioblastoma. *J. Hematol. Oncol.* 10:5. doi: 10.1186/s13045-016-0377-8
- Grill, J., Massimino, M., Bouffet, E., Azizi, A. A., McCowage, G., Cañete, A., et al. (2018). Phase II, open-label, randomized, multicenter trial (HERBY) of bevacizumab in pediatric patients with newly diagnosed high-grade glioma. *J. Clin. Oncol. Off. J. Am. Soc. Clin. Oncol.* 36, 951–958. doi: 10.1200/JCO.2017.76.0611
- Griveau, A., Seano, G., Shelton, S. J., Kupp, R., Jahangiri, A., Obernier, K., et al. (2018). A glial signature and Wnt7 signaling regulate glioma-vascular interactions and tumor microenvironment. *Cancer Cell* 33, 874.e–889.e. doi: 10.1016/j.ccell.2018.03.020
- Guan, X., Hasan, M. N., Maniar, S., Jia, W., and Sun, D. (2018). Reactive astrocytes in glioblastoma multiforme. *Mol. Neurobiol.* 55, 6927–6938. doi: 10.1007/s12035-018-0880-8
- Hainsworth, J. D., Becker, K. P., Mekhail, T., Chowdhary, S. A., Eakle, J. F., Wright, D., et al. (2019). Phase I/II study of bevacizumab with BKM120, an oral PI3K inhibitor, in patients with refractory solid tumors (phase I) and relapsed/refractory glioblastoma (phase II). *J. Neurooncol.* 144, 303–311. doi: 10.1007/s11060-019-03227-7
- Hall, C. N., Reynell, C., Gesslein, B., Hamilton, N. B., Mishra, A., Sutherland, B. A., et al. (2014). Capillary pericytes regulate cerebral blood flow in health and disease. *Nature* 508, 55–60. doi: 10.1038/nature13165
- Hara, Y., Nomura, T., Yoshizaki, K., Frisén, J., and Osumi, N. (2010). Impaired hippocampal neurogenesis and vascular formation in ephrin-A5-deficient mice. *Stem Cells Dayt. Ohio* 28, 974–983. doi: 10.1002/stem.427
- Hashizume, R., Ozawa, T., Gryaznov, S. M., Bollen, A. W., Lamborn, K. R., et al. (2008). New therapeutic approach for brain tumors: Intranasal delivery of telomerase inhibitor GRN163. *Neuro-Oncol.* 10, 112–120. doi: 10.1215/15228517-2007-052
- Heide, M., Huttner, W. B., and Mora-Bermúdez, F. (2018). Brain organoids as models to study human neocortex development and evolution. *Curr. Opin. Cell Biol.* 55, 8–16. doi: 10.1016/j.ccb.2018.06.006
- Herflinger, U., Schäfer, N., Steinbach, J. P., Weyerbrock, A., Hau, P., Goldbrunner, R., et al. (2016). Bevacizumab plus irinotecan versus temozolomide in newly diagnosed O6-methylguanine-DNA methyltransferase nonmethylated glioblastoma: the randomized GLARIUS trial. *J. Clin. Oncol. Off. J. Am. Soc. Clin. Oncol.* 34, 1611–1619. doi: 10.1200/JCO.2015.63.4691
- Iadecola, C. (2017). The neurovascular unit coming of age: a journey through neurovascular coupling in health and disease. *Neuron* 96, 17–42. doi: 10.1016/j.neuron.2017.07.030
- Idbaih, A., Canney, M., Belin, L., Desseaux, C., Vignot, A., Bouchoux, G., et al. (2019). Safety and feasibility of repeated and transient blood-brain barrier disruption by pulsed ultrasound in patients with recurrent glioblastoma. *Clin. Cancer Res.* 25, 3793–3801. doi: 10.1158/1078-0432.CCR-18-3643
- Igarashi, Y., Utsumi, H., Chiba, H., Yamada-Sasamori, Y., Tobioka, H., Kamimura, Y., et al. (1999). Glial cell line-derived neurotrophic factor induces barrier function of endothelial cells forming the blood-brain barrier. *Biochem. Biophys. Res. Commun.* 261, 108–112. doi: 10.1006/bbrc.1999.0992
- Iwamoto, N., Higashi, T., and Furuse, M. (2014). Localization of angulin-1/LSR and tricellulin at tricellular contacts of brain and retinal endothelial cells in vivo. *Cell Struct. Funct.* 39, 1–8. doi: 10.1247/csf.13015
- Kalpathy-Cramer, J., Chandra, V., Da, X., Ou, Y., Emblem, K. E., Muzikansky, A., et al. (2017). Phase II study of tivozanib, an oral VEGFR inhibitor, in patients with recurrent glioblastoma. *J. Neurooncol.* 131, 603–610. doi: 10.1007/s11060-016-2332-5
- Kang, W., Kim, S. H., Cho, H. J., Jin, J., Lee, J., Joo, K. M., et al. (2015). Talin1 targeting potentiates anti-angiogenic therapy by attenuating invasion and stem-like features of glioblastoma multiforme. *Oncotarget* 6, 27239–27251. doi: 10.18632/oncotarget.4835
- Kannan, R. Y., Salacinski, H. J., Butler, P. E., Hamilton, G., and Seifalian, A. M. (2005). Current status of prosthetic bypass grafts: a review. *J. Biomed. Mater. Res. B Appl. Biomater.* 74B, 570–581. doi: 10.1002/jbm.b.30247
- Kobrinisky, N. L., Packer, R. J., Boyett, J. M., Stanley, P., Shiminski-Maher, T., Allen, J. C., et al. (1999). Etoposide with or without mannitol for the treatment of recurrent or primarily unresponsive brain tumors: a Children's Cancer Group Study, CCG-9881. *J. Neurooncol.* 45, 47–54. doi: 10.1023/A:1006333811437
- Kooij, G., Kopplin, K., Blasig, R., Stuijver, M., Koning, N., Govers, G., et al. (2014). Disturbed function of the blood-cerebrospinal fluid barrier aggravates neuroinflammation. *Acta Neuropathol. (Berl.)* 128, 267–277. doi: 10.1007/s00401-013-1227-1
- Kröger, S., Wolburg, H., and Warth, A. (2004). Redistribution of aquaporin-4 in human glioblastoma correlates with loss of agrin immunoreactivity from brain capillary basal laminae. *Acta Neuropathol. (Berl.)* 107, 311–318. doi: 10.1007/s00401-003-0812-0
- Kronstein, R., Seebach, J., Grossklau, S., Minten, C., Engelhardt, B., Drab, M., et al. (2012). Caveolin-1 opens endothelial cell junctions by targeting catenins. *Cardiovasc. Res.* 93, 130–140. doi: 10.1093/cvr/cvr256
- Lakka, S. S., and Rao, J. S. (2008). Antiangiogenic therapy in brain tumors. *Expert Rev. Neurother.* 8, 1457–1473. doi: 10.1586/14737175.8.10.1457
- Langhans, S. A. (2018). Three-dimensional in vitro cell culture models in drug discovery and drug repositioning. *Front. Pharmacol.* 9:6. doi: 10.3389/fphar.2018.00006
- Langlet, F., Mullier, A., Bouret, S. G., Prevot, V., and Dehouck, B. (2013). Tanyocyte-like cells form a blood-cerebrospinal fluid barrier in the circumventricular

- organs of the mouse brain. *J. Comp. Neurol.* 521, 3389–3405. doi: 10.1002/cne.23355
- Larson, D. M., Carson, M. P., and Haudenschild, C. C. (1987). Junctional transfer of small molecules in cultured bovine brain microvascular endothelial cells and pericytes. *Microvasc. Res.* 34, 184–199. doi: 10.1016/0026-2862(87)90052-5
- Lee, E. Q., Reardon, D. A., Schiff, D., Drappatz, J., Muzikansky, A., Grimm, S. A., et al. (2015). Phase II study of panobinostat in combination with bevacizumab for recurrent glioblastoma and anaplastic glioma. *Neuro-Oncol.* 17, 862–867. doi: 10.1093/neuonc/nou350
- Liebner, S., Dijkhuizen, R. M., Reiss, Y., Plate, K. H., Agalliu, D., and Constantin, G. (2018). Functional morphology of the blood–brain barrier in health and disease. *Acta Neuropathol. (Berl.)* 135, 311–336. doi: 10.1007/s00401-018-1815-1
- Lien, C. F., Mohanta, S. K., Frontczak-Baniewicz, M., Swinny, J. D., Zablocka, B., and Górecki, D. C. (2012). Absence of glial α -dystrobrevin causes abnormalities of the blood–brain barrier and progressive brain edema. *J. Biol. Chem.* 287, 41374–41385. doi: 10.1074/jbc.M112.400044
- Lokman, N. A., Elder, A. S. F., Ricciardelli, C., and Oehler, M. K. (2012). Chick chorioallantoic membrane (CAM) assay as an in vivo model to study the effect of newly identified molecules on ovarian cancer invasion and metastasis. *Int. J. Mol. Sci.* 13, 9959–9970. doi: 10.3390/ijms13089959
- Lombardi, G., De Salvo, G. L., Brandes, A. A., Eoli, M., Rudà, R., Faedi, M., et al. (2019). Regorafenib compared with lomustine in patients with relapsed glioblastoma (REGOMA): a multicentre, open-label, randomised, controlled, phase 2 trial. *Lancet Oncol.* 20, 110–119. doi: 10.1016/S1470-2045(18)30675-2
- Louis, D. N., Perry, A., Reifenberger, G., von Deimling, A., Figarella-Branger, D., Cavenee, W. K., et al. (2016). The 2016 World Health Organization classification of tumors of the central nervous system: a summary. *Acta Neuropathol. (Berl.)* 131, 803–820. doi: 10.1007/s00401-016-1545-1
- Ma, L., Zhang, B., Zhou, C., Li, Y., Li, B., Yu, M., et al. (2018). The comparison genomics analysis with glioblastoma multiforme (GBM) cells under 3D and 2D cell culture conditions. *Colloids Surf. B Biointerfaces* 172, 665–673. doi: 10.1016/j.colsurfb.2018.09.034
- Ma, S., Kwon, H. J., and Huang, Z. (2012). A functional requirement for astroglia in promoting blood vessel development in the early postnatal brain. *PLoS One* 7:e48001. doi: 10.1371/journal.pone.0048001
- Mahringer, A., and Fricker, G. (2016). ABC transporters at the blood–brain barrier. *Expert Opin. Drug Metab. Toxicol.* 12, 499–508. doi: 10.1517/17425255.2016.1168804
- Massa, S., Sakr, M. A., Seo, J., Bandaru, P., Arneri, A., Bersini, S., et al. (2017). Bioprinted 3D vascularized tissue model for drug toxicity analysis. *Biomicrofluidics* 11:044109. doi: 10.1063/1.4994708
- Mathiisen, T. M., Lehre, K. P., Danbolt, N. C., and Ottersen, O. P. (2010). The perivascular astroglial sheath provides a complete covering of the brain microvessels: an electron microscopic 3D reconstruction. *Glia* 58, 1094–1103. doi: 10.1002/glia.20990
- McCoy, M. G., Nyanyo, D., Hung, C. K., Goerger, J. P., Zipfel, W. R., Williams, R. M., et al. (2019). Endothelial cells promote 3D invasion of GBM by IL-8-dependent induction of cancer stem cell properties. *Sci. Rep.* 9:9069. doi: 10.1038/s41598-019-45535-y
- Menezes, M. J., McClenahan, F. K., Leiton, C. V., Aranmolate, A., Shan, X., and Colognato, H. (2014). The extracellular matrix protein laminin α 2 regulates the maturation and function of the blood–brain barrier. *J. Neurosci. Off. J. Soc. Neurosci.* 34, 15260–15280. doi: 10.1523/JNEUROSCI.3678-13.2014
- Meng, W., and Takeichi, M. (2009). Adherens junction: molecular architecture and regulation. *Cold Spring Harb. Perspect. Biol.* 1:a002899. doi: 10.1101/cshperspect.a002899
- Miranda-Gonçalves, V., Bezerra, F., Costa-Almeida, R., Freitas-Cunha, M., Soares, R., Martinho, O., et al. (2017). Monocarboxylate transporter 1 is a key player in glioma-endothelial cell crosstalk. *Mol. Carcinog.* 56, 2630–2642. doi: 10.1002/mc.22707
- Mizee, M. R., Nijland, P. G., van der Pol, S. M., Drexhage, J. A., van Het Hof, B., Mebius, R., et al. (2014). Astrocyte-derived retinoic acid: a novel regulator of blood–brain barrier function in multiple sclerosis. *Acta Neuropathol. (Berl.)* 128, 691–703. doi: 10.1007/s00401-014-1335-6
- Musah-Eroje, A., and Watson, S. (2019). A novel 3D in vitro model of glioblastoma reveals resistance to temozolomide which was potentiated by hypoxia. *J. Neurooncol.* 142, 231–240. doi: 10.1007/s11060-019-03107-0
- Nagelhus, E. A., and Ottersen, O. P. (2013). Physiological roles of aquaporin-4 in brain. *Physiol. Rev.* 93, 1543–1562. doi: 10.1152/physrev.00011.2013
- Nestor, M. W., Mok, L.-P., Tulapurkar, M. E., and Thompson, S. M. (2007). Plasticity of neuron–glial interactions mediated by astrocytic EphARs. *J. Neurosci. Off. J. Soc. Neurosci.* 27, 12817–12828. doi: 10.1523/JNEUROSCI.2442-07.2007
- NICE (2018). *Recommendations | Brain Tumours (Primary) and Brain Metastases in Adults | Guidance | NICE*. Available online at: <https://www.nice.org.uk/guidance/ng99/chapter/Recommendations> (accessed July 11, 2018).
- Nitta, T., Hata, M., Gotoh, S., Seo, Y., Sasaki, H., Hashimoto, N., et al. (2003). Size-selective loosening of the blood–brain barrier in claudin-5-deficient mice. *J. Cell Biol.* 161, 653–660. doi: 10.1083/jcb.200302070
- Niu, G., Sapoznik, E., and Soker, S. (2014). Bioengineered blood vessels. *Expert Opin. Biol. Ther.* 14, 403–410. doi: 10.1517/14712598.2014.880419
- Oberoi, R. K., Parrish, K. E., Sio, T. T., Mittapalli, R. K., Elmquist, W. F., and Sarkaria, J. N. (2016). Strategies to improve delivery of anticancer drugs across the blood–brain barrier to treat glioblastoma. *Neuro-Oncol.* 18, 27–36. doi: 10.1093/neuonc/nov164
- Odia, Y., Sul, J., Shih, J. H., Kreisl, T. N., Butman, J. A., Iwamoto, F. M., et al. (2016). A Phase II trial of tandutinib (MLN 518) in combination with bevacizumab for patients with recurrent glioblastoma. *CNS Oncol.* 5, 59–67. doi: 10.2217/cns-2015-0010
- Ohtsuki, S., Yamaguchi, H., Katsukura, Y., Asashima, T., and Terasaki, T. (2008). mRNA expression levels of tight junction protein genes in mouse brain capillary endothelial cells highly purified by magnetic cell sorting. *J. Neurochem.* 104, 147–154.
- Ommaya, A. K. (1984). Implantable devices for chronic access and drug delivery to the central nervous system. *Cancer Drug Deliv.* 1, 169–179. doi: 10.1089/cdd.1984.1.169
- Peck, M., Dusserre, N., McAllister, T. N., and L'Heureux, N. (2011). Tissue engineering by self-assembly. *Mater. Today* 14, 218–224. doi: 10.1016/S1369-7021(11)70117-1
- Pellerin, L., Pellegri, G., Bittar, P. G., Charnay, Y., Bouras, C., Martin, J. L., et al. (1998). Evidence supporting the existence of an activity-dependent astrocyte–neuron lactate shuttle. *Dev. Neurosci.* 20, 291–299. doi: 10.1159/000017324
- Pfaff, D., Fiedler, U., and Augustin, H. G. (2006). Emerging roles of the Angiopoietin-Tie and the ephrin-Eph systems as regulators of cell trafficking. *J. Leukoc. Biol.* 80, 719–726. doi: 10.1189/jlb.1105652
- Philips, A., Henshaw, D. L., Lamburn, G., and O'Carroll, M. J. (2018). Brain tumours: rise in glioblastoma multiforme incidence in England 1995–2015 suggests an adverse environmental or lifestyle factor. *J. Environ. Public Health* 2018, 1–10. doi: 10.1155/2018/7910754 doi: 10.1155/2018/2170208 doi: 10.1155/2018/2170208
- Piao, Y., Park, S. Y., Henry, V., Smith, B. D., Tiao, N., Flynn, D. L., et al. (2016). Novel MET/TIE2/VEGFR2 inhibitor altiratinib inhibits tumor growth and invasiveness in bevacizumab-resistant glioblastoma mouse models. *Neuro-Oncol.* 18, 1230–1241. doi: 10.1093/neuonc/now030
- Podjaski, C., Alvarez, J. I., Bourbonniere, L., Larouche, S., Terouz, S., Bin, J. M., et al. (2015). Netrin 1 regulates blood–brain barrier function and neuroinflammation. *Brain* 138, 1598–1612. doi: 10.1093/brain/awv092
- Preston, J. E., Joan Abbott, N., and Begley, D. J. (2014). Transcytosis of macromolecules at the blood–brain barrier. *Adv. Pharmacol. San Diego Calif.* 71, 147–163. doi: 10.1016/bs.apha.2014.06.001
- Raizer, J. J., Giglio, P., Hu, J., Groves, M., Merrell, R., Conrad, C., et al. (2016). A phase II study of bevacizumab and erlotinib after radiation and temozolomide in MGMT unmethylated GBM patients. *J. Neurooncol.* 126, 185–192. doi: 10.1007/s11060-015-1958-z
- Reardon, D. A., Brandes, A. A., Omuro, A., Mulholland, P., Lim, M., Wick, A., et al. (2020). Effect of nivolumab vs bevacizumab in patients with recurrent glioblastoma: the checkmate 143 phase 3 Randomized clinical trial. *JAMA Oncol.* 6:1003. doi: 10.1001/jamaoncol.2020.1024
- Reardon, D. A., Lassman, A. B., Schiff, D., Yunus, S. A., Gerstner, E. R., Cloughesy, T. F., et al. (2018). Phase 2 and biomarker study of trebananib, an angiopoietin-blocking peptide, with and without bevacizumab for patients with recurrent glioblastoma. *Cancer* 124, 1438–1448. doi: 10.1002/cncr.31172
- Reyes-Butera, G., Cartalat-Carel, S., Chinot, O. L., Barrie, M., Taillandier, L., Beauchesne, P., et al. (2018). Temozolomide plus bevacizumab in elderly patients with newly diagnosed glioblastoma and poor performance status:

- an ANOCEF Phase II trial (ATAG). *Oncologist* 23, 524–e44. doi: 10.1634/theoncologist.2017-0689
- Rong, X., Huang, B., Qiu, S., Li, X., He, L., and Peng, Y. (2016). Tumor-associated macrophages induce vasculogenic mimicry of glioblastoma multiforme through cyclooxygenase-2 activation. *Oncotarget* 7, 83976–83986. doi: 10.18632/oncotarget.6930
- Safa, A. R., Saadatzadeh, M. R., Cohen-Gadol, A. A., Pollok, K. E., and Bijangi-Vishehsaraei, K. (2015). Glioblastoma stem cells (GSCs) epigenetic plasticity and interconversion between differentiated non-GSCs and GSCs. *Genes Dis.* 2, 152–163. doi: 10.1016/j.gendis.2015.02.001
- Sandmann, T., Bourgon, R., Garcia, J., Li, C., Cloughesy, T., Chinot, O. L., et al. (2015). Patients with proneural glioblastoma may derive overall survival benefit from the addition of bevacizumab to first-line radiotherapy and temozolomide: retrospective analysis of the AVAglio trial. *J. Clin. Oncol. Off. J. Am. Soc. Clin. Oncol.* 33, 2735–2744. doi: 10.1200/JCO.2015.61.5005
- Scherer, H. J. (1940). THE FORMS OF GROWTH IN GLIOMAS AND THEIR PRACTICAL SIGNIFICANCE. *Brain* 63, 1–35. doi: 10.1093/brain/63.1.1
- Seo, B. R., DelNero, P., and Fischbach, C. (2014). In vitro models of tumor vessels and matrix: engineering approaches to investigate transport limitations and drug delivery in cancer. *Adv. Drug Delivery Rev.* 6, 205–216. doi: 10.1016/j.addr.2013.11.011
- Serres, E., Debarbieux, F., Stanchi, F., Maggiorrella, L., Grall, D., Turchi, L., et al. (2014). Fibronectin expression in glioblastomas promotes cell cohesion, collective invasion of basement membrane in vitro and orthotopic tumor growth in mice. *Oncogene* 33, 3451–3462. doi: 10.1038/onc.2013.305
- Sharma, M., Schilero, C., Peereboom, D. M., Hobbs, B. P., Elson, P., Stevens, G. H. J., et al. (2019). Phase II study of Dovitinib in recurrent glioblastoma. *J. Neurooncol.* 144, 359–368. doi: 10.1007/s11060-019-03236-6
- Shi, Y., Sun, L., Wang, M., Liu, J., Zhong, S., Li, R., et al. (2020). Vascularized human cortical organoids (vOrganoids) model cortical development in vivo. *PLoS Biol.* 18:e3000705. doi: 10.1371/journal.pbio.3000705
- Shin, Y., Han, S., Jeon, J. S., Yamamoto, K., Zervantonakis, I. K., Sudo, R., et al. (2012). Microfluidic assay for simultaneous culture of multiple cell types on surfaces or within hydrogels. *Nat. Protoc.* 7, 1247–1259. doi: 10.1038/nprot.2012.051
- Silvestri, V. L., Henriët, E., Linville, R. M., Wong, A. D., Searson, P. C., and Ewald, A. J. (2020). A tissue-engineered 3D microvessel model reveals the dynamics of mosaic vessel formation in breast cancer. *Cancer Res.* 80:canres.1564.2019. doi: 10.1158/0008-5472.CAN-19-1564
- Sohet, F., Lin, C., Munji, R. N., Lee, S. Y., Ruderisch, N., Soung, A., et al. (2015). LSR/angulin-1 is a tricellular tight junction protein involved in blood-brain barrier formation. *J. Cell Biol.* 208, 703–711. doi: 10.1083/jcb.201410131
- Song, H.-H. G., Rumma, R. T., Ozaki, C. K., Edelman, E. R., and Chen, C. S. (2018). Vascular tissue engineering: progress, challenges, and clinical promise. *Cell Stem Cell* 22, 340–354. doi: 10.1016/j.stem.2018.02.009
- Song, J. W., and Munn, L. L. (2011). Fluid forces control endothelial sprouting. *Proc. Natl. Acad. Sci. U.S.A.* 108, 15342–15347. doi: 10.1073/pnas.1105316108
- Suri, C., Jones, P. F., Patan, S., Bartunkova, S., Maisonpierre, P. C., Davis, S., et al. (1996). Requisite role of angiopoietin-1, a ligand for the TIE2 receptor, during embryonic angiogenesis. *Cell* 87, 1171–1180. doi: 10.1016/s0092-8674(00)81813-9
- Sweeney, M. D., Ayyadurai, S., and Zlokovic, B. V. (2016). Pericytes of the neurovascular unit: key functions and signaling pathways. *Nat. Neurosci.* 19, 771–783. doi: 10.1038/nn.4288
- Sweeney, M. D., Zhao, Z., Montagne, A., Nelson, A. R., and Zlokovic, B. V. (2019). Blood-brain barrier: from physiology to disease and back. *Physiol. Rev.* 99, 21–78.
- Valdor, R., García-Bernal, D., Bueno, C., Ródenas, M., Moraleda, J. M., Macian, F., et al. (2017). Glioblastoma progression is assisted by induction of immunosuppressive function of pericytes through interaction with tumor cells. *Oncotarget* 8, 68614–68626. doi: 10.18632/oncotarget.19804
- Vegran, F., Boidot, R., Michiels, C., Sonveaux, P., and Feron, O. (2011). Lactate influx through the endothelial cell monocarboxylate transporter MCT1 supports an NF- κ B/IL-8 pathway that drives tumor angiogenesis. *Cancer Res.* 71, 2550–2560. doi: 10.1158/0008-5472.can-10-2828
- Wang, R., Chadalavada, K., Wilshire, J., Kowalik, U., Hovinga, K. E., Geber, A., et al. (2010). Glioblastoma stem-like cells give rise to tumour endothelium. *Nature* 468, 829–833. doi: 10.1038/nature09624
- Wang, X.-Y., Jin, Z. H., Gan, B. W., Lv, S. W., Xie, M., and Huang, W. H. (2014). Engineering interconnected 3D vascular networks in hydrogels using molded sodium alginate lattice as the sacrificial template. *Lab. Chip* 14, 2709–2716. doi: 10.1039/c4lc00069b
- Watkins, S., Robel, S., Kimbrough, I. F., Robert, S. M., Ellis-Davies, G., Sontheimer, H., et al. (2014). Disruption of astrocyte–vascular coupling and the blood–brain barrier by invading glioma cells. *Nat. Commun.* 5:4196.
- Weathers, S.-P., Han, X., Liu, D. D., Conrad, C. A., Gilbert, M. R., Loghin, M. E., et al. (2016). A randomized phase II trial of standard dose bevacizumab versus low dose bevacizumab plus lomustine (CCNU) in adults with recurrent glioblastoma. *J. Neurooncol.* 129, 487–494. doi: 10.1007/s11060-016-2195-9
- Weinberg, C. B., and Bell, E. (1986). A blood vessel model constructed from collagen and cultured vascular cells. *Science* 231, 397–400. doi: 10.1126/science.2934816
- Wen, P. Y., Drappatz, J., de Groot, J., Prados, M. D., Reardon, D. A., Schiff, D., et al. (2018). Phase II study of cabozantinib in patients with progressive glioblastoma: subset analysis of patients naive to antiangiogenic therapy. *Neuro-Oncol* 20, 249–258. doi: 10.1093/neuonc/nox154
- Wick, W., Gorlia, T., Bendszus, M., Taphoorn, M., Sahm, F., Harting, I., et al. (2017). Lomustine and bevacizumab in progressive glioblastoma. *N. Engl. J. Med.* 377, 1954–1963.
- Wirsching, H.-G., Tabatabai, G., Roelcke, U., Hottinger, A. F., Jörger, F., Schmid, A., et al. (2018). Bevacizumab plus hypofractionated radiotherapy versus radiotherapy alone in elderly patients with glioblastoma: the randomized, open-label, phase II ARTE trial. *Ann. Oncol. Off. J. Eur. Soc. Med. Oncol.* 29, 1423–1430.
- Wolburg, H., Noell, S., Fallier-Becker, P., Mack, A. F., and Wolburg-Buchholz, K. (2012). The disturbed blood–brain barrier in human glioblastoma. *Mol. Aspects Med.* 33, 579–589.
- Zhao, Y.-L., Song, J.-N., and Zhang, M. (2014). Role of caveolin-1 in the biology of the blood-brain barrier. *Rev. Neurosci.* 25, 247–254.
- Zhou, Y., Wang, Y., Tischfield, M., Williams, J., Smallwood, P. M., Rattner, A., et al. (2014). Canonical WNT signaling components in vascular development and barrier formation. *J. Clin. Invest.* 124, 3825–3846.
- Zong, H., Verhaak, R. G., and Canoll, P. (2012). The cellular origin for malignant glioma and prospects for clinical advancements. *Expert Rev. Mol. Diagn.* 12, 383–394.

Conflict of Interest: The authors declare that the research was conducted in the absence of any commercial or financial relationships that could be construed as a potential conflict of interest.

Copyright © 2021 Guyon, Chapouly, Andrique, Bikfalvi and Daubon. This is an open-access article distributed under the terms of the Creative Commons Attribution License (CC BY). The use, distribution or reproduction in other forums is permitted, provided the original author(s) and the copyright owner(s) are credited and that the original publication in this journal is cited, in accordance with accepted academic practice. No use, distribution or reproduction is permitted which does not comply with these terms.

Titre : Nouveaux mécanismes du développement des tumeurs cérébrales

Résumé :

Le glioblastome (GBM) est la tumeur cérébrale maligne la plus fréquente et la plus agressive chez l'adulte. Il est hautement prolifératif et invasif et se caractérise par une forte angiogenèse et la présence d'un métabolisme altéré.

Afin de mieux comprendre son développement, nous avons créé des modèles cellulaires tridimensionnels permettant de se rapprocher au mieux de l'architecture complexe de la tumeur. Nous avons également affiné des méthodes in vitro, tels que des essais de croissance ou d'invasion en collagène de type I, pour analyser certaines caractéristiques des GBMs.

L'infiltration diffus des GBMs complique la prise en charge thérapeutique et est à l'origine des récurrences tumorales. Les cellules qui envahissent le parenchyme cérébral sain peuvent former de nouveaux foyers tumoraux à distance de la tumeur originelle. En utilisant une analyse de protéomique sur des échantillons de tumeurs humaines dans des cerveaux de souris récupérées par microdissection laser, nous avons identifié de potentiels acteurs de l'invasion tumorale. Les protéines PLP1 (proteolipid protein 1) et DNM1 (dynamin-1) ont été retrouvées enrichies dans la partie invasive. Leur inhibition in vitro a permis la réduction de la capacité invasive des GBMs et pourrait représenter de potentielles cibles thérapeutiques.

En adaptant son métabolisme glycolytique et oxydatif, les cellules de GBM sont capables de résister à la chimio- et radiothérapie. Le lactate est un des métabolites centraux de la physiologie cérébrale, il est impliqué dans la navette astrocyte-neurone ainsi que dans le développement tumoral. En l'absence de glucose, le lactate alimente la production d'énergie des GBMs par le biais du cycle de Krebs. Les lactates déshydrogénases (LDHs) sont les enzymes qui catalysent l'interconversion du pyruvate et du lactate. La simple perte d'expression des isoformes LDHA ou LDHB ne perturbe pas significativement le développement des GBMs. Cependant, la double extinction de LDHA et LDHB (KO LDHA/B) induit une réduction de la croissance tumorale, de l'invasion et en conséquence, allonge la survie des souris. Les analyses comparatives des données de transcriptomique et de métabolomique révèlent que la lignée double KO LDHA/B augmente le métabolisme oxydatif sensibilisant la tumeur à l'irradiation et augmentant la survie des souris. L'utilisation d'un médicament antiépileptique inhibiteur de l'activité de LDHA et LDHB a permis d'augmenter la survie des souris en association avec le bevacizumab, un médicament anticancéreux ciblant l'angiogenèse. Cette étude met en évidence le réseau métabolique complexe dans lequel LDHA et LDHB sont intriqués. Elle souligne l'importance de la double inhibition de LDHA/LDHB pour impacter le développement tumoral.

Mots clés : Glioblastome, Métabolisme, Lactate déshydrogénase, Sphéroïdes, Invasion, Angiogenèse

Unité de recherche

LAMC - Inserm U1029

Title : Novel mechanisms of brain tumor development

Abstract :

Glioblastoma (GBM) is the most common and malignant primary brain tumor in adults. It can be recognized by its angiogenic and invasive growth, in addition to its altered metabolism.

To study GBM, we developed three-dimensional models to better mimic its complex architecture of tumors. We have also refined in vitro methods, such as spheroid growth or invasion in collagen I matrix, to analyze certain characteristics of GBMs.

Diffuse infiltration of GBMs complicates therapeutic management and is the cause of tumor recurrence. Invading cells into the healthy brain may form new tumor foci from the original tumor. A proteomic analysis of laser microdissection-captured human tumor pieces revealed potential actors of tumor invasion. PLP1 (proteolipid protein 1) and DNM1 (dynamin-1) was found enriched in the invasive part. In vitro inhibition of these protein lead to decrease GBM invasion and may represent potential therapeutic targets.

By adapting their glycolytic or oxidative metabolism, GBM stem-like cells are able to resist chemo- and radiotherapy. Lactate is a central metabolite in brain physiology, involved in the astrocyte-neuron lactate shuttle, but also contributes to tumor development. We show herein that lactate fuels GBM anaplerosis by replenishing the TCA cycle in absence of glucose. Lactate dehydrogenases (LDH) catalyze the interconversion of pyruvate and lactate. Deletion of either LDHA or LDHB did not alter significantly GBM growth and invasion. However, ablation of both LDH isoforms led to a reduction of tumor growth, and, consequently, to an increase in mouse survival. Comparative transcriptomics and metabolomics revealed metabolic rewiring involving high oxidative phosphorylation (OxPhos) in the double LDHA/B KO group which sensitized tumors to cranial irradiation, massively improving mice survival. Survival was also increased when control mice were treated by an antiepileptic which targets LDH activity. Taken together, this highlights the complex metabolic network in which both LDH A and B are integrated and underscores that combined inhibition of LDHA and B is necessary to impact tumor development.

Keywords : Glioblastoma, Metabolism, Lactate dehydrogenase, Spheroids, Invasion, Angiogenesis